

DOE/ER/40913--T1

TECHNICAL PROGRESS REPORT

Nuclear Physics Laboratory

University of Colorado at Boulder

Department of Physics

October 1, 1996

DISCLAIMER

This report was prepared as an account of work sponsored by an agency of the United States Government. Neither the United States Government nor any agency thereof, nor any of their employees, makes any warranty, express or implied, or assumes any legal liability or responsibility for the accuracy, completeness, or usefulness of any information, apparatus, product, or process disclosed, or represents that its use would not infringe privately owned rights. Reference herein to any specific commercial product, process, or service by trade name, trademark, manufacturer, or otherwise does not necessarily constitute or imply its endorsement, recommendation, or favoring by the United States Government or any agency thereof. The views and opinions of authors expressed herein do not necessarily state or reflect those of the United States Government or any agency thereof.

DISTRIBUTION OF THIS DOCUMENT IS UNLIMITED

ng

MASTER

INTRODUCTION

This report summarizes experimental and theoretical work in basic nuclear physics carried out between October 1, 1995, the closing of our last Progress Report, and September 30, 1996 at the Nuclear Physics Laboratory of the University of Colorado, Boulder, under contracts DE-FG03-93ER-40774 and DE-FG03-95ER-40913 with the United States Department of Energy.

The experimental contract supports broadly-based experimental research in intermediate energy nuclear physics. This report includes results from studies of Elementary Systems involving the study of the structure of the nucleon via polarized high-energy positron scattering (the HERMES experiment) and lower energy pion scattering from both polarized and unpolarized nucleon targets. Results from pion- and kaon-induced reactions in a variety of nuclear systems are reported under the section heading Meson Reactions; the impact of these and other results on understanding the nucleus is presented in the Nuclear Structure section. In addition, new results from scattering of high-energy electrons (from CEBAF/TJNAF) and pions (from KEK) from a broad range of nuclei are reported in the section on Incoherent Reactions. Finally, the development and performance of detectors produced by the laboratory are described in the section titled Instrumentation.

The main thrusts of the nuclear theory program at the University of Colorado are (1) the development of field theoretic models of nuclear and subnuclear phenomena and (2) the study of electroweak interactions in the nuclear domain. The former includes studies of scalar and fermion field theories at zero and finite temperatures in the context of the Wilson renormalization group. The latter involves isolating the weak coupling of Z^0 bosons to quarks in the nuclear medium, and studying electroweak radiative corrections, including those involving the axial and isospin-breaking structure of hadrons.

This report contains two Progress Reports, separated for the experimental and theoretical programs.

DISCLAIMER

**Portions of this document may be illegible
in electronic image products. Images are
produced from the best available original
document.**

University of Colorado

Experimental Program

1996 Progress Report

TABLE OF CONTENTS

	Page
I. INTRODUCTION.....	iii
II. EXPERIMENTAL PROGRAM.....	1
A. ELEMENTARY SYSTEMS.....	1
1. Measurement of the Spin Structure of the Nucleon.....	1
2. The CHAOS Collaboration.....	4
a. Measurement of $\pi^+\pi^- \rightarrow \pi^+\pi^-$ Cross Sections with CHAOS.....	5
b. $\pi^\pm p$ Analyzing Powers with CHAOS: TRIUMF Experiment 560.....	7
c. $^4\text{He}(\pi^-, \pi^- pp)$ Invariant Mass Measurement with CHAOS, TRIUMF Experiment 719.....	9
d. π Production in Nuclei.....	13
3. Pion Single Charge Exchange on Deuterium at Low Energies.....	13
4. Pion-Proton Integral Cross Section Measurements	16
5. Exclusive Photodisintegration of the Deuteron at High Photon Energy.....	20
B. MESON REACTIONS.....	22
1. Pion-induced Fission.....	22
2. Coincidence Measurement of Pion Double Charge Exchange: $^4\text{He}(\pi^+, \pi^- p)3p$	24
3. Total and Reaction Cross Sections for π^- -Nucleus Collisions at 400 - 500 MeV.....	26

4.	Preparation for a hypernuclear experiment using stopped kaons at the AGS.....	29
5.	Meson-Nucleus Optical Potentials and the DWIA.....	32
C.	INCOHERENT REACTIONS.....	37
1.	Spin Observables from 600 MeV Polarized Deuteron Quasielastic Scattering.....	37
2.	The Energy Dependence of Nucleon Propagation in Nuclei as Measured in the (e,e'p) Reaction.....	40
3.	QuasiElastic Scattering of 950 MeV/c π Mesons.....	45
D.	NUCLEAR STRUCTURE AND REACTIONS.....	49
1.	Production of ^6He , $^6,7\text{Li}$ and ^7Be in the $\alpha + \alpha$ Reaction above 160 MeV,.....	49
2.	Unfolding of Nucleon Sizes.....	51
3.	IntraNuclear Cascade Calculations for Pion Single Charge Exchange.....	52
E.	INSTRUMENTATION.....	55
1.	HERMES Front Drift Chambers.....	55
2.	Proton Radiography at the AGS.....	59
3.	The Pierre Auger Project.....	62
4.	Pion Soft Error Cross Sections in High Density Memory Chips.....	63
F.	OTHER.....	65
1.	Interactions Between Solar Neutrinos and Solar Magnetic Fields.....	65
G.	PUBLICATIONS AND REPORTS.....	71
H.	PERSONNEL.....	76

INTRODUCTION

This report summarizes work carried out between October 1, 1995 and September 30, 1996 at the Nuclear Physics Laboratory of the University of Colorado, Boulder, under contract DE-FG03-95ER-40913 with the United States Department of Energy. This contract supports experimental work in intermediate energy nuclear physics. The past year has seen research activity in a number of areas, including bringing the four front chambers at HERMES into full operation and completion of the first cycle of data acquisition, finishing a large pion scattering experiment at KEK, and participation in two experiments at CEBAF.

II. EXPERIMENTAL PROGRAM

A. ELEMENTARY SYSTEMS

1. **Measurement of the Spin Structure of the Nucleon**, J. E. Belz,^a J. T. Brack, B. Fox, E. R. Kinney, D. J. Mercer,^b G. Rakness, R. A. Ristinen, W. R. Smythe,^c D. van Westrum (University of Colorado); the HERMES Collaboration; R. Milner, Spokesman.

One of the mysteries of nucleon structure is how in fact the spin is made up from the motion and spin orientation of its constituents. There is not only the spin wavefunction of the valence quarks, but also the possibility of angular momentum contributions, and similar contributions arising from the virtual sea of quark-antiquark pairs and the gluonic fields. The amount of the spin carried by the quarks (valence and sea) is measured in inclusive charged lepton scattering via the inclusive spin structure function $g_1(x, Q^2)$ where Q^2 is the invariant mass of the virtual photon and x is the Bjorken scaling variable $Q^2/2M\nu$ (see Fig. 1 for definition of variables). In the infinite momentum frame, this structure function can be simply interpreted as the measure of the fraction of the quarks with spin aligned parallel to the spin of the nucleon minus the fraction with spin aligned antiparallel to that of the nucleon.

The goal of the HERMES experiment is to explore the result of the scattering of longitudinally polarized leptons (positrons) from longitudinally polarized nucleons. This includes measurement of the inclusive asymmetry which can be related directly to the spin structure function $g_1(x, Q^2)$. New quantities investigated by HERMES are semi-inclusive asymmetries and cross section ratios where a leading hadron (probably containing the initially struck quark) is detected in coincidence with the scattered positron. Measuring these new observables should allow one to separate the contributions from the different quark flavors, the valence and sea quarks and possibly even the angular momentum and gluonic pieces.

The recent history of the HERMES experiment begins when the American collaborators of the HERMES experiment received funding late in 1993 and began construction of their components of the apparatus. The basic experiment consists of a polarized gas target internal to the HERA (27.5 GeV) positron storage ring at DESY, followed by spectrometer magnet instrumented with tracking chambers before, after, and inside. A combination of a gas threshold Čerenkov detector, plastic scintillator hodoscopes, transition radiation detector and lead glass calorimeter are used to identify positrons and hadrons resulting from deep inelastic interactions¹. The Colorado group was responsible for providing drift chambers in the region before scattered particles enter a spectrometer magnet, as described elsewhere in this progress report.² Installation of the target and apparatus took place in the winter of 1994/1995 and the first commissioning data acquisition began in June 1995. High quality data production with polarized positrons began in August 1995 and continued through December 1995.

During the first year's running, the collaboration decided to investigate the scattering from polarized ^3He , given its higher figure-of-merit as a polarized tar-

get. To a good approximation, a polarized ^3He target can be considered a polarized neutron target, since the protons' spins mostly couple to zero. Typical areal densities and polarizations obtained were 1×10^{15} nucleons/cm² and 50%. In addition, data were taken with unpolarized high density hydrogen and deuterium gas targets. Over the data production period of the run, approximately 5.6 million deep inelastic scattering events were recorded.

This was also the first year that operators of the accelerator learned to provide longitudinally polarized positrons to HERMES as well as high luminosity for the other experiments using HERA in its role as positron beam and proton beam collider. The positrons are polarized in the ring via the radiation of synchrotron light which has a spin dependent asymmetry in the production rate. The transverse polarization so produced is rotated into and out of the direction of the beam momentum by a magnet chicane before and after the experiment. Typical beam polarizations were in the range 50%–60%, occasionally reaching 70%.

Analysis of the data began immediately in the summer and by the end of the 1995 run, software to manage the concentrated conversion of raw instrumental data for each event into physical quantities, e.g., tracks, momentum, particle identification, and vertex position, was in place, allowing for the efficient analysis of the entire 1995 data set on the Silicon Graphics CPU farm at DESY. As with any large detector with open geometry, monte carlo simulation of the spectrometer was also intensively investigated in order to check with actual data. After this intense effort of calibration and analysis, the collaboration was able to produce a preliminary measurement of g_1 in April 1996, presented at the Rome Conference³. Further detailed analysis is ongoing and a final analysis is expected to be completed in October 1996. An additional result from inclusive scattering was a measurement of the ratio of the neutron to proton unpolarized structure functions F_2 , which was produced using the scattering from unpolarized H and D targets⁴. In parallel with the analysis of the inclusive scattering, determination of semi-inclusive asymmetries is underway and preliminary results were presented at the SPIN96 conference in Amsterdam. Yields of pions, ρ 's, neutral kaons, ϕ 's, Λ 's, J/Ψ 's and D_0 's have been observed so far. In the case of the ρ 's, one can also look at the exclusive channel $^3\text{He}(e,e'\rho)^3\text{He}$; effects being investigated are so-called color transparency, hadronic components of the virtual photon and the polarization of the ρ . An example of a mass spectrum for the ρ is shown in Fig 2. There is also intensive investigation of deeply virtual Compton scattering, which has been proposed by Ji to be a measure of the angular momentum of the quarks in the nucleon⁵. The yields of mesons with open and hidden charm are being studied in order to study the component of the spin arising from the gluonic field. The present apparatus is not well suited to detecting these mesons because of the large angles between the momenta of the decay products. New apparatus is being planned to enhance the capabilities of HERMES in this exciting area.

Work on all these topics is ongoing and in parallel with the support of the ongoing experiment both in its hardware and software aspects. The collaboration installed a polarized proton source in the winter shutdown, and a number of detectors were improved based on experience from the 1995 run, and the next data production cycle began with an unpolarized positron beam in July 1996; the accelerator began reliably providing high polarization in mid-August. The current

plan of the accelerator is to run with high current polarization until the beginning of December (96), followed by a much shorter winter shutdown, returning to high current polarization operation in March 97, continuing through October or November 1997. Assuming no major problems occur, this should allow the HERMES experiment to complete its measurement of g_1 . There will then be a long shutdown to allow the installation of better vacuum pumps on the accelerator, in which the HERMES experiment will likely install either the polarized ^3He target or a polarized deuterium target. In addition, the long shutdown will be used to upgrade the HERMES apparatus' ability to detect charmed mesons. Another roughly 18 month accelerator production run will follow this long shutdown.

^a Current Address: TRIUMF, 4004 Wesbrook Mall, Vancouver, Canada.

^b Current Address: 2905 Bridge Hampton Court, Falls Church, VA.

^c Retired, Fall 1995.

¹ HERMES Technical Design Report

² Colorado 1996 Progress Report, Sect. II.E.1

³ M.C. Vetterli *et al.* (The HERMES Collaboration), "Overview of the Status of Polarised Structure Functions," *Proceedings of the Workshop on Deep Inelastic Scattering and Related Phenomena*, April 15-19, 1996, Rome.

⁴ K. Ackerstaff, "First Results from the HERMES Experiment using Unpolarized Targets," U. Hamburg, 1996 (unpublished).

⁵ X. Ji, preprint U. of Maryland, PP#97-026, Sept. 1996.

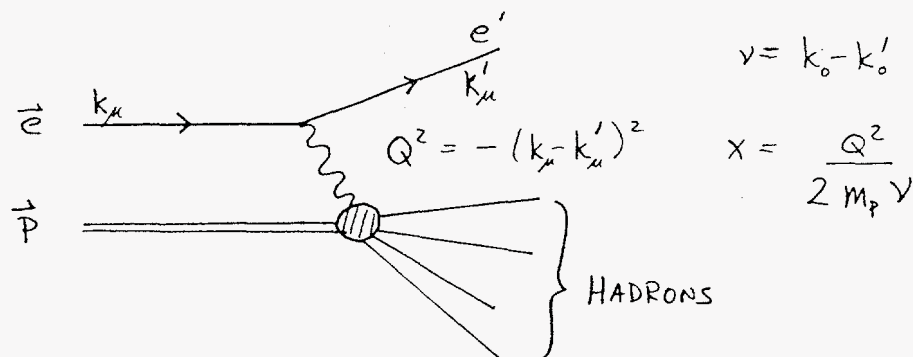


Figure 1.1 Definition of deep inelastic scattering variables.

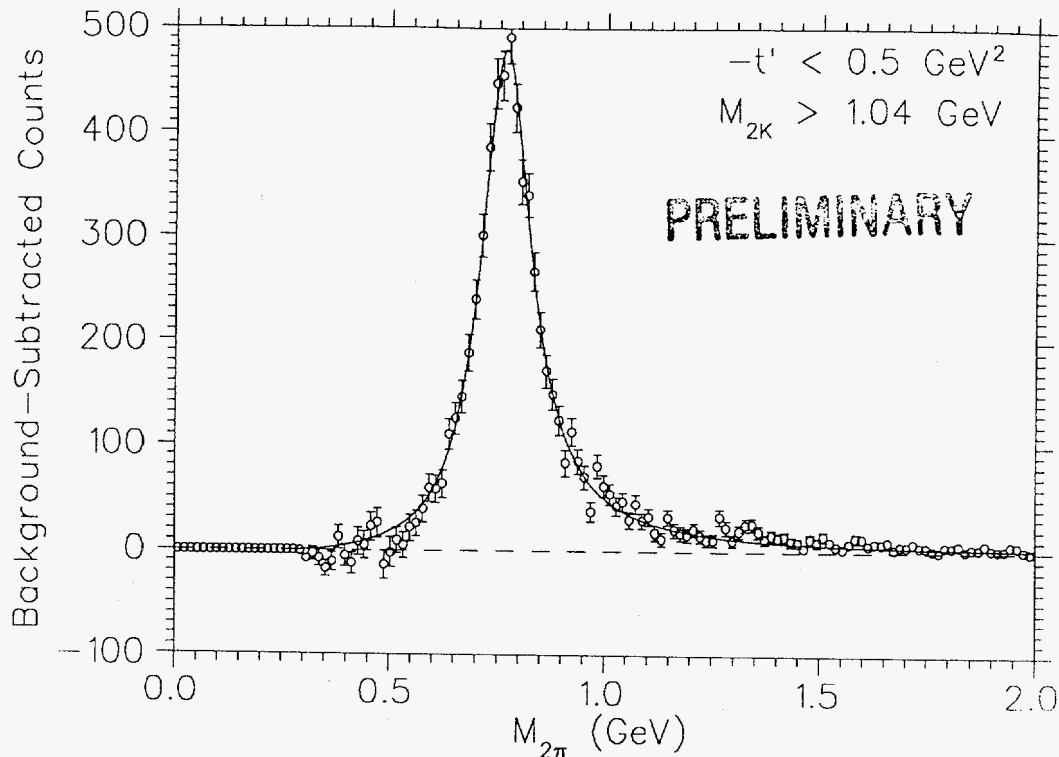


Figure 1.2 Preliminary results of ρ yield as a function of 2π invariant mass.

2. The CHAOS collaboration: TRIUMF, U. of British Columbia, U. of Colorado, U. of Trieste, U. of Regina. J.T. Brack

The CHAOS spectrometer^{1,2} at TRIUMF is a complex detector with tracking capabilities, multi-level triggering, and over 4500 readout channels. Since being commissioned in 1993, it has proved capable of delivering its primary design goals of 1% momentum resolution, rate capability in excess of 5 MHz, and complete angular coverage.

The spectrometer has been in use on TRIUMF's M11 channel for nearly three years now, and 8 low energy pion-induced interaction experiments have been completed. Data from the earliest of these have either been published³, are being prepared for publication^{4,5,6}, or are in the last stages of analysis⁷. Three of these^{4,6,7} are discussed below. Also discussed below are preliminary results from the on-going TRIUMF Experiment 719 ($\pi d \rightarrow \Delta n$).

For the future, several new proposals have been submitted^{8,9}. The latter of these has been reviewed and received the highest priority from the TRIUMF Experiment Evaluation Committee. For this experiment, CHAOS would be moved to the low energy M13 channel, where the low-energy continuation of the high-priority experiment E560⁷ would also be conducted.

- ¹ G. R. Smith, *et al.*, NIM A362, 349-360 (1995).
 - ² J. T. Brack, *Technical Progress Report, September 1995, University of Colorado at Boulder Nuclear Physics Laboratory*, (1995) 7.
 - ³ A Dependence of the $(\pi^+, \pi^+\pi^\pm)$ Reaction near the $2m_\pi$ Threshold, F. Bonutti, P. Camerini, E. Fragiaco, N. Grion, R. Rui, P.A. Amaudruz, J.T. Brack, L. Felawka, E.F. Gibson, G.J. Hofman, M. Kermani, S. McFarland, R. Meier, D. Ottewell, K. Raywood, M.E. Sevier, G.R. Smith, and R. Tacik, *Phys. Rev. Lett.* 77, 603 (1996).
 - ⁴ On the Process of Pion Production in Nuclei, F. Bonutti, P. Camerini, E. Fragiaco, N. Grion, R. Rui, J.T. Brack, L. Felawka, E.F. Gibson, G.J. Hofman, M. Kermani, E.L. Mathie, S. McFarland, R. Meier, D. Ottewell, K. Raywood, M.E. Sevier, G.R. Smith, and R. Tacik, Submitted to *Phys. Rev. C*, September 1996.
 - ⁵ Pion Initial State Interactions in the $^{12}\text{C}(\pi^+, ppp)$ reaction, TRIUMF Proposal for Experiment 722.
 - ⁶ $\pi^+\pi^- \rightarrow \pi^+\pi^-$ Cross Sections near Threshold, M.Kermani, F. Bonutti, P. Camerini, E. Fragiaco, N. Grion, R. Rui, J.T. Brack, L. Felawka, E.F. Gibson, G. Hofman, E.L. Mathie, S. McFarland, R. Meier, D. Ottewell, O. Patarakin, K. Raywood, M.E. Sevier, G.R. Smith, R. Tacik and V. Tikhonov, Submitted to *Phys. Rev. Lett.*, September 1996.
 - ⁷ Low Energy $\pi^\pm p$ Analyzing Powers, Triumf Experiment 560.
 - ⁸ Investigation of the $\pi\pi$ Invariant Mass Distributions of Nuclear $(\pi^+, \pi^-\pi^+)$ Reactions, TRIUMF Proposal for Experiment 781.
 - ⁹ $\pi^\pm p$ Differential Cross sections in the Coulomb-Nuclear Interference Region, TRIUMF Proposal for Experiment 778.
- 2a. **Measurement of $\pi^+\pi^- \rightarrow \pi^+\pi^-$ Cross Sections with CHAOS** J.T. Brack (Univ. of Colorado); G.R. Smith, P.A. Amaudruz, L. Felawka, R. Meier, D.Ottewell (TRIUMF); M. Kermani, G. Hofman, S. McFarland, K. Raywood, (Univ. of B.C.); F. Bonutti, P. Camerini, E. Fragiaco, N. Grion, R. Rui (Univ. of Trieste); M.E. Sevier (Univ. of Melbourne); E.L. Mathie, R. Tacik (Univ. of Regina); E.F. Gibson (CSU Sacramento); O. Patarakin, V. Tikhonov (Kurchatov Institute, Moscow)

The application of QCD in the low-energy region through the use of phenomenological Lagrangians such as chiral perturbation theory¹ has made low energy $\pi\pi$ scattering of great interest. This is mainly due to the fact that $\pi\pi$ scattering observables provide a sensitive tool for studying the explicit breaking of chiral symmetry in strong interactions and because, in the chiral limit, the $\pi\pi$ scattering lengths vanish exactly. In addition, $\pi\pi$ scattering phase shifts and scattering lengths are required in order to establish the parameters of chiral perturbation theory and other effective low-energy models.

Due to the absence of colliding pion beams, all of the experimental data on $\pi\pi$ observables have been determined via indirect methods. To date, the main sources of the $\pi\pi$ scattering parameters are K_{e4} decay and $\pi N \rightarrow \pi\pi N$ reactions. The former suffers from a small branching ratio (4×10^{-5}). In the latter case, the required information is obtained by separating the contribution of the one-pion exchange (OPE) diagram via extrapolation to the pion pole. In the past, this approach has been used for incident pion momenta p_π in the 4–10 GeV/c range, but the extrapolation procedure is not strictly unambiguous. The contribution of the non-pion components (Δ , N^*) can affect the reliability of the results.

The present experiment has obtained $\pi\pi$ scattering parameters in the important region near threshold. The required data on the $\pi^- p \rightarrow \pi^+ \pi^- n$ interaction were obtained for five projectile kinetic energies $220 \leq T_\pi \leq 300$ MeV with the CHAOS spectrometer during TRIUMF Experiment 568. Pions were incident on a liquid hydrogen target, inserted in the central bore of the CHAOS magnet. The experiment was designed to look for several pion production mechanisms, including $\pi^+ p \rightarrow \pi^+ \pi^+ n$, $\pi^+ p \rightarrow \pi^+ \pi^0 p$, $\pi^- p \rightarrow \pi^- \pi^0 p$, and $\pi^- p \rightarrow \pi^+ \pi^- n$, by making use of different configurations of the flexible CHAOS 2nd Level Trigger². Only the latter data are reported here. The others are still under analysis.

For acquisition of the present data, two triggers were used. The first required the presence of two charged particles exiting the target region, one positive and one negative. This trigger obtained data for this reaction and for the $\pi^- p \rightarrow \pi^- \pi^0 p$ reaction simultaneously. The second trigger selected events with a single positively charged particle in the correct momentum range for the π^+ from the $\pi^- p \rightarrow \pi^+ \pi^- n$ reaction, since this momentum provides a unique signature for the reaction.

An analysis of the resulting $\pi^- p \rightarrow \pi^+ \pi^- n$ cross sections, following the Chew-Low³ extrapolation method to the unphysical point $t = m_{\pi\pi}$, has provided the $\pi\pi$ cross section at center-of-mass energy $m_{\pi\pi}$. Dispersion-type relations, based on the Roy equations⁴, have been applied in order to obtain self-consistent $\pi\pi$ scattering amplitudes, including physical considerations such as unitarity and analyticity. From these, the value of the isospin zero S-wave scattering length a_0^0 has been determined. A publication has been prepared for Physical Review Letters.

¹ J. Gasser, H. Leutwyler, Ann. Phys. **158** (1984) 142.

² K.J. Raywood, P.A. Amaudruz, S.J. McFarland, M.E. Sevier, G.R. Smith, NIM **A357** (1995) 296.

³ G.F. Chew and F.E. Low, Phys. Rev. **113** (1959) 1640.

⁴ S.M. Roy, Phys Lett. **B36** (1971) 353.

2b. $\pi^\pm p$ Analyzing Powers with CHAOS: TRIUMF Experiment 560

J.T. Brack, R.A. Ristinen, R.J. Peterson, J.J. Kraushaar (Univ. of Colorado);
G.R. Smith, P.A. Amaudruz, L. Felawka, R. Meier, D. Ottewell (TRIUMF);
G. Hofman, M. Kermani, S. McFarland, G. Tagliente, T. Ambardar (University of British Columbia); N. Grion, R. Rui, P. Camerini (Univ. of Trieste);
M.E. Sevier (Univ. of Melbourne); E.L. Mathie, R. Tacik (Univ. of Regina);
E.T. Boschitz (Univ. of Karlsruhe)

A second phase of TRIUMF E560 has been completed on TRIUMF's M11 channel. Data have been collected over a range of angles from about 60° to 180° , at 10 incident pion energies between 117 and 270 MeV. Sufficient data were taken during six weeks in May and June to provide asymmetries with statistical uncertainties of $\pm 1\text{-}2\%$ for most of this angular range.

Analysis of the data from the first (1995) phase of E560¹ revealed that, although CHAOS detector performance was flawless, the online target polarization data were unreliable. Further, the TRIUMF target group could not recover these data offline. This forced a decision to repeat most of the first phase of the experiment during the 1996 beam cycle. However, at the beginning of this cycle, it became apparent that polarization information would still not be accurate, forcing a revision in the experimental game plan.

The new plan involved determining the target polarization in situ by measuring the π^+p asymmetry at 140 MeV. A unique feature of the asymmetries at this energy is that all previous experimenters, and all phase shift analyses^{2,3,4}, agree on precise values for an angular distribution of a πp observable. Using this fact, the target was polarized (to some unknown value) and inserted into CHAOS. Data were then taken at a series of energies, beginning and ending with 140 MeV. This sequence was then repeated with some opposite (but still unknown) polarization. The average target polarization could then be extracted from the 140 MeV data at the beginning and end of each sequence, and thus it was known at any time in between, and could be used for calculating asymmetries at the other energies.

Using this technique, it was determined that the average target polarization was about 40%, about 25-35% lower than planned. The polarization is a dominant factor in determining the statistics needed to obtain a fixed final uncertainty in the asymmetry (see Figure 2.1). A final δA_y of less than 0.04 is required if the results are to be useful in the πp database for future phase shift analysis. This led to a decision that the original goal be modified from acquiring data at energies between 67 and 140 MeV to energies between 117 and 270 MeV, where the cross sections are larger.

The data acquired during this beam cycle are being analyzed at a rapid rate using software and techniques developed from the earlier analysis. An example of preliminary results is shown in Figure 2.2, compared to two phase shift analyses^{3,4}.

The CHAOS group will return to this experiment to complete the experimental objectives, including the lower energy phase at energies down to 50 MeV, when an improved target is available.

- ¹ J.T. Brack, *et al.*, *Technical Progress Report, September 1995, University of Colorado at Boulder Nuclear Physics Laboratory*, (1995) 7.
- ² M.E. Sevior *et al.*, *Phys. Rev. D* **48**, 3994 (1993)
- ³ KH80 PSA Solutions of the Karlsruhe Group, as taken from SAID on-line program.
- ⁴ R. A. Arndt and L. O. Roper, SAID on-line program, version SM95.

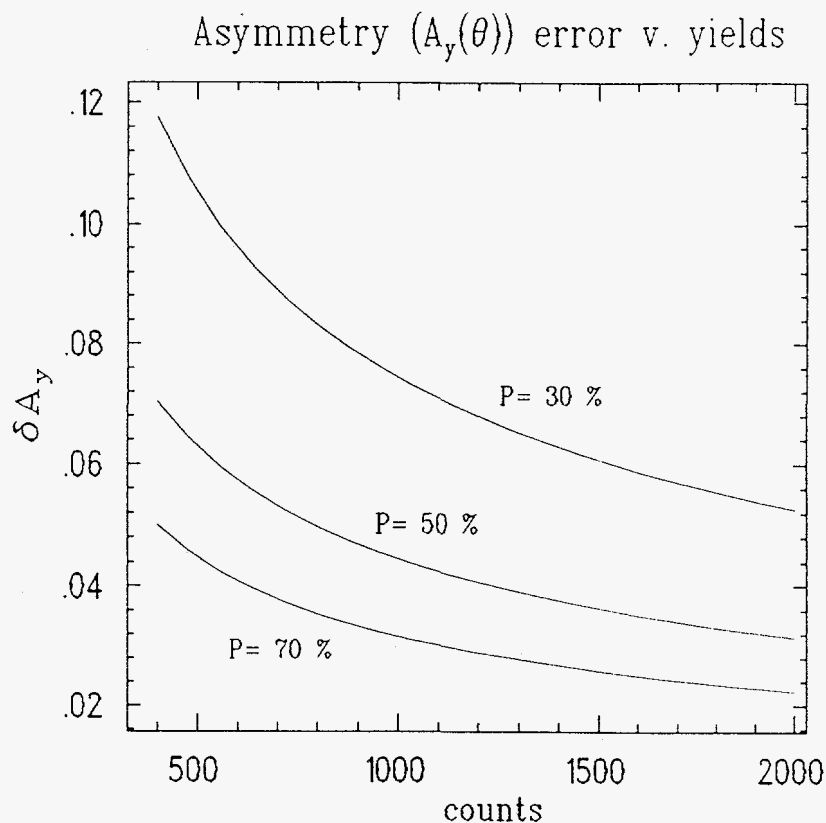


Figure 2.1 Asymmetry uncertainty is plotted as a function of yield, for an example case of 86 MeV π^-p at 50° . The lines represent target polarizations of 70, 30 and 50%. The desired 0.04 uncertainty is obtained with about 500 counts for 70% target polarization, but this grows to 2000 counts or more when the polarization drops to less than 50%.

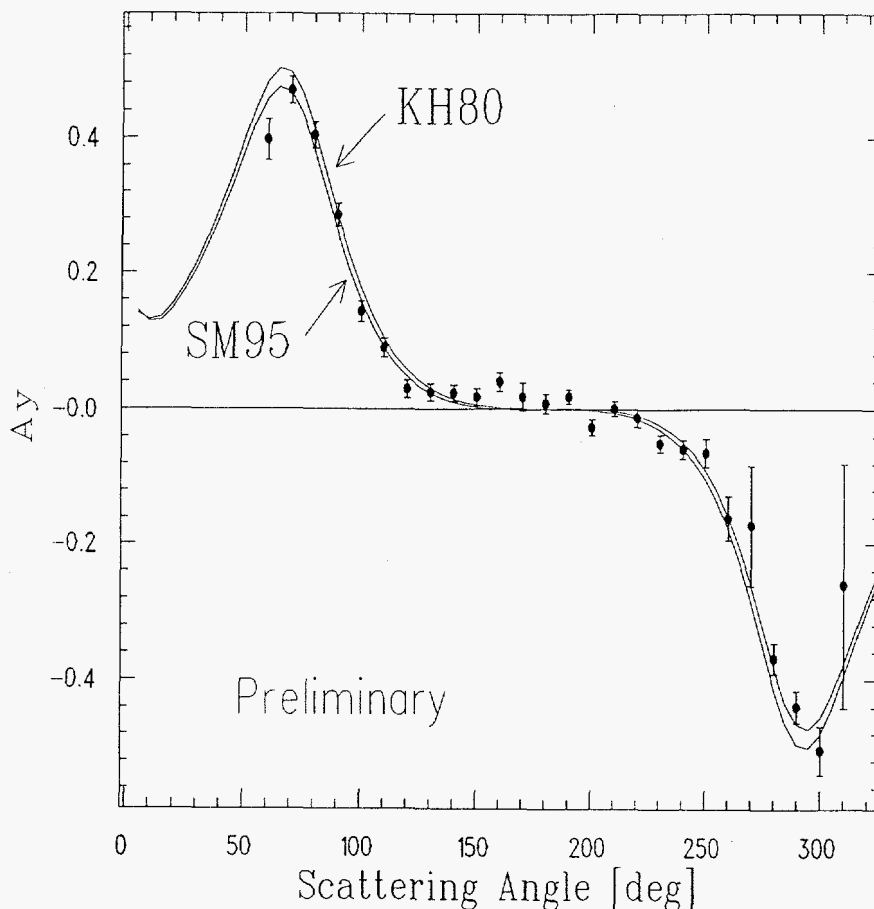


Figure 2.2 Preliminary asymmetries from the 1996 data, for π^+p at 155 MeV. The lines represent the phase shift analyses of the Karlsruhe and SAID groups.

- 2c. $^4\text{He}(\pi^-, \pi^- pp)$ Invariant Mass Measurement with CHAOS, TRIUMF Experiment 719 J.T. Brack (University of Colorado); R. Meier, P. Amaudruz, L. Felawka, D. Ottewell, G. R. Smith (TRIUMF); T. Ambardar, G. Hofman, M. Kermani, G. Tagliente (University of British Columbia); J. Clark, M. Sevier (University of Melbourne); P. Hong, E. L. Mathie, R. Tacik (University of Regina); J. Gräter, G. J. Wagner (University of Tübingen); F. Bonutti, P. Camerini, N. Grion, R. Rui (University of Trieste)

In the recent past a great deal of attention has focussed on the possible existence of a dibaryon candidate (called the d') which may exist at 2.06 GeV. Such a state is predicted in QCD inspired models to exist at about this energy with $J^\pi = 0^-$, and composition consisting of a diquark with $l=1$ relative to a spin one, four quark cluster. Indirect evidence for such a state, with a width of $\Gamma_{\pi NN}=0.5$ MeV, has been claimed to exist¹ in measurements of the excitation function of inclusive pion DCX on a variety of target nuclei. The narrow width seems plausible given that the quantum numbers prohibit decay into the NN channel, and the mass is only just above the πNN threshold.

The available data for the total DCX cross section on ^4He favor the predicted sharp rise of the cross section above the d' threshold of about $T_\pi = 85$ MeV².

Unfortunately, the few data in the critical region from 80 to 120 MeV suffer from large error bars or systematic uncertainties due to extrapolations necessary to account for finite detector acceptances.

In contrast to the inclusive DCX experiments, the invariant mass of the dibaryon decay product π^-pp in the ${}^4\text{He}(\pi^+, \pi^-pp)pp$ reaction near the predicted peak of the dibaryon production cross section provides a model independent view of the process. Observation of a peak in this invariant mass distribution on top of the broad DCX background would provide evidence for the existence of a dibaryon in the πNN system. The CHAOS detector provides a unique opportunity to investigate this issue. No other detection system in the world presently exists which could be used to measure the invariant mass of the d' in a pion-induced reaction.

Therefore, the CHAOS group is looking for the d' by investigating the double charge exchange reaction $\pi^+ {}^4\text{He} \rightarrow \pi^-pppp$. If the d' is present, a large part of the DCX cross section in a region above the d' production threshold should be due to the reaction $\pi^+ {}^4\text{He} \rightarrow d'pp \rightarrow (\pi^-pp)pp$ ³. Preliminary online results from this experiment indicate a behavior of the cross section consistent with the d' hypothesis¹.

Additional evidence has surfaced from other laboratories. Recently, the WASA/PROMICE collaboration at CELSIUS reported a four sigma signal at 2063 MeV in the two pion production reaction $pp \rightarrow \pi^+\pi^-pp$ ³.

In the CHAOS detector, charged particles were accepted over 325° in the scattering plane, and within $\pm 7^\circ$ out of plane. In the region of the incoming and outgoing beam, the drift chambers WC3 and WC4 were switched off (the incoming beam was reconstructed from the hits in the proportional chambers WC1 and WC2). The detector was set up to detect simultaneously a π^- and at least two protons from the ${}^4\text{He}(\pi^+, \pi^-pp)pp$ reaction. For the outgoing pion, a complete track was required, leaving information in all four wire chambers and the scintillation and Cerenkov counters. The protons had to come out at least to the second wire chamber. Then, with track information in WC1 and WC2, and with the vertex information from the pion track, a momentum reconstruction is possible. Consideration of short proton tracks lowered the minimum proton energy threshold, substantially improving the acceptance. The trigger design was based on these requirements, asking for one negative track and four hits each in WC1 and WC2. A ${}^4\text{He}$ gas target at standard temperature and pressure was used to minimize energy loss for the protons. The helium gas filled the volume surrounded by WC1.

Figure 2.3 shows a DCX event recorded during the beam time in February 1996. An incoming π^+ reacted in the ${}^4\text{He}$ target, and the π^- track and two proton tracks were recorded. In this case, pions and protons were identified by their energy loss in the scintillators.

From the measured momenta of the three detected particles, the invariant mass of the π^-pp system was calculated; the d' should show up as a peak in the invariant mass spectrum. As only two of the four protons in the final state can possibly come from the d' , the peak will be accompanied by a combinatorical background from detecting one or two protons not from the d' . Simulations show that the shape

of this combinatorical background is very similar to the spectra expected from nonresonant DCX, assuming five body phase space for the final state.

Data were taken for two weeks in January/February 1996 at an incoming pion kinetic energy of 115 MeV, taking about 120 million events. A large number of triggers were produced by events with more than one incoming pion and by events with positive pions backscattering from the CFT blocks. After applying cuts to the number of tracks found, the trajectories of incoming pions, the identification of one negative pion and two protons in the expected momentum ranges, restrictions for the vertex position and for track pairs which have an angle close to 180° relative to each other, and excluding certain CFT blocks from the analysis, about 100 DCX events were found. Good DCX events were lost in the highly restrictive cuts of this first pass of the analysis, therefore an improved analysis is under way which should increase the number of recognized events substantially.

Figure 2.4 shows the invariant mass spectrum for the DCX events identified so far. Clearly, the poor statistics do not allow definitive conclusions. Nevertheless, an enhancement can be seen over the simulated nonresonant DCX background in the region of 2060 MeV. The non-resonant background shown in Fig. 2 describes 5 body phase space and was obtained using the CERN program FOWL. More complete simulations have also been performed using the CERN program GEANT, which fully describes the detector and folds in the CHAOS event reconstruction. The GEANT results are consistent with FOWL. The enhancement has a statistical significance of about two sigma. Data acquisition at this energy continued in July and August, and will continue this fall until the statistics allow a solid statement. Should the enhancement persist, it would be a strong indication for the existence of the d' .

¹ R. Bilger et al., Z. Phys. **A343**, 491 (1992); Phys. Rev. Lett. **71**, 42 (1993).

² H. Clement et al., Phys. Lett. **B337**, 43 (1994).

³ W. Brodowski et al., Preprint Univ. Tübingen (1996), Z. Phys. (in Press).

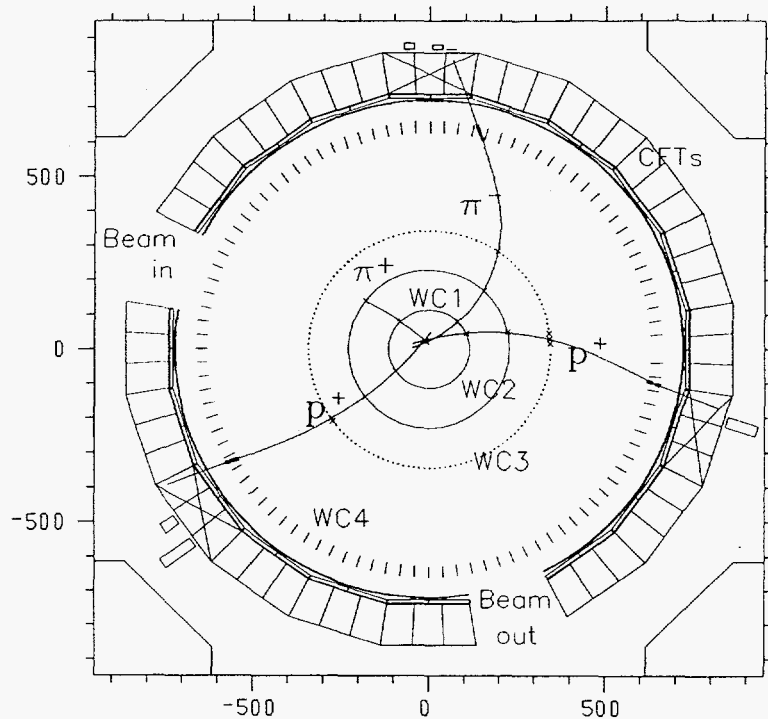


Figure 2.3 ${}^4\text{He}(\pi^+, \pi^- pp)pp$ event detected in CHAOS.

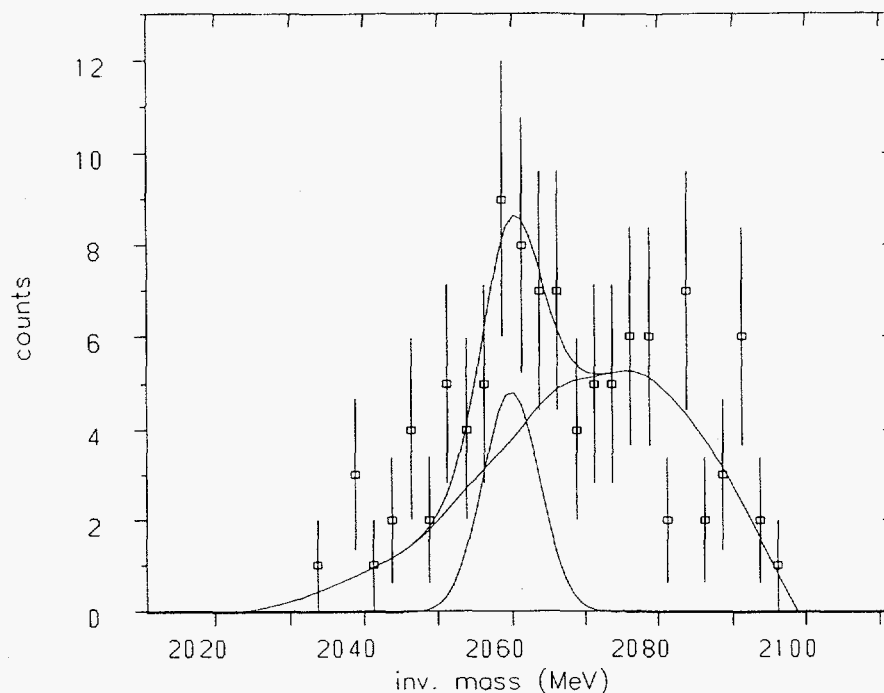


Figure 2.4 Spectrum of the invariant mass. The overlaid curve is the sum of a Gaussian peak in the region of the enhancement at 2060 MeV, and a wide background, describing nonresonant DCX (5 body phase space). The width of the peak was set to 9 MeV FWHM, the detector resolution expected from GEANT simulations. The size of the enhancement is about 2σ .

2d. π Production in Nuclei J.T. Brack (Univ. of Colorado); G.R. Smith, L. Felawka, R. Meier, D. Ottewell (TRIUMF); M. Kermani, G. Hofman, S. McFarland, K. Raywood, (Univ. of B.C.); F. Bonutti, P. Camerini, E. Fragiaco, N. Grion, R. Rui (Univ. of Trieste); M.E. Sevior (Univ. of Melbourne); E.L. Mathie, R. Tacik (Univ. of Regina); E.F. Gibson (CSU Sacramento)

The pion production reaction in pion-nucleus collisions has been investigated at TRIUMF using the CHAOS spectrometer. A 5 MHz beam of positive pions at 283 MeV kinetic energy was incident on nuclear targets of ^2H , ^{12}C , ^{40}Ca and ^{208}Pb , and the reactions $(\pi^+, \pi^+\pi^-)$ and $(\pi^+, \pi^+\pi^-p)$ were studied. All designated charged particles in the final state were observed, using a CHAOS trigger requiring at least two outgoing tracks in the first level, and either two tracks of opposite polarity or three tracks having a vertex within a fixed target region in the second level. Events passed the first and second levels of trigger at rates of about 4kHz and 60Hz and, with about 15% dead time, were written to tape at about 50Hz.

In analysis, particle identification was made on the basis of pulse height distributions in the first level trigger scintillators, and on particle momentum, from the reconstructed radius of curvature in the CHAOS field. Several loose software cuts were made, including one demanding the two-particle opening angle to be greater than 2 degrees, thus excluding e^+e^- background pairs from the analysis. For the remaining events, calculations were made of the nucleus (or missing) recoil momentum, the proton energy (this is directly measured when the proton was observed, and calculated otherwise), and the missing energy.

Histograms of these quantities reveal interesting features of the pion production process. For instance, since the calculated proton energy spectra ignore final state interactions (FSI) while the measured spectra necessarily include FSI, the fact that the measured and calculated proton energy spectra are nearly identical indicates that final state interactions for the proton are nearly negligible. It is also concluded that FSI are negligible for the exiting pion pair, and that $(\pi, 2\pi)$ is essentially a quasifree process.

A publication has been submitted to Physical Review C.

3. Pion Single Charge Exchange on Deuterium at Low Energies M. V. Keilman, D. J. Mercer, R. J. Peterson (University of Colorado), M. A. Espy (University of Minnesota), S. P. Blanchard, Q. Zhao (New Mexico State University), K. Johnson (University of Texas), J. F. Amann, R. L. Boudrie, C. L. Morris, R. M. Whitton, J. D. Zumbro (Los Alamos National Laboratory), and I. Supek (Rudjer Boskovic Institute).

In October of 1994, we did an experiment at the EPICS channel at LAMPF, using the Neutral Meson Spectrometer to measure the cross section of the reaction $d(\pi^-, \pi^0)$ at 65 MeV and 96.5 MeV. This work complements experiments done at 164 MeV¹, 263 and 371 MeV², and 500 MeV³.

The crates of the NMS were set in two configurations at each energy (here called the "0°" and "90°" settings), to cover forward angles with some degree of overlap.

To this end, the target was less than a meter from the crates, providing an angular acceptance of about 50°. The deuterium came in the form of CD₂. CH₂ and C targets, approximately matched for carbon content, were run for normalization. The total running time was about two weeks.

Despite the built-in normalization afforded by the CH₂, an acceptance must be generated via monte carlo, in this case by the well-established code PIANG. This not only provides broad neighborhoods around the hydrogen peak, but also is convincing evidence that the NMS behavior is understood. It need not be accurate in an absolute sense, because cross sections are ultimately to be viewed relative to known free charge exchange values; but to avoid a large correction, the simulation ought to be parameterized to mimic the machine at run-time as closely as possible.

The effort to do so has hardware and software steps. Three hardware factors affect the NMS's behavior: geometry, conversion efficiency, and trigger logic. The positions and orientations of the crates determine the range of angles and energies that it can see. These are set in PIANG by a matrix which is computed via surveys done during the runs. The conversion efficiency of the BGO selects some fraction of the accepted events, and can be modelled by the EGS tracking code. Finally, events converted in each crate must pass an energy threshold below which no trigger is generated. The values are inferred from data and given to PIANG. Once hardware conditions are matched, any software tests imposed on replayed data must also be matched. These primarily include gates on π^0 mass, the location of the reaction point, and tests setting the fiducial regions of the crates. Beyond all this, there may yet be differences between the real NMS acceptance and PIANG's calculation. They should fold into a single energy- and angle-independent factor at each geometry, gotten through a comparison of hydrogen data to accepted numbers.

The 65 MeV data are pictured in Figures 3.1 and 3.2. Fig. 3.1 is the hydrogen spectrum, calculated with the formula

$$\frac{d\sigma}{d\Omega}(\theta) = \frac{N_H(\theta)}{N_{\pi^-} \cdot n_H \cdot \epsilon(\theta) \cdot d\Omega}, \quad (1)$$

where N_H is the number of counts in a given angle bin, N_{π^-} is the number of π^- striking the target, n_H is the areal density of hydrogen in the target, and ϵ is the acceptance and efficiency as produced by PIANG. The numbers so generated were multiplied by a uniform factor of 1.055 at the 0° (diamonds) configuration and 2.57 at 90° (squares); the solid line denotes the standard SAID phase-shift calculation⁴. The results for deuterium are displayed in Figure 3.2. Raw cross-sections were obtained in a manner similar to the hydrogen case, then modified according to

$$\frac{d\sigma}{d\Omega}(\theta)_D = \frac{\frac{d\sigma}{d\Omega}_{raw}}{\frac{d\sigma}{d\Omega}_H} \cdot \frac{d\sigma}{d\Omega}_{SAID}. \quad (2)$$

In this way, strong dependences on the model are divided out, including the "fudge factor" above. The solid line in this plot depicts a theoretical model of the cross-section, incorporating hydrogen spin-flip amplitudes and a simple Pauli-blocked

modification of non spin-flip amplitudes. The uncertainties in both figures reflect statistics only. Analogous treatment of the 96.5 MeV data is underway and nearing completion.

While some tweaking yet needs to be done with the model, the data as presented above are essentially final, and close the analytical portion of the experiment.

¹ H. Garcilazo, Phys. Rev. C **47**, 957 (1993).

² H. J. Park *et al.*, Phys Rev. C **51**, 1613 (1995).

³ R. J. Peterson *et al.*, Phys Rev. C **52**, 33 (1995).

⁴ SM95 solutions.

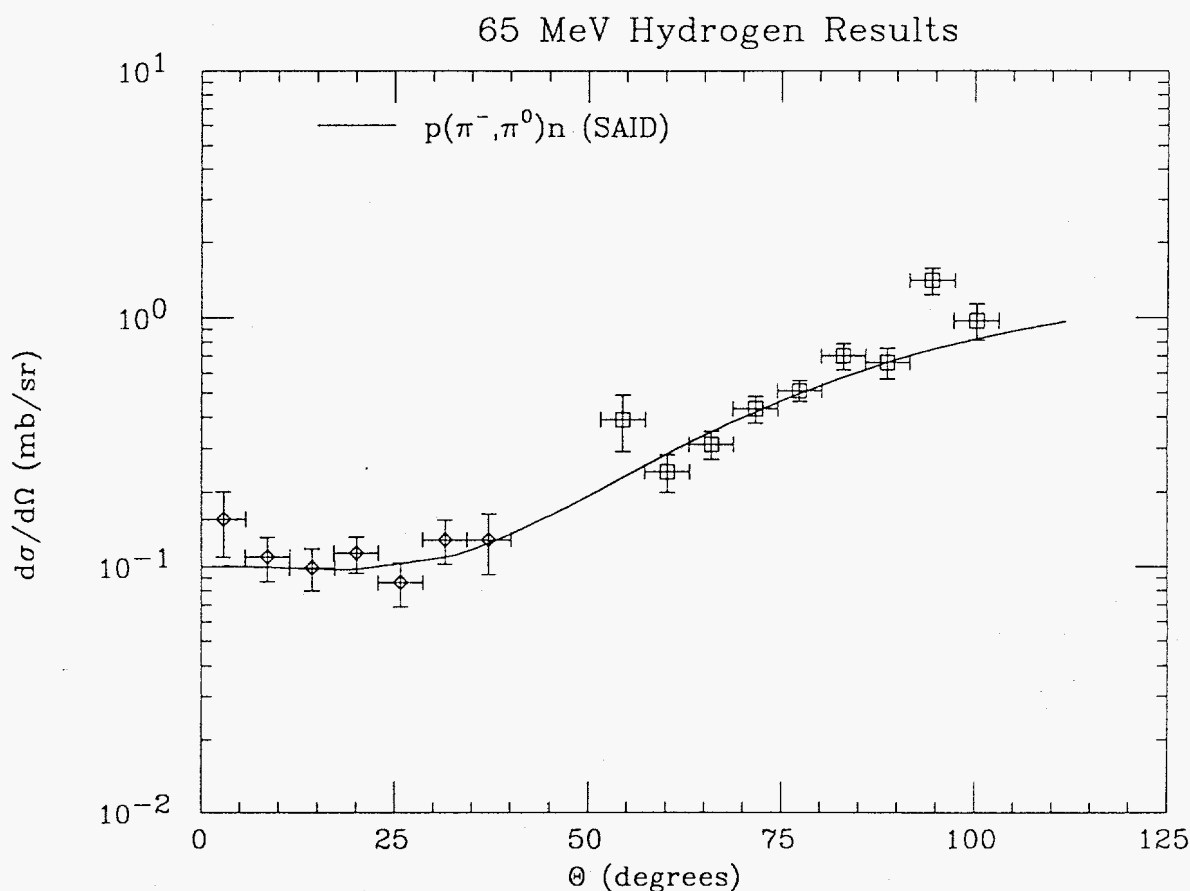


Figure 3.1 Corrected differential cross section for $p(\pi^-, \pi^0)n$ at 65 MeV. The solid line is the free cross section as calculated by SAID. The two symbols indicate data sets from the two different geometries employed.

65 MeV Deuterium Results

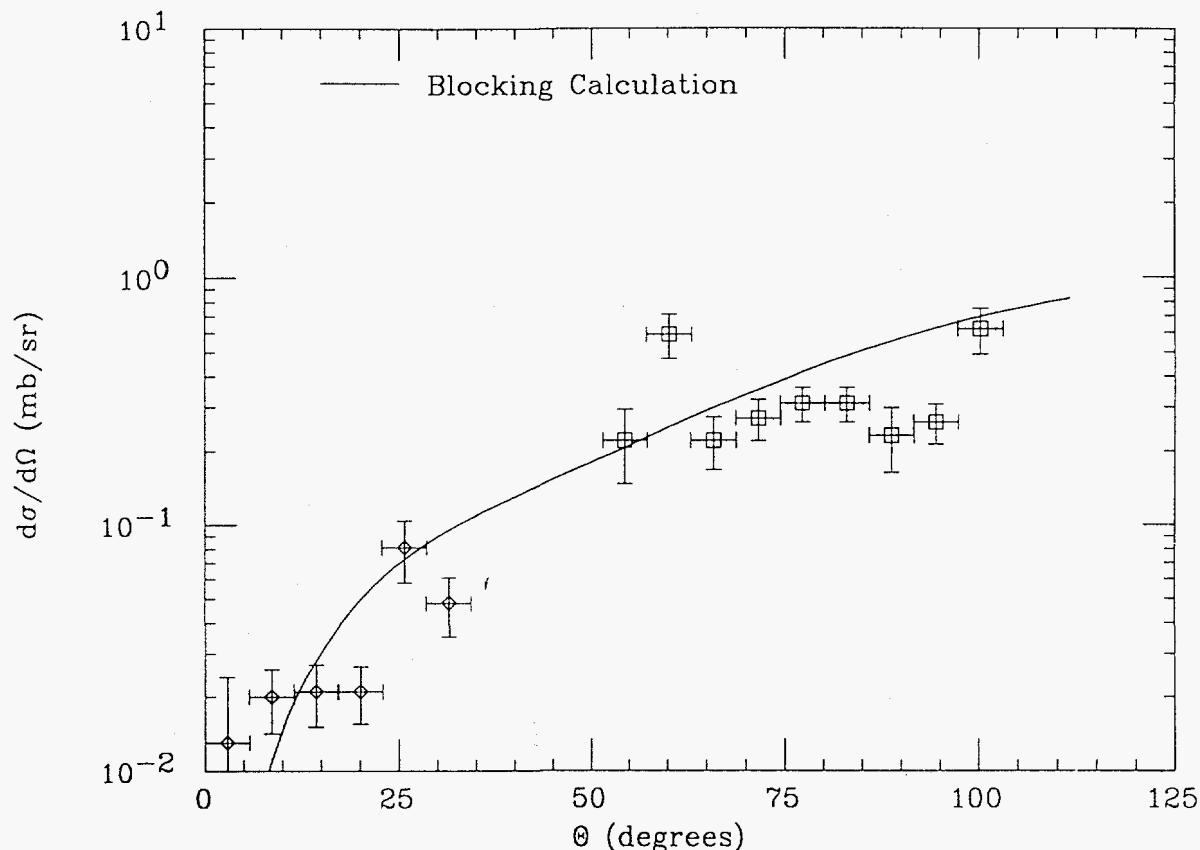


Figure 3.2 Differential cross section for $d(\pi^-, \pi^0)$ at 65 MeV. The solid line is a Pauli blocking calculation.

4. **Pion-Proton Integral Cross Section Measurements**, B. J. Kriss, R. A. Ristinen, S. Høibråten, M. D. Holcomb, M. D. Kohler, J. J. Kraushaar, A. Saunders, W. R. Smythe (University of Colorado); C. L. Morris, M. Rawool-Sullivan, R. M. Whitton (Los Alamos National Laboratory); J. T. Brack (University of British Columbia); E. F. Gibson (California State University); J. L. Langenbrunner (University of Minnesota)

Analysis of the data from LAMPF Experiment 1190, measurements of $\pi^\pm p$ integral cross sections, is complete. The goal of this experiment was twofold. First, to measure in one experiment $\pi^\pm p$ integral cross sections in a continuous sweep from the low energy region over the P33 resonance. Second, to provide those measurements with combined normalization and statistical errors of less than 5%. It was felt that this range of uncertainty was adequate to address the differences between several sets of recently published $\pi^\pm p$ differential cross sections^{1,2,3,4} which disagree with the popular phase shift solutions of the Karlsruhe and VPI groups^{5,6} and the recent $\pi^+ p$ integral cross section measurements of Friedman *et al.*^{7,8,9} which agree with those phase shift solutions.

Experiment 1190 used the transmission technique to measure integral or partial total cross sections. The definition of the transmission technique and a detailed description of the experimental setup was included in the 1995 Technical Progress

Report. The measured π^+p partial total cross section is just the integral of the elastic scattering cross section outside of some forward angle. For the π^-p interaction, the measurement is slightly different. The π^- integral cross section contains not only the partially integrated elastic scattering cross section, but also the total single charge exchange cross section. Our experiment measured integral cross sections for π^+p scattering into angles greater than 30° (lab) at 45 energies from 40 to 500 MeV. A similar measurement was made at 18 energies from 80 to 450 MeV for the π^-p integral cross section. In addition, several $\pi^\pm p$ integral cross sections were measured at energies greater than 260 MeV for pions scattering into angles greater than 20° . It should be noted that at pion kinetic energies greater than 300 MeV, our data need to be corrected for single pion production reactions that contribute unwanted events to the integral cross sections. The five single pion production reactions are:

$$\begin{aligned}\pi^+p &\longrightarrow \pi^+\pi^+n, \\ \pi^+p &\longrightarrow \pi^+\pi^0p, \\ \pi^-p &\longrightarrow \pi^-\pi^0p, \\ \pi^-p &\longrightarrow \pi^-\pi^+n, \\ \pi^-p &\longrightarrow \pi^0\pi^0n.\end{aligned}$$

Because of this problem, we will not report any results in this progress report for pion energies greater than 300 MeV.

All phases of the analysis, including cross section extraction, target thickness determination, and beam energy calibration, are completed. This past year saw the completion of all GEANT¹⁰ Monte Carlo simulations used to generate corrections to both the beam and scattered pions. The results that we present in this report are final but are plotted with only statistical error bars. There is an additional normalization uncertainty of $\pm 3\%$ for the integral cross sections. The additional error primarily reflects systematic uncertainties in the target thickness and beam energy measurements. In Figure 4.1, the measured integral cross sections for π^+p scattering greater than 30° from 40 to 300 MeV are compared to the latest results from the Friedman group, to one set of integrated differential cross sections, and to two phase shift solutions. The KH80⁵ phase shift solutions are used as the basis for comparing all the different results. The new Friedman results shown have not yet been published; they represent a new analysis of the earlier published results^{7,8,9} with corrections mainly due to a new determination of their energy calibration¹¹. Both partial total cross section experiments show good agreement with the KH80 phase shift solutions on resonance, and both show significant deviation from KH80 at energies lower than 100 MeV. VPI's latest phase shift solution, SM95¹², is also included for comparison. Our integral cross sections are appreciably higher than SM95 between about 100 and 170 MeV. Neither of the partial total experiments yield cross sections as low as those from the integrated differential measurements of Brack *et al.*^{1,2,3,4}. The reasons for the discrepancies between the partial total cross sections and the integrated differential cross sections are not understood. Our results for π^-p integral cross sections, scattering greater than 30° , from 80 to 300 MeV are shown in Figure 4.2. The π^- cross sections and the phase shifts include both the elastic and single charge exchange contributions.

- ¹ J. T. Brack, J. J. Kraushaar, J. H. Mitchell, R. J. Peterson, R. A. Ristinen, J. L. Ullmann, D. R. Gill, R. R. Johnson, D. Ottewell, F. M. Rozon, M. E. Sevier, G. R. Smith, F. Tervisidis, R. P. Trelle, and E. L. Mathie, Phys. Rev. C **34**, 1771 (1986).
- ² J. T. Brack, J. J. Kraushaar, D. J. Rilett, R. A. Ristinen, D. F. Ottewell, G. R. Smith, R. G. Jeppesen, and N. R. Stevenson, Phys. Rev. C **38**, 2427 (1988).
- ³ J. T. Brack, R. A. Ristinen, J. J. Kraushaar, R. A. Loveman, R. J. Peterson, G. R. Smith, D. R. Gill, D. F. Ottewell, M. E. Sevier, R. P. Trelle, E. L. Mathie, N. Grion, and R. Rui, Phys. Rev. C **41**, 2202 (1990).
- ⁴ J. T. Brack, P. A. Amaudruz, D. F. Ottewell, G. R. Smith, M. Kermani, M. Pavan, D. Vetterli, R. A. Ristinen, S. Høibråten, M. D. Kohler, J. J. Krahshaar, B. J. Kriss, J. Jaki, M. Metzler, and E. F. Gibson, Phys. Rev. C **51**, 929 (1995).
- ⁵ R. Koch, Nucl. Phys. **A448**, 707 (1986).
- ⁶ R. A. Arndt and L. D. Roper, SAID on-line program.
- ⁷ E. Friedman, A. Goldring, G. J. Wagner, A. Altman, R. R. Johnson, O. Meirav, M. Hanna, and B. K. Jennings, Phys. Lett. B **231**, 39 (1989).
- ⁸ E. Friedman, A. Goldring, G. J. Wagner, A. Altman, R. R. Johnson, O. Meirav, and B. K. Jennings, Nucl. Phys. **A514**, 601 (1990).
- ⁹ E. Friedman, A. Goldring, R. R. Johnson, D. Vetterli, J. Jaki, M. Metzler, and B. K. Jennings, Phys. Lett. B **254**, 40 (1991).
- ¹⁰ GEANT Version 3.16, Application Software Group, Computing and Networks Division, CERN.
- ¹¹ M. Pavan, *et al.* to be published.
- ¹² R. A. Arndt, private communication.

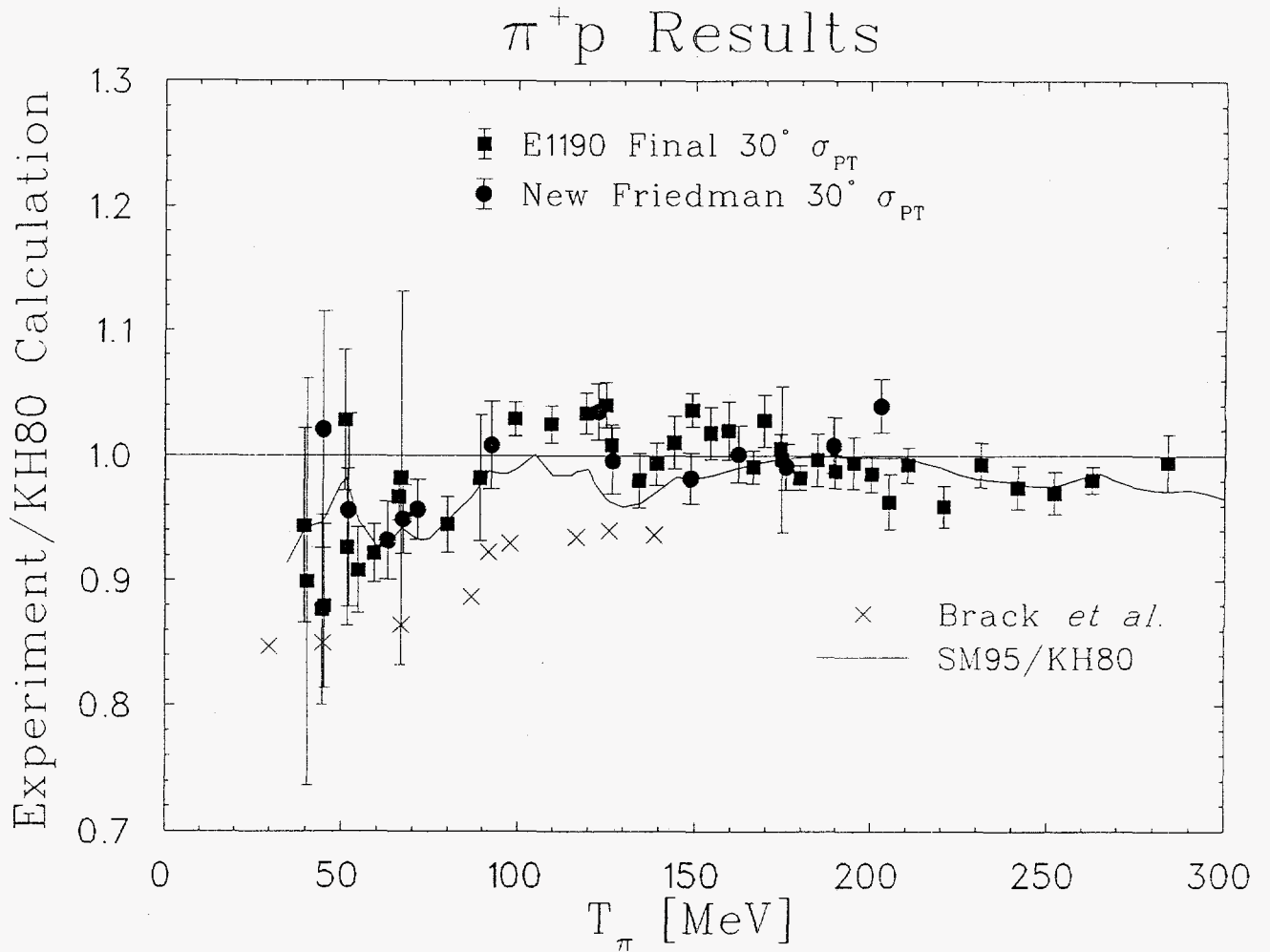


Figure 4.1. The ratios of the π^+p integral cross sections outside $\theta_\pi^{lab} = 30^\circ$ relative to the KH80 phase shift solutions integrated over the same angular range. The Friedman integral measurements are from Refs. 7, 8, and 9 but with a new energy calibration. A second calculation from phase shifts, SM95, is also shown as a ratio to KH80. Integrated differential cross sections from the Brack experiments are also shown. The differential cross sections were fit by a polynomial function and integrated over the angular range of available data, and are shown as a ratio to the integral of KH80 over the same angular range. We estimate uncertainties of a few percent due to this process. Those uncertainties are insufficient to explain the differences between the partial total measurements and the integral of the Brack data.

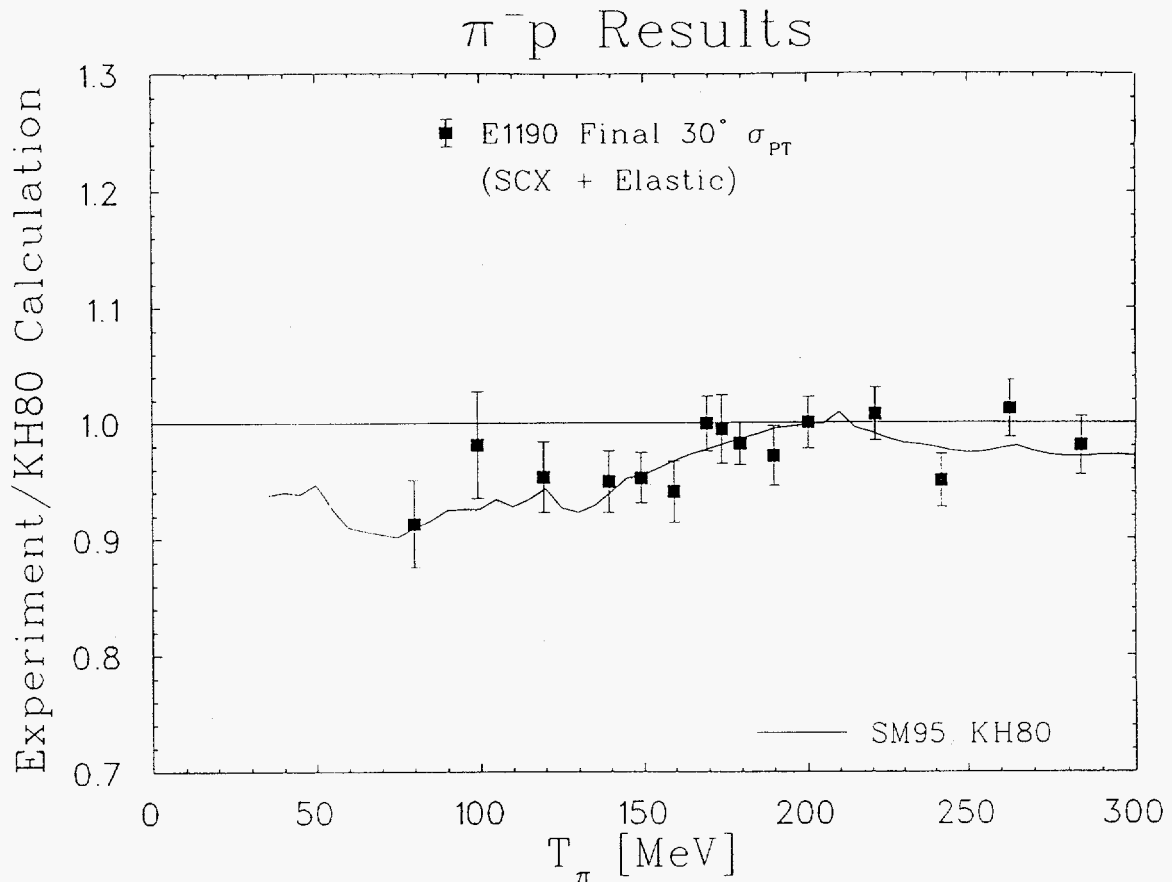


Figure 4.2. The ratios of the π^-p integral cross sections outside $\theta_\pi^{lab} = 30^\circ$ relative to the KH80 phase shift solutions integrated over the same angular range. The single charge exchange contribution to the cross section is included. A second calculation from phase shifts, SM95, is also shown as a ratio to KH80.

5. Exclusive Photodisintegration of the Deuteron at High Photon Energy

J. E. Belz, E. R. Kinney, G. L. Rakness, D. van Westrum, CEBAF E89-012 Collaboration, R. J. Holt, Spokesman

The two-body photodisintegration of the deuteron continues to be one of the most basic tests of our understanding of simple nuclear systems. In this particular case, one is using the exclusive character of the reaction to probe the nucleon-nucleon interaction at quite high momentum transfer,¹ yet without the production of pions or other mesons through soft interactions. In recent years, as experiments^{2,3} at SLAC have pushed to higher photon energies in the GeV range, one has looked to see if the quark-gluon substructure of the nucleons would somehow manifest itself. One way to test for this manifestation is to look for simple scaling dependence on kinematic variables. At energies much larger than any mass scales in the reaction, it is expected that the differential cross section $d\sigma/dt$ at a fixed center-of-mass angle should fall as a simple power of the invariant square of the energy s given by the number of fundamental constituents participating in the reaction minus two. For particle reactions such as photopion production on the proton, these so-called constituent counting rules^{4,5,6} have been quite successful for energies above a few GeV. Surprisingly, when applied to a nuclear reaction such

as deuteron photodisintegration, they also appear to describe the reaction at 90° c.m. angle, as shown in the SLAC experiments; the same experiments did not find scaling at other c.m. angles.

CEBAF experiment E89-012 was proposed to investigate the two-body breakup over the full energy range of CEBAF, 1-4 GeV and over a broad angular range in the center-of-mass, 37° - 114° , and thereby confirm the findings of the earlier SLAC measurements and extend them in order to test the reality of the apparent onset of the constituent scaling at only 1-2 GeV photon energy. The experimental technique is to use a high-flux photon beam created by bremsstrahlung of the electron beam in a copper radiator. Both the photons and the residual electrons impinge on the liquid deuterium target, so separate data are taken with electron beam only, in order to subtract the contribution to the yield from electrodisintegration. Two-body kinematics constrain the highest energy protons to be those arising from reaction with the highest energy photons, so it is not necessary to detect the neutron in coincidence to confirm the two-body final state. When the proton energy is low enough so that it could have arisen from either two-body or three body final states, the technique is no longer valid and the rest of the spectrum is discarded.

Because the experimental procedure is a simple one-arm detection of protons in a spectrometer, this experiment was one of two commissioning experiments for the Hall C experimental equipment. The need for high-power cryogenic H and D targets also made it a useful means to ensure the development and deployment of the targets. Data acquisition began in February 1996 and was completed by May 1996. Analysis of the data has already yielded first preliminary results which have been presented at the PANIC96 and Elba conferences. These results, appear to confirm the scaling at 90° seen earlier at SLAC. In addition, for the first time it is observed that the cross sections obtained at other angles may be starting to exhibit scaling behavior.

Further detailed analysis at Illinois is ongoing and new results may be expected by spring 1997. Already, the new results are sufficiently interesting that the original collaboration is proposing to measure the same reaction at the higher beam energies (5-6 GeV) which are planned to be available at CEBAF by the end of 1997.

- ¹ R. J. Holt, Phys. Rev. C 41 (1990) 2400.
- ² J. Napolitano *et al.*, Phys. Rev. Lett. 61 (1988) 2530; S.J. Freedman *et al.*, Phys. Rev. C 48 (1993) 1864.
- ³ J. E. Belz *et al.*, Phys. Rev. Lett. 74 (1995) 646.
- ⁴ S. J. Brodsky and G.R. Farrar, Phys. Rev. Lett. 31 (1973) 1153.
- ⁵ V. Mateev *et al.*, Nuovo Cimento Lett. 7 (1973) 719.
- ⁶ G. P. LePage and S.J. Brodsky, Phys. Rev. D 22 (1980) 2157.

B. MESON REACTIONS

1. **Pion-induced Fission** R. J. Peterson and C. J. Gelderloos (University of Colorado); S. deBarros (Federal University of Rio de Janeiro); A. G. DaSilva, J. C. Suita (Nuclear Engineering Institute, Rio de Janeiro); I. E. Qureshi, S. Mansoor and H. A. Khan (PINSTECH, Islamabad Pakistan)

Cross sections from the 1995 exposures of fission targets with Solid State Nuclear Track Detectors (SSNTD) are now becoming available. Our priority in the analyses has been on the search for high nuclear excitations from the high energy exposures at the AGS (E899) and on the detailed mass study with separated isotopes using resonance energy pions from LAMPF.

The AGS exposures were at π^- beam energies of 500, 672, 1068 and 1665 MeV. Track counting has found very few events with three tracks, contrary to what would be expected if complete absorption of the pions had occurred. The high excitations that would result from true absorption would lead to initial energies such that high multiplicities would be expected if that energy were sustained until fission, by analogy to the analyses of heavy ion data¹. It appears that the probability of ternary fission at these beam energies is very similar to what we have found near 100 MeV².

Track densities at 500 MeV were higher for targets of Bi and Sn in the forward hemisphere, relative to the backward hemisphere, in our 4π counting geometry. The ratio is very near what would be expected for isotropic fission, with the compound system moving with the beam momentum. Fission is rare for these light systems, requiring quite high nuclear excitations, which would be most readily attained with full absorption of the pion. Our data at higher energies from the AGS and from a companion LAMPF exposure at 255 MeV should give a clear signature of this absorption by the forward/backward ratios on these two targets. Data for Au and a few points with low accuracy using Cu will sharpen the interpretation.

At 150 MeV, we exposed a range of isotopically separated targets to both pion beam signs, for a smooth trend of fission cross sections and probabilities in the mass region where fissility is changing most rapidly. Our cross sections were converted to fission probabilities by dividing by computed nuclear reaction cross sections. The results are shown in Figure 1.1, using the fissility axis found in our previous papers, with the charge of the target plus the pion sign and the full target mass. It is noted that the smooth trends for the two signs do not quite match, indicating that this is not the proper scale of fissility. Indeed, if we use the compound nucleus resulting from 100 MeV pions, as computed by Iljinov et al.³, to compute the fissility, the curves for the two pion signs match quite well. The curve in Figure 1.1 shows the fitted form that generally matched a wide range of our fission data at this and lower beam energies⁴. The data points for that fit were much sparser than those of this study, and included many actinide points⁵.

An observant reader will note two data points, one for each sign, that slip away from the general trends in Figure 1.1. These are for the ^{208}Pb target. We have analyzed the relation between the excitation energy and the fission barrier for these data, and find that the barrier for ^{208}Pb is not different from that of the

neighboring nuclei. The deviations in P_f for ^{208}Pb arise from the greatly different neutron binding energies of the systems formed by π^+ and by π^- .

These data and a careful study of the energy dependence for π^+ fission of Bi are being analyzed in Rio and in Islamabad. We expect soon to complete our study of pion-induced fission by SSNTD techniques. A draft of a manuscript on the 150 MeV data is nearly complete.

¹ L. Moretto *et al.*, Phys. Rev. Lett. **71**, 3935 (1993).

² H. A. Khan *et al.*, Phys. Rev. C **35**, 645 (1987).

³ A. S. Iljinov *et al.*, Phys. Rev. C **39**, 1420 (1989).

⁴ R. J. Peterson *et al.*, Zeit. Phys. **A352**, 181 (1995).

⁵ S. de Barros *et al.*, Nucl. Phys. **A542**, 511 (1992).

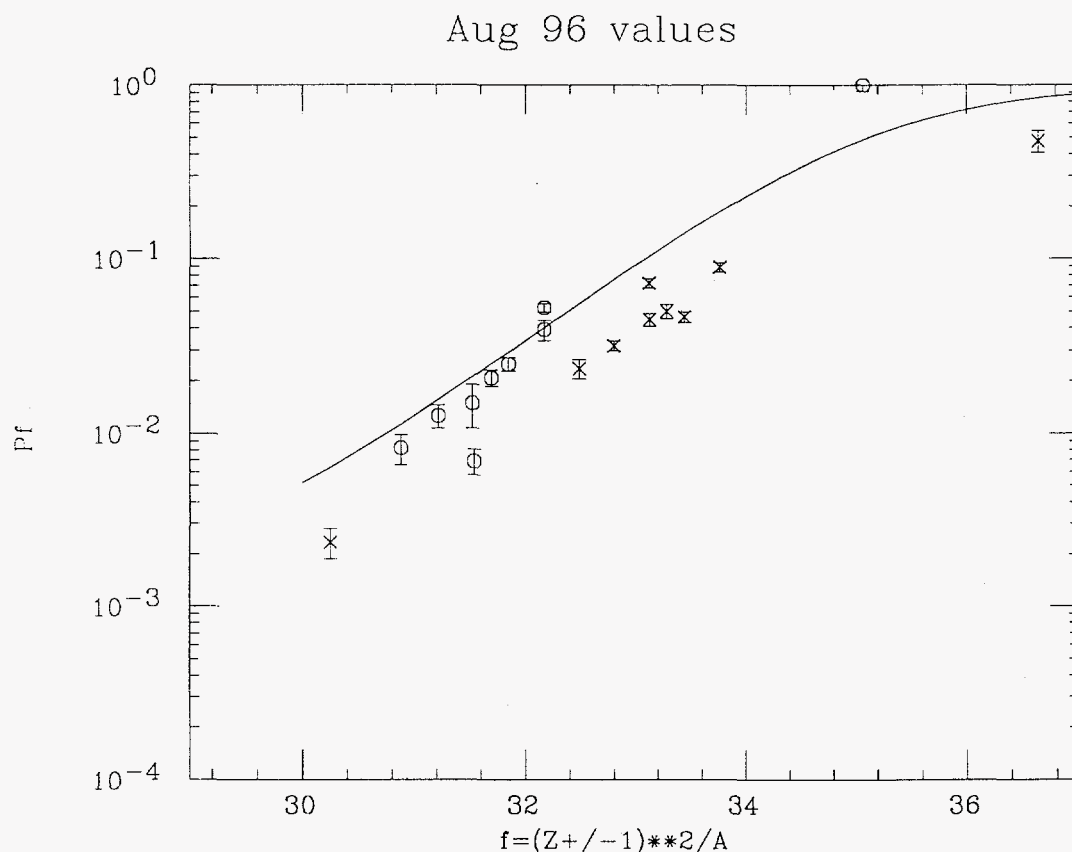


Figure 1.1. Fission probabilities for targets from ^{181}Ta through ^{231}Pa are shown for 150 MeV pion beams, with π^- data to the left. The fissility axis is that for the target mass and the target charge added to the pion beam sign. The curve shows the parametrized shape found to match reasonably well a wide range of data in Ref. 4.

2. Coincidence Measurement of Pion Double Charge Exchange:

${}^4\text{He}(\pi^+, \pi^- p)3p$ A. Saunders, M. D. Holcomb, E. R. Kinney, B. J. Kriss (University of Colorado); P. A. M. Gram (Los Alamos National Laboratory); W. Fong, M. T. Harvey, J. L. Matthews, H. Park, S. F. Pate, L. L. Vidos, V. V. Zelevinsky (Massachusetts Institute of Technology); D. A. Roberts (University of Michigan); G. A. Rebka, Jr. (University of Wyoming)

We have completed a coincidence measurement of the inclusive double charge exchange reaction ${}^4\text{He}(\pi^+, \pi^- p)3p$. The present experiment, LAMPF E978, is the latest in a series of experiments by this group investigating pion double charge exchange (DCX). The previous experiments used a wide range of target nuclei, incident pions of both positive and negative charge, and pion kinetic energies between 120 and 270 MeV¹⁻⁶. While providing ample information about the energy and angle distributions of the outgoing pion from the DCX reaction, the previous experiments made no attempt to detect the outgoing nucleons. The purpose of the present experiment was to elucidate the DCX reaction mechanism by detecting one or more of the outgoing nucleons, protons in this case, in coincidence with the outgoing pion. The experiment measured the angle and energy of both the pion and protons.

The details of the experiment were described in our 1993 Technical Progress Report. In brief, the experiment detected outgoing pions and protons in coincidence from the DCX reaction. The pions were detected by a magnetic spectrometer, while the coincident protons were detected by an array of scintillator stacks. The incident beam consisted of 240 MeV π^+ , so that the DCX reaction took place near the $\Delta_{3,3}$ resonance. The outgoing pions were detected at an angle of 32° . The experiment consisted of two parts: in one, the outgoing pions were detected at kinetic energies of 45 and 135 MeV in coincidence with outgoing protons; in the other, the protons were ignored and the pions were detected over a kinetic energy range of 30 to 190 MeV. The pion-only results were collected to connect this experiment to the previous experiments in this series.

The analysis of the pion-detection arm of the experiment is now complete. Two major problems with the magnetic spectrometer data were detected and corrected this year. First, the acceptance of the spectrometer was found to have changed during the experiment. Once detected, this change was easy to account for by using different instances of our redundant spectrometer acceptance measurements for different parts of the experiment. Second, the spectrometer included a Čerenkov detector to discriminate between pions and electrons. Unfortunately, the gains of this detector's two phototubes were found to shift during the experiment. The gain shifts are now corrected in the analysis software, allowing us to more accurately determine the number of pions detected in the spectrometer. The doubly differential cross sections resulting from the pion-only measurement are shown in Figure 1. The two-peaked shape of the spectrum matches the shape of the similar energy spectra measured at outgoing pion angles of 25° and 50° by this group in a previous experiment⁴.

Data acquisition was completed in November, 1993. Enough data were collected at each of the two outgoing pion energies for approximately 10% statistics in each of 225 bins (fifteen proton angles times fifteen 10 MeV proton energy bins).

Final analysis of the coincidence data is currently in progress. This analysis will lead to quadruply differential cross sections,

$$\frac{d^4\sigma}{dE_\pi d\Omega_\pi dE_p d\Omega_p},$$

measured at one outgoing pion angle (32°), two pion energies (45 and 135 MeV), and over a range of proton energies and angles.

- ¹ S. A. Wood, LANL Report LA-9932-T (1983).
- ² S. A. Wood *et al.*, Phys. Rev. Lett. **54**, 635 (1985).
- ³ J. L. Matthews, Proceedings of LAMPF Workshop on Pion Double Charge Exchange (January, 1985).
- ⁴ E. R. Kinney *et al.*, Phys. Rev. Lett. **57** (1986) 3152.
- ⁵ Progress at LAMPF, LA-10429-PR, p.61 (1985).
- ⁶ P. A. M. Gram in Proceedings of the Workshop on Pion-Nucleus Physics: Future Directions and New Facilities at LAMPF (1987).

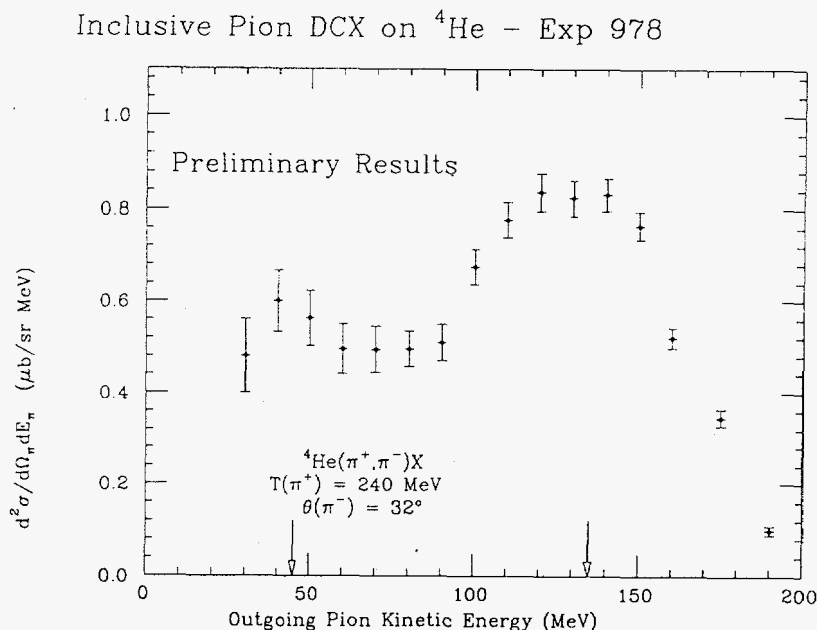


Figure 2.1. The doubly differential cross sections resulting from the pion-only measurement of the DCX reaction. The uncertainties are statistical only. The two arrows pointing to the horizontal axis show the two pion energies used for the coincidence measurements, 45 and 135 MeV.

3. Total and Reaction Cross Sections for π^- -Nucleus Collisions at 400 – 500 MeV C. J. Gelderloos, J. T. Brack, M. D. Holcomb, M. V. Keilman, D. J. Mercer, R. J. Peterson, R. A. Ristinen, and A. Saunders (University of Colorado)

Experiment 1279, run during August/September 1995 at LAMPF, has been analysed, and final attenuation cross sections have been determined. Beams of 410, 464, and 492 MeV π^- were incident on targets ranging in mass from CD_2 through Pb. The experiment was designed to extract total and reaction cross sections for these targets, so as to test and constrain reaction models. Cross sections for the heavier targets in particular have not been previously measured.

Attenuation cross sections were measured using the transmission method, in which the number of beam pions scattered outside of a given solid angle is counted for a series of solid angles subtended by a transmission counter. These attenuation cross sections as a function of solid angle are then used to extrapolate to $\Omega = 0$ to determine the final cross section after several corrections have been applied. This extrapolation procedure eliminates many sources of systematic error in the measurement, such as pion production, since many spurious processes have probabilities which approach zero at zero solid angle.

The first series of corrections that are required to be made to the raw attenuation cross sections are for known effects that could not be expediently eliminated during on-line data acquisition. Among these effects are muons included in the beam definition, multiple scattering in the target, delta ray production, and pion decay. Due to the complex interplay of these effects, the corrections were made by Monte Carlo methods. A detailed GEANT simulation was constructed that explicitly accounted for these effects. Muon contamination in the beam was determined to be less than 0.5%, while post-target effects were always less than 2%. It is worth noting that the primary post-target correction is due to pion decay, but that two competing effects cancel one another quite closely to first order, namely pions that would have hit the target but decayed with the muon subsequently missing the detector, and pions that would not have hit but the decay muon did.

Two examples of these correction factors for known effects are shown as a function of solid angle in Figure 1. Since these Monte Carlo corrections are much smaller than other sources of systematic uncertainty, and since the corrections are very CPU intensive, these corrections will be included in the final systematic uncertainties.

One additional correction that must be made to the attenuation cross sections in order to extract a reaction cross section is the subtraction of the elastic contribution. The total reaction cross section, σ_R , can be expressed as

$$\sigma_R = \sigma_{att} - \sigma_{el}.$$

In practice, this subtraction of the elastic cross section is done for each solid angle setting of the transmission counter, such that

$$\sigma_R(\Omega) = \sigma_{att}(\Omega) - \int_{\Omega}^{\pi} \left(\frac{d\sigma}{d\Omega} \right)_{el} d\Omega.$$

The elastic differential cross section has been calculated by the eikonal model of Chen, *et al.*¹ which uses a local optical potential with an eikonal propagator. The model was developed by matching it to a "model-exact" microscopic momentum-space optical model with excellent agreement. The calculated results have been exhaustively checked against all existing pion elastic-scattering data sets with good agreement in all cases. In addition, the model has been tested using several different point particle distributions with minimal variation in the differential cross section (less than 1%). These comparisons provide confidence in the subtraction of the elastic contribution.

A significant correction to the smallest solid angle points was found to occur due to plural, or Moliere, scattering². While not a significant contributor in the Monte Carlo corrections, its role is exaggerated during the subtraction of the elastic component due to the steepness of the elastic differential cross section at small angles. In effect, the distribution of particles scattered at a given angle is broadened by plural scattering, thus smearing the differential cross section by some amount. When integrating this cross section, significant deviations can be seen. Even the inclusion of a gaussian approximation for plural scattering is insufficient for the smallest angles, as can be seen in Figure 2.

Preliminary reaction cross sections as a function of the kinetic energy of the incoming pions is shown in Figure 3 for Li, C, and Al targets. Systematic uncertainties are not shown.

Total cross sections (not shown) are obtained by adding back the nuclear elastic contribution to $\sigma_R(\Omega)$. This is done practically by computing the elastic differential cross section with the charge of the incoming pion turned off.

¹ C. M. Chen, D. J. Ernst, and M. B. Johnson, *Phys. Rev. C* **48**, 841 (1993).

² W. R. Leo, *Techniques for Nuclear and Particle Physics Experiments*, (Springer-Verlag, Berlin, 1994).

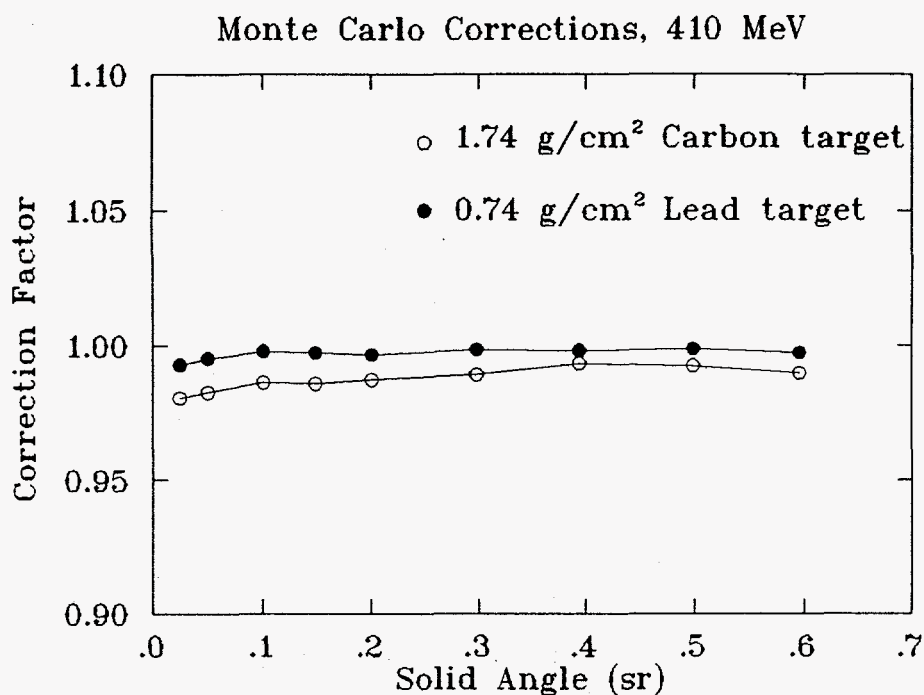


Figure 3.1 Correction factors for C (open) and Pb (closed) at 410 MeV, as computed by Monte Carlo simulations using GEANT.

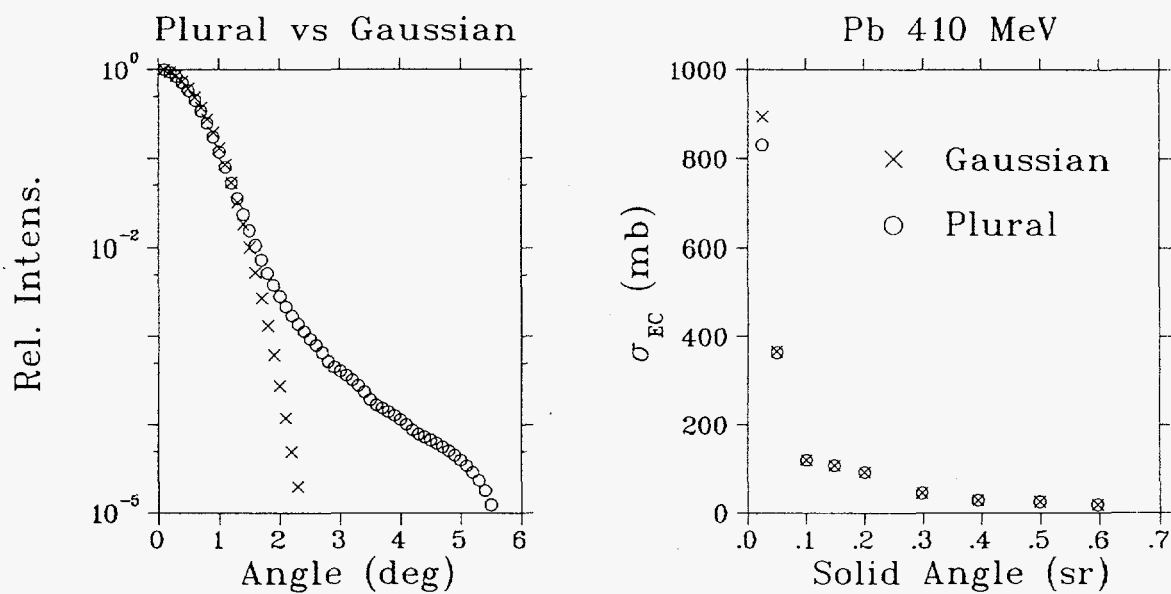


Figure 3.2 Angular distribution for Gaussian vs. plural scattering and its effects on the calculated elastic correction (σ_{EC}).

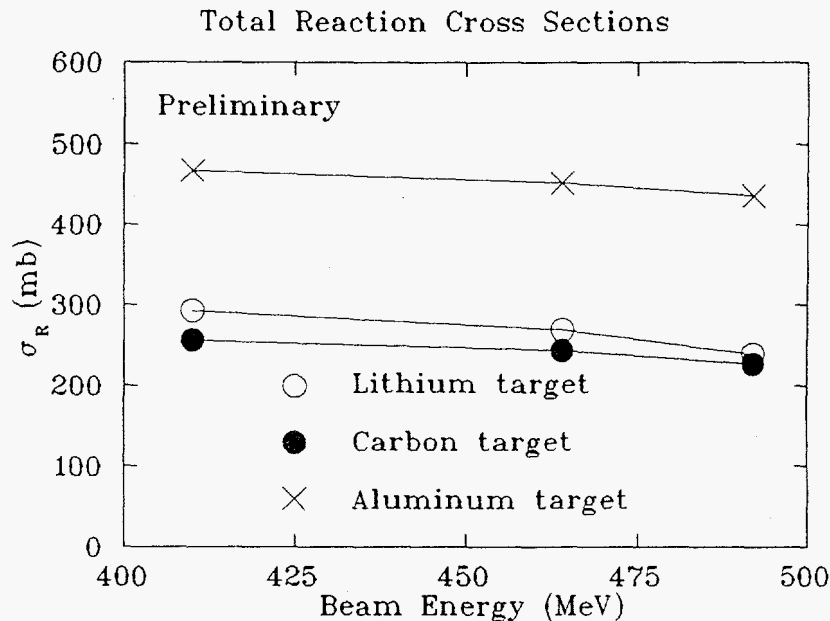


Figure 3.3 Total reaction cross sections for Li, C, and Al as a function of kinetic energy of the incident pion.

4. **Preparation for a hypernuclear experiment using stopped kaons at the AGS** A. Saunders (Univ of Colorado); M. Ahmed, X. Cui, E. V. Hungerford, A. Ramirez (Univ. of Houston); D. Boudrie, J. C. Peng (Los Alamos National Lab); R. E. Chrien, P. Pile, A. Rusek, R. Sawafta, R. Sutter (Brookhaven National Lab); D. Dehnhard, J. Gerald, J. M. O'Donnell (Univ. of Minnesota); C. Gaulard (Arizona State University); I. Supek (Rudjer Boskovic Institute); V. Zeps (Univ. of Kentucky)

AGS Experiment 907 was proposed to study hypernuclear physics. This experiment uses the (K, π) reaction to study hypernuclear energy states. In the past, the (K^-, π^-) and (π^+, K^+) reactions have been used to study some hypernuclear states¹⁻⁴. Both of these reactions, however, generate hypernuclear states which are mostly neutron-hole, lambda-particle in nature. The current experiment uses the (K^-, π^0) reaction to study states in which the Λ particle is created from a proton instead of a neutron in the target. This complementary reaction is interesting for three reasons. First, if the target is an isospin-zero nucleus, the (K^-, π^-) and (K^-, π^0) reactions produce mirror hypernuclei. Any difference in the observed energies of the mirror hypernuclear states would reveal further information about charge symmetry breaking in hypernuclei, which has already been observed in the $A=4$ case⁵. Second, if the target is neutron rich, the (K^-, π^0) reaction preferentially produces $T+\frac{1}{2}$ states, while the (K^-, π^-) reaction produces both $T+\frac{1}{2}$ and $T-\frac{1}{2}$ states. Therefore, comparing the two measurements will reveal the isospin of the hypernuclear states. Finally, hypernuclear states will be reached with the present experiment that could not be reached with the (K^-, π^-) reaction.

The present experiment was made possible by the availability of a new Neutral Meson Spectrometer (NMS) from LAMPF. Using the NMS's high resolution and

wide acceptance, an active target (to give information about the location of the reaction in the target), and a stopped kaon beam (to give an exact value for the initial energy of the reaction), resolutions of better than 1 MeV should be possible. Since the NMS has proved to require substantial tuning time in the past and the ability to produce an acceptable kaon stopping rate in the target was unproven, the experiment is divided into two parts: an engineering run and a data acquisition run. The engineering run took place in May and June of 1996, and included University of Colorado collaboration.

The experiment has two major components. The first is the collection of detectors and hardware in the beamline, which are used to produce, detect and identify stopped kaons in the target. The beamline components are shown in Figure 1. The beam, consisting of 650 MeV/c K^- , passes through a lucite Čerenkov counter (to eliminate slow particles), a timing scintillator, and a wedge shaped degrader made at the University of Colorado. The degrader is wedge shaped because the beam energy and horizontal position are correlated at that point in the beam. After the degrader, the beam passes through a pair of scintillators which use energy loss to discriminate against other fast beam particles. Finally, the beam enters the active target. The active target consists of three slabs of target material separated by drift chambers. The drift chambers measure the position of the reaction in the plane transverse to the beam, and also limit the location of the reaction to one of the three target slabs. The chambers also detect any charged particles emerging from decaying hypernuclei after the reaction. The beamline components were mounted on a frame designed and built at the University of Colorado.

The second major component is the NMS, whose task it is to detect the neutral pions emerging from the target. The NMS has been used for several years to detect neutral pions at LAMPF, and its capabilities are therefore well understood. It has been fully described in a previous Technical Progress Report⁶, but, briefly, it measures the energy of a π^0 by detecting the two gamma rays produced by the decaying pion. It uses BGO planes to convert the gammas to showers of charged particles. Wire chambers track the showers for purposes of vertex reconstruction, and banks of CsI crystals catch the showers for calorimetry. The NMS has two crates. One detects each of the outgoing gamma rays from the π^0 .

The engineering run had three major goals. First, the NMS was tuned for use for the first time at the AGS. Second, the kaon beam was tuned to maximize the stopping rate of kaons in the target. Finally, the active target was installed and integrated with the rest of the experiment. The NMS tuning consisted of two phases. First, the location of the bins had to be known to a few millimeters or better for optimum pion energy resolution. These locations were measured and monitored with a theodolite surveying system. Second, CsI crystals had to be calibrated to improve the calorimetry. The crystals were calibrated using the $p(\pi^-_{stopped}, \gamma)n$ reaction. The π^- were stopped in a cylinder of hydrogen gas, yielding monoenergetic gamma rays. These gammas were then used to check the gains of the calorimetry system.

The kaon beam had to be tuned for maximum stopping rate in the target. This task was accomplished by mounting a target consisting of a stack of scintillators in place of the active target. This target allowed us to monitor the stopping

position along the beamline of the beam kaons, and finely tune the beam to find the optimum stopping rate.

Finally, the scintillator target was replaced with the active target and it was integrated with the rest of the detector system.

The engineering run was completed in May and June of this year, after meeting its goals. The experiment is ready to move on to the next phase: the data acquisition run.

- ¹ A. Gal, *Advances in Nuclear Physics* **8**, 1 (1977).
- ² B. Povh, *Ann. Rev. Nucl. Part. Sci.* **28**, 1 (1978).
- ³ C. Milner *et al.*, *Phys. Rev. Lett.* **54**, 1237 (1985).
- ⁴ P. H. Pile *et al.*, *Phys. Rev. Lett.* **66**, 2585 (1991).
- ⁵ B. F. Gibson and D. R. Lehman, *Phys. Lett.* **83B**, 289 (1979).
- ⁶ M. V. Keilman *et al.*, *NPL Technical Progress Report*, **50** (1993).

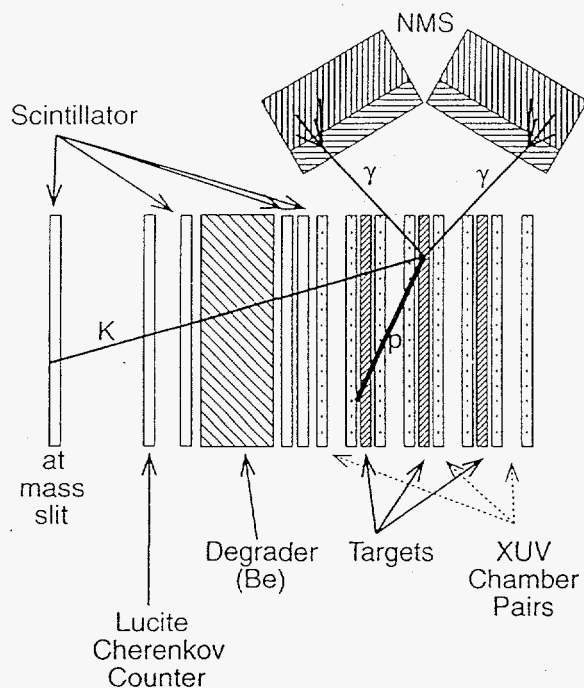


Figure 4.1. The experimental setup. Not to scale.

5. Meson-Nucleus Optical Potentials and the DWIA R. J. Peterson (University of Colorado); A. A. Ebrahim (Assiut University, Assiut, Egypt); H.C. Bhang (Seoul National University, Seoul, Korea)

Two distorted wave impulse approximation codes that have been used for years at the NPL have been modified. For pion scattering analyses, we have updated the pion-nucleon interactions in the codes DOPI2 and DWPIES to reflect the newest data base, including the many experimental results from this laboratory. We have also altered the first-order code DOPI to provide predictions of K^+ -nucleus scatterings.

The pion codes based their pion-nucleon scattering on a set of parameters representing the phase shifts known from the data base in 1978¹. There have been significant improvements to this information, particularly in negative pion data and charge exchange and at low pion energies. The world data base for pion-proton observables was edited and refit in the form of phase shifts in 1995², making possible a reconsideration of the DWIA calculations.

We have fit these phase shifts from SAID² in the form initially used in Reference 1, as

$$\frac{\tan \delta_\ell}{q^{2\ell+1}} = b + cq^2 + dq^4 + \frac{x\Gamma\omega_0 q_0^{-(2\ell+1)}}{\omega_0^2 - \omega^2}. \quad (1)$$

The newest information on the positions, widths and strengths of the lowest resonance for each partial wave was included³. These are listed in Table 5.1. The starting parameters for the fits to the parameters b,c,d were taken to be the same as the final results from Reference 1. The energy range of our fits was from 30 MeV to 300 MeV of pion laboratory kinetic energy, limited to the range where the phase shifts could be treated as real. Very good fits were found to the numerical values of the phase shifts from Reference 2. The parameters found from our fits are listed in Table 5.2. No uncertainties are given, since no agreed-upon system of assigning uncertainties to the phase shifts we fit could be used. Note that charge independence is assumed in our formulation.

The validity of the fitted parameters was checked by putting the phase shifts computed from Equation 1 into the program SAID², and comparing the computed observables to a wide range of pion-proton data. Good agreement was found in all cases. In contrast, use of the original parameters of Reference 1 yielded computed observables notably different from the data in some cases, most strikingly so for elastic π^+ and π^- scattering at 141 MeV⁴ and charge exchange at 129 MeV⁵.

With these new parameters, we computed pion-nucleus observables from the codes DOPI and DWPIES for comparison to a wide range of data for pion-nucleus reactions from 30 to 300 MeV. These were also compared to calculations using the original parameters of Reference 1 to test the sensitivity of our changes and the reliability of conclusions drawn from the many analyses using the original parameters. Here we give two examples with Figures 5.1 and 5.2.

In Figure 5.1 we show elastic scattering data with both signs at 180 MeV from $^{42}\text{Ca}^6$, compared to solid curves computed with DOPI with the present set of modernized π -nucleon amplitudes. These computed cross sections are essentially identical to those using the parameters of RSL, shown as the dotted curves. Similar close agreement is found for inelastic scattering calculations near resonance. In Figure 5.2 we show 30 MeV elastic π^+ data from $^{208}\text{Pb}^7$, compared to DWPIES calculations using a set of second-order parameters taken from work on lighter nuclei. Again, calculations shown as a solid curve agree closely with those using the RSL set, shown as the dotted curve.

A number of other cases were studied using the two parameter sets, including charge exchange calculations. Our conclusion from this modernization of pion-nucleus DWIA calculations is that results from the use of the parameters of Reference 1 are remarkably robust, and that no important reappraisal is necessary.

A paper containing a more complete description of this work on pion-nucleon and pion-nucleus interactions has been accepted for publication in the Physical Review C.

We have carried out a parallel analysis of K^+ -proton phase shifts, using again the fitted phase shifts from Reference 2 and the form of Equation 1, but without resonance terms. We restricted our fitting range to be below 750 MeV/c of K^+ momentum to maintain elastic phase shifts. In contrast to the pion case, there has not been any recent significant change in the data base for these mesons. Parameters for our fits are listed in Table 5.3.

The pion-nucleus first-order code DOPI used above was then modified to treat K^+ -nucleus scattering, by changing the masses of the projectile and by altering the isospin couplings. Numerical tests on the integrations carried out by the codes were made.

Computed total, reaction, and differential elastic K^+ scattering cross sections from these codes were then compared to recent data^{8,9,10}, and good agreement was found. An example is shown in Figure 5.3, for elastic K^+ scattering at 715 MeV/c from ^6Li and C^{10} . The error bars include the systematic uncertainty in the solid angle. The computed curves lie below the data, as found in other optical model theories. The difference is the source of recent excitement on medium modifications.

We are completing these calculations, including the effects of the removal of nucleon sizes from nuclear charge distributions as presented in this Report¹¹. We will use this altered code to estimate the inelastic cross sections that may be contributing to the spectra of Reference 10, and we will use the code to examine sensitivities to medium alterations of the meson-nucleon interactions as well as sensitivities to the distributions assumed for nucleons within complex nuclei.

¹ G. Rowe, M. Salomon and R. Landau, Phys Rev C **18**, 584 (1978).

² SAID, a program maintained by R. A. Arndt *et al.*, Phys Rev C **52**, 2120 (1995).

³ Particle Data Group, Phys Rev D **50**, 1173 (1994).

- ⁴ M. Pavan, PhD Thesis, Univ. Of British Columbia, 1995.
- ⁵ R. F. Jenefsky *et al.*, Nucl. Phys. A **290**, 407 (1977).
- ⁶ K. G. Boyer *et al.*, Phys. Rev. C **29**, 182 (1984).
- ⁷ B. M. Freedom *et al.*, Phys. Rev. C **23**, 1134 (1981).
- ⁸ R. Weiss *et al.*, Phys Rev. C **49**, 2569 (1994).
- ⁹ A. Gal *et al.*, to be published.
- ¹⁰ R. Michael *et al.*, to appear in Phys Lett B.
- ¹¹ J. Patterson and R. J. Peterson, section D-2 of this Progress Report.

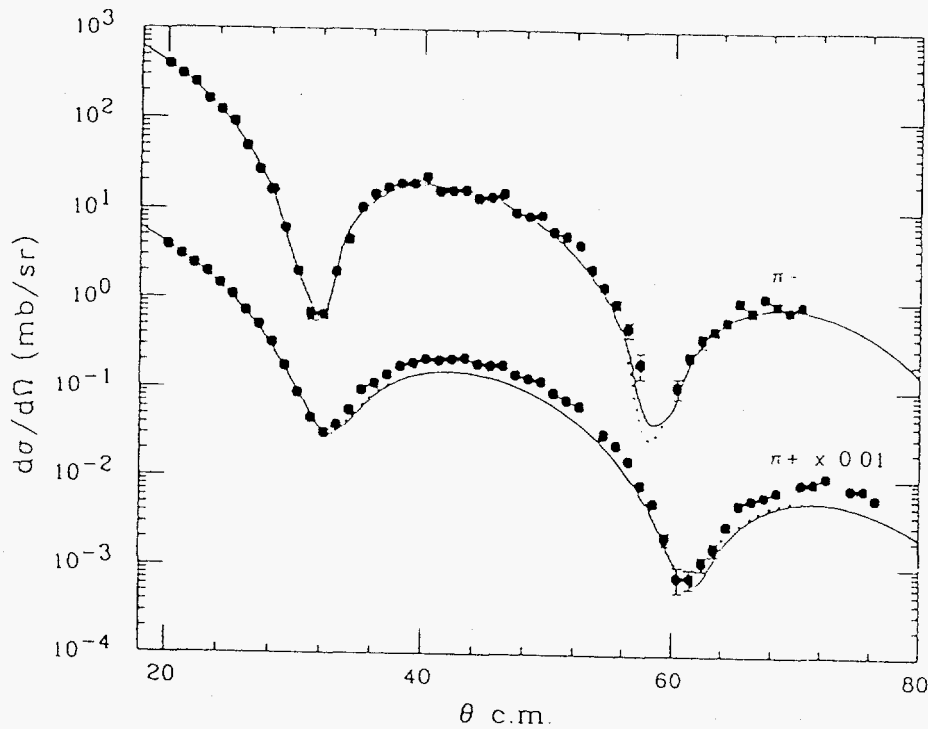


Figure 5.1. Pion elastic scattering data⁶ at 180 MeV are compared to calculations using a first-order optical potential with all usages and parameters the same except that our more modern parametrization of the π -nucleon phase shifts is used for the solid curves and the original RSL parameters are used for the dotted curves.

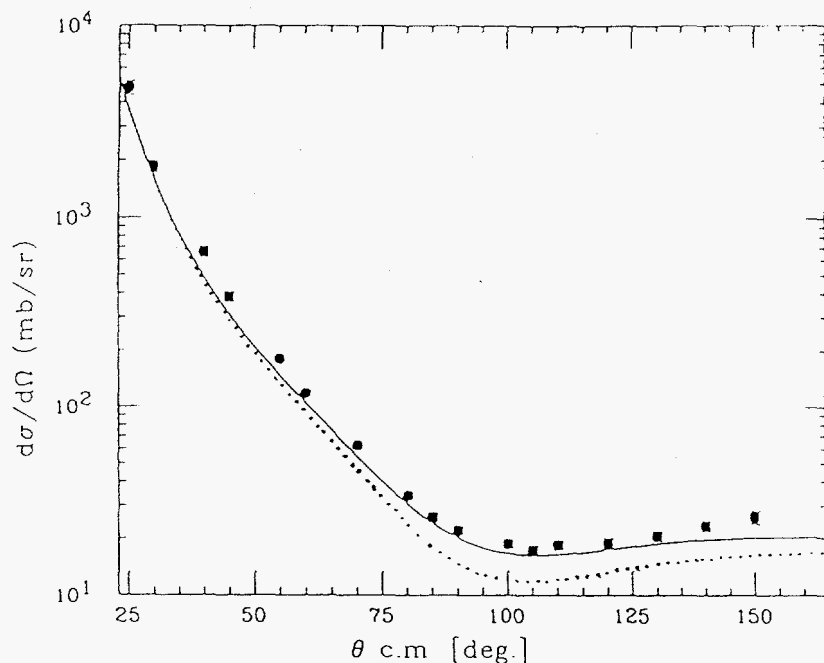


Figure 5.2. Positive pion elastic scattering data at 30 MeV⁷ are compared to calculations using a second-order optical potential with all usages and parameters the same except that our more modern parametrization for the π -nucleon phase shifts is used for the solid curves and the original RSL values are used for the dotted curve.

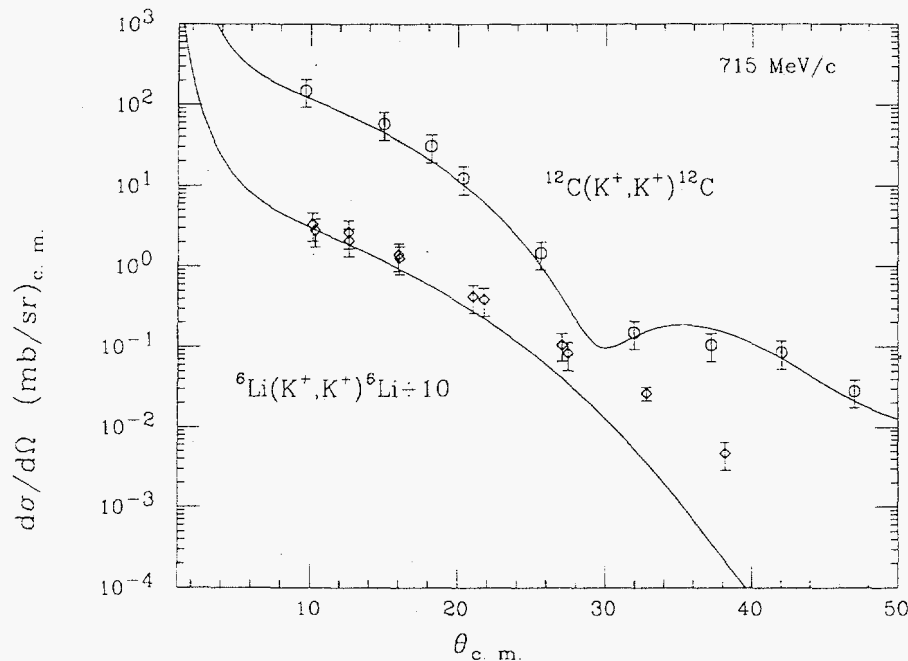


Figure 5.3 Data for 715 MeV/c K^+ elastic scattering from ${}^6\text{Li}$ and C^{10} are compared to calculations from the optical model code we recently modified.

Table 5.1 Resonance parameters for Equation 1, using the lightest resonance for each partial wave. The resonance energy is ω_0 , its width is Γ , and $|r|$ is the absolute value of the residue. For Equation 1 we use $x = \frac{2|r|}{\Gamma}$ and q_0 for the center of mass momentum of the π -N system to reach ω_0 . These values are from Reference 3.

Channel	x	ω_0 (MeV)	q_0 (MeV/c)	Γ (MeV)	$ r $ (MeV)
S11	0.31	1535	464	150	23
S31	0.25	1620	527	150	19
P11	0.23	1440	482	350	40
P13	0.20	1720	594	150	15
P31	0.30	1910	717	250	38
P33	0.83	1232	228	120	50
D13	0.53	1520	457	120	32
D15	0.31	1675	566	150	23

Table 5.2 Parameters b, c, d in units of (MeV/c) for Equation 1 for pions.

Channel	b	c	d
S11	1.053099E-03	-1.123708E-08	5.366957E-14
S31	-7.709957E-04	-1.465965E-08	8.485826E-14
P11	-1.720423E-08	5.382523E-13	-3.055784E-18
P13	-7.300847E-09	9.093504E-14	-4.633992E-19
P31	-1.313602E-08	1.481661E-13	-7.853222E-19
P33	4.810577E-08	-2.268685E-13	-1.291258E-18
D13	7.714106E-14	-1.444489E-18	9.919875E-24
D15	6.636850E-14	-1.325509E-18	8.011451E-24

Table 5.3 Parameters b, c, d in units of (MeV/c) for Equation 1 for K^+ nucleon scattering.

Channel	b	c	d
S01	-4.518421E-05	-1.521372E-08	6.408447E-14
S11	-1.650726E-03	1.184280E-09	-6.170316E-15
P01	1.091461E-08	8.053471E-14	-3.693214E-19
P03	-1.360311E-08	1.383292E-13	-4.162344E-19
P11	-1.751352E-08	1.611811E-13	-4.790802E-19
P13	8.103663E-09	-6.598389E-14	1.948645E-19
D03	2.905353E-13	-3.555722E-18	1.121378E-23
D05	7.389264E-14	-8.338051E-19	2.354998E-24
D13	-8.424199E-16	-3.428781E-20	1.721274E-25
D15	-2.182536E-14	2.477331E-19	-7.647003E-25

C. INCOHERENT REACTIONS

1. **Spin Observables from 600 MeV Polarized Deuteron Quasielastic Scattering** M. D. Holcomb, R. J. Peterson (University of Colorado); M. Morlet, A. Willis, J. Guillot, H. Langevin-Joliot, L. Rosier (Institute de Physique Nucleaire, Orsay); E. Tomasi-Gustafsson (Laboratoire National Saturne, Saclay); B. Johnson (University of South Carolina, Columbia)

The analysis of data from Saturne experiment 248 was completed this year. At momentum transfers $q = 345$ and 500 MeV/c, final vector and tensor analyzing powers A_y and A_{yy} were evaluated for our five targets: hydrogen (CH_2), deuterium (CD_2), carbon, calcium, and lead. The spin transfer observable $K_y^{y'}$ was also calculated for all of the targets at the same momentum transfers. We attempted to combine these data with the well known nucleon-nucleon amplitudes¹ and deuteron form factors to make longitudinal and transverse isoscalar spin responses, but the lack of an absolute beam normalization and other problems made it impossible to do a meaningful calculation.

The experiment was completed in September 1992 at the Laboratoire National Saturne. It has been described in detail in previous progress reports, but a brief summary may be in order. The Saturne beam source provided two different polarized deuteron beam configurations, referred to as the two-state beam and the four-state beam. The two-state beam was vector polarized only, and the sign of the polarization changed on alternating beam bursts. The four-state beam was both vector and tensor polarized, and cycled through all four polarized sign combinations, i.e. $(+,+)$, $(-,+)$, $(+,-)$, $(-,-)$ for the (vector, tensor) polarization. The four-state beam was used in conjunction with the magnetic spectrometer SPES1 to measure unnormalized cross sections for each beam polarization state. The cross sections were combined to give A_y and A_{yy} for our targets. During two-state beam runs, the polarimeter POMME was used to measure $P_{y'}$, the vector polarization of the scattered deuterons. In analysis, $P_{y'}$ and analyzing power data were combined to give the spin transfer observable $K_y^{y'}$. Vector analyzing powers were also measured with the two state beam.

Analysis of the experiment was complicated by the lack of a reliable absolute beam normalization. There were two uncalibrated scintillator stacks downstream of the target that counted beam \times target, and these gave just enough information to allow us to calculate analyzing powers. Target to target normalization had to be done by comparing the number of beam bursts among different runs, as was necessary for subtracting the carbon from the CD_2 missing mass spectra. Although it was not possible to calculate meaningful responses, the data could be combined to give the spin-flip signatures S_d^y and σ_1 . S_d^y is the signature for transferring one unit of spin in the y-direction, and was first used by Morlet in reference 2. The signature for transferring one unit of total spin (rather than just the y-component) is σ_1 , which is discussed by Suzuki in reference 3. The signatures are given by

$$S_d^y = \frac{4}{3} + \frac{2}{3}A_{yy} - 2K_y^{y'} \quad (1)$$

$$\sigma_1 = 2 + 2A_{yy} - 3K_y^{y'} \quad (2)$$

Final S_d^y and σ_1 for all targets at both q are shown.

1. R. A. Arndt, L. D. Roper, R. A. Bryan, R. B. Clark, B. J. VerWest, Physical Review D **28**, 97 (1983).
2. M. Morlet, A. Willis, J. Van de Wiele, N. Marty, J. Guillot, H. Langevin-Joliot, L. Bimbot, L. Rosier, E. Tomasi-Gustafsson, G. W. R. Edwards, R. W. Ferguson, C. Glashauser, D. Beatty, A. Green, C. Djalali, F. T. Baker, J. C. Duchazeaubeneix, Phys. Lett. B **247**, 228 (1990).
3. T. Suzuki, Prog. Theor. Phys. **86**, 1129 (1991).

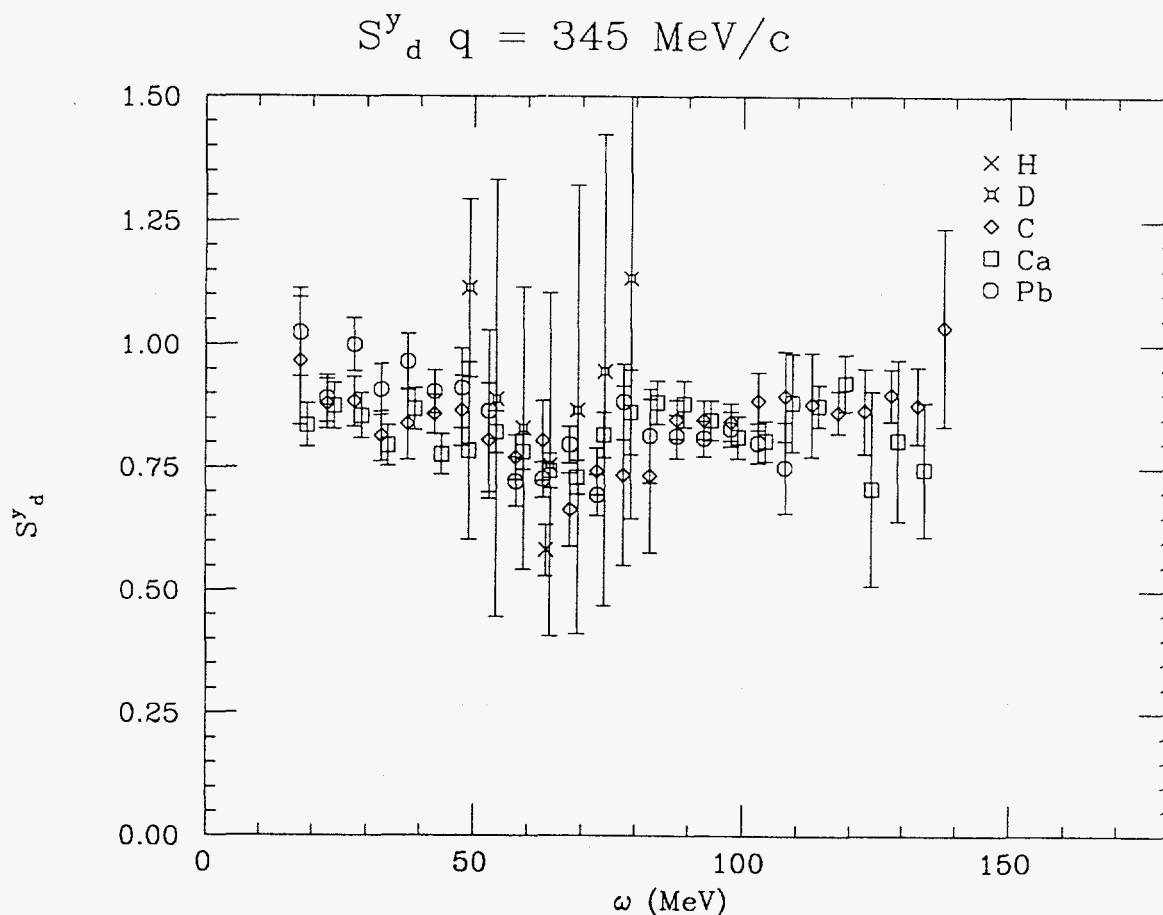


Figure 1.1 The spin-flip partial cross section S_d^y at $q = 345 \text{ MeV}/c$. Energy loss ω is defined as energy lost by the deuteron. This places the hydrogen elastic point and the centers of the quasielastic peaks of the heavier targets all at $\omega = 63.4 \text{ MeV}$.

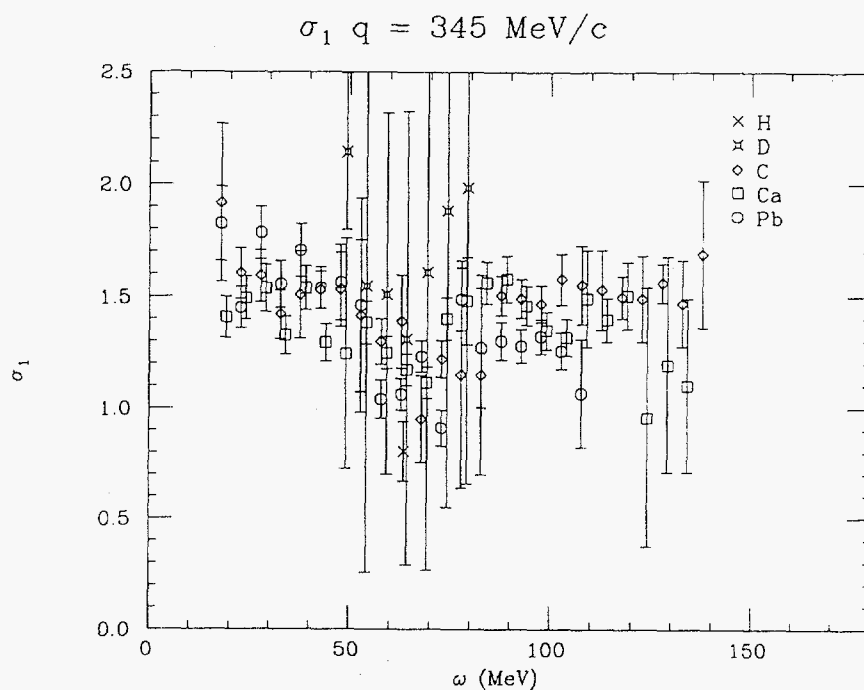


Figure 1.2 The total spin transfer partial cross section σ_1 at $q = 345 \text{ MeV/c}$.

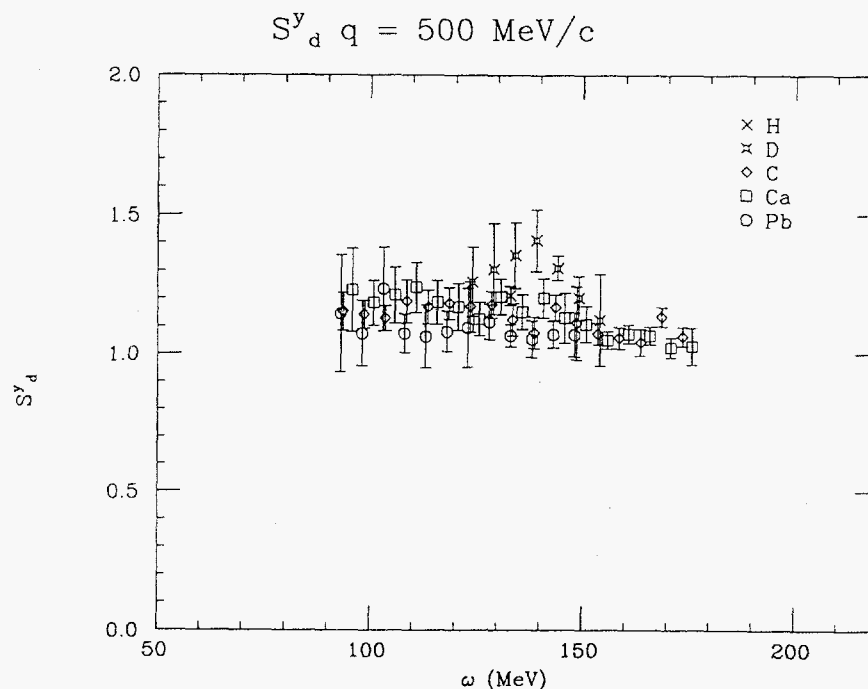


Figure 1.3 S_d^y at $q = 500 \text{ MeV/c}$. Here the energy loss for scattering from a free nucleon is $\omega = 133 \text{ MeV}$. The relative flatness of these data compared to the corresponding $q = 345 \text{ MeV/c}$ data may indicate that the effects of collectivity expected at smaller q have disappeared.

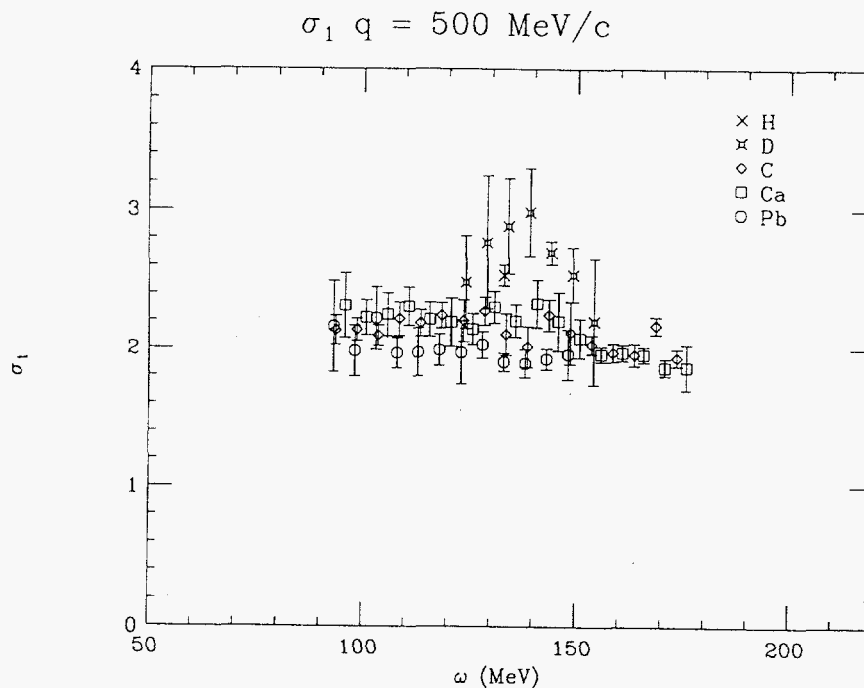


Figure 1.4 The total spin transfer partial cross section σ_1 at $q = 500 \text{ MeV}/c$. Again, the relative flatness may be an indication of the incoherence expected at this momentum transfer.

2. The Energy Dependence of Nucleon Propagation in Nuclei as Measured in the $(e,e'p)$ Reaction D. van Westrum, E. Belz, E. R. Kinney (University of Colorado); the TJNAF E91-013 Collaboration (D.F. Geesaman, spokesman).

The Nuclear Physics Laboratory (NPL) at Boulder is a member of the Thomas Jefferson National Accelerator Facility (TJNAF) experiment E91-013 collaboration. The experiment was one of two commissioning experiments for the Hall C experimental area, and was performed to measure the energy and A dependence of proton propagation in nuclei. The experiment ran in two parts; November-December 1995 and May 1996.

We studied the $(e,e'p)$ reaction on three targets: ^{12}C , ^{56}Fe , and ^{197}Au , with four-momentum transfer, $Q = 0.81, 1.14, 1.34$, and $1.79 \text{ GeV}/c$. In all but the highest Q , the High Momentum Spectrometer (HMS) was used to detect the scattered electrons, and the Short Orbit Spectrometer (SOS) was used to detect the recoiling protons. The roles of the spectrometers were reversed at $Q = 1.79 \text{ GeV}/c$. To further study the reaction mechanism, at $Q = 0.81$ and $1.34 \text{ GeV}/c$ two "Rosenbluth" separations were performed. That is, at the same four-momentum transfer, the kinematics were chosen such that the yields came from virtual photons with either primarily longitudinal or transverse polarization. The experiment also commissioned the Hall C cryogenic target, using liquid Hydrogen for normalization purposes.

Thus far, the preliminary results of the experiment are "nuclear transparency" measurements. The transparency is defined as the ratio of the experimental coin-

cidence yield to that expected in the Plane Wave Impulse Approximation (PWIA), and as such, is a measure of the probability of the struck proton traversing the nucleus without further interaction. Figure 2.1 shows the transparency as a function of Q , the momentum transfer, for $Q = 0.81, 1.14$, and 1.34 GeV/c. In all cases the statistical uncertainty is smaller than the plotting character, and the bars on the symbols indicate a preliminary systematic uncertainty of 10%. For comparison, data from an experiment at Bates¹ (filled circles) and SLAC experiment NE18² (filled squares) are shown. In the final analysis, the combined statistical and systematic uncertainties are expected to be on the order of 3%.

The PWIA yields are calculated in a Monte Carlo program adapted from the NE18 experiment. Much of the current effort is going into making sure the code correctly models the Hall C apparatus. Figure 2.2 shows a comparison of data and monte carlo for $H(e,e'p)$, and, with a few exceptions, the results look quite good. The first nine plots are focal plane quantities, and the last four are reconstructed values at the target. Figure 2.3 shows a comparison between data and monte carlo for $C(e,e'p)$ missing energy and momentum spectra. Again, the agreement is reasonable, and one should note that the missing energy resolution is expected to decrease as the spectrometer optics are improved. In addition, enhancement of the model spectral functions for all three targets is planned.

The second goal of the experiment is to perform Rosenbluth separations at $Q = 0.81$ and 1.34 GeV/c. Because such separations are especially sensitive to uncertainties in kinematics, the results must wait until the optics are more fully understood. However, a preliminary view of the separated data are afforded by comparing missing energy spectra. Figure 2.4 shows $C(e,e'p)$ for $Q = 0.81$ GeV/c. The solid line is for missing energy with an ϵ (a parameter related to the ratio of the longitudinal and transverse yields) of 0.93 and scattered electron momentum of 2.075 GeV/c at 20.5 degrees. The dashed line, at the same Q , has an ϵ of 0.38 and scattered electron momentum of 0.475 GeV/c at 78.5 degrees.

Because E91-013 is a Hall C commissioning experiment, a complete knowledge of the apparatus has not yet been achieved. To this end, particular emphasis has been placed on understanding the spectrometer optics and the responses and efficiencies of the various detectors. Future projects include modifications to the model spectral functions in the simulation, enhancements to the event reconstruction algorithm, and a detailed study of run to run consistency. Analysis of the data is expected to continue through the spring of 1997.

¹ D. F. Geesaman, *et al.*, Phys. Rev. Lett. **63**, 734 (1989).

² T. G. O'Neill, *et al.*, Phys. Lett. **B351**, 87 (1995).

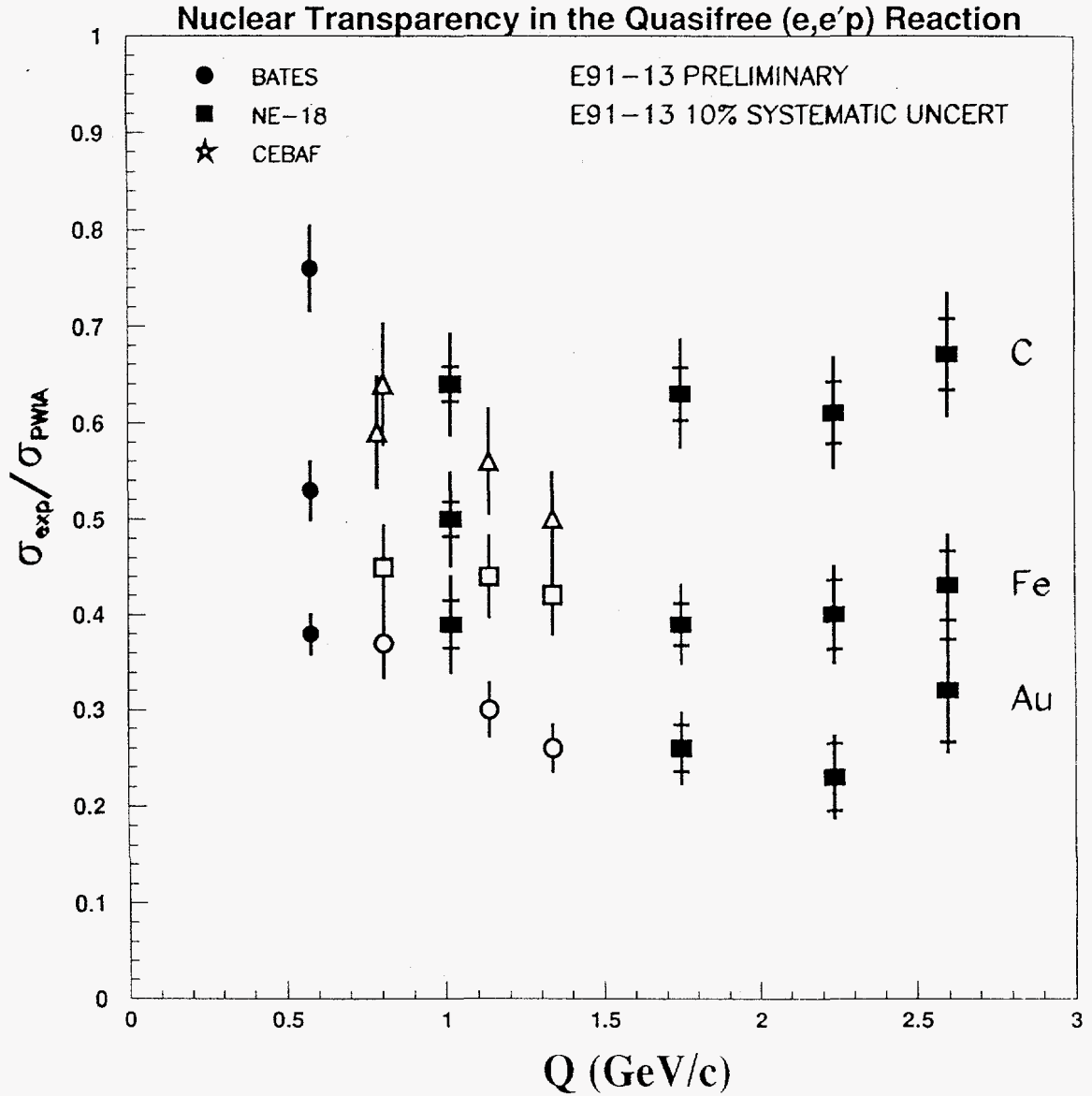


Figure 2.1 Nuclear Transparency in the Quasifree (e,e'p) Reaction.

Preliminary nuclear transparency (ratio of experimental yield to Plane Wave Impulse Approximation yield) plotted as a function of the momentum transfer, Q . Closed circles are Bates data, and closed squares are SLAC NE18 data. TJNAF data are shown with open symbols: triangles for Carbon, squares for Iron, and circles for Gold. For the E91-013 data, the statistical uncertainty is smaller than the plotting symbols and the bars indicate a preliminary systematic uncertainty of 10%.

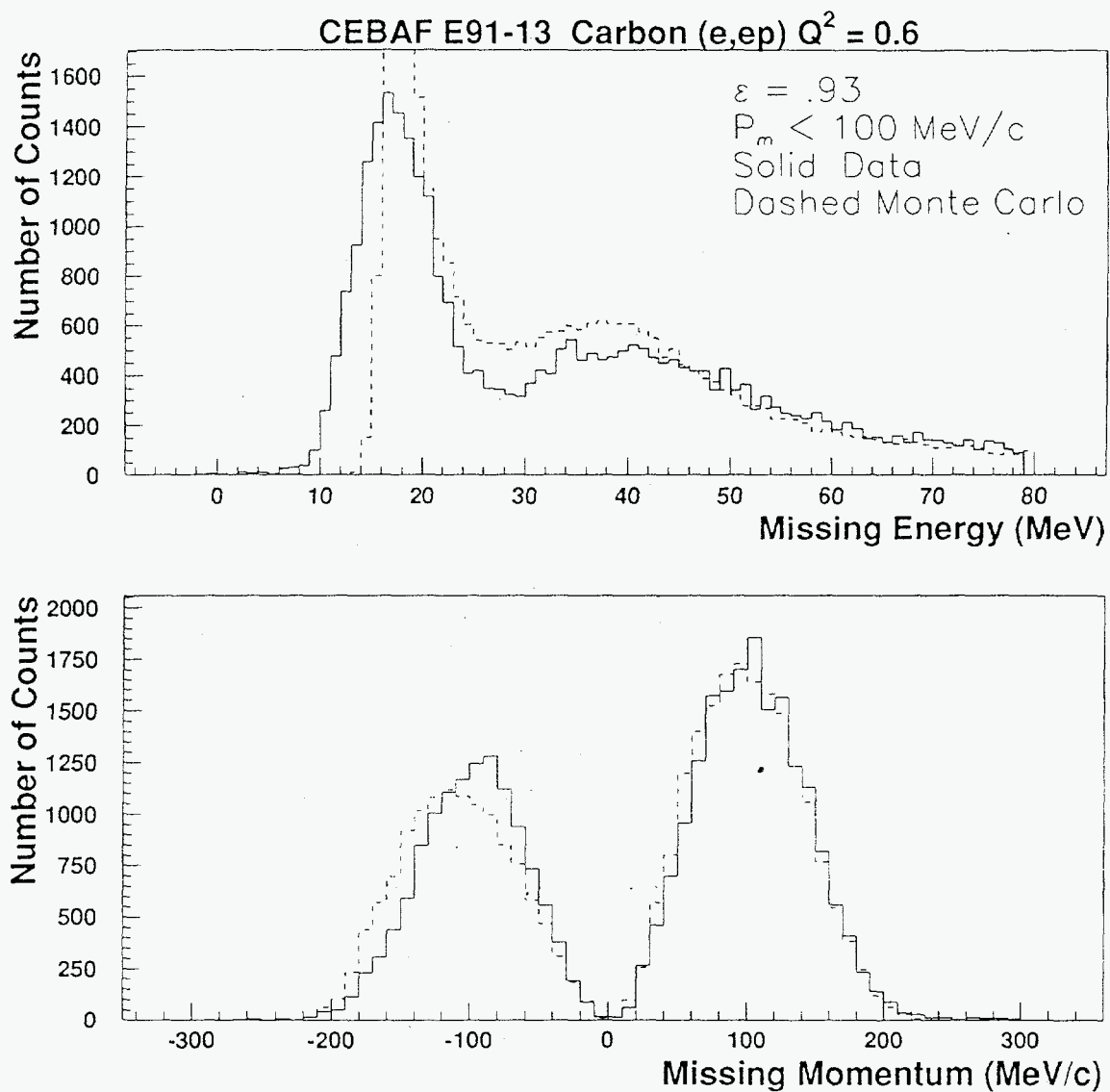


Figure 2.2 Comparison of Data and Monte Carlo Simulation.

Shown is a comparison of $H(e,e'p)$ data and simulation for various quantities with a beam energy of 3.245 GeV, scattered electron momentum of 2.255 GeV/c at 28.6 degrees, and proton momentum of 1.55 GeV/c at 41.3 degrees. The data are dashed and the simulation is solid. The first nine plots are focal planes quantities, and the last four are reconstructed values at the target.

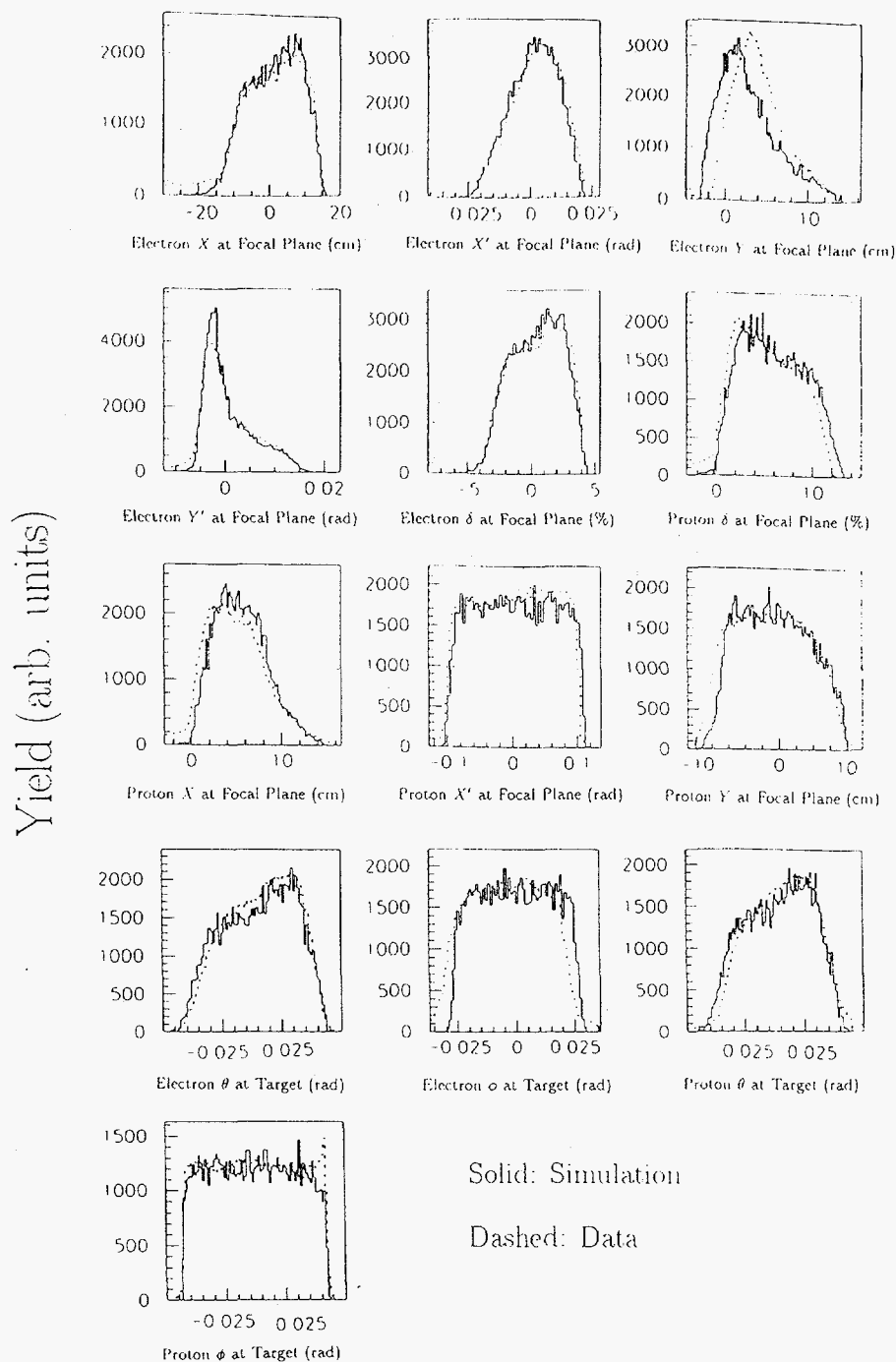


Figure 2.3 Data and Monte Carlo Simulation Comparison for Carbon Missing Energy and Momentum.

Plotted is the missing energy and momentum for $C(e,e'p)$ with a beam energy of 2.445 GeV, scattered electron momentum of 2.075 GeV/c and angle of 20.5 degrees, and proton momentum of 0.840 GeV/c and angle of 55.4 degrees. The data are solid and the simulation is dashed. The sign of the missing momentum is assigned depending on the direction of the three-momentum, q : positive missing momentum corresponds to missing momentum vectors on the larger-scattering-angle side of the q vector.

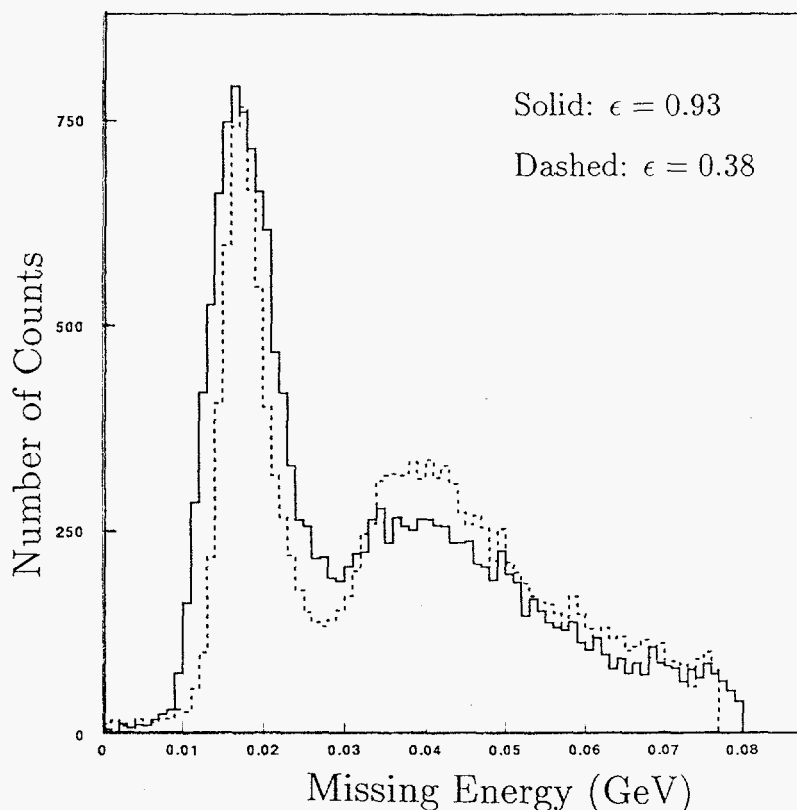


Figure 2.4 Separated Missing Energy Spectra for $Q = 1.34$ GeV/C.

Plotted is the missing energy spectra for $C(e,e'p)$ in GeV. The solid line is data with $\epsilon = 0.93$, scattered electron momentum of 2.255 GeV/c at 28.6 degrees. The dashed line is the more transverse response with $\epsilon = 0.38$, scattered electron momentum of 0.675 GeV/c at 80.0 degrees.

3. **QuasiElastic Scattering of 950 MeV/c π Mesons** C. J. Gelderloos, J. T. Brack, M. V. Keilman, and R. J. Peterson (University of Colorado); R. Sawafta (Brookhaven National Laboratory); M. Hotchi, Y. Ohta, H. Ohta, Y. Sato, M. Sekimoto, and M. Youn (INS, Univ of Tokyo); K. Aoki, H. Noumi (National Laboratory for High Energy Physics - KEK); M. Itoh, H. Sakaguchi, H. Takeda (Kyoto University); T. Kishimoto (Osaka University); H. C. Bhang, H. Park (Seoul National University); Y. Fujii, O. Hashimoto, T. Nakagawa and T. Takahashi (Tohoku University)

We have completed E352 at the Japanese High Energy Physics Laboratory (KEK) and analysis has begun. Negative pion beams from the Proton Synchrotron were used in the North Hall, with the superconducting SKS spectrometer to measure the spectra of outgoing pions. The SKS was fixed at a 30° scattering angle, with its wide acceptance covering angles from 18° to 43° . Most of our data were taken at a beam momentum of 950 MeV/c, such that the 30° scattering angle gives a momentum transfer of 500 MeV/c to the center of the broad quasifree scattering peak. At this beam momentum, we scattered from targets of CH_2 , CD_2 , 6Li , C, Ca, Zr and ${}^{208}Pb$, with energy losses up to 400 MeV in most cases. This covers the nuclear response to energies well beyond the quasifree peak.

In order to understand the acceptance and efficiency of the SKS over the wide range of outgoing pion energies we studied, we used elastic scattering from hydrogen at a number of pion beam momenta for each of four spectrometer field setting at which field maps exist. Figure 3.1 shows a sample of these data, taken with a CH_2 target at the highest field setting of the SKS. Stripes of elastic scattering events from H are shown for four beam momenta, compared to their expected kinematic loci. The nominal acceptance in angle and momentum of the SKS is shown by the box. The events shown correspond to only 3% of our data for these calibration runs. We will use these spectra and the known π^- - proton elastic cross sections, with the measured field map data, to generate the acceptance of the SKS very well for this current setting. The small numbers of counts at large angles reflect the small elastic cross sections expected for free scattering. Similar calibration runs at lower field settings used beam momenta down to 700 MeV/c for CH_2 scattering. Our field settings give good overlap of the continuum spectra, so we can anticipate a very reliable absolute scale to our cross section data.

Figure 3.2 shows spectra for 950 MeV/c π^- scattered from CH_2 and from a normalized sample of events for carbon. Counts from the array of events across the wide angle acceptance were collected into 2° angle bins at fixed lab angle for the four spectra shown. Only 3% of the data were analyzed for these samples. The clear peak for free scattering sets the scale, at momentum transfers near 325, 379, 446 and 504 MeV/c for the four angles. Our final analysis will collect events in stripes of fixed q , to generate spectra in the same fashion that they are computed in response calculations. It is evident from this sample that we will have very high quality quasifree spectra out to momentum transfers near 600 MeV/c.

These measured spectra will be converted into responses, by including the free cross sections and the computed effective number of nucleons sensed by quasifree scattering, in just the same fashion we have used for our K^+ ¹ and pion scattering^{2,3} experiments on the same targets at the same momentum transfers, and to electron scattering responses. The wide range of target masses we examined will enable us to understand the role of this computed effective number of nucleons.

The data from E352 are sensitive mainly to the $S=T=0$ nuclear correlations, very similar to our K^+ data, but with different distortions. Together, we will be able to provide a very clear demonstration of the density and momentum transfer dependence of this important correlation.

We also obtained extensive data for a large range of momentum transfers and low energy losses on carbon in order to bin events into spectra of fixed scaling variable y . The range of beam momenta covers the low energy edge of the D15 (1675) MeV resonance, which is the second largest feature in free π -nucleon scattering (after the P33 (1232)). We know that the carbon nucleus exhibits scaling in this range⁴, and so we can invert the problem to obtain the effective in-medium π -nucleon cross section.

Our spectra for some targets were taken to very large energy losses in order to address the question of 'pion transport' through the nuclear medium. This beam energy is far above those available from LAMPF, where data and INC calculations have been compared⁵. Appropriate INC calculations will be carried out for comparison to the data from E352, as described elsewhere in this report.

Data reduction will be a demanding task, using the complex analyzer needed for the SKS and involving a very large set of data. Track reconstruction is particularly important due to the extra events often found in the large acceptance SKS system. Our new work station is now able to run this analyzer, and the final tests of the system are being carried out. After the normalized spectra are available, we will be able to arrange, sort and collect the events to address several interesting questions.

¹ C. M. Kormanyos *et al.*, Phys Rev C **51**, 669 (1995).

² R. J. Peterson *et al.*, Phys Lett B **297**, 238 (1992).

³ J. E. Wise *et al.*, Phys Rev C **48**, 1840 (1993).

⁴ J. M. Finn *et al.*, Phys Rev C **29**, 2230 (1984).

⁵ J. D. Zumbro *et al.*, Phys Rev Lett **71**, 1796 (1993).

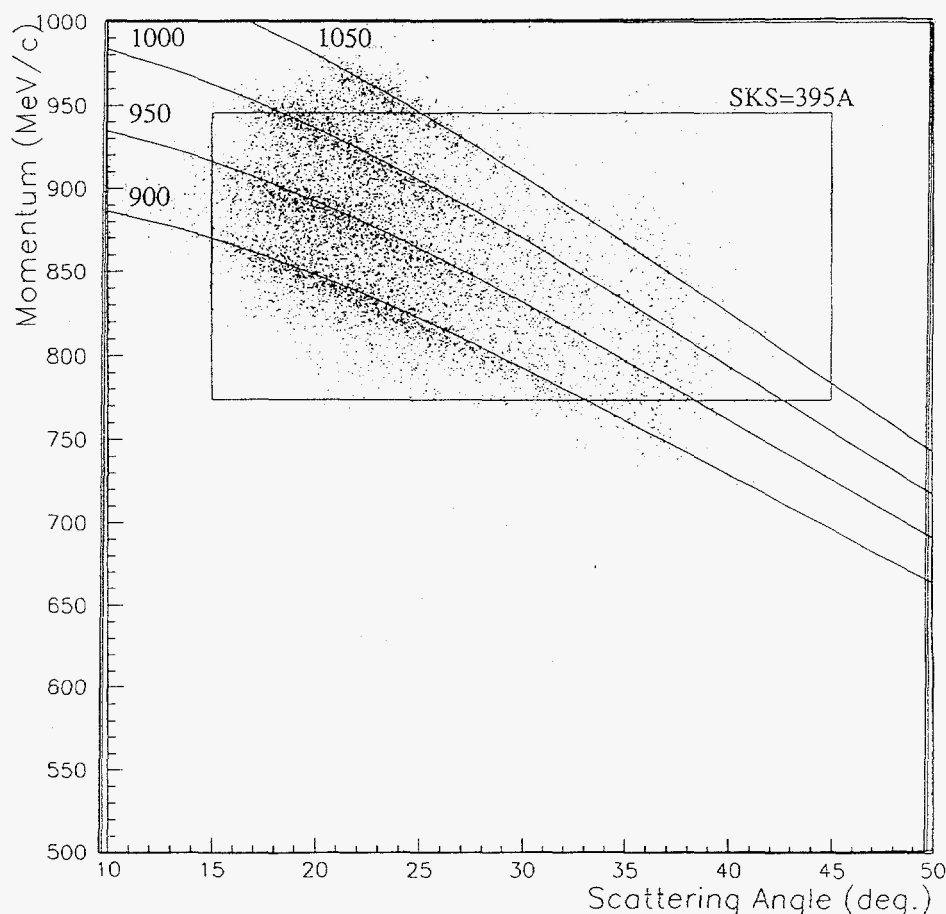


Figure 3.1 Spectra of pions scattered from CH₂ at four beam momenta are shown across the angle and momentum acceptance of the SKS spectrometer at a fixed field setting. The curves show the kinematic loci for scattering from free protons. These and other data will be used to establish the acceptance of the spectrometer. The nominal acceptance is shown by the box.

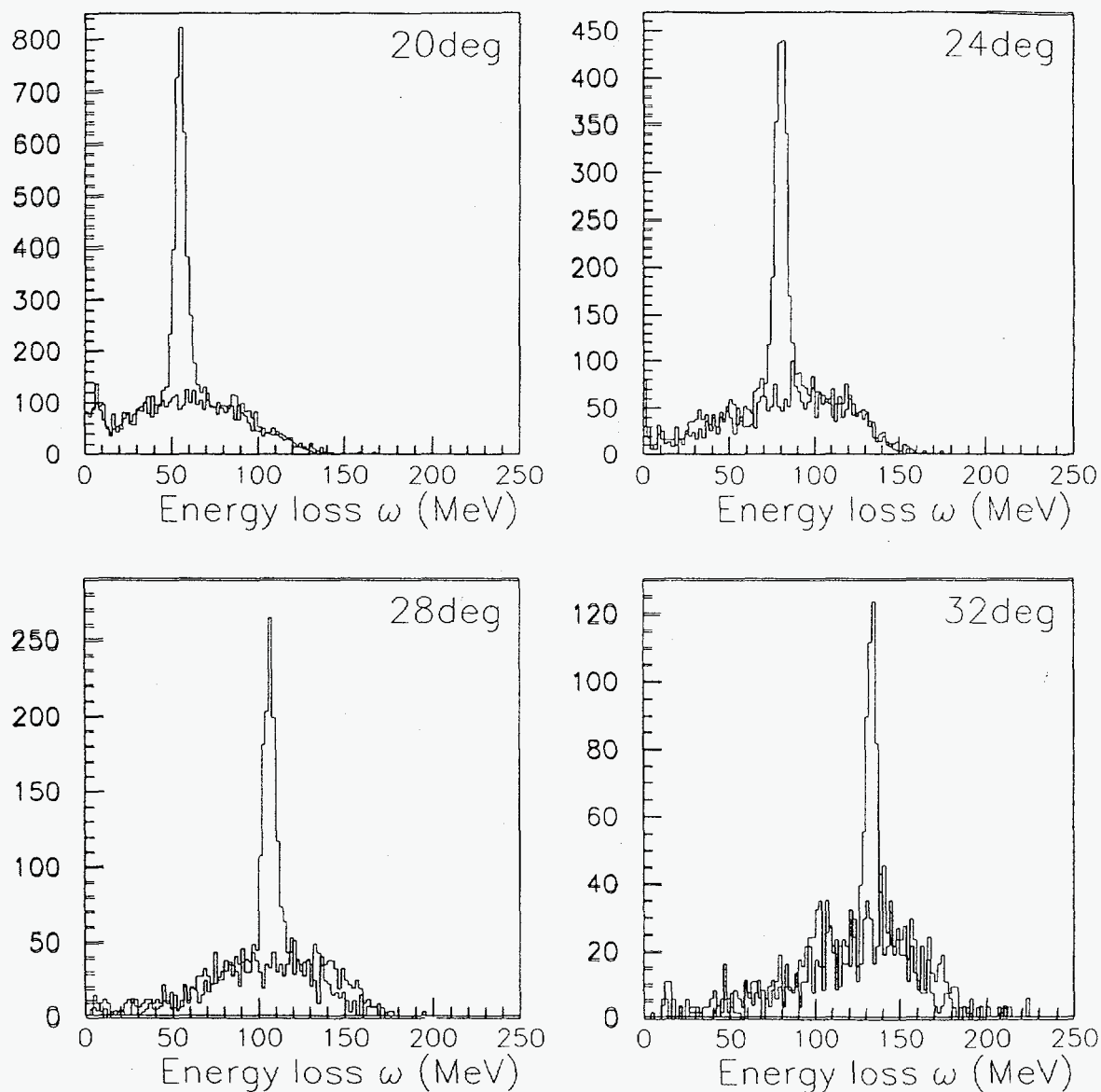


Figure 3.2 Overlaid normalized spectra from CH_2 and C are shown for 950 MeV/c π^- scattered into four bins of fixed laboratory scattering angle. The corresponding free momentum transfers are near 325, 379, 446 and 504 MeV/c. Only 3% of the carbon events were analyzed for these sample spectra. We anticipate good statistical accuracy for our quasielastic scattering data out to momentum transfers near 600 MeV/c.

D. NUCLEAR STRUCTURE AND REACTIONS

1. Production of ${}^6\text{He}$, ${}^6,7\text{Li}$ and ${}^7\text{Be}$ in the $\alpha + \alpha$ Reaction above 160 MeV, D. J. Mercer (University of Colorado); S. M. Austin, J. A. Brown, S. A. Danczyk, S. E. Hirzebruch, J. H. Kelley (National Superconducting Cyclotron Laboratory); D. A. Roberts (University of Michigan); and T. Suomijärvi (National Superconducting Cyclotron Laboratory/l'Institut de Physique Nucleaire d'Orsay)

We have measured the differential and total cross sections for production of ${}^6\text{He}$, ${}^6\text{Li}$, ${}^7\text{Li}$ and ${}^7\text{Be}$ when a target of ${}^4\text{He}$ is bombarded with α particles at energies of 160, 280, and 620 MeV. These cross sections are needed to calculate galactic cosmic ray (GCR) production of lithium in the early Galaxy. Previous to our experiment, no cross section data were available for $A = 6$ isotopes above 200 MeV bombarding energy, and only loose upper limits were available for $A = 7$. Using realistic assumptions about the GCR flux, the lack of high-energy cross section data led to a factor of 3 uncertainty in early galaxy production of lithium. Our new measurement resolves this uncertainty, with less than 2% of the calculated lithium production occurring above 620 MeV.

We employed a novel experimental technique, described in detail in Reference 1, which eliminates the traditional helium gas target cell and thus reduces potential background scattering. Analysis of the fusion cross sections for $A = 6, 7$ is now complete, and the results may be seen in Figures 1.1 and 1.2. As can be seen, the cross sections for all four isotopes continues to decrease rapidly with increasing energy. For $A=7$ our measurements are in excellent agreement with those of Glagola *et al.*² at 160 MeV, and may be interpolated to good agreement with Woo *et al.*³ at 200 MeV. Our upper limits at 620 MeV offer a significant improvement over those of Yiou *et al.*⁴. For $A=6$ our results at 160 MeV disagree with original results of Glagola *et al.* by a factor of 2, although we agree with the recently reanalyzed results of Glagola *et al.*. Of greatest interest to astrophysics calculations are our new high-energy measurements for ${}^6\text{Li}$, which greatly constrain early-Galaxy GCR nucleosynthesis of this isotope.

¹ "Production of $A=6,7$ nuclides in the $\alpha + \alpha$ reaction at 160, 280, and 620 MeV," D.J. Mercer, Sam M. Austin, J.A. Brown, S.A. Danczyk, S.E. Hirzebruch, J.H. Kelley, T. Suomijärvi, and D. A. Roberts (submitted to Phys. Rev. C).

² B.G. Glagola, V.E. Viola, Jr., H. Breuer, N.S. Chant, A. Nadasen, P.G. Roos, S.M. Austin, and G.J. Mathews, Phys. Rev. C **25**, 34 (1982); "Suggested correction to ${}^6\text{He}$, ${}^6,7\text{Li}$, and ${}^7\text{Be}$ production cross sections in $\alpha + \alpha$ reactions between 60 and 160 MeV," D.J. Mercer, B.G. Glagola, and Sam M. Austin, (submitted to Phys. Rev. C).

³ L.W. Woo, K. Kwiatkowski, S.H. Zhou, and V.E. Viola, Jr., Phys. Rev. C **32**, 706 (1985).

⁴ F. Yiou and G.M. Raisbeck, in *Proceedings of the 15th International Cosmic Ray Conference*, (Plovdiv, Bulgaria, 1977) O.G. 133.

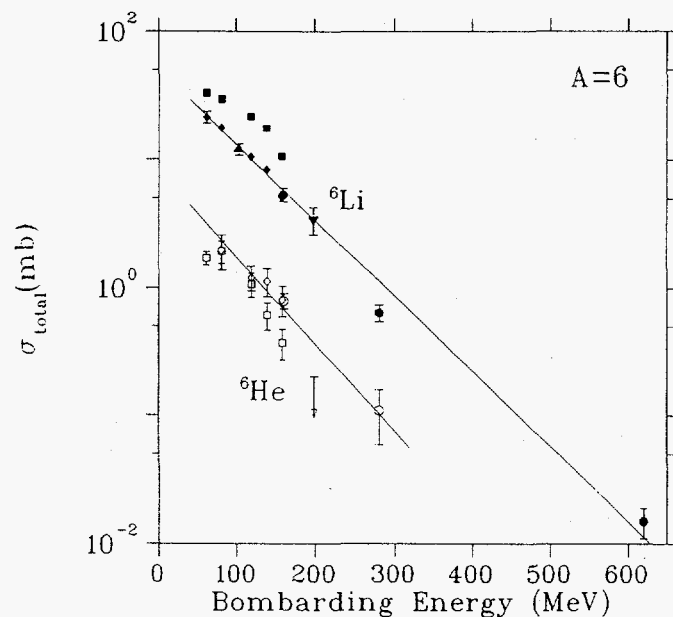


Figure 1.1 Total cross sections for production of ${}^7\text{Be}$ (solid points, shown $\times 10$) and ${}^7\text{Li}$ (open points). Diamonds are from Glagola *et al.*, triangles are from Woo *et al.*, stars are limits from Yiou *et al.*, and circles are from the present experiment. Solid lines show a fitted exponential curve common to ${}^7\text{Be}$ and ${}^7\text{Li}$.

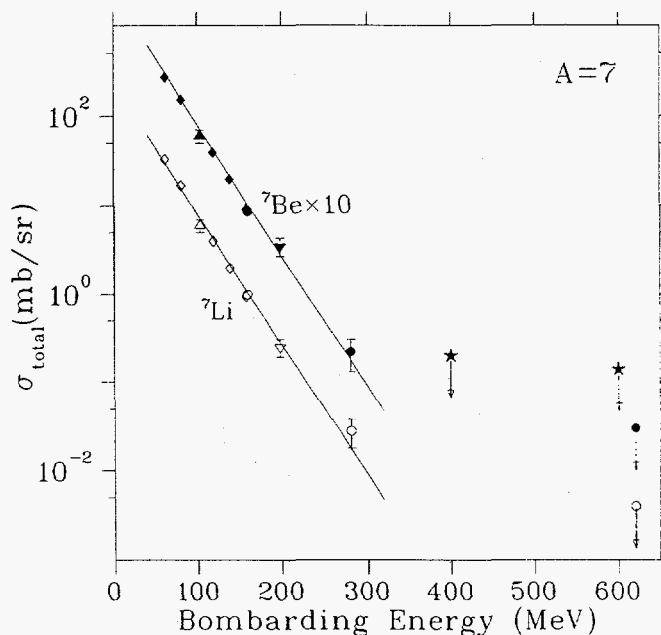


Figure 1.2 Total cross sections for production of ${}^6\text{Li}$ (solid points) and ${}^6\text{He}$ (open points). Diamonds are from Glagola *et al.*, squares are reanalyzed data of Glagola *et al.*, triangles and the ${}^6\text{He}$ limit are from Woo *et al.*, and circles are from the present experiment. Solid lines show fitted exponential curves.

2. Unfolding of Nucleon Sizes J. Patterson and R. J. Peterson (University of Colorado)

The goal of this project is to extract the density of protons in various nuclei from the data published in De Vries, Jager, and De Vries¹. Those authors fitted elastic electron scattering data and mesonic atomic spectra to several different multi-parameter functional forms to model and fit the total charge distribution within a given nucleus. They then compiled a table that lists, among other relevant data, the numerical values of the fitted parameters, along with their uncertainties, of the functional forms that model the total charge distributions of the various nuclei. Some of these functional forms are the two and three parameter Fermi functions, the three parameter Gaussian function, and the Harmonic Oscillator model. We wished to compile a similar table using the same functional forms as the original table, but fitting and listing, along with the corresponding uncertainties, the numerical values of the parameters that characterize the distribution of the centers of individual protons within each nucleus. The motivation for compiling the above table is that these distributions enter into the hadron-nucleus impulse approximation calculations.

We modeled the total charge distribution of a particular nucleus as the folding integral of the distribution of the charge within a single nucleon present in the nucleus with the distribution of the individual centers of all the nucleons within the nucleus, over all space. So if we assume functional forms of the nucleon charge and center locations distributions we can construct, via a folding integral over all space, an alternate functional form for the total charge distribution that does not depend explicitly upon the parameters already published in the aforementioned table, but depends upon the parameters that characterize the model of the nucleon centers distribution. We then applied a numerical multi-parameter fitting routine to this alternative functional form to fit it to the appropriate functional form of the total charge distribution, utilizing the parameters found in the already published table. The parameters of the alternate functional form, after fitting to the original data, are the parameters that characterize the distribution of the centers of the individual nucleons.

For our initial analysis we imitated the authors of the original table by considering all distributions to be spherically symmetric, with only radial dependence, which greatly simplified the mathematics of the modeling. We also followed their lead in each fitting we performed by choosing for the model of the distribution of the individual centers of charges the same functional form they used to model the total charge distribution of the nucleus.

In all of our fitting up to this point, we have modeled the distribution of the charge of the nucleons as a Gaussian centered around the geometric center of the nucleon, but we can consider other functional forms in the future. To correctly model the distribution of charge within a single nucleon, no matter what functional form we use, we must consider the physical size of an individual nucleon. We are using the published value of the rms radius of a proton of 0.85 fm. From this value we can write down an analytic expression that models the charge distribution within a free proton.

Notice that to evaluate the alternative functional form of the total charge distribution, an integral over all space must be performed. Since the Gaussian is

angularly dependent, we exercised caution in performing the integration. We had to perform a standard multipole expansion on the Gaussian, and keep only the central portion of the expansion. We then proceeded to use standard techniques of separating the integral into two independent integrands: one that is solely dependent on the radial coordinate, and the other solely dependent upon the angular coordinate. Due to the orthogonality of Spherical Bessel functions, only the first term in the angular portion survives the integration. The radial portion of the integral is not so easily carried out though. For the product of a Gaussian with most of the functional forms considered to correctly model the distribution of individual centers of charge an antiderivative does not exist, hence the radial integral must be numerically evaluated.

To perform the fitting of the alternative form of the total charge distribution to the already published data, we used a standard multi-parameter fitting algorithm that is based upon minimizing chi-squared in parameter space.

All the machinery has now been built to evaluate and fit the alternative form of the total charge distribution that is dependent upon the parameters that characterize the distribution of centers of nucleons. We have performed this procedure on several well behaved, spherical nuclei with much success. We will now perform this procedure on all nuclei listed in the original table and compile our own corresponding table. We will then proceed by considering other functional forms for the distribution of charge in a single nucleon, and also deviate from the functional forms used for each nucleus by the authors of the original table.

- ¹ H. De Vries, C. W. de Jager, C. De Vries, Atomic Data and Nuclear Data Tables **36**, 495 (1987).

3. IntraNuclear Cascade Calculations for Pion Single Charge Exchange

R. J. Peterson (University of Colorado); J. D. Zumbro (Los Alamos National Laboratory); H. C. Bhang (Seoul National University)

The inclusive spectra of pions emerging from a complex target after bombardment with medium energy pions includes all features of how the pions are transmitted through the nuclear medium. This might include scattering from one nucleon at a time, absorption, and pion production. For noncharge exchange scattering (NCX) Zumbro *et al.* found that data at 500 MeV failed to match the calculations from an IntraNuclear Cascade model¹. In particular, the strong self-absorption expected for pions near laboratory energies of 180 MeV due to the very strong delta resonance was not seen in the data. A 'hadronization time' of 2 fm/c was introduced, meaning that pions made from ($\pi, 2\pi$) reactions would be forbidden to interact for that time. This removed much of the strong self-absorption resulting from the simple INC calculation, and greatly improved the comparison to the data. A possible reason to impose this hadronization time would be to allow for the creation of a σ meson when two pions result from a single nucleon reaction, and this σ meson may not decay promptly in the nuclear medium.

We have carried out the same INC calculations for neutral emerging pions with a 500 MeV beam to check this idea with another reaction, using the data of Ouyang². Since the acceptance of the π^0 detector follows completely different

systematics than does a magnetic spectrometer such as used for the charged pions, the π^0 data would confirm the experimental facts in an independent way. Also, the isoscalar σ meson must decay into oppositely charged pions for NCX, but into two neutral pions in SCX. Further, the SCX spectra can be cleanly measured down to much smaller scattering angles. Another feature of our new analysis is the inclusion of data from ${}^7\text{Li}$, which has about half the density of the carbon target used in Reference 1. We anticipate this to be an important analysis since a large body of neutral pion data from heavy ion collisions exists, and have been of great interest.

Figure 3.1a shows the negative pion data at 50° for ${}^7\text{Li}$ in a seven degree angle bin² compared to the INC calculation without a hadronization time. The normalization is arbitrary, to make the quasifree peak near 400 MeV match. Although the SCX data do not reach to large energy losses, it appears that the data lie well above the calculations near 200 MeV. Note that the INC calculations have allowed us to keep track of the pions emerging after no pion production from those from pion production. That contribution to the spectra is shown by the dashed line.

Below, in Figure 3.1b, the same data on a different scale are compared to the INC calculation with the same 2 fm/c hadronization time used for NCX. Again the scale of the data has been adjusted to match the quasifree peak. The calculated spectrum and that measured are now seen to agree well, confirming the conclusions drawn from NCX spectra¹. The dashed pion production curve is what has increased to yield agreement with the data.

We are also making comparisons to our SCX data at 500 MeV for negative pions for carbon and other targets at other angles, and we will also treat our data for positive 500 MeV pions². The lack of symmetry for ${}^7\text{Li}$ may be of special interest. Our 500 MeV SCX experiment also included detection of recoil protons, and we will investigate the use of the INC code for these triply differential cross sections.

The data shown in Fig 3.1 do not extend down to the very low outgoing pion energies needed to test the INC calculation completely. We will use the code to generate comparisons to our data set for negative pion SCX at 475 MeV^{3,4}, which extend down to near 50 MeV outgoing energy. If we just slip the INC calculations seen in Figure 3.1 by 25 MeV, they seem to be very similar to our data at 475 MeV.

Completion of this SCX analysis will provide a valuable complement to the similar analyses carried out for NCX and DCX. Indeed, the comparison of data and INC calculations seen in Fig 3.1b is superior to that found for NCX on carbon. Whether this is due to the density of lithium or to the use of neutral pions will be known soon.

¹ J. D. Zumbro *et al.*, Phys Rev Lett. **71**, 1796 (1993).

² J. Ouyang, Ph.D. thesis, University of Colorado (1992); Los Alamos Report LA-12457-T.

³ B. L. Clausen *et al.*, Phys Rev C **35**, 1028 (1987).

⁴ M. R. Braunstein, Ph.D. thesis, University of Colorado; Los Alamos Report LA-12056-T.

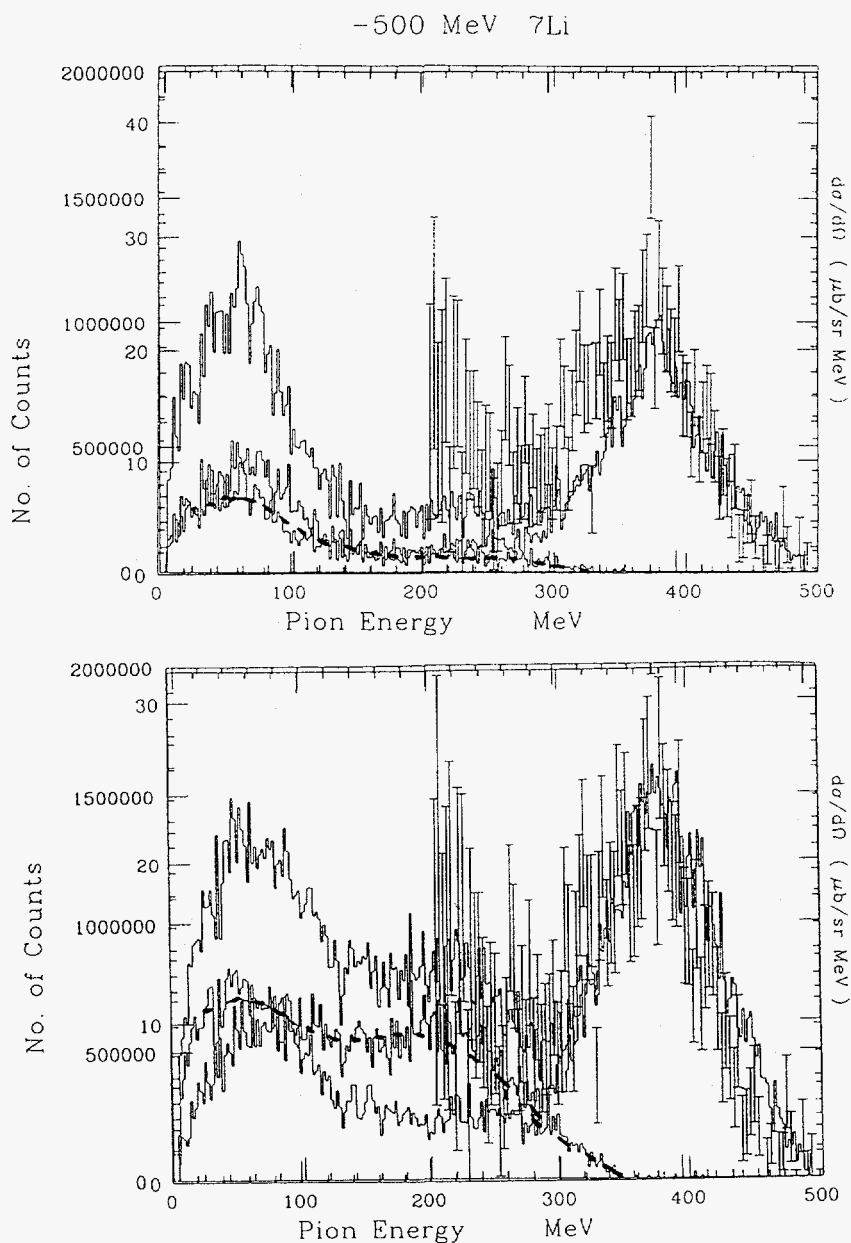


Figure 3.1 Above are shown 500 MeV pion SCX data at 50° on a ^7Li target². INC calculations are compared with an arbitrary normalization, using no hadronization time. The connecting dashed line indicates those pions resulting from pion production reactions within the target. When added to the events arising from reactions without pion production, the highest curve for the sum of all emerging pions is formed. The same data are compared to INC calculations including a 2 fm/c hadronization time in the lower figure, again with the dashed line to show the contribution of pions from production reactions. This prescription increases the yield of pions near 200 MeV, in agreement with the data, and in concord with the conclusions reached in an analysis of NCX data¹.

E. INSTRUMENTATION

1. **HERMES Front Drift Chambers** J. T. Brack, J. E. Belz, D. Edmonds, C. D. Hoyle, E. R. Kinney, D. J. Mercer, D. Prull, G. Rakness, R. A. Ristinen, W. R. Smythe (University of Colorado)

In 1994 and 1995, a large fraction of the efforts of the University of Colorado nuclear physics group went toward construction of the front drift chambers (FCs) for the HERMES experiment at the DESY Laboratory, in Hamburg, Germany¹. The CU group signed on to the HERMES collaboration and took over the FC contract at a comparatively late date. In spite of the resulting tight construction schedule the FCs were installed on time in the HERA tunnel at DESY by early 1995, and a period of commissioning for the full HERMES detector followed. As production data acquisition began in mid-summer, it became apparent that the FCs were the only fully functional tracking component at the front-end of the detector. The other front-end components could not be repaired because of lack of spare parts, or insufficient access time since the tunnel was sealed for the beam period. At the spring collaboration meeting the experiment spokesperson acknowledged to the collaboration that the success of the FCs was a key element in the successful acquisition of useful data during the 1995 beam period.

Although the FCs were fully functional in 1995, optimal resolution was not achieved, primarily due to insufficient shielding of the electronics from RF noise in the experimental area. Possible noise sources were identified as RF pickup from the polarized target just 1.5m upstream and saturating ferric inductors on the preamplifier cards, caused by the fringe field of the magnet a few cm downstream.

During the four month access period in the winter of 1995-96, several modifications were made to the FCs to improve the noise level on the chamber electronics. To lessen the RF pickup, the RF-shielding on the housing boxes for the electronics was made tighter. Some 200 screws were added to the side plates and new aluminum pieces were machined and chromated to replace the original rubber top plates. In addition, thin grounded Cu plates were inserted between, and parallel to, the pin connectors on top of the chambers. This is at the input point to the preamplifier, and is the most sensitive point for noise pickup.

To lessen the effects of the fringe field, the original ferric inductors were replaced with a non-ferric type. These inductors are positioned between the pre-amp and discrimination stages of each channel (2304 channels total) of the electronics cards and are intended to reduce high frequency noise. Tests performed in Boulder using modified electronics cards and a large magnet confirmed that the new inductors saturate at about 500 G, which is about 25% higher than the originals.

The effect of the increased RF-shielding and the inductor change on the noise level is that the thresholds can now be reduced by 70% compared to last year. This has resulted in improved resolution (see Figures 1.1 and 1.2) and increased efficiency of approximately 98-99%.

In addition to the above changes during the winter access, several small gas leaks were found in the chambers leading to a factor of three improvement in the leak rate; two sticking alignment target actuators were repaired, and one damaged target was replaced; and, to accommodate a new detector element (hodoscope H0)

immediately upstream of the FCs, some cables (LV and HV) were re-routed and the upper LV distribution box was moved.

Concerns about aging effects on the FCs has lead to a study² of chamber aging while using the 90:5:5% gas mixture of Ar/CO₂/CF₄ in a high radiation environment. Earlier studies³ imply that the CF₄ component will reduce aging effects dramatically, but to date no study has been specifically done on this gas mixture.

Construction of two spare chambers, identical to the original four, was completed in spring of 1996 at the formal request of the HERMES collaboration. As with the originals¹, these chambers were fabricated and assembled in Boulder, while the stringing operation was performed at LANL. These spares greatly reduce the threat due to aging or catastrophic failure of the chambers now in use.

HERMES hardware projects for the future include construction of a new larger set of FCs, pending DOE approval of a proposal. This would allow study of possible gluon spin in nucleons by observing muons from J/Ψ and D* meson decay⁵. To this end, work has begun on a design (see Figure 1.3) based on the original FCs, but with doubled vertical acceptance. These chambers would use all the peripheral devices from the original FCs, including the complete electronics boxes, electronics cards, optical alignment devices, and HV, gas and cooling systems. To cover the added vertical acceptance, 16 extra wires are required for the 30 degree U and V planes, requiring four additional electronics cards per chamber. Minor modifications to the electronics boxes would be necessary to allow for mounting these cards.

¹ D. J. Mercer, *et al.*, *Technical Progress Report, September 1995, University of Colorado at Boulder Nuclear Physics Laboratory*, (1995) 55.

² C. D. Hoyle, *Wire Chamber Aging with Ar/CO₂/CF₄ (90:5:5)*, Senior Thesis Project, CU Dept. of Physics, April 1996.

³ R. Openshaw, *et al.*, *IEEE Transactions in Nuclear Science* **36**, 567 (1989).

⁴ E. R. Kinney, this progress report.

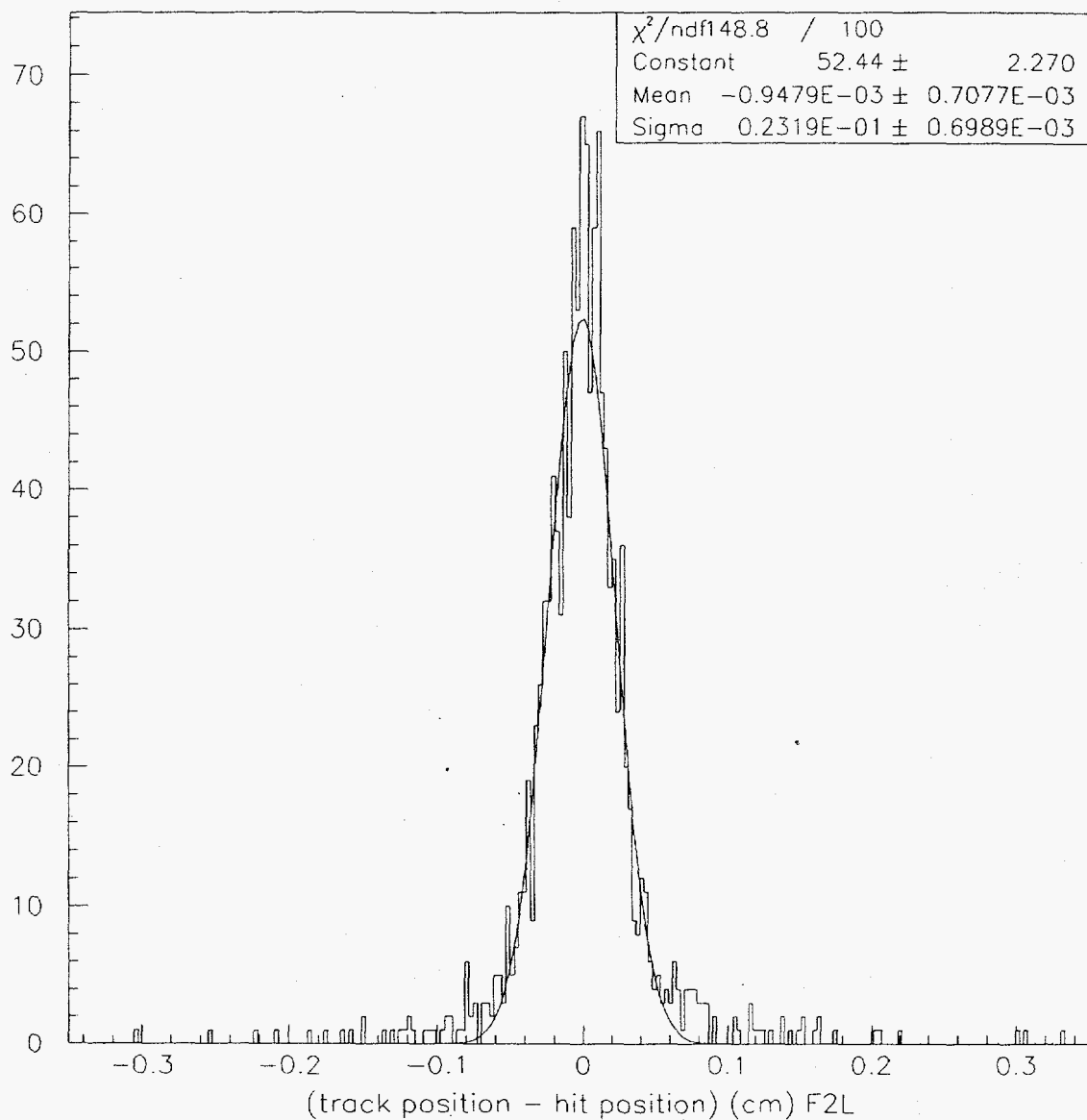


Figure 1.1 Tracking residuals (fitted track position minus hit position) for a sample FC plane. Resolution of the FCs with electronics modifications is now about $250\ \mu\text{m}$. For comparison, the best pre-modification resolution was about $340\ \mu\text{m}$.

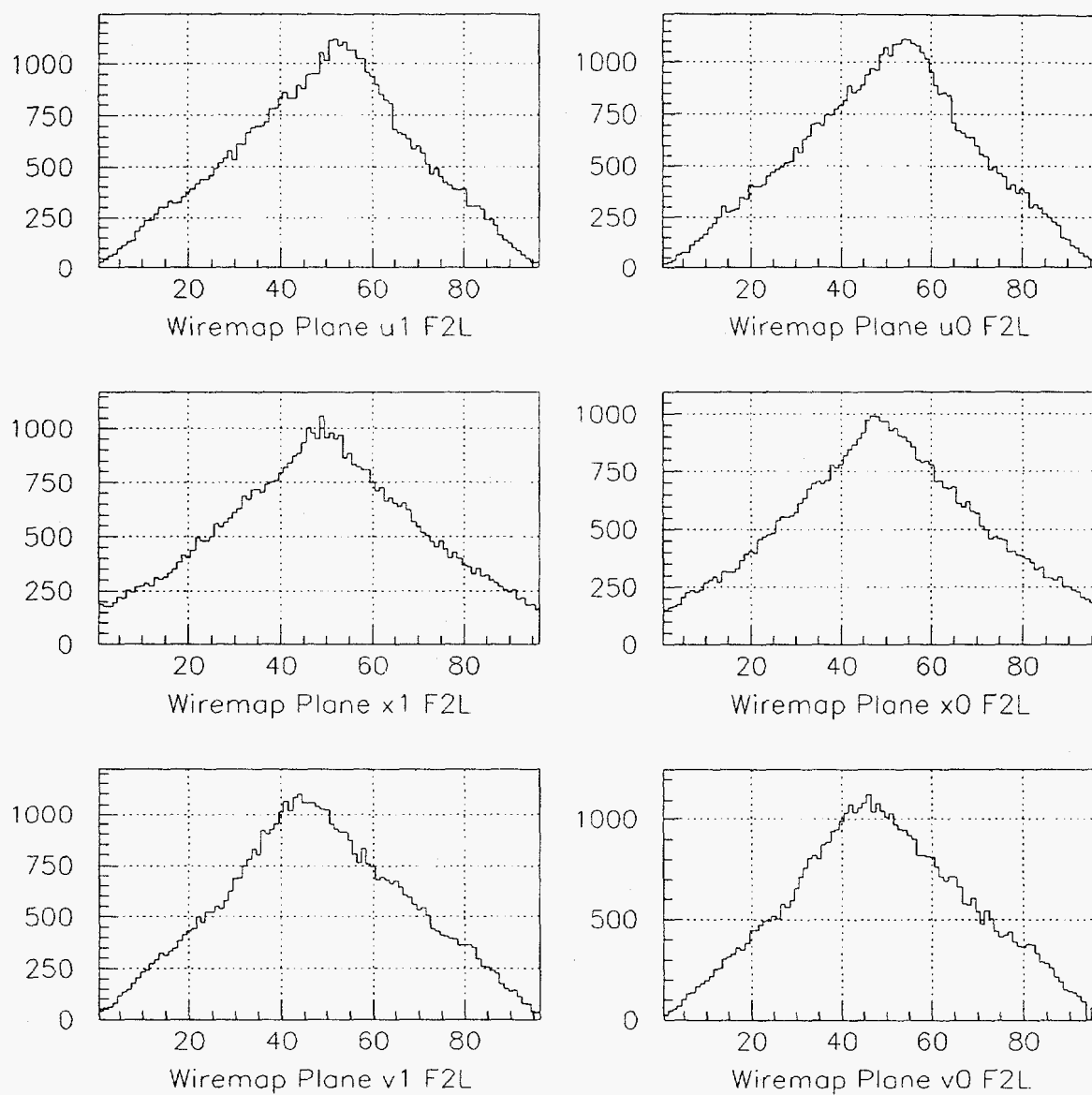


Figure 1.2 Wire maps for one of the chambers, showing the uniformity of distribution typical after the latest modifications. The distributions show peaking due to small-angle scattering.

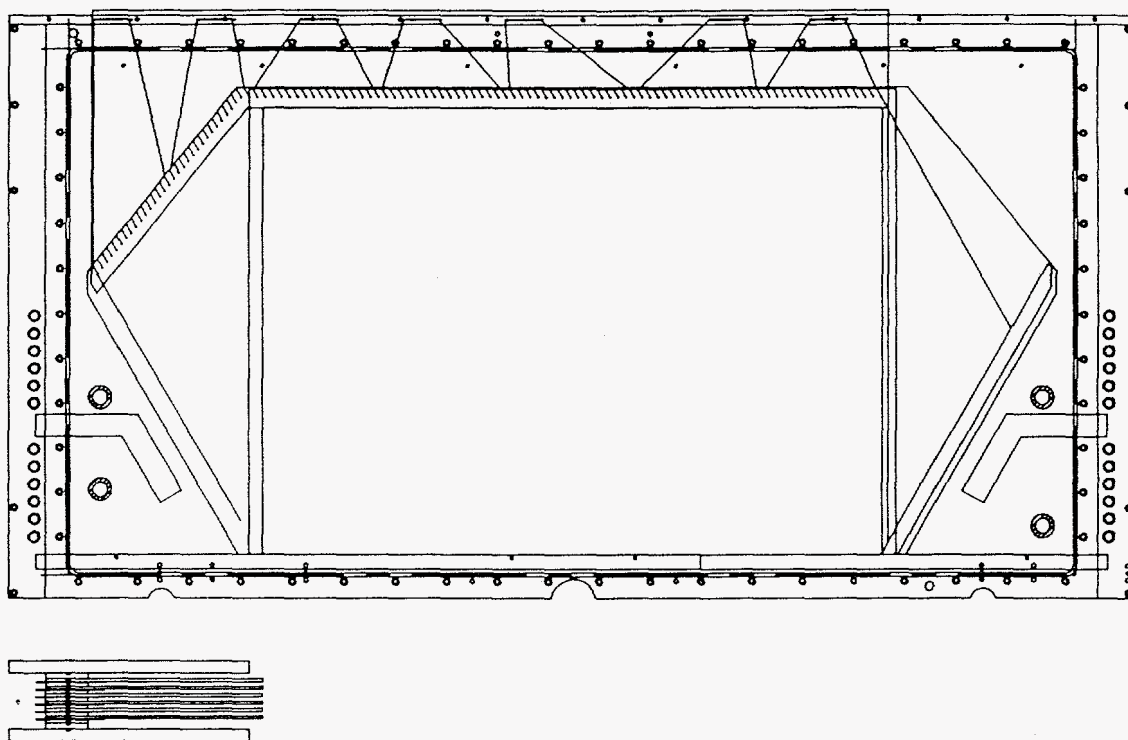


Figure 1.3 Conceptual overlay drawing of the new larger-acceptance HERMES front chambers, showing the top aluminum plate overlaid on one of the 6 G10 anode boards. Most of the design is similar to the existing FCs. An additional 16 anode wires, on the extreme left for the $+30^\circ$ plane shown, cover the lower left corner of the expanded active area.

2. **Proton Radiography at the AGS** A. Saunders, (Univ. of Colorado); J. Amann, K. Mueller, R. Hill, G. Hogan, N. King, G. Yates, J. McClelland, C. Morris, K. Morley, J. Sarracino, H. Ziock, J. Zumbro, S. Jaramillo, P. Pazuchanics (Los Alamos National Labs); E. Hartouni (Lawrence Livermore National Labs); J. Tinsley (Bechtel, Santa Barbara); R. Prigl, J. Scaduto (Brookhaven National Labs).

BNL experiment P920 was proposed to test the concept of using high energy and high intensity proton beams to create images of the interiors of objects built of high atomic number (Z) materials, also known as proton radiography. The usual X-ray techniques used for normal objects break down for those made of high Z materials, since X-rays cannot penetrate those objects. High energy protons can penetrate to the center of objects made of even the heaviest known elements. A particle accelerator is used to supply the high energy (tens of GeV) protons, a system of magnetic lenses is used to deliver the beam to the object and focus the outgoing beam, and one of a variety of imaging systems collects the resulting image. The purpose of experiment P920, which ran in June and July at Brookhaven National Lab, was to investigate the second and third links in the above chain. A system of quadrupole magnets was arranged to get the beam to the object and focus the beam, and three different imaging systems were used to collect the resulting

image. The protons were supplied at about 10 GeV by the Alternating Gradient Synchrotron (AGS) at BNL.

In order for the protons to be focussed successfully, the characteristics of the incoming beam had to be known precisely. Therefore, the beam coming from the accelerator was as close as possible to a pencil beam. That is, it was a parallel beam of the minimum possible diameter. The object to be imaged was about 25 cm in diameter, however, so the beam passed through a tungsten diffuser immediately after entering the experimental area. Multiple scattering in the diffuser caused the beam to have a known distribution in angle at that location. The beam then passed through a pair of quadrupole magnets known as the condenser magnets. The purpose of these magnets was to make the protons meet a precise condition, which allowed them to be focussed by the lens downstream. The condition was that the angle of each proton's path relative to the beamline had to be proportional to the distance of that proton from the beamline center when it hit the object.

After passing through the condenser, the beam hit the object to be studied. Various objects were used in this experiment. The first was the French Test Object, which consisted of a set of concentric spheres of different materials. The innermost sphere was about 2 cm in diameter and made of air. The next was about 8 cm in diameter and made of tungsten. The next was about 10 cm in diameter and made of copper. Finally, a foam sphere of about 24 cm diameter surrounded the whole object. One goal of the experiment was to image the air-filled hole at the center of the tungsten sphere. The second object was a stack of tungsten plates 5 inches thick just downstream of a steel plate one half inch thick. The steel plate had letters engraved in it, with bars one quarter inch deep and one quarter inch wide. The goal with this object was to be able to read the letters in the image through the 5 inches of tungsten. The final object was a stack of tungsten plates forming a staircase, so that different parts of the beam saw different thicknesses of tungsten. In this case, the goal was to image clearly the transition between each different thickness of tungsten, all the way from no tungsten at all to six inches, in one inch steps.

After passing through the object or being scattered or absorbed there, the protons entered another set of quadrupole magnets. These four magnets formed the lens, which focussed the beam on an image plane farther downstream. Between the first and second pairs of lens magnets was a collimator, which defined the angular acceptance of the lens system. The collimator consisted of a toroidal magnetic field surrounding the beam. Any protons passing near the center of the beamline would be unaffected by the collimator, but those passing far enough from the center of the beamline to enter the field would be deflected away from the beam and removed from the experiment. By installing different collimators, the angular acceptance of the experiment could be adjusted.

Three different imaging systems were used in parallel. The first was a particle identification and tracking system using wire chambers, scintillators, and a Cerenkov detector. The purpose of this system was to give complete particle identification and tracking information about a small fraction of the protons passing through the experiment. The system consisted of scintillators mounted at the diffuser, the object plane, and the image plane, for triggering and time-of-flight information; a Cerenkov detector near the diffuser to identify other fast particles

in the beam, such as pions; and delay line wire chambers at the object and image planes to give complete tracking information on each particle detected by this system. This system was characterized by a relatively slow data acquisition rate, so it could not give sufficient statistics to form an image of the objects. Its tracking information was necessary to set the condenser and lens magnets properly to form the matching condition at the object plane and to focus the protons at the image plane. Also, the particle identification results allowed a quantitative study of the composition of the beam.

The second imaging system was a phosphor plate system otherwise used in medical applications. The high energy protons excited metastable states in the plates with an efficiency of about 16%. The plates were later read out using a laser and photodetector system. This system had the advantages of being capable of nearly 100% efficiency (by stacking plates in series in the beam, a proton could be assured of being detected in at least one plate), and of being nearly independent of the beam rate. However, it had the disadvantage that the plates had to be removed from the beam for the time consuming readout process.

The third imaging system was the one that would probably be used in a real application of this technique. A bundle of scintillating optical fibers was placed in the beam. Any incident proton would create light in one of the fibers. The visible light emerging from the end of the fiber bundle was then focussed on a CCD detector, which transmitted the image to a computer. This system never actually worked. We suspect the reason is that the scintillator bundle was damaged by previous exposure to radiation, reducing its light output to 20% of the expected level. This reduced the signal from the CCD to much less than its dark current, making image detection impossible. If the CCD system had worked, it would have had the advantage that it can collect the light very quickly, and can be read out instantaneously.

Except for the failure of the CCD imaging system, all the experimental goals were achieved during the 1996 run. The other two imaging systems and the lens and condenser magnets all performed as expected. The phosphor plate system allowed us to detect the hole in the center of the French Test Object and the letters engraved in the steel plate in the second object. Analysis will also allow us to identify the material composing each part of the object. Protons scatter in the target because of two processes: electron multiple scattering and hadronic interactions. These two processes have different angular dependence and behavior as a function of Z (the atomic number of the object material) and A (the atomic mass of the object material). Multiple scattering is proportional to the number of electrons in the object, while hadronic scattering is approximately proportional to the number of nucleons in the object. Therefore, by varying the angular acceptance of the detector (by using different collimators), the ratio of Z/A in the object material can be determined. This sort of comparison between different runs will be done later, in the analysis.

3. The Pierre Auger Project J. T. Brack, C. J. Gelderloos, R. A. Ristinen, S. J. Pollock, C. D. Zafiratos, (University of Colorado); A. R. Barker, U. Nauenberg (High Energy Physics Group, University of Colorado)

The Pierre Auger Project is a large international collaboration directed toward constructing a system of ground-based detectors for study of the very highest energy cosmic ray particles. These cosmic rays, of energy exceeding 10^{20} eV, are expected to be incident on the earth's atmosphere at a rate of about one per square mile per steradian per century. Eight showers in this energy range have been observed over the past thirty years, but no known mechanism can account for their production. The project will develop two sites: one in the southern hemisphere, and another in the northern hemisphere. Each of the two sites will have about 1600 3000 gallon water Čerenkov detectors arrayed over a 3000 km² area, as well as a system of fluorescence detectors similar to the Fly's Eye system which has been operating for many years in Utah. The spokesman for the project, which has been in its planning stage for a few years, is Professor James Cronin of the University of Chicago. The project is not yet fully funded.

A project meeting was held at the Nuclear Physics Laboratory in Boulder in June 1996 to discuss organizational matters and site selection. Presentations were heard from groups not yet members of the project, but interested in joining. One of the main items of discussion at this meeting was the method by which a single candidate site in the United States would be selected at an August meeting at Fermilab. The chosen U.S. site then would be presented for consideration by the full collaboration at a meeting in Argentina in September. Groups from Arizona, Colorado, New Mexico, and Utah presented candidate sites at the Fermilab meeting; a site in Utah was selected from these by the Collaboration Board. The larger collaboration meeting in Argentina then considered three northern hemisphere candidate sites in Mexico, Spain, and Utah. The Utah site was chosen as the northern hemisphere site. The southern hemisphere site had been chosen earlier to be in Argentina.

The CU group worked together with physicists from Colorado State University in Fort Collins in planning for the selection of a candidate site in Colorado, and in thinking about what contributions the two Colorado groups could make to the project.

One of the issues considered by the Colorado groups was protection of the water-filled tanks from freezing. It appears that normal thermal insulation, and possibly maintaining good thermal contact with the ground at some depth beneath the tanks, will suffice to prevent freezing in the most severe weather on record at the northern site.

The interests of both Colorado groups center on the water Čerenkov detectors, with possible focus on data acquisition electronics, telemetry, and photomultiplier systems. Responsibility for a specific part of the project has not yet been assigned to the CU NPL group.

Membership of the Colorado groups in the collaboration was approved at the Argentina meeting.

4. Pion Soft Error Cross Sections in High Density Memory Chips

R. J. Peterson and C. J. Gelderloos (University of Colorado); J.D. Shell and M.E. Nelson (US Naval Academy); J. F. Ziegler (IBM)

We have measured the cross sections for soft errors in modern 16Mb dRAM chips from several vendors. The internal constructions of the memory units are not the same, and this has been shown to influence upset probabilities due to 14 MeV neutrons¹. At air traffic altitudes, pions are a significant part of the cosmic ray intensity, and could be of importance to commercial and military avionics.

We used pion beams from the EPICS channel, after transmission through a vacuum window. Relative beam normalization used an ion chamber in the beam, and absolute cross sections were obtained by the standard ¹¹C activation method². Memory chips were placed directly in the beam in a circuit that alternately wrote and read ones and zeroes at 10 MHz. Errors were determined by encountering the wrong next value, and counted from an LED readout.

A great variation was found among samples from four vendors, ranging up to a factor of about 1000 between the least and the most resistant samples. Data at five pion beam energies are shown in Figure 4.1, from 65 MeV to 260 MeV, for the most sensitive sample. Statistical uncertainties are small, but a 6% uncertainty arises from the ¹¹C activation cross sections used for normalization. The data for π^+ and π^- are very similar in Figure 4.1, as might be expected from the symmetry of the ²⁸Si dominant in the samples. Also shown in Figure 4.1 are pion-²⁸Si reaction cross sections, computed in a first-order optical model code. There is some similarity between the data and this shape at the lower energies.

This project has been extended to include new data for proton-induced soft errors, using beams from the Harvard cyclotron up to 150 MeV. At that energy, soft error cross sections for a given sample are nearly ten times greater for pions than for protons. Evidently, the pions produce greater damage in spite of the similarity in total reaction cross sections, 450 mb for protons³ and 600 mb for positive pions⁴. With a reasonable estimate of the relative pion and proton cosmic ray fluxes at 30,000 feet, we estimate that pions are causing most of the soft errors in memory chips at this altitude.

These results are being presented at relevant conferences and are being prepared for publication.

¹ J. D. Shell, 'Radiation Induced Single Event Upsets of Dynamic and Static RAM Memory Devices', M.S. Thesis, Univ. of Maryland (1995).

² B. J. Dropesky *et al.*, Phys. Rev. C **20**, 1844 (1979).

³ R. M. DeVries and J.-C. Peng, Phys. Rev C **22**, 1055 (1980).

⁴ D. Ashery *et al.*, Phys. Rev. C **23**, 2173 (1981).

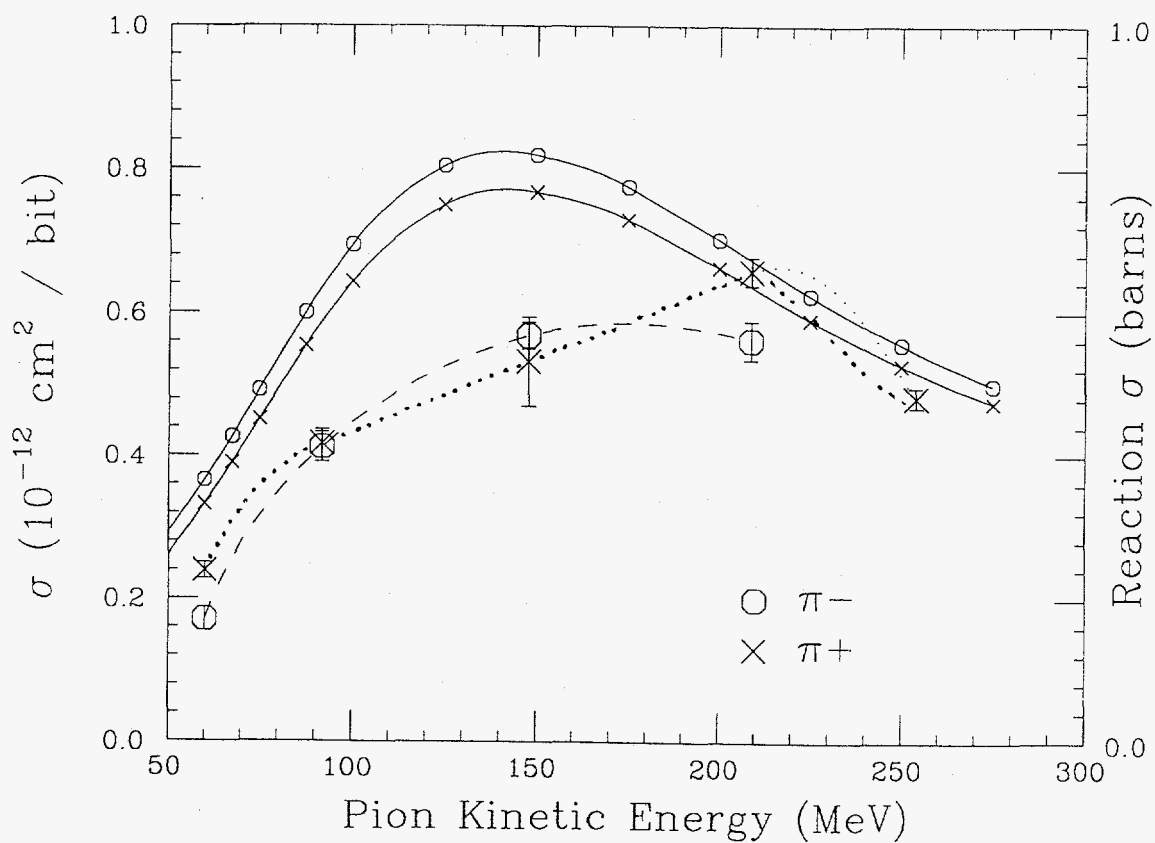


Figure 4.1 Data points are shown for pion-induced upsets of a 16Mb dRAM device for a range of pion beam energies across the 3-3 resonance, using the left hand scale. Also shown for comparison are computed pion- ^{28}Si reaction cross sections, using the right hand scale.

F. OTHER

1. Interactions Between Solar Neutrinos and Solar Magnetic Fields D. S. Oakley (Colorado Christian University)

The mystery of the missing solar neutrinos, which impacts our understanding of the Standard (electro-weak) Model, solar magnetic fields, solar-nuclear processes, and cosmology, continues to deepen as more data are collected. Discrepancies between theory and solar-neutrino experiments, as well as between the experiments themselves, have lead to investigations of experimental errors, of flaws in solar models, and energy-dependent processes which remove neutrinos before they reach Earth.

We are now exploring this latter possibility in looking for anticorrelations between the solar neutrinos and the strong equatorial-magnetic fields they encounter in the solar interior. To correlate with the magnetic fields near the solar equator, along the neutrino-Earth path, the solar-latitude dependence is investigated. If we assume that these deep field structures are strong enough to affect the neutrinos before rising to the solar surface, furthermore, then any neutrino-magnetic correlation studies should explore the question of timing. For example, in the event of neutrino interactions with interior fields which precede the surface measurements by one year, the strongest anticorrelations should be found in a data set where the surface fields are delayed accordingly, i.e. a 1985 neutrino would interact with the field proxied by the 1986 surface.

In this work we are using all available neutrino data (from GALLEX, SAGE, Kamiokande, and Homestake) with time-delayed magnetograph measured solar surface magnetic fields from Mt. Wilson. In particular, the Homestake data, which have a longer running time than any other solar neutrino experiment, are correlated against magnetic data using the Spearman rank-order correlation, which has been used in previous studies^{1,2}. The important statistic here, along with the correlation coefficient itself, is the significance level attached to it which gives the probability that correlation against a random array would give an equal or greater coefficient. Note, therefore, that a *low* significance level is indicative of a meaningful correlation, and by convention a correlation is considered 'highly significant' when the significance level is less than 1%.

The remaining solar neutrino data, from GALLEX, SAGE, and Kamiokande, do not span enough solar cycles to allow such a rank-order correlation analysis. Here, however, we can employ scatter plots, regressions, and explore general trends. Such techniques have been used to demonstrate null correlation in previous work⁴.

The results of correlation studies between Homestake neutrino capture rate and proxies for interior magnetic fields are shown in Figure 1.1 where the Spearman correlation coefficients and significance levels are plotted as a function of time-delayed surface magnetic fields. These show that indeed the strongest anticorrelation occurs when the central-band surface magnetic flux is delayed, which implies better correlations with the solar interior. The strongest result is obtained when the surface field, at disk center, is delayed by 1.4 years, i.e. a 1980 neutrino anticorrelates with a 1981.4 surface field. Here we find a coefficient of -38% and a significance level of 0.04% . It is useful to illustrate this correlation by plotting the Homestake data against the delayed surface magnetic fields (Figure 1.2).

This small significance may be misleading, however, because while the probability of an accidental -38% correlation is 0.04% , we correlated over many different data sets (delays) to arrive at this optimum delay. Statistically, if the number of data sets were large enough, we could guarantee a small significance. A more reliable number is perhaps the centroid of the curve of Figure 1.1. From an average of the correlation coefficients, we find a mean delay of 0.34 years, a mean coefficient of -23% , and a significance level of 0.29% . This implies a high anticorrelation probability ($> 99\%$) between the neutrinos and interior fields that rise to the surface in 0.34 years. If we find the centroid of the inverse of the significance level instead of the correlation coefficient, we find an optimum delay of 1.0 year with a mean correlation coefficient of -35% and a significance level of 0.46% . This method places a stronger emphasis on the very small significance levels observed around 1 year of delay. There are, of course, many other techniques which can be used to find the optimum delay in Figure 1.1, but all of them should find strong correlations with physically reasonable delay times of 0.3-1.5 years (as opposed to negative delays which would indicate that the surface magnetic response precedes the interior).

If we smooth by binning the magnetic data (no delays) into 10 degree intervals (except $0-5^\circ$) then we can compare the resulting correlations with theoretical neutrino-flux rates expected from these intervals. This is shown in Figure 1.3, where the solid curve represents the correlation results and the dashed curves represent the predicted^{5,6} flux rates from p+p and ^8B , the most important source for Homestake neutrinos. In this figure, it can be seen that all curves drop outside of 10° , with the ^8B dropping the most dramatically. It should be pointed out that *only* the $0-5^\circ$ interval shows a reasonable significance level, 0.5% , while the rest of the intervals range from 2.5% for $5-10^\circ$ to 21% for $30-35^\circ$.

The correlation curve in Figure 1.3 should not be expected to drop as fast as the ^8B curve because the magnetic fields themselves experience no sharp boundaries at 10° . Numerically, the source of the stronger anticorrelation between neutrino captures and disk-center surface flux, as opposed to surface flux from the whole Sun, is the 0.70-year lag between solar maximum at 25° and the time when the strongest flux arrives at the equator (not to be confused with the lag from the solar interior). These *negative* delays are clearly seen in Table I.

If neutrinos do interact with solar-magnetic fields then perhaps information about the solar cycle itself can also be gleaned from these interior and latitude-dependent correlation studies. For example, the maxima of correlation vs. time-delay plots (as in Figure 1.1) for the central and outer bands are separated by more than 0.7 years. Might this imply that fields are held down longer near equator than elsewhere? This would be a further implication of our results if these strong anticorrelations are not simply accidental but due to a physical process.

It has been suggested that no correlation is seen between the Kamiokande data and total sunspot number^{3,4}. If we employ the same statistical methods on central band and time delayed magnetic fields, however, a clear anti-correlation provides the best fit. To illustrate this for all of the available neutrino data, Figure 1.4 shows neutrino data from all four experiments plotted against the delayed magnetic

data (interior fields). The solid line shows the two year average Homestake data. Because of the large errors and low number of data points to date, this result may again be accidental, but anticorrelation can not be ruled out.

The next focus of our work will be to investigate a possible asymmetry seen in correlation studies involving the coronal green line above and below the solar equator⁷. The corrections for solar tilt should also be employed, and further investigations as to the possibility that the missing neutrino problem itself is a solely magnetic phenomenon are underway.

As more solar-neutrino flux information is gathered, experiments that are flavor sensitive and energy dependent would help resolve the inconsistencies between the different experiments themselves. The question of whether these anticorrelations are physical or statistical in nature, however, requires data that span several solar cycles. Future correlation studies should also focus on the actual magnetic fields the neutrinos encounter in the solar interior. These are most plausibly the central-band surface fields delayed in time; i.e. just those fields that we have found to give the strongest anticorrelations.

- ¹ J. Bahcall and W. Press, *Ap. J.* **370**, 730 (1991).
- ² D. S. Oakley, H. Snodgrass, R. Ulrich, and T. VanDeKop, *App.J. Lett.* **437**, 63 (1994).
- ³ K. S. Hirata et al., *Phys. Rev. Lett.* **65**, 1297 (1990).
- ⁴ D. R. O. Morrison, *Particle World* **3**, 30 (1992).
- ⁵ J. Bahcall, W. Huebner, S. Lubow, P. Parker, and R. Ulrich, *Rev. Mod. Phys* **54**, 767 (1982).
- ⁶ G. Caughlan, W. Fowler, M. Harris, and B. Zimmerman, *Atomic Data and Nuc. Data Tables* **32**, 197 (1985).
- ⁷ S. Massetti and M. Storini, *Ap. J.* (in press).

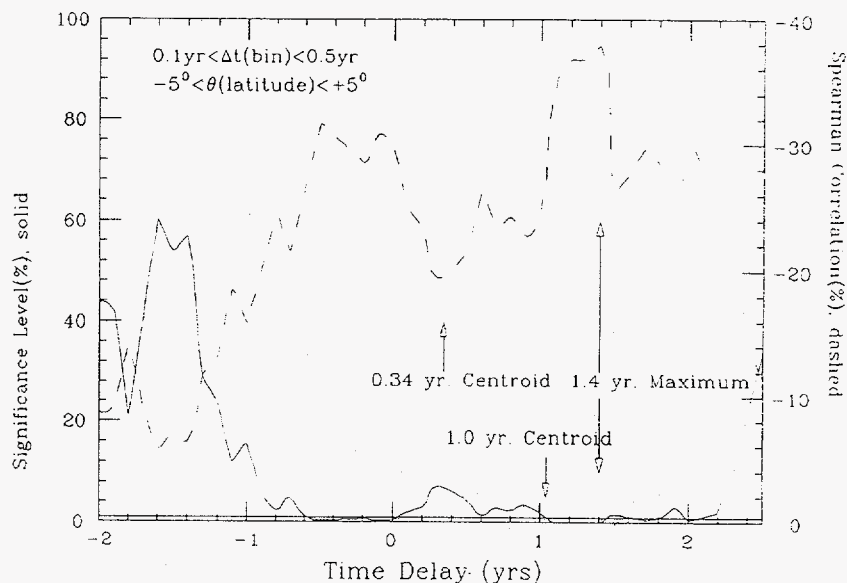


Figure 1.1 Results obtained from correlations of the Homestake solar neutrino capture rate with the time-delayed surface magnetic flux (central-band). The dashed line represents the Spearman rank-order correlation coefficients while the solid line represents the corresponding significance levels, both plotted as a function of solar-magnetic interior-to-surface time delay.

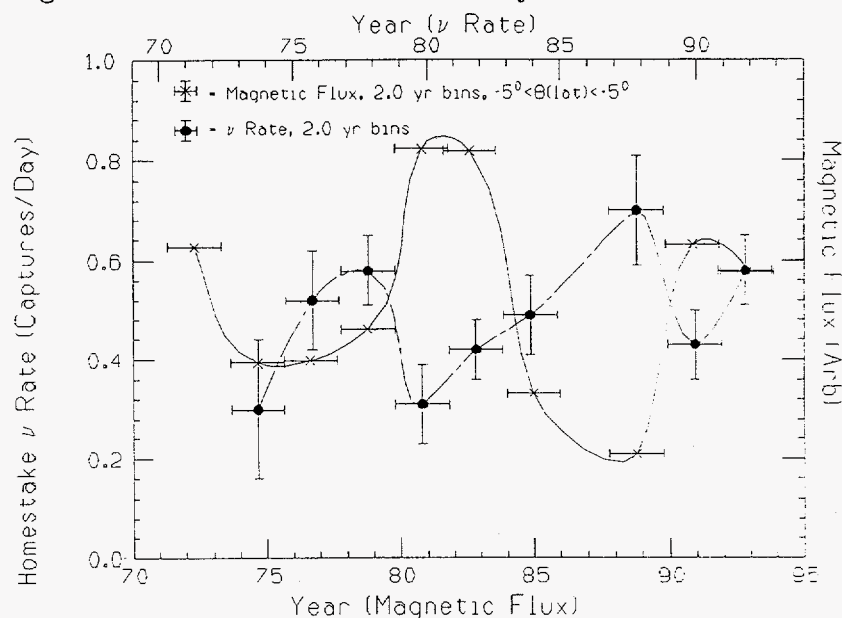


Figure 1.2 The Homestake solar neutrino capture rate and central-band solar-surface magnetic flux plotted as a function of the year the data were collected. The neutrino data are in 2-year bins and are represented by the closed circles (and the broken line, to guide the eye). The magnetic-flux data are also in 2-year bins and are represented by the crosses (and the solid line, to guide the eye). Notice, the magnetic scale is shifted by 1-year (delayed to plot a 1984 neutrino with a 1984 interior field, proxied by a 1985 surface field).

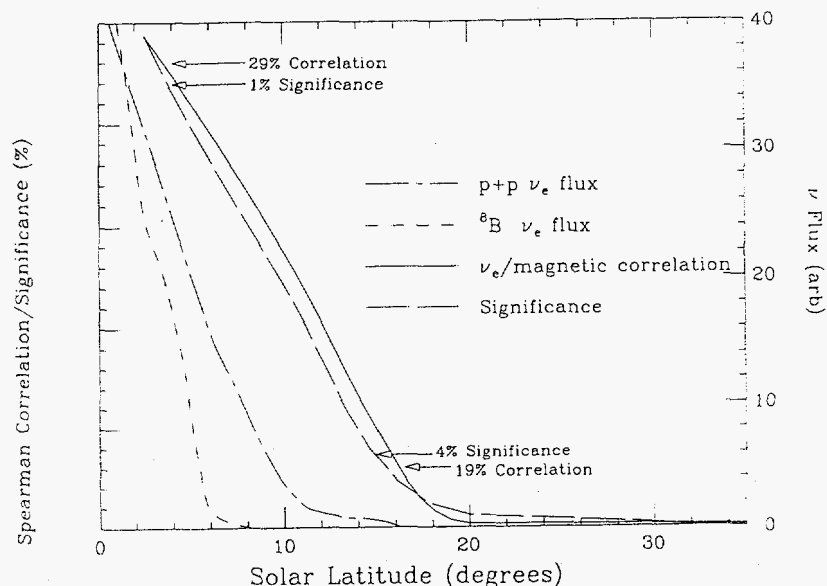


Figure 1.3 Results obtained from correlations of the Homestake capture rate with the surface magnetic flux (no time delay) in 10° angle bins (except for $0-5^\circ$) plotted with the theoretical neutrino flux expected^{5,6} from these intervals, dashed lines. While Homestake is most sensitive to the ^8B flux, similar flux magnitudes are shown to compare shapes.

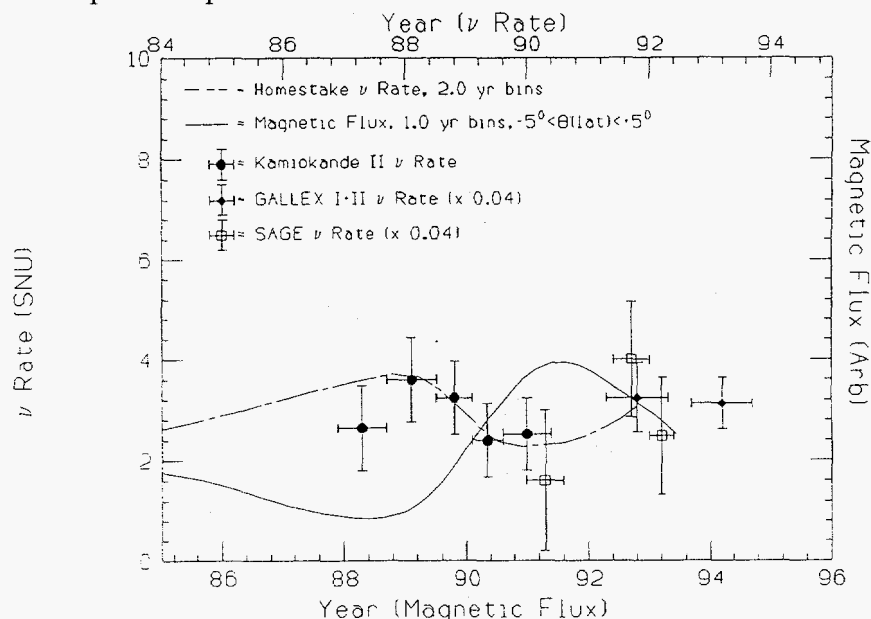


Figure 1.4 Solar neutrino capture rates from Kamiokande (circles), GALLEX (diamonds), and SAGE (squares) plotted as a function of the year the data were collected. The neutrino data are in the time bins shown. The 2 year averages of Homestake and the central-band solar-surface magnetic flux are also shown; represented by the broken and solid lines, respectively, as a guide to the eye. Notice, the magnetic scale is shifted by 1-year (again delayed to plot a 1984 neutrino with a 1984 interior field, proxied by a 1985 surface field).

Table 1.1 Correlations of the Homestake solar neutrino flux with time-delayed surface magnetic fields within various latitude bands.

Band (Deg)	Corr. ^(a) (%)	Sig. ^(a) (%)	Delay ^(a) (yrs)
$-5^0 < \theta < +5^0$	-23	0.29	0.34
$-10^0 < \theta < +10^0$	-23	0.56	0.26
$-15^0 < \theta < +15^0$	-22	1.26	0.10
$-20^0 < \theta < +20^0$	-21	1.36	-0.14
$-25^0 < \theta < +25^0$	-17	2.88	-0.28

^(a) From the centroid of the correlation coefficients (see Figure 1.1).

G. PUBLICATIONS AND REPORTS (Oct. 1, 1995 - Sept. 30, 1996)

1. Published Articles

- a. "Time Relationships between Direct Particle Emission and Fragmentation: A Probe for Nuclear Expansion Prior to Fragment Freezeout," C.J. Gelderloos, J.M. Alexander, N.N. Ajitanand, E. Bauge, A. Elmaani, T. Ethvignot, L. Kowalski, R.A. Lacey, M.E. Brandon, A. Giorni, D. Heuer, S. Kox, A. Lleres, A. Menchaca-Rocha, F. Merchez, D. Rebreyend, J.B. Viano, B. Chambon, B. Cheynis, D. Drain, and C. Pastor, *Phys. Rev. Lett.* **75**, 3082-3085 (1995).
- b. "Emission Times for Energy Selected $^{1,2,3}\text{H}$ Ejectiles From Central Collisions: 1360 MeV $^{40}\text{Ar} + \text{Ag}$," C.J. Gelderloos, R. Sun, N.N. Ajitanand, J.M. Alexander, E. Bauge, A. Elmaani, T. Ethvignot, R.A. Lacey, M.E. Brandon, A. Giorni, D. Heuer, S. Kox, A. Lleres, A. Menchaca-Rocha, F. Merchez, D. Rebreyend, J.B. Viano, B. Chambon, B. Cheynis, D. Drain, and C. Pastor, *Phys. Rev.* **C52**, R2834-R2838 (1995).
- c. "Correlation Measurements of Light Charged Particles Emitted from $^{32}\text{S} + ^{27}\text{Al}$ Reactions at Energies of 105 MeV and 215 MeV," P.A. DeYoung, N.N. Ajitanand, J.M. Alexander, V. Datar, C.J. Gelderloos, G. Gilfoyle, M.S. Gordon, R.L. McGrath, G.F. Peaslee, and J. Sarafa, *Phys. Rev.* **C52**, 3488-3491 (1995).
- d. "Pion-Nucleus Total and Reaction Cross Sections," R.J. Peterson, *Few-Body Systems Supp.* **9**, 17 (1995).
- e. "Conference Summary," R.J. Peterson, *Few-Body Systems Supp.* **9**, 510 (1995).
- f. "A Technique to Probe Time Relationships: Direct Particle Emission and Fragmentation," C.J. Gelderloos, J.M. Alexander, E. Bauge, A. Elmaani, T. Ethvignot, L. Kowalski, R.A. Lacey, M.E. Brandon, A. Giorni, D. Heuer, S. Kox, A. Lleres, A. Menchaca-Rocha, F. Merchez, D. Rebreyend, J.B. Viano, B. Chambon, B. Cheynis, D. Drain, and C. Pastor, *Proceedings of Corinne II, International Workshop on Multi-Particle Correlations and Nuclear Reactions*, ed. J. Aichelin and D. Ardouin, World Scientific, Singapore, pp. 396-406 (1995).
- g. "Evidence for Virtual Compton Scattering from the Proton," J.F.J. van den Brand, R. Ent, P.L. Anthony, R.G. Arnold, J. Arrington, E.J. Beise, J.E. Belz, P.E. Bosted, H.-J. Bulten, M.S. Chappone, H. Gao, R.A. Gearhart, D.F. Geesaman, J.-O. Hansen, R.J. Holt, H.E. Jackson, C.E. Jones, C.E. Keppel, E.R. Kinney, S. Kuhn, K. Lee, W. Lorenzon, A. Lung, N.C.R. Makins, D.J. Margoziotis, R.D. McKeown, R.G. Milner, B. Mueller, J. Napolitano, T.G. O'Neill, V. Papavassiliou, G.G. Petratos, D.H. Potterveld, S.E. Rock, M. Spengos, Z.M. Szalata, L.H. Tao, K. van Bibber, D.A. Wasson, J.L. White, and B. Zeidman, *Phys. Rev. D* **52**, 4868 (1995).

- h. "Proton and Deuteron Structure Functions in Muon Scattering at 470-GeV by E665 Collaboration," M.R. Adams, S. Aid, P.L. Anthony, D.A. Averill, M.D. Baker, B.R. Baller, A. Banerjee, A.A. Bhatti, U. Bratzler, H.M. Braun, T.J. Carroll, H.L. Clark, J.M. Conrad, R. Davisson, I. Derado, F.S. Dietrich, W. Dougherty, T. Dreyer, V. Eckardt, U. Ecker, M. Erdmann, G.Y. Fang, J. Figiel, R.W. Finlay, H.J. Gebauer, D.F. Geesaman, K.A. Griffioen, R.S. Guo, J. Haas, C. Halliwell, D. Hantke, K.H. Hicks, H.E. Jackson, D.E. Jaffe, G. Jancso, D.M. Jansen, Z. Jin, S. Kaufman, R.D. Kennedy, E.R. Kinney, T. Kirk, H.G. Kobrak, A.V. Kotwal, S. Kunori, J.J. Lord, H.J. Lubatti, P. Madden, D. McLeod, S. Magill, A. Manz, H. Melanson, D.G. Michael, H.E. Montgomery, J.G. Morfin, R.B. Nickerson, J. Novak, S. O'Day, K. Olkiewicz, L. Osborne, R. Otten, V. Papavassiliou, B. Pawlik, F.M. Pipkin, D.H. Potterveld, E.J. Ramberg, A. Roser, J.J. Ryan, C.W. Salgado, A. Salvarani, H. Schellman, M. Schmitt, N. Schmitz, G. Siegert, A. Skuja, G.A. Snow, S. Soldner-Rembold, P. Spentzouris, H.E. Stier, P. Stopa, R.A. Swanson, H. Venkataramania, M. Wilhelm, R. Wilson, W. Wittek, S.A. Wolbers, A. Zghiche, T. Zhao, *Z. Phys.* **C67**, 403 (1995).
- i. "Anomalous Angular Distribution in Pion and Alpha Particle Scattering to the 2+2 State of ^{52}Cr ," D. S. Oakley, R.J. Peterson, C.L. Morris, and H.T. Fortune, *Phys. Rev. C* **53**, 689 (1996).
- j. "Reaction and Total Cross Sections for Low Energy π^+ and π^- on Isospin Zero Nuclei," A. Saunders, S. Hoibraten, J.J. Kraushaar, B.J. Kriss, R.J. Peterson, R.A. Ristinen, J.T. Brack, G. Hofman, E.F. Gibson and C.L. Morris, *Phys. Rev. C* **53**, 1745-1752 (1996).
- k. " K^+ Elastic Scattering from ^{12}C and ^6Li at 715 MeV/c," R. Michael, M. B. Barakat, S. Bart, R.E. Chrien, B.C. Clark, D.J. Ernst, S. Hama, K.H. Hicks, W. Hinton, E.V. Hungerford, M.J. Jiang, T. Kishimoto, C.M. Kormanyos, L.J. Kurth, L. Lee, B. Mayes, R.J. Peterson, L. Pinsky, R. Sawaf, R. Sutter, L. Tang and J.E. Wise, *Phys. Lett. B* **382**, 29 (1996).
- l. "Fusionlike Reactions of ^{40}Ar up to 1.36 GeV: Prethermalization and Postthermalization Particles and Fragments," M.T. Magda, E. Bauge, A. Elmaani, T. Braunstein, C.J. Gelderloos, N.N. Ajitanand, J.M. Alexander, T. Ethvignot, P. Bier, L. Kowalski, P. Desequelles, H. Elhage, A. Giorni, S. Kox, A. Lleres, F. Merchez, C. Morand, P. Stassi, J.B. Benrachi, B. Chambon, B. Cheynis, D. Drain, and C. Pastor, *Phys. Rev. C* **53**, R1473-R1477 (1996).
- m. "A Dependence of the $(\pi^+, \pi^+\pi^\pm)$ Reaction near the $2m_\pi$ Threshold," F. Bonutti, P. Camerini, E. Fragiaco, N. Grion, R. Rui, P.A. Amaudruz, J.T. Brack, L. Felawka, E.F. Gibson, G.J. Hofman, M. Kermani, S. McFarland, R. Meier, D. Ottewell, K. Raywood, M.E. Sevier, G.R. Smith, and R. Tacik, *Phys. Rev. Lett.* **77**, 603 (1996).

- n. "Search for Narrow Sum-Energy Lines in Electron-Positron Pair Emission from Heavy-Ion Collisions near the Coulomb Barrier," D.J. Mercer and the APEX Collaboration, *Phys. Rev. Letters* **75**, 2658 (1996).
- o. "A Solenoidal Spectrometer for Positron-Electron Pairs Produced in Heavy-Ion Collisions," D.J. Mercer and the APEX Collaboration, *Nucl. Instr. Meth.* **A370**, 539 (1996).
- p. "Isovector Giant Resonances in ${}^6\text{He}$, ${}^{12}\text{B}$, ${}^{90}\text{Y}$, ${}^{120}\text{In}$, and ${}^{208}\text{Tl}$," J. Jänecke, T. Annakkage, K. Pham, D.A. Roberts, J.A. Brown, G. Crawley, S. Danczyk, D.J. Mercer, J. Stasko, J.S. Winfield, G.H. Yoo, G.P.A. Berg, and M. Fujiwara, *Nucl. Phys.* **A599**, 191 (1996).
- q. "Inclusive Electron Scattering from Nuclei at $x \simeq 1$," J. Arrington, P. Anthony, R.G. Arnold, E.J. Bejse, J.E. Belz, P.E. Bosted, H.-J. Bulten, M.S. Chapman, K.P. Dietrich, R. Ent, M. Epstein, B.W. Filippooone, H. Gao, R.A. Gearhart, D.F. Geesaman, J.-O. Hansen, R.J. Holt, H.E. Jackson, C.E. Jones, C.E. Keppel, E.R. Kinney, S. Kuhn, K. Lee, W. Lorenzon, A. Lung, N.C.R. Makins, D.J. Margaziotis, R.D. McKeown, R.G. Milner, B. Mueller, J. Napolitano, J. Nelson, T.G. O'Neill, V. Papavassiliou, G.G. Petratos, D.H. Potterveld, S.E. Rock, M. Spengos, Z.M. Szalata, L.H. Tao, K. van Bibber, J.F.J. van den Brand, J.L. White, D. Winter, and B. Zeidman, *Phys. Rev. C* **53**, 2248 (1996).

2. Articles Accepted or Submitted for Publication

- a. "Classical Tests for Statistical Evaporation at 680 MeV ${}^{40}\text{Ar} + {}^{nat}\text{Ag}$," C.J. Gelderloos, J.M. Alexander, J. Boger, M.T. Magda, A. Narayanan, P. DeYoung, A. Elmaani, M.A. McMahan, *Phys. Rev. C*, in press.
- b. "Structure of the Neutron-Halo Nucleus ${}^6\text{He}$," J. Jänecke, T. Annakkage, G.P.A. Berg, B.A. Brown, J.A. Brown, G. Crawley, S. Danczyk, M. Fujiwara, D.J. Mercer, K. Pham, D.A. Roberts, J. Stasko, J.S. Winfield, and G.H. Yoo, *Phys. Rev. C*, in press.
- c. "Parametrization of Pion-Nucleon Phase Shifts and Effects upon Pion-Nucleus Scattering Calculations", A.A. Ebrahim and R.J. Peterson, accepted for publication in *Phys. Rev. C*.
- d. "Pion Scattering to 6^- Stretched States of ${}^{32}\text{S}$ ", B.L. Clausen, T.W. Johnson, R.A. Lindgren, K. Kromer, R.J. Peterson, A.D. Bacher, H. Ward and A.L. Williams, submitted to *Phys. Rev. C*.
- e. "Pion-Nucleus Spin-Flip Strength at Low and Resonance Energies", B.G. Ofenloch, R.A. Ginnelli, B.G. Ritchie, J.M. O'Donnell, J.N. Knudson, C.L. Morris, C.M. Kormanyos, A. Saunders, J.Z. Williams, R.A. Lindgren, and B.L. Clausen, submitted to *Phys. Rev. C*.
- f. "Suggested Correction to ${}^6\text{He}$, ${}^6,{}^7\text{Li}$, and ${}^7\text{Be}$ Production Cross Sections in $\alpha + \alpha$ Reactions between 60 and 160 MeV," D.J. Mercer, B.G. Glagola, and S.M. Austin, submitted to *Phys. Rev. C*.

- g. "Production of A=6,7 Nuclides in the $\alpha + \alpha$ Reaction at 160, 280, and 620 MeV," D.J. Mercer, S.M. Austin, J.A. Brown, S.A. Danczyk, S.E. Hirzebruch, J.H. Kelley, T. Suomijärvi, and D.A. Roberts, submitted to Phys. Rev. C.
- h. "On the Process of Pion Production in Nuclei," F. Bonutti, P. Camerini, E. Fragiaco, N. Grion, R. Rui, J.T. Brack, L. Felawka, E.F. Gibson, G.J. Hofman, M. Kermani, E.L. Mathie, S. McFarland, R. Meier, D. Ottewell, K. Raywood, M.E. Sevier, G.R. Smith, and R. Tacik, submitted to Phys. Rev. C, September 1996.
- i. " $\pi^+\pi^- \rightarrow \pi^+\pi^-$ Cross Sections near Threshold," M. Kermani, F. Bonutti, P. Camerini, E. Fragiaco, N. Grion, R. Rui, J.T. Brack, L. Felawka, E.F. Gibson, G. Hofman, E.L. Mathie, S. McFarland, R. Meier, D. Ottewell, O. Patarakin, K. Raywood, M.E. Sevier, G.R. Smith, R. Tacik and V. Tikhonov, submitted to Phys. Rev. Lett., September 1996.
- j. "Search for Mono-Energetic Positron Emission from Heavy-Ion Collisions at Coulomb-Barrier Energies," The APEX Collaboration: I. Ahmad, S.M. Austin, B.B. Back, R.R. Betts, F.P. Calaprice, K.C. Chan, A. Chisti, P. Chowdhury, C. Conner, R.W. Dunford, J.D. Fox, S.J. Freedman, M. Freer, S.B. Gazes, A.L. Hallin, T. Happ, D. Henderson, N.I. Kaloskamis, E. Kashy, W. Kutschera, J. Last, C.J. Lister, M. Liu, M.R. Maier, D.J. Mercer, D. Mikolas, P.A.A. Perera, M.D. Rhein, D.E. Roa, J.P. Schiffer, T.A. Trainor, P. Wilt, J.S. Winfield, M.R. Wolanski, F.L.H. Wolfs, A.H. Wousmaa, G. Xu, A. Young, and J.E. Yurkon, submitted to Phys. Rev. Lett.
- k. "A Study of Internal Pair Conversion Following Heavy Ion Collisions," D.J. Mercer and the APEX Collaboration, submitted to Physics Letters.
- l. "Pion-Nucleus Spin-Flip Strength at Low and Resonance Energies," B.G. Ofenloch, R.A. Giannelli, B.G. Ritchie, J.M. O'Donnell, J.N. Knudson, C.L. Morris, C.M. Kormanyos, A. Saunders, J.Z. Williams, R.A. Lindgren, and B.L. Clausen, submitted to Phys. Rev. C.
- m. "Pion Double Charge Exchange and Inelastic Scattering on ^3He ," M. Yuly, W. Fong, E.R. Kinney, J.L. Matthews, C.J. Maher, T. Soos, J. Vail, M.Y. Wang, S.A. Wood, P.A.M. Gram, G.A. Rebka, D.A. Roberts, submitted to Physical Review C.

3. Abstracts

- a. "Isospin Selectivity in Baryon and Hyperon Spectroscopy by Detecting Neutral Particle Final States with the Crystal Ball", M.E. Sadler, L.D. Isenhower, H. Spinka, J. Comfort, M. Clajus, S. McDonald, T. Moriwaki, B.M.K. Nefkens, W.B. Tippens, J.R. Peterson, J. Birscoe, Z. Papandreou, U.A. Efendiev, M. Manley, V. Abaev, V. Bekrenev, N. Kozlenko, S. Kruglov, I. Lopatin, A. Starostin, M. Batinic, A. Marusic, I. Slaus, I. Supek, A. Svarc, and D. Koetke, Bull. Am. Phys. Soc. **41**, 1023 (1996).

- b. "Quasi Elastic Pion Scattering at 0.95 GeV/c," R.J. Peterson, S. Ajimura, K. Aoki, H.C. Bhang, J.T. Brack, Y. Fujii, C.J. Gelderloos, O. Hashimoto, M. Hotchi, M. Itoh, M.V. Keilman, T. Kishimoto, T. Nakagawa, H. Noumi, Y. Ohta, H. Ota, H. Park, H. Sakaguchi, Y. Sato, R. Sawafuta, M. Sekimoto, T. Takahashi, H. Takeda, and M. Youn, *XIV International Conference of Particles and Nuclei, (PANIC 96)*, 1996.
- c. "Total and Reaction Cross Sections for π^- -Nucleus Collisions at 400 - 500 MeV," C.J. Gelderloos, J.T. Brack, M.D. Holcomb, M.V. Keilman, D.J. Mercer, R.J. Peterson, R.A. Ristinen, and A. Saunders, presented at *XIV International Conference of Particles and Nuclei, (PANIC 96)*, 1996.
- d. "First Results from HERMES: The $g_1^n(x)$ Structure Function," L.H. Kramer *et.al* (The HERMES Collaboration), presented at *XIV International Conference of Particles and Nuclei, (PANIC 96)*, 1996.
- e. "Overview of the Status of Polarised Structure Functions," M.C. Vetterli *et al.* (The HERMES Collaboration), *Proceedings of the Workshop on Deep Inelastic Scattering and Related Phenomena*, April 15-19, 1996, Rome.
- f. "Inclusive Spin-Dependent DIS from the Nucleon with HERMES," D. De Schepper *et.al* (The HERMES Collaboration), *Proceedings of the Workshop on Deep Inelastic Scattering and Related Phenomena*, April 15-19, 1996, Rome.

H. NUCLEAR PHYSICS LABORATORY PERSONNEL

(Experimental Program)

1. Academic and Scientific

E. J. Belz ¹	Research Associate
B. D. Fox ²	Research Associate
C. J. Gelderloos	Research Associate
E. R. Kinney	Assistant Professor
J. J. Kraushaar	Professor Emeritus
D. A. Lind	Professor Emeritus
D. J. Mercer ³	Research Associate
R. J. Peterson	Professor
R. A. Ristinen	Professor
W. R. Smythe	Professor Emeritus
C. D. Zafiratos	Professor

2. Technical and Support Staff

J. T. Brack	Professional Research Assistant
D. P. Edmonds	Laboratory Coordinator
D. E. Prull	Principal Systems Analyst
S. Spika	Administrative Assistant

3. Research Assistants

M. Holcomb	J. D. Patterson
M. Keilman	G. Rakness
W. D. Kirwin	A. Saunders
B. J. Kriss	D. van Westrum

4. Affiliated Researchers

H. C. Bhang	Seoul National University, Seoul, Korea
A. A. Ebrahim	Assuit University, Assuit, Egypt
D. S. Oakley	Colorado Christian University, Denver, Colorado

5. Other Students (part-time)

R. Grignon ⁴
Y. Laor ⁵
J. D. Moulin ⁶

¹Appointment ended January 1996

²Appointed July 1996

³Appointment ended April 1996

⁴Appointment ended May 1996

⁵Appointment ended May 1996

⁶Appointed October 1996

University of Colorado

Nuclear Theory

1996 Progress Report

CONTENTS

A.	1996 PROGRESS REPORT.....	1
	1. Electron-nucleon cross section in (e,e'p) reactions.....	1
	2. Electroweak excitation of the Δ : hadron structure and new physics.....	10
	3. $U_A(1)$ breaking and scalar mesons in the Nambu and Jona-Lasinio Model.....	21
	4. Higgs mechanism in a non-perturbative approximation to the scalar ϕ^4 theory coupled to a gauge field	31
	5. Weinberg sum rules in an effective chiral field theory	38
	6. Positivity restrictions in polarized deep-inelastic electron scattering from the deuteron	44
	7. Hara's theorem in the constituent quark model.....	50
	8. Renormalization group effective potentials for bosons and Yukawa cou- pled fermions at finite temperature.....	56
	9. Renormalization group flow equations for sigma models.....	60
	10. Renormalization group effective potentials in ϕ^4 scalar field theories at finite temperature.....	65
B.	PUBLICATIONS AND REPORTS.....	72
C.	PERSONNEL.....	73

In the interpretation of electron-nucleus scattering experiments one must make a choice of how to describe the interaction between an electron and a bound nucleon. Only the scattering of an electron on a free, on-shell nucleon is determined model independently. The kinematics of the scattering on a bound, off-shell nucleon is necessarily different and therefore there exists no well defined unique procedure for the theoretical description of the nuclear scattering process.

In trying to describe the nuclear reaction by means of the free electromagnetic current of the nucleon, assumptions have to be made. They lead to a non-conserved nuclear current, an unphysical feature that is usually remedied in an *ad hoc* fashion. The most commonly used 'conserved current' (cc) prescription for the $(e, e'p)$ reaction was introduced by de Forest [1]. This prescription also makes it possible to factorize the PWIA cross section into a part containing the electron-nucleon cross section and a nuclear structure part. By comparing some variations within this class of recipes, it is often concluded that the uncertainty due to this procedure is small and that 'off-shell' effects are negligible.

Clearly, this last point needs to be critically examined before one can draw conclusions from *e.g.* $(e, e'p)$ experiments about subtle or exotic effects, either concerning nuclear structure or the influence of the medium on the reaction mechanism. An example of a reaction where this consideration enters is the recent $(e, e'p)$ measurement by Makins *et al.* [2]. It was motivated by the suggestion of a particular medium effect, color transparency.

It is the purpose of this note to briefly review the various approximations which go into the standard descriptions of the $(e, e'p)$ reaction and result in a non-conserved nuclear current. We discuss in detail prescriptions to restore conservation of the electromagnetic current of the off-shell nucleon and relate them to particular choices of a gauge. Since there is much interest in the $(e, e'p)$ experiment by Makins *et al.* [2], we give examples for the kinematics of this experiment even though they are at the peak of the quasielastic cross section and the initial nucleon is not far off its mass shell. Our general conclusion is that the ambiguities connected to the electromagnetic current of an off-shell nucleon cannot be dismissed even if predictions among some currently used prescriptions are in close agreement.

There has been considerable work on general aspects of the electromagnetic interaction with the nucleons in a nucleus (see *e.g.* [3], [4], [5], [6], [7], [8]). The nuclear wavefunction, the electromagnetic vertex and *e.g.* the final state interaction need to be dealt with consistently. We will not repeat this discussion here and comment only on the assumptions that go into the often used recipe by de Forest [1] for the cross section for a bound, off mass shell nucleon. They are good examples for the problems one encounters in general and for the approximations one makes in practice.

The general form of the nuclear current is

$$J_\mu = \bar{\Psi}_f \Gamma_\mu \Psi_i, \quad (1)$$

where $\Psi_{i,f}$ denote the initial and final wavefunctions and Γ_μ is the electromagnetic vertex operator. It is quite common to consider only the contributions due to one body currents. In practice, to obtain a manageable description additional *ad hoc* assumptions are made concerning the wavefunctions, the vertex operator, the kinematics and current conservation. For simplicity,

we will consider the $(e, e'p)$ reaction in PWIA, where the initial nucleon is bound and the final one is in a plane wave, on mass shell state.

Wavefunction: The assumption made in Ref. [1] is that the wavefunction of both the plane wave final nucleon and also the initial bound nucleon is given by the Dirac spinor for an on-shell nucleon. For the initial nucleon it is assumed that this spinor is determined through its three momentum, \vec{p} , the missing momentum of the initial nucleon, and the corresponding on-shell energy, $E_{on} = \sqrt{\vec{p}^2 + M^2}$.

Vertex operator: The general vertex for an off-shell nucleon, appearing between the nucleon wavefunctions, has been discussed in the literature, e.g. in Ref. [9]. The operator structure can be much more complex than the one one encounters in expressions for the free current. Furthermore, the associated form factors can depend in addition to q^2 , the photon four-momentum, on other scalar variables such as the invariant mass of the initial nucleon, p^2 . Rather than using this general expression (which would prevent factorization), all commonly used recipes make use of the free current. However, there are a variety of ways to write the free on-shell current in terms of two independent vertex operators and associated form factors. De Forest uses two forms

$$J_1^\mu = e\bar{u}(\vec{p}') \left\{ [F_1(q^2) + F_2(q^2)]\gamma^\mu - F_2(q^2)\frac{(p + p')^\mu}{2M} \right\} u(\vec{p}), \quad (2)$$

and

$$J_2^\mu = e\bar{u}(\vec{p}') \left\{ F_1(q^2)\gamma^\mu + F_2(q^2)\frac{i\sigma^{\mu\nu}q_\nu}{2M} \right\} u(\vec{p}), \quad (3)$$

which can be transformed into each other by means of the Gordon decomposition. While for on-shell nucleons the two currents are equivalent, the results obtained when one tries to use them in the off-shell case are different.

Kinematics: In the $(e, e'p)$ reaction the energy transfer by the electron, ω , and the energy of the detected nucleon, E' , determine the energy of the initial bound nucleon to be $E = E' - \omega \neq E_{on}$. However, the use of a free on-shell spinor in the construction of the current involves the on-shell energy E_{on} for the initial nucleon. In the current based on eq. (2), the energy of the initial nucleon also appears explicitly not only in the spinor, but also in the vertex operator and the usual prescription is to use E_{on} in the operator. An alternative is discussed in Ref. [4].

Current conservation: After the above manipulations, it is clear that the resulting current is not conserved. The last step then is to make the current conserved by hand. We will discuss three possibilities to do this and apply these methods to the two ways to write the free on-shell current, eqs. (2) and (3).

(a) The method chosen in Ref. [1] is to replace the longitudinal component J_q , parallel to \vec{q} , by the charge density J_0 :

$$J_q \rightarrow J'_q = \frac{\omega J_0}{|\vec{q}|}. \quad (4)$$

and thus work with a four-current

$$J_\mu^{(\ell)} = (\vec{J}_t, \frac{\omega J_0}{|\vec{q}|}, J_0). \quad (5)$$

This would be correct and of no consequence if the current indeed was conserved. It has been argued that Siegerts theorem suggests this substitution when the current is not exactly conserved, but this long wavelength argument doesn't apply for the one-body current one is concerned with here, nor can it be expected to hold at the energies we consider below. The cross sections arising from this recipe, the often used prescriptions by de Forest, will be referred to simply as ' σ_{cc} '.

(b) Of course, one could take care of current conservation in the opposite way by eliminating the charge density instead [4], [10]:

$$J_0 \rightarrow J'_0 = \frac{\vec{J} \cdot \vec{q}}{\omega}, \quad (6)$$

and to use

$$J_\mu^{(0)} = (\vec{J}, \frac{\vec{J} \cdot \vec{q}}{\omega}). \quad (7)$$

The resulting cross section will be referred to as σ_{cc}^0 .

(c) In other recipes [11] one subtracts a term proportional to q_μ to obtain a divergence free current:

$$J_\mu \rightarrow J_\mu^{(q)} = J_\mu - \frac{J \cdot q}{q^2} q_\mu. \quad (8)$$

The cross section obtained from this recipe will be referred to as σ_{cc}^q .

Connection to the gauge choice: As will be shown below, these different ways to restore current conservation can be seen as a choice of a gauge, which in principle should have no effect on the results. That these choices lead to different results shows the inconsistencies inherent in the commonly chosen approach to deal with the electromagnetic interaction of bound nucleons. The electron scattering matrix element can be written as

$$M = j^\mu \Pi_{\mu\nu} J^\nu, \quad (9)$$

where Π denotes the photon propagator and j the electron current. The explicit form of the propagator is gauge dependent and, as a consequence, so is the form of the matrix element.

In the covariant Lorentz class of gauges one has

$$M_L = \frac{i}{q^2} (-j \cdot J + (1 - \xi) \frac{(q \cdot J)(q \cdot j)}{q^2}), \quad (10)$$

where ξ is a free gauge parameter. It is common practice to work in the Feynman gauge, $\xi = 1$. In this case, one obtains

$$M_F = \frac{i}{q^2} (-j \cdot J). \quad (11)$$

This of course is always the case in the covariant Lorentz gauges since the electron current, j , is conserved and the second term in Eq. (10) vanishes. We will now show that the matrix elements resulting from the above three modified 'conserved' currents, eqs. (5), (7), and (8),

when used in the Feynman gauge yield the same matrix elements one obtains with the original, non-conserved current, but evaluated in different gauges.

Coulomb gauge: The well-known Coulomb gauge is an example of a non-covariant gauge. Using the Coulomb gauge propagator for $\Pi_{\mu\nu}$, the general matrix element, eq. (9), reduces to

$$M_C = \frac{i}{\vec{q}^2} j_0 J_0 + \frac{i}{q^2} (\vec{j} \cdot \vec{J} - \frac{(\vec{q} \cdot \vec{J})(\vec{q} \cdot \vec{j})}{\vec{q}^2}). \quad (12)$$

This is precisely the same matrix element one would obtain in the Feynman gauge, upon using the replacement given in eq. (4). The second part of eq. (12) is the contribution of the transverse parts of the current, defined as

$$\vec{J}_t = \vec{J} - \frac{\vec{q} \cdot \vec{J}}{\vec{q}^2} \vec{q}. \quad (13)$$

Depending on whether one uses the current J_1^μ given in eq. (3) or J_2^μ eq. (2), one obtains σ_{cc1} and σ_{cc2} from M_C . These are the widely used cross sections proposed by de Forest [1].

Weyl gauge: Another non-covariant gauge is the Weyl (or temporal) gauge. Using the photon propagator in this gauge, the charge densities do not explicitly contribute to the matrix element:

$$M_W = \frac{i}{q^2} (\vec{j} \cdot \vec{J} - \frac{(\vec{q} \cdot \vec{J})(\vec{q} \cdot \vec{j})}{\omega^2}). \quad (14)$$

Again, it is readily seen that this is the same expression one would have obtained in the Feynman gauge upon using the replacement given in eq. (6), yielding σ_{cc1}^0 or σ_{cc2}^0 , depending on the form for the on-shell current one used to approximate the off-shell current.

Landau gauge: Finally, another example from the covariant Lorentz class is the Landau gauge, defined by the gauge parameter $\xi = 0$. As one can see from eq. (10), this yields σ_{cc1}^q and σ_{cc2}^q , the same result as in the Feynman gauge with the *ad hoc* subtraction defined in eq. (8) that guarantees a conserved current. In fact, one would obtain this result if one did nothing and simply used the original non-conserved current in eq. (11).

Of course, physical observables should not depend on the choice of the gauge. Indeed, for conserved currents all the matrix elements given above can easily be shown to be equivalent. However, for non-conserved currents, *i.e.* broken gauge invariance, choosing a different gauge gives a different result. This is the situation for the approximation for the bound nucleon current: the results are not the same. The choice of which component to eliminate in favor of another or to simply make the *ad hoc* subtraction, eq. (8), can thus be related to the choice of a gauge. The connection between a choice of the gauge and non-contributing parts of the currents is formally always present. However, it is only exact for conserved currents.

Estimates of the differences between cc prescriptions: The formal connection between gauge choices and different cc prescriptions can be used for getting estimates of the uncertainties *within* the cc-class. The starting point is that the nucleon current J , is not conserved. Different matrix elements are obtained in non-covariant gauges. Since the electron current is conserved, all covariant Lorentz class gauges yield the same result. These differences between the cc recipes will be used below for different kinematics to get an impression of the uncertainty introduced by dealing with the off-shell current in an *ad hoc* fashion. It should be emphasized that the

differences can only give a rough indication of these ambiguities as a function of the relevant kinematical variables. These estimates are not based on any dynamical input, but only on the connection between the cc prescriptions explained above.

A measure of how far one is from the on-shell kinematics is provided by the energy transfer. The actual energy transfer to the nucleon, ω , is determined by the electron kinematics. If the initial nucleon was on its mass shell, its energy E_{on} would be $(\vec{p}^2 + M^2)^{1/2}$, where \vec{p} is the missing momentum. The energy transfer, ω' , which one would have in that case is given by

$$\omega' = E' - E_{on}. \quad (15)$$

How far one is off-shell is therefore indicated by the difference, $\Delta\omega$,

$$\Delta\omega = \omega - \omega'. \quad (16)$$

In Figs. 1 through 4 we show results for the off-shell electron-nucleon scattering cross section for the various cc choices. We choose kinematics which correspond roughly to the extremes of the kinematics sampled by Makins *et al.* [2]. Shown are the deviations of different prescriptions from σ_{cc2} , the prescription used in Ref. [2] for the interpretation of their data. The cross sections are plotted as a function of γ , the angle [1] between the outgoing proton and the direction of \vec{q} . Positive γ corresponds to protons scattered *between* the incident beam direction and \vec{q} , negative γ is for protons scattered *beyond* \vec{q} . (The experimental data in Ref. [2] correspond to negative γ only.) All the figures assume that the recoil proton is in the electron scattering plane. Note that as $|\gamma|$ increases, the missing momentum generally also increases. We have chosen ranges of γ which correspond to missing momentum up to ≈ 250 MeV.

The electron scattering kinematics in Fig. 1 is $Q^2 = 1.04$ GeV², $|\vec{q}| = 1.2$ GeV, and the cross sections are shown for $|\vec{p}'| = |\vec{q}|$, *i.e.* in perpendicular kinematics. The missing energy is 47 MeV at the center of the plot, and depends very weakly on γ . ($E_m = 45$ MeV at $\gamma = \pm 12^\circ$) The missing momentum ranges from 0 to 250 MeV/c, resulting in a $\Delta\omega$ from 47 to 80 MeV. The curves correspond to different prescriptions: how the current is made to be conserved (or which gauge is chosen) and which on-shell form for the current is used to start with, eq. (2) or (3). We see that there is a spread of more than $\pm 5\%$ among the different prescriptions relative to σ_{cc2} .

In Fig. 2, we fix the momentum of the knocked out nucleon at a value *lower* than $|\vec{q}|$, in order to access a larger missing energy. In this case, with $|\vec{p}'|$ reduced by 10% from its value in Fig. 1, the missing energy is approximately 140 MeV at $\gamma = 0$, and the missing momentum ranges from 120 to 270 MeV/c. This leads to an increased $\Delta\omega$ between 148 and 180 MeV. Consequently, the largest difference between the cross sections grows to more than $\pm 10\%$.

In Fig. 3, we use the kinematics of the measurement with the highest incident energy: $Q^2 = 6.8$ GeV², $|\vec{q}| = 4.5$ GeV, again in perpendicular kinematics with $|\vec{p}'| = |\vec{q}|$; the missing energy is 9 MeV at $\gamma = 0$. In this case one is closer to the on-shell kinematics: $\Delta\omega$ is between 9 and 40 MeV and the differences between cross sections typically around 1%. In Fig. 4, $|\vec{p}'|$ is reduced (by 3%) to access a higher missing energy and momentum. In this case the missing energy is 137 MeV at $\gamma = 0$, (135 MeV at $\gamma = \pm 3^\circ$) and the missing momentum ranges from 130 to 280 MeV/c, resulting in a $\Delta\omega$ from 148 to 179 MeV, comparable to Fig. 2, and the spread among the prescriptions grows to about 5%.

It should be stressed that variations of up to 10% occur solely due to the choice of gauge, indicating the severity of the approximations used to make the current conserved. The figures

also illustrate another - somewhat smaller - uncertainty due to another assumption: differences between recipes labeled as '1' and '2', *i.e.* show the effect of choosing one of the two equivalent ways to write the on-shell current as given in eqs. (2) and (3). For given electron kinematics, also this difference grows as we go away from on-shell kinematics, *i.e.* for larger $\Delta\omega$.

That the cross sections appear somewhat less sensitive to gauge choices at the higher energy kinematics can be understood from the following qualitative estimates which apply to a fixed choice of the on-shell current. A measure for the violation of current conservation is in each case given by [4]

$$q \cdot J = \omega J_0 - \vec{q} \cdot \vec{J} \equiv \chi, \quad \chi \approx \Delta\omega[J], \quad (17)$$

where the quantity $[J]$ denotes (part of) the nuclear current density. The matrix element in the Coulomb gauge, eq. (12), is

$$M_C = \frac{-i}{q^2} j \cdot J + \frac{i}{q^2} \left(\frac{\omega j_0 \chi}{\vec{q}^2} \right). \quad (18)$$

Similarly, one obtains in the Weyl gauge, (14)

$$M_W = \frac{-i}{q^2} j \cdot J + \frac{i}{q^2} \left(\frac{j_0 \chi}{\omega} \right). \quad (19)$$

For conserved currents, such as with the subtraction in eq. (8), we have $\chi = 0$, and the matrix elements obviously reduce to the Feynman gauge matrix expression, eq. (11). Since also the electron current is conserved, the matrix elements in all Lorentz gauges, such as Feynman and Landau gauge, are identical: $M_F = M_L$.

With the above expressions for the matrix elements, M_C , M_W and M_L , we can estimate the relative differences between the various prescriptions. We start with comparing Coulomb and Lorentz gauges. Using eqs. (11) and (18), one easily finds that

$$\frac{M_C - M_L}{M_L} \simeq - \frac{\omega j_0 \Delta\omega[J]}{\vec{q}^2(j \cdot J)}. \quad (20)$$

For the purpose of getting order of magnitude estimates, we approximate $j_0[J] \simeq j \cdot J$ and find

$$\frac{M_C - M_L}{M_L} \simeq - \frac{\omega \Delta\omega}{\vec{q}^2}. \quad (21)$$

For a given choice of the on-shell current this expression yields the right magnitude of the difference between the cross sections in the figures, *i.e.*, the difference between $\sigma_{cc1,2}^0$ and $\sigma_{cc1,2}^q$. Similarly, one can obtain the corresponding expression for the Weyl gauge,

$$\frac{M_W - M_L}{M_L} \simeq - \frac{\Delta\omega}{\omega}, \quad (22)$$

which gives the right magnitude for the differences between $\sigma_{cc1,2}^0$ and $\sigma_{cc1,2}^q$. For the comparison of Coulomb and Weyl gauges, two non-covariant gauges, we can approximate the difference as

$$\frac{M_C - M_W}{M_C} \simeq \frac{-\omega \Delta\omega(1/\vec{q}^2 - 1/\omega^2)}{1 - \omega \Delta\omega/\vec{q}^2}. \quad (23)$$

In the kinematical region under consideration this can be further approximated by

$$\frac{M_C - M_W}{M_C} \simeq -\omega \Delta\omega \left(\frac{1}{\vec{q}^2} - \frac{1}{\omega^2} \right), \quad (24)$$

to obtain an estimate for the differences between $\sigma_{cc1,2}$ and $\sigma_{cc1,2}^0$. All the above estimates can explain the relative differences among the cross sections shown in the figures for the kinematics of the SLAC experiment; they also explain the larger differences found in other applications [4].

Our discussion does not provide any estimates for the differences between prescriptions based on different on-shell currents, only for different ways to restore current conservation. What we have shown are the effects due to different prescriptions in the literature for restoring current conservation that are used in the interpretation of $(e, e'p)$ experiments. We also showed the variation due to different on-shell equivalent electromagnetic currents. We have not discussed other aspects of scattering from a bound nucleon or showed the general framework in which all such aspects should be treated consistently, such as the nuclear wavefunction, final state interactions or modifications of the electromagnetic vertex operator. The latter has been considered *e.g.* in meson loop models and relatively small effects were found [12], [13]. Until a complete and fully consistent theoretical description of the $(e, e'p)$ reaction has been achieved, one really cannot know what a reasonable approximation would be and which of the prescriptions we discussed is 'best'. The differences of the results we have shown give an idea of size of the present uncertainty in the interpretation of $(e, e'p)$ experiments.

-
- [1] T. de Forest, Jr., Nucl. Phys. **A392**, 232 (1983).
 - [2] N.C.R. Makins *et al.*, Phys. Rev. Lett. **72**, 1986 (1994).
 - [3] S. Frullani and J. Mougey, Adv. Nucl. Phys. **14**, 1 (1984).
 - [4] H.W.L. Naus, S.J. Pollock, J.H. Koch and U. Oelfke, Nucl. Phys. **A509**, 717 (1990).
 - [5] H. Ito, W.W. Buck and F. Gross, Phys. Rev. **C43**, 2483 (1991).
 - [6] F. Gross and H. Henning, Nucl. Phys. **A537**, 344 (1992).
 - [7] H. Henning, P.U. Sauer and W. Theis, Nucl. Phys. **A537**, 367 (1992).
 - [8] X. Song, J.P. Chen and J.S. McCarthy, Z. Phys. **A 341**, 275 (1992).
 - [9] A. M. Bincer, Phys. Rev. **118**, 855 (1960).
 - [10] J.A. Caballero, T.W. Donnelly and G.I. Poulis, Nucl. Phys. **A555**, 709 (1993).
 - [11] J. Mougey *et al.*, Nucl. Phys. **A262**, 461 (1976).
 - [12] H.W.L. Naus and J.H. Koch, Phys. Rev. **C36**, 2459 (1987).
 - [13] P.C. Tiemeijer and J.A. Tjon, Phys. Rev. **C42**, 599 (1990).

FIGURES

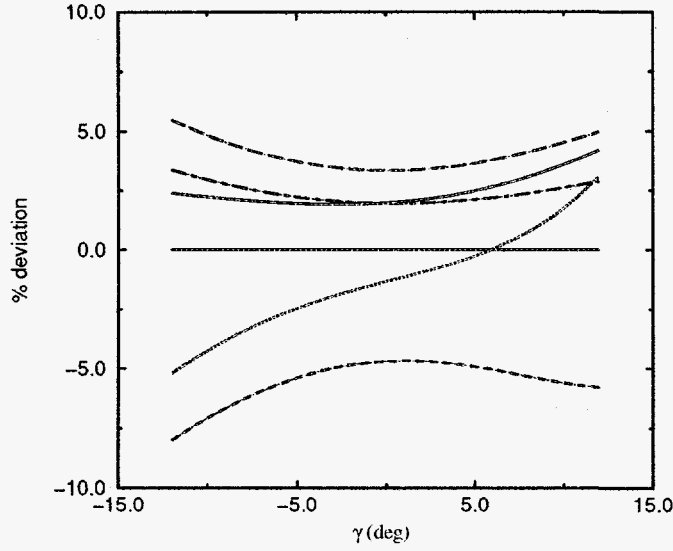


FIG. 1. Deviation of calculated cross sections from de Forest's "cc2" prescription as a function of the angle γ between the ejected proton and the momentum transfer direction. Here incident electron energy = 2.02 GeV, $Q^2=1.04$ GeV², $|\vec{q}|=1.2$ GeV, $|\vec{p}'|=1.2$ GeV, and $E_m=47$ MeV at the center of the plot. Solid curve: σ_{cc1} , dotted curve: σ_{cc1}^0 , dashed curve: σ_{cc2}^0 , long-dashed curve: σ_{cc1}^q , dot-dashed curve: σ_{cc2}^q .

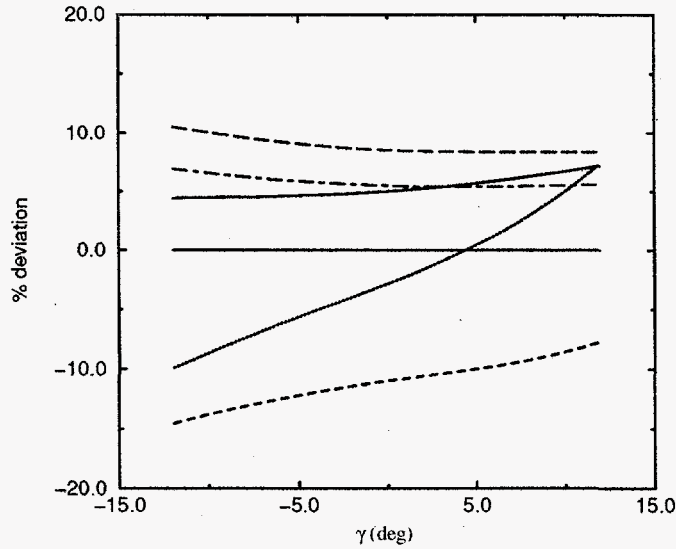


FIG. 2. Same as Fig. 1, but with outgoing proton momentum fixed at $|\vec{p}'|=1.08$ GeV, which reaches a larger missing energy (≈ 140 MeV at the center of the plot.)

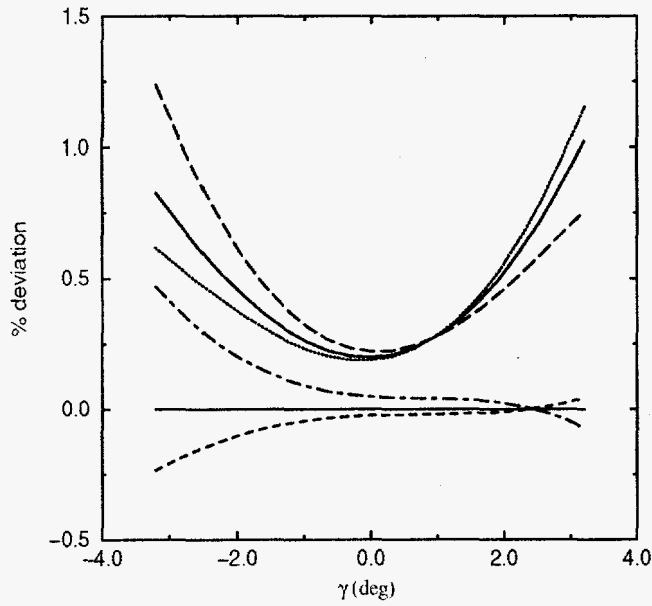


FIG. 3. Same as Fig. 1, but with incident energy = 5.12 GeV, $Q^2 = 6.77 \text{ GeV}^2$, $|\vec{q}| = 4.48 \text{ GeV}$, $|\vec{p}'| = 4.48 \text{ GeV}$, and missing energy 9 MeV at $\gamma=0$. ($E_m = 6 \text{ MeV}$ at $\gamma = \pm 3^\circ$)

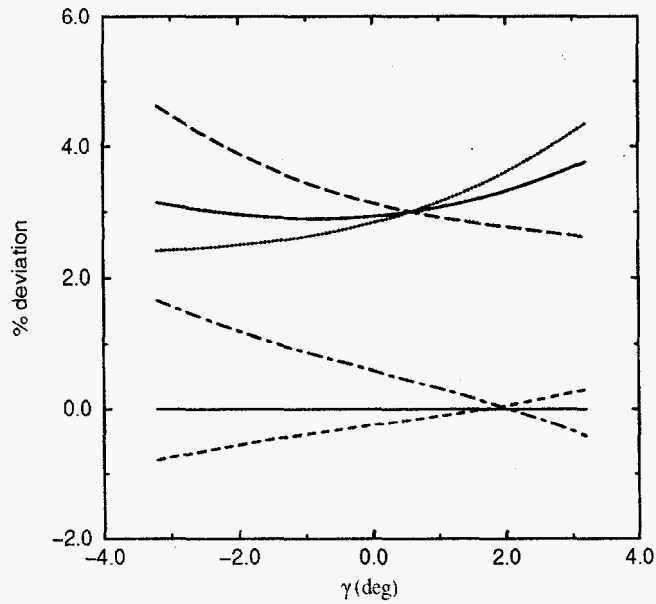


FIG. 4. Same as Fig. 3, but with outgoing proton momentum fixed at $|\vec{p}'| = 4.35 \text{ GeV}$, which reaches a large missing energy ($\approx 137 \text{ MeV}$ at the center of the plot.)

With the advent of continuous beam electron accelerators at Mainz and CEBAF, studies of the hadronic electroweak response at low- and intermediate-energy have entered a new era. One hopes to use these facilities to develop a better understanding of the structure of hadrons in terms of quark and gluon degrees of freedom of QCD. In addition, there exists the possibility of performing new searches for physics beyond the Standard Model (SM) of electroweak interactions. From both standpoints, an interesting class of observables are those which depend on target or electron spin. Indeed, recent advances in polarization technology have opened the way to precise determinations of spin observables. Information gleaned from these observables provides a more detailed probe of hadron structure and “new physics” than does data from spin-independent measurements alone.

As an example of the information which spin-observables might provide, we consider the electroweak excitation of the $\Delta(1232)$ resonance, $N \xrightarrow{V} \Delta(1232)$, where N is the nucleon and $V = \gamma, W^\pm$, or Z^0 . The SM has been tested with high precision in a variety of sectors, so that one knows the basics of the probe reactions extremely well. In principle, then, one may use these electroweak processes to study hadron structure as it bears on the $N \rightarrow \Delta$ transition amplitudes. Conversely, were one to have the hadronic current matrix elements sufficiently well in hand, one might exploit this transition as a probe of possible “new physics” beyond the standard electroweak theory.

The $N \rightarrow \Delta$ transition is particularly useful for either purpose since (i) the $\Delta(1232)$ resonance is nicely isolated from the plethora of other densely populated nucleon resonance states that appear at higher energies, and (ii) it is a pure isovector, spin-flip transition. The first of these features simplifies the theoretical extraction of the matrix element $\langle \Delta | J_\mu | N \rangle$ (J_μ is the appropriate electroweak current) from the experimental observables, while the second affords one a kind of “filter” for selecting on various aspects of hadron structure or new physics. For example, there has been considerable interest recently in the strange quark content of non-strange hadrons. (See ref. [1] for a recent review.) Since $s\bar{s}$ pairs contribute only to *isoscalar* current matrix elements, the N to Δ transition filters out (presently highly uncertain) $s\bar{s}$ contributions. Similarly, the isovector character of this transition gives it a different sensitivity to possible contributions from additional heavy particles not appearing in the SM than does, say, the weak charge measured in atomic parity violation. The $N \rightarrow \Delta$ offers the additional advantage that it only couples strongly to one outbound channel, viz., $N\pi$. This allows one, in principle, to treat the unitarity issue quite rigorously [2] implementing in the theoretical analysis the constraints of the Fermi-Watson theorem [3].

The electromagnetic (EM) $N \rightarrow \Delta$ processes yield three resonant helicity amplitudes for the virtual photons, $A_{1/2}^T$, $A_{3/2}^T$ and $A_{1/2}^L$: two transverse and one longitudinal indicated by the appropriate superscript. The longitudinal amplitude is absent for real photons. The weak neutral current (NC) and charged current (CC) reactions are sensitive to the weak vector current analogues of these amplitudes as well as to new helicity structures associated with the weak axial vector current. One motivation for considering CC and NC reactions, despite the experimental challenges involved in measuring very small weak interaction observables, is to obtain access to these axial vector helicity amplitudes.

Each EM, CC, or NC observable contains contributions from non-resonant backgrounds

as well as from the Δ resonance. From a single parity violation measurement on the proton, one has no way experimentally to separate the two contributions. The efficacy with which one can extract a resonant helicity amplitude depends on one's ability to subtract out these backgrounds. In the following discussion, we evaluate the prospects for making this separation. Of the nucleon electroweak excitation processes one might consider, the $N \rightarrow \Delta$ is the simplest, having only one possible resonant contribution and probably the least complex background.

To date, the primary information regarding the vector helicity amplitudes has been obtained from EM processes while information on the axial vector amplitudes has been gleaned from CC reactions. The vector helicity amplitudes for the $N \rightarrow \Delta$ transition are presently known at the precision at $\pm 15\%$ through the exploration of the photo- and electroproduction of pions off nucleons [2]. The charged current reactions do provide a corroboration of the present knowledge of the vector form factors [4], but without any ability to improve upon the precision obtained via the electromagnetic processes. Since the classic work of Adler [5] on the $N \rightarrow \Delta$ electroweak amplitudes (in the form of numerical values of so-called Adler form factors) a large number of investigators have examined these form factors. Some recent studies are the works of Hammert, Holstein and Mukhopadhyay [6], and Líu, Mukhopadhyay and Zhang [7]. From the QCD point of view, Leinweber, Draper and Woloshyn [8] have succeeded in computing the $N \rightarrow \Delta$ vector transition amplitudes on the lattice. The magnetic transition amplitude is as in the non-relativistic quark model, about 30% less than what is inferred from the data. The E2 amplitude is too noisy to be of value as a point of comparison. In the Skyrmon approach [9], the soliton is quite deformed, with a much larger $E2/M1$ ratio than in the other models. To date, no complete investigations on all Adler form factors are available in bag models, soliton models, or lattice QCD.

We focus on the NC process and illustrate how knowledge of the NC $N \rightarrow \Delta$ helicity amplitudes might complement existing information. Early work on this process includes refs [10]; for a more detailed list, see e.g. section 4.7 of [1]. The NC helicity amplitudes can be obtained from the parity-violating (PV) helicity-difference, or "left-right", asymmetry for the scattering of longitudinally polarized electrons from a nucleon target [1]:

$$A_{LR} = \frac{N_+ - N_-}{N_+ + N_-} = \frac{-G_\mu |q^2|}{\sqrt{2} 4\pi\alpha} [\Delta_{(1)}^\pi + \Delta_{(2)}^\pi + \Delta_{(3)}^\pi], \quad (1)$$

where N_+ (N_-) is the number of detected, scattered electrons for a beam of positive (negative) helicity electrons; q^2 is the square of the four-momentum transfer to the target; α and G_μ are, respectively, the electromagnetic fine structure constant and the Fermi constant measured in μ -decay.

The quantities $\Delta_{(i)}^\pi$ ($i = 1, \dots, 3$) denote the three primary contributions to the asymmetry. Specifically, one has

$$\Delta_{(1)}^\pi = 2(1 - 2\sin^2 \theta_W) \quad (2)$$

in the Standard Model at tree level. $\Delta_{(2)}^\pi$ gives contributions from *non-resonant* background transitions. $\Delta_{(3)}^\pi$ involves the axial-vector hadronic coupling of nucleon to Δ :

$$\Delta_{(3)}^\pi \approx 2(1 - 4\sin^2 \theta_W) F(q^2, s) \quad , \quad (3)$$

$F(q^2, s)$ involves a ratio of PV and parity-conserving (PC) electroweak response functions. The variable s gives the square of the total energy in the center of mass frame. In writing down the RHS of Eq. (3), we have ignored non-resonant axial vector contributions.

The physics of interest lies in $\Delta_{(1)}^\pi$ and $\Delta_{(3)}^\pi$. The background term $\Delta_{(2)}^\pi$ introduces a theoretical uncertainty into the extraction of the other two terms. A determination of the first term, $\Delta_{(1)}^\pi$, would provide a window on physics beyond the SM. This term is ostensibly independent of any hadronic matrix elements and involves only the product of NC electron and isovector NC quark couplings. The latter has never been determined independently from the other hadronic vector NC couplings. The Z^0 -pole observables can be relatively opaque to many examples of non-standard physics, in contrast to the situation with low-energy observables like $A_{LR}(N \rightarrow \Delta)$.

As a benchmark, we will consider the constraints on new physics which a one percent determination might yield and compare these prospective constraints with those obtainable from other low-energy NC observables. We also consider the experimental conditions under which a one percent determination might be made, along with the theoretical uncertainties which may enter at that level. We find that a one percent determination would provide constraints roughly comparable to the present constraints obtained from atomic PV. A fairly demanding experimental setup, e.g. 1000 hours of high energy (≈ 3 GeV) CEBAF beam at forward angles could achieve this level, if the non-resonant backgrounds can be understood at roughly $\pm 20\%$ levels or better. Improving the statistical error by a factor of two requires four times the running time. Hence, a difficult, but potentially feasible, SM test is possible by the measurement of $A_{LR}(N \rightarrow \Delta)$.

The third term, $\Delta_{(3)}^\pi$, is interesting from the standpoint of hadron structure. In most effective models of QCD, the nucleon and Δ are closely related, and $N \rightarrow \Delta$ transition properties are as fundamental and calculable as properties of the nucleon itself, such as the magnetic moment, β -decay constant, strong couplings, and e.g. the G-T relation. Relations between these quantities are often even independent of the details of specific quark-model wavefunctions. To a good approximation, the function $F(q^2, s)$ contained in $\Delta_{(3)}^\pi$ is essentially proportional to the ratio of two transition form factors: C_5^A/C_3^V , where V (A) correspond to the hadronic vector (axial vector) current. This ratio is the off-diagonal analog of the G_A/G_V ratio extracted from neutron β -decay. A measurement of $\Delta_{(3)}^\pi$ would correspondingly provide an opportunity to test low-energy consequences of chiral symmetry, such as the off-diagonal Goldberger-Treiman (G-T) relation and its chiral corrections. (Note, conversely, that G-T involves, but does not constrain, the value of C_5^A/C_3^V .)

A separate determination of C_5^A is also of interest in light of results [2] for the vector current transition form factors from photo- and electroproduction of pions. A recent theoretical examination of these quantities [6] in the quark model finds magnetic form factors underestimated by $\approx 30\%$ based on photoproduction data. For the transition charge radius, the disagreement arises at the 20% level [2]. An interesting question here is if the deficit of the transition magnetism in quark models is mirrored in the transition "axial electricity": in this same model, the dominant axial transition form factors are more than 35% below the central value of experimental extractions [4]. These results are roughly consistent with the predictions of Adler [5] based on PCAC.

A variety of scenarios have been proposed to account for these discrepancies, such as the role of the meson clouds around the quark core, change of the value of the quark magneton and so on. Gluonic hyperfine corrections apparently do not account for the observed level of SU(6) violation [6]. A recent approach which may offer some deeper understanding is the technique of heavy baryon chiral perturbation theory. [11]. Here, higher order meson loop corrections do not obey

the SU(6) symmetries of the underlying quark model. This method has been used to examine threshold weak pion production [12], but this is well below the dominant $\Delta(1232)$ resonance. This technique has also been used to look directly at the Δ region [13], but so far only for EM properties. These authors have claimed that they should be able to handle the resonant axial coupling in the near future. Lattice QCD calculations are another promising theoretical means to understand the transition amplitudes. Estimates of the magnetic M1 transition amplitude is in approximate agreement with the quark model results described above [8] (thus, significantly below experiment), but we know of no lattice calculation of the axial resonant form factor to date.

Since the present data from neutrino cross sections remains so ambiguous in the axial sector, ($\sim 50\%$ accuracy [4]) a separate determination of C_5^A would provide an important additional test of these scenarios. We find that a $\sim 30\%$ (statistical) determination of C_5^A/C_3^V could be made with ≈ 700 hours of beam time at $|q^2| \sim 0.2 \text{ GeV}^2$. For example, with beam energies below about 1 GeV, the relative contribution of the axial term to the overall asymmetry exceeds 10% for forward angles, and the statistical uncertainty (with arbitrary but plausible experimental conditions) is around 3%. Modulo background uncertainties as discussed soon, this may provide an opportunity to improve our knowledge of C_5^A by a factor of roughly 2 over neutrino measurements, with much *less* sensitivity to the resonant weak vector amplitudes, themselves still uncertain at the $\approx 30\%$ level.

Whether these benchmarks for the determination of $\sin^2 \theta_W$ and C_5^A/C_3^V can be realized depends, in part, on the degree to which theoretical uncertainties entering the interpretation of $A_{LR}(N \rightarrow \Delta)$ are sufficiently small. The most serious uncertainties appear in two guises: (i) background contributions, contained in $\Delta_{(2)}^\pi$, and (ii) hadronic contributions to electroweak radiative corrections, which enter both $\Delta_{(1)}^\pi$ and $\Delta_{(3)}^\pi$. A recent analysis of the background contributions was reported in Ref. [14], where they present a region of values of CM energy W for which the background contribution appears to be less than 5%. That enhances the prospect to determine $\sin^2 \theta_W$ and the $N \rightarrow \Delta$ C_5^A/C_3^V ratio.

An early calculation of the $N \rightarrow \Delta$ asymmetry which included the axial transition amplitude was given by Jones and Petcov [10]. We can easily recover their formulae if we ignore the contribution of the background and further assume that the magnetic dipole amplitude dominates in the $N \rightarrow \Delta$ vector excitation, an approximation supported by both quark model studies [7] and by the phenomenological multipole analysis [2]. We then have

$$\Delta_{(2)}^\pi = 0, C_5^V(q^2) \approx 0, C_4^V(q^2) \approx -\frac{M}{M_\Delta} C_3^V(q^2). \quad (4)$$

where the C 's are conventional spin 1/2-3/2 transition form factors [5]. Making the assumption that $C_3^A \approx 0$, which follows from the quark model, we find that the axial correction, $\Delta_{(3)}^\pi$, is given in this approximation by

$$\Delta_{(3)}^\pi = 2(1 - 4 \sin^2 \theta_W) \frac{C_5^A}{C_3^V} \left[1 + \frac{W q^0}{M^2} \frac{C_4^A}{C_5^A} \right] \mathcal{P}, \quad (5)$$

where \mathcal{P} is a kinematic function

$$\mathcal{P}(Q^2, s) = \frac{M M_\Delta ((s - M^2) + (s - M_\Delta^2) - Q^2)}{\frac{1}{2} (Q^2 + (M_\Delta + M)^2) (Q^2 + (M_\Delta - M)^2) + (s - M^2)(s - M_\Delta^2) - Q^2 s}, \quad (6)$$

An expression for the function $F(q^2, s)$ appearing in Eq. (3) can now be read off. One does not *have* to make the assumptions in Eq. (4) (nor that $C_3^A = 0$) based on the quark model, but this adds some algebraic complication. (For example, one can no longer ignore longitudinal contributions to the total cross section.) In the context of specific models that violate Eq. (4), we can compute the fully corrected asymmetry, but numerically we find this has very little effect.

The background contributions are those that do not need the explicit participation of the Δ resonance at the tree level [14]. Thus, the tree approximation for the resonance multipoles takes the form $m^{TA} = m_B^{TA} + N/\varepsilon$, where m_B^{TA} is the non-resonant Born amplitude, ε is the resonant denominator $(M_\Delta^2 - s)^{-1}$ and N is a suitable resonant residue. This form of the amplitude does not satisfy the Watson theorem [3], which is in force when one considers one strong and another weak channel. The unification of the multipoles of our interest is model-dependent and there are numerous ways of doing it [2]. One of the most common ones is to interpret the m^{TA} as K-matrix elements, then the resonant multipoles can be written in the unitary form

$$\mathcal{M} = \cos\delta e^{i\delta} \left(m_B^{TA} + \frac{N}{\varepsilon} \right), \quad (7)$$

where δ is the phase of the 33-resonance, $\Delta(1232)$. This form explicitly obeys the Watson theorem, and immediately reproduces one of the unitarization procedures adopted by Adler [5]. It is now easy to see from the form of Eq. 7 that we have a *theorem* for this K-matrix Ansatz of the resonant matrix element; we state it as follows:

For the K-matrix unitarization of the resonant multipoles, the electroweak asymmetry A is independent of the Watson phase. The tree-level result for A is the same as that obtained from the K-matrix unitarization.

Each hadron amplitude for the resonant $\Delta(1232)$ satisfies the Watson theorem. The bilinears $\bar{T}^* T^W$, $\bar{T}_C^* T_C$, $U^* T$ all generate $\cos^2 \delta e^{i\delta} e^{-i\delta}$, giving the factor $\cos^2 \delta$ in the numerator, to be cancelled with the same factor arising out of the bilinears of electromagnetic amplitudes in the denominator. The importance of the above theorem is that the tree level results for the resonant matrix elements are entirely adequate for the calculation of the background amplitudes, if we are interested in the electroweak asymmetry.

There have been several theoretical studies on the background contributions to the asymmetry. These are very similar in spirit to those for pion photoproduction [2]; apart from some uncertainties from the analytic structure of the form factors at relatively low Q^2 , their general structures are very well-known. Explicit considerations of the background contributions to the asymmetry have been made by Li *et al.* [15], and Pollock [16]. Hammer and Drechsel [14] have recently done a thorough job of modeling the backgrounds in the resonance region. They point out that there is a kinematical region of W where the background contributions essentially cancel against their interference with resonance. The crucial point about the role of background in the asymmetry is that there exists a special region of the excitation energy where the net background contribution is negligible. Hammer and Drechsel get this excitation energy to be right on the Δ peak. This, along with the absence of any significant contribution from the unitarity corrections, discussed above, in the context of the K-matrix theorem, suggests that we can learn, from the measurement of the asymmetry, physics coming from the standard model influencing the vector excitation of the Δ , and small, yet significant, corrections from the

axial-vector excitation of the Δ , around $W \sim 1.23\text{GeV}$, largely free from the background uncertainties. To be conservative about the background uncertainties, we shall look for the design of the future experiments where effects due to axial vector excitations are measurably larger than the level of 5% uncertainty of the asymmetry coming from the background contributions.

For an estimate of the best design of a future experiment on the measurement of the asymmetry, we start with some standard inputs that represent a typical run sequence in the Hall A at CEBAF. The percent error for the asymmetry is calculated by the formula

$$\frac{\Delta A}{A} = \frac{1}{A} \frac{\Delta \sigma}{\sigma} = \frac{1}{A\sqrt{N}}. \quad (8)$$

(The "figure of merit" is traditionally given as the inverse square of this quantity, $FOM = A^2 N$) In order to improve our numerical estimates, we use an accurate effective parameterization of the pion production cross sections.

Focusing first on $\Delta_{(1)}^\pi$, we note that it is a constant, independent of ϵ or θ_{lab} . As we see from Eq. 1, the overall asymmetry grows linearly with Q^2 , but the counting rate (N_+ and N_-) drops rapidly with Q^2 , due to transition form factors. Thus, there is in general a kinematical compromise required, and only some limited range of energy and scattering angle maximizes the statistical figure of merit defined above. In addition, independent of the figure of merit, one must also seek kinematics which suppress the uncertain non-resonant backgrounds, as well as the axial transition term. The latter requirement forces one towards larger incident energies, but the need for moderate Q^2 (to keep the figure of merit high) then demands smaller scattering angles. (This in turn may reduce the available solid angle of detection, and hence also the figure of merit.) There is no completely unambiguous final choice for kinematic variables, the tradeoffs will ultimately depend on the specific experimental setup.

If instead we seek to *measure* $\Delta_{(3)}^\pi$, the required kinematic conditions are changed. The figure of merit must still be kept high (i.e. the statistical uncertainty in the total measured asymmetry must be kept low), but in addition, the relative contribution of $\Delta_{(3)}^\pi$ to the asymmetry must be as large as possible, certainly larger than the statistical uncertainty in the total asymmetry, and in addition larger than the uncertain part of the background term $\Delta_{(2)}^\pi$. In Fig. 1, we show $\Delta_{(3)}^\pi$ as a function of Q^2 for various incident energies. This figure demonstrates that $\Delta_{(3)}^\pi$ is enhanced at lower incident energies, as we argued from basic kinematic coefficients. In the figure, the error bar is constructed simply by using various different models for the Adler amplitudes, and should be considered a crude measure of the theoretical uncertainty in this quantity. Fig. 2 shows $\Delta_{(3)}^\pi$ as a function of both energy and scattering angle. Again, we see the simple functional dependence on energy, and the relative lack of sensitivity to scattering angle. Table I provides more detailed numbers for a variety of kinematics, but only for a single parameterization of the Adler form factors.

In figure 3, we show a plot of $\Delta_{(3)}^\pi/A_{\text{stat}}$, versus both incident energy, ϵ , and electron scattering angle, θ_{lab} . The region shown spans roughly what might be accessible at CEBAF. Selected values from this plot are also collected in Table I. In order to best extract $\Delta_{(3)}^\pi$, the plotted quantity should be as large as possible. Forward scattering angles are favored, as is moderate to high energy. From this figure alone one might conclude that larger energies and smaller angles are better still, but both numerator and denominator in the plotted quantity decrease with increasing energy. The condition $\Delta_{(3)}^\pi/A_{\text{tot}} > 5\%$ is a rough requirement to assure that uncertainties in the background term, $\Delta_{(2)}^\pi$, do not begin to dominate. The shading in this

figure indicates the absolute value of $\Delta_{(3)}^\pi$, and this constrains experiments to stay at smaller energies where the axial term is more important. (Darker shades mean smaller values of $\Delta_{(3)}^\pi$.) A decent compromise might be e.g. incident energy in the range $1 \text{ GeV} < \epsilon < 2 \text{ GeV}$, scattering angle $10^\circ < \theta < 20^\circ$. Throughout this range, $\Delta A_{\text{stat}}/A_{\text{tot}}$ stays below $\approx 5\%$, while $\Delta_{(3)}^\pi$ is more than a factor of 2 larger than ΔA_{stat} , and also $\Delta_{(3)}^\pi$ stays bigger than 5% of the total asymmetry as well. At the optimal kinematics points, we find $\Delta_{(3)}^\pi/\Delta A_{\text{stat}} \approx 3 - 4$, which implies at best a 25-30% measurement of the axial form factor is possible.

Returning to the issue of Standard Model tests, i.e. a high precision measurement of $\Delta_{(1)}^\pi$, we show in Fig. 4 a plot of the figure of merit, $A^2 N$ (scaled) versus incident energy and electron scattering angle. On this scale, reaching 1 corresponds to a 1% statistical uncertainty, and this is achievable for a narrow range of experimental conditions. There is a much broader range of kinematics where the curve exceeds 0.04, which corresponds to a 5% measurement of the asymmetry. To avoid contamination from $\Delta_{(3)}^\pi$ (arbitrarily keeping it below $\approx 6\%$ of the total asymmetry) one should keep the incident energy above $\approx 2 \text{ GeV}$ for forward angles, or $\approx 1.2 \text{ GeV}$ at more backward angles. More detailed numbers can be extracted from Table I. E.g., there we see that at 3 GeV , $\theta = 10^\circ$, the expected statistical uncertainty in the measurement is $\Delta A_{\text{stat}}/A_{\text{tot}} \sim 1\%$, and the total expected contribution from $\Delta_{(3)}^\pi$ here is 3.6% of the total asymmetry. Thus, an a priori 30% uncertainty in the axial coupling would still allow close to a 1% extraction of $\sin^2 \theta_W$. Improvements in experimental assumptions (including time, beam polarization, or solid angle) decrease ΔA_{stat} as their square root.

To summarize, the electroweak excitation of the Δ resonance can be directly observed by the reaction $N(\vec{e}, e')\pi N'$ where the excitation energy is at the peak of the Δ resonance. The asymmetry is dominated by the vector excitation of the Delta resonance, which can be very accurately computed in the standard model. However, the axial vector amplitude makes a small, but measurable contribution. While there is a contribution from the non-resonant background, we have discussed conditions where this may not be overwhelming. The experiments are best done with an electron incident energy below 1 or 2 GeV, with small lab scattering angles and with detectors with large solid angles. The Δ peak at $W = 1.23 \text{ GeV}$ is the best value of W , for which the background contributions are small.

Compared in difficulty with two other kinds of experiments mentioned in this paper, viz., neutrino scattering and chiral pion production, this one falls somewhere in the middle. The neutrino experiments are relatively free from physical background, but have to deal with very small cross-sections and as many as eight electroweak N to Δ transition form factors. The soft pion production by electron, along with a hard Δ emission off a nucleon, is the easiest experiment to do, but is beset with theoretical difficulties of extrapolation and as-yet-unknown background contributions. Our suggestion, to measure the electroweak asymmetry in the Delta peak region, is challenging in its difficulty, but is easier than a neutrino experiment. The theoretical complications from the background contributions appear to be not too problematic.

The ultimate theoretical goal of an experimental study probing the vector and the axial vector nucleon to Δ transition form factors is to understand them in the framework of QCD. At low Q^2 , QCD is in the non-perturbative domain. Rigorous calculations in this framework would most likely come from lattice investigations. We hope our proposed experiment would generate impetus for such research in real earnest. This brings us to our final question: might we use this experiment to learn about the physics *beyond* the standard model? Issues that are relevant to this context deal with an analysis of the radiative corrections and roles of e.g.

extra Z-bosons. Very difficult, but experimentally feasible studies are possible with electroweak interaction to look for physics beyond the standard model. These would be second generation experiments at facilities like CEBAF.

- [1] M. J. Musolf *et al.*, Phys. Rep. **239**, 1 (1994).
- [2] R. M. Davidson and N. C. Mukhopadhyay, Phys. Rev. **D 42**, 20 (1990); R. M. Davidson, N. C. Mukhopadhyay and R. S. Wittman, *ibid.*, **D 43**, 71 (1991).
- [3] K. M. Watson, Phys. Rev. **95**, 228 (1954); E. Fermi, Supp. Nuovo Cim. **10**, 17 (1955).
- [4] T. Kitagaki *et al.*, Phys. Rev. **D42**, 1331 (1990).
- [5] S. L. Adler, Ann. Phys. **50**, 89 (1968); Phys. Rev. **D12**, 2644 (1975).
- [6] T. R. Hemmert, B. R. Holstein and N. C. Mukhopadhyay, Phys. Rev. **D51**, 158 (1995).
- [7] J. Liu, N. C. Mukhopadhyay and L. Zhang, Phys. Rev. **C52**, 1630 (1995).
- [8] D. Leinweber, T. Draper and R. M. Woloshyn, Phys. Rev. **D 46**, 3067 (1992).
- [9] L. Zhang and N. C. Mukhopadhyay, Phys. Rev. **D50**, 4668 (1994).
- [10] D. Jones and S. Petcov, P. Lett. **91B**, 137 (1980), R. Cahn and F. Gilman, P. Rev. **D17**, 1313 (1978).
- [11] E. Jenkins and A. V. Manohar, Phys. Lett. **B 259**, 353, (1991), D. B. Leinweber, Phys. Rev. **D 53**, 5115 (1996).
- [12] V. Bernard, N. Kaiser, U-G. Meißner, Phys.Lett. **B331**, 137 (1994)
- [13] T. Hemmert, B. Holstein, J. Kambor, Los Alamos archive hep-ph/9606456.
- [14] H. -W. Hammer and D. Drechsel, Mainz preprint MKPH-T-95-10 (1995).
- [15] S. -P. Li, E. M. Henley and W. -Y. P. Hwang, Ann. Phys. **143**, 372 (1982).
- [16] S. J. Pollock, Ph. D. Thesis, Stanford University, (1987).

TABLES

$E(\text{GeV})$	$\theta_{\text{lab}}(^{\circ})$	$Q^2(\text{GeV}^2)$	$10^5 A_{\text{tot}}$	$\frac{\Delta A_{\text{stat}}}{A_{\text{tot}}}(\%)$	$\frac{\Delta_{(3)}^{\pi}}{A_{\text{tot}}}(\%)$	$\frac{\Delta_{(3)}^{\pi}}{\Delta A_{\text{stat}}}$
.4	10.	.001	-.01	156.5	23.2	.1
.6	10.	.005	-.06	25.5	17.7	.7
.8	10.	.011	-.12	11.0	13.7	1.2
.4	15.	.002	-.02	105.5	23.2	.2
.6	15.	.011	-.12	17.5	17.6	1.0
.8	15.	.025	-.28	7.8	13.6	1.8
.4	20.	.003	-.04	80.4	23.1	.3
.6	20.	.018	-.22	13.7	17.5	1.3
.8	20.	.042	-.48	6.3	13.5	2.2
.4	45.	.013	-.16	41.0	22.4	.5
.6	45.	.078	-.90	8.1	16.4	2.0
.8	45.	.173	-1.93	4.5	12.5	2.8
.4	90.	.035	-.43	29.5	21.0	.7
.6	90.	.192	-2.18	7.8	14.3	1.8
.8	90.	.399	-4.34	5.7	10.6	1.8
.4	180.	.054	-.65	28.2	19.8	.7
.6	180.	.276	-3.08	9.0	12.7	1.4
.8	180.	.547	-5.85	7.6	9.3	1.2

TABLE I. SM prediction of the asymmetry, the experimental statistical uncertainty for the asymmetry, the percentage contribution of the axial-vector excitation of the Δ , and ratio of the latter two, as functions of energy and scattering angle. Q^2 is calculated assuming we are sitting on the Δ peak. See text for specifications of the experiment. The axial contribution is estimated using the parameter set of Adler-Kitagaki, but assuming C_4^V is constrained by the quark model relation, Eq. 4.

FIGURES

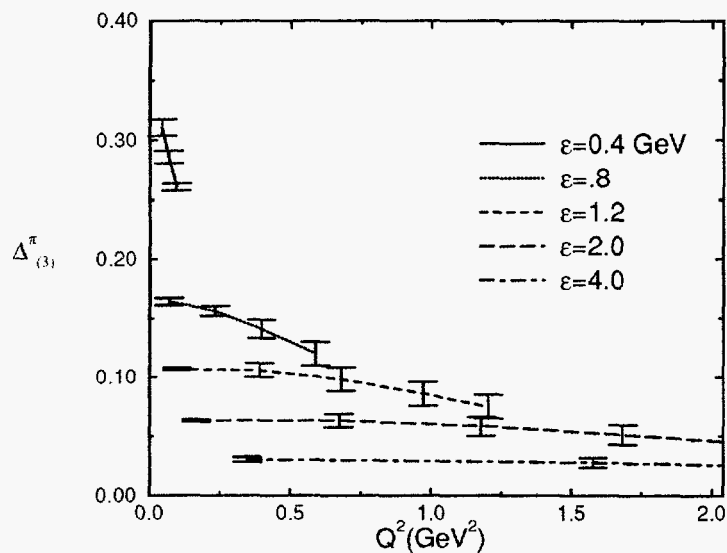


FIG. 1. $\Delta_{(3)}^\pi$ as a function of Q^2 in GeV^2 for different incident electron energies. We computed with the Jones and Petcov [10], Adler-Kitagaki [4] calculations of form factors for the nucleon to Δ transition. The error bars represent the rough spread of these model results.

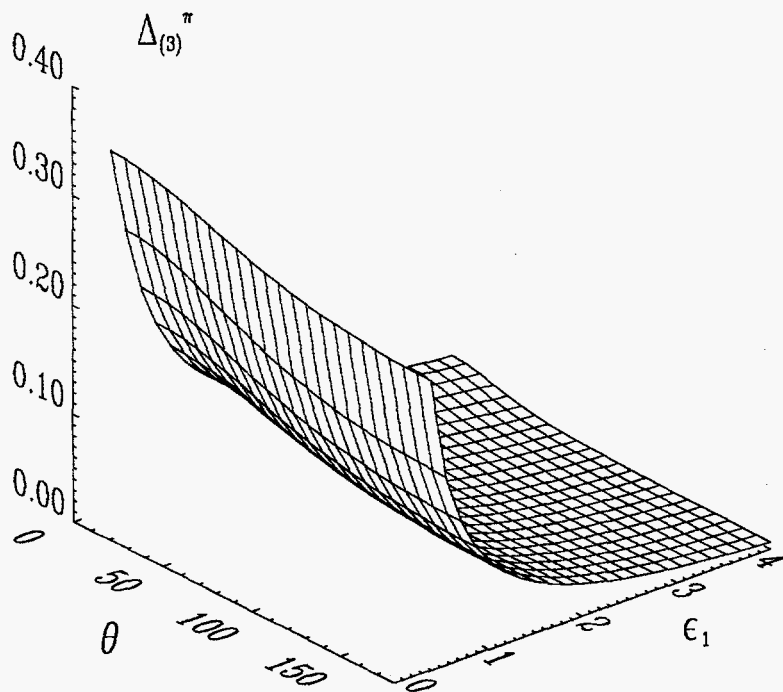


FIG. 2. As above, with $\Delta_{(3)}^\pi$ plotted in 3 dimensions versus both incident energy, ϵ , and electron scattering angle, θ_{lab} . We have computed only with the Adler-Kitagaki [4] parametrization here.

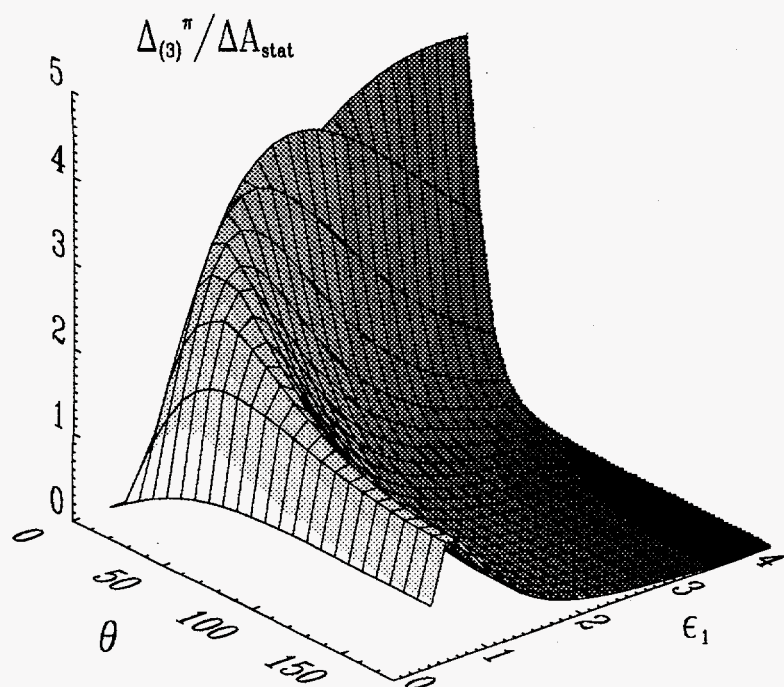


FIG. 3. As above, a 3-D plot of $\frac{\Delta_{(3)}^{\pi}/A_{\text{tot}}}{\Delta A_{\text{stat}}/A_{\text{tot}}}$, versus both incident energy and electron scattering angle. (The shading is determined by the value of $\Delta_{(3)}^{\pi}$, smaller values are shaded darker)

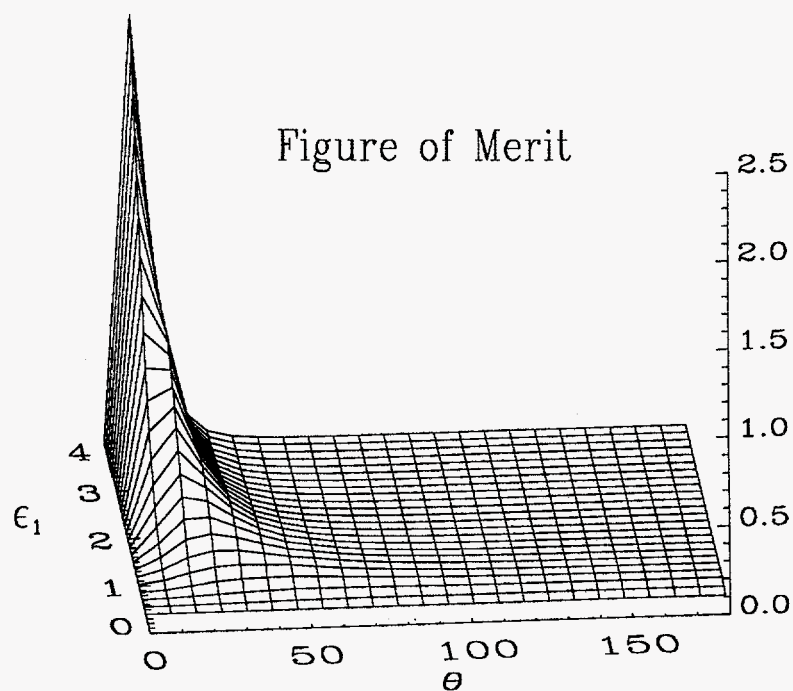


FIG. 4. As above, a 3-D plot of the figure of merit $\equiv A^2 N$, scaled by 10^4 , versus incident energy and electron scattering angle.

The constituent quark model of mesons has been a highly successful tool for classification of mesons and elucidation of their interactions [1,2]. The model correctly predicts the mass splittings within a large number of meson multiplets, as well as the mass splittings among the multiplets themselves. In this way it provides a dynamical explanation of well-known flavor $SU(3)$ broken-symmetry results, such as the Gell-Mann-Okubo relation [1,2]. Furthermore, historically it provides the conceptual foundation of QCD. There are only a few exceptions to the ubiquitous success of this model and they are invariably connected with pseudoscalar (ps) and scalar (s) mesons.

In the case of ps mesons the leading problem was the anomalously low mass of the pion. There are two lines of thought in attempts to resolve this problem: The almost universally accepted explanation is (i) that the low mass of the pion is related to the broken chiral symmetry *via* the Gell-Mann-Oakes-Renner (GMOR) relation [3]; The explanation within the nonrelativistic constituent quark model (ii) lies in the large strong hyperfine interaction between the quark and the antiquark, only to open the question of relativistic corrections.

The scalar meson problem in the quark model can be roughly described as consisting of two parts: (a) The absence of clear experimental evidence for many members of the $q\bar{q}$ scalar meson nonet; (b) An excess of observed neutral scalar states that do not fit into familiar theoretical schemes. While the latter (b) is not necessarily a disaster in view of the fact that this is the channel where glueballs and other exotic states are expected to be seen, the former is a potentially serious embarrassment. The existence of four scalar states [4] (isoscalar f_0 and isovector a_0) with masses around 980 MeV is now beyond doubt, although their widths are still a matter of dispute. At first sight these f_0 and a_0 seem like perfect examples of degenerate ideally mixed isosinglet and isotriplet $q\bar{q}$ mesons made of light quarks u, d , very much like ω, ρ in the vector channel. This is exactly how they were classified by the PDG94 [4]. With mass around 980 MeV, they are, however, about 300 MeV lighter than the predictions of the simple constituent quark model. To make things worse, these mesons are comparatively narrow for hadronically decaying resonances, they couple only weakly to the non-strange ($\pi\pi$) channels and rather strongly to the strange ones ($K\bar{K}$). Finally, there are no strange scalar states around 1100 MeV that would correspond to K_0^* . This led the PDG96 [5] to declare as unknown all but four ($K_0^*(1430)$) states in the scalar $q\bar{q}$ nonet.

There are too many scalar isoscalar states and they misfit their presumed $SU(3)$ assignments. This sort of a problem is not new, however: the ninth pseudoscalar meson $\eta'(960)$ was also found to lie far outside of the $SU(3)$ mass relations' bounds. The resolution in that case is the explicit breaking of the $U_A(1)$ symmetry, which is believed to be induced by instantons in QCD [6]. We would like to point out a potential solution to the scalar meson problem here: the same mechanism of $U_A(1)$ symmetry breaking may resolve the f_0' mass problem. Since it is *a priori* not clear that either $SU_L(N_f) \times SU_R(N_f)$ chiral invariance or $U_A(1)$ symmetry breaking have anything to do with scalar mesons, the present work is primarily meant to be a demonstration of relevance of these symmetries to the problem on hand. Although we will present a fairly detailed analysis of the experimental data from our theoretical point of view, that does not mean that we view this paper as the final word on the subject. Indeed, the opposite is true.

Since the experimental data are still in a state of great flux, we cannot be certain that the present particle assignments will survive until the next edition of PDG tables. Hence, we must view this work only as the first indication of a new and potentially important phenomenon. Our complete analysis will be made within the confines of a specific nonconfining chiral quark model. We will show some evidence, though, that our conclusions may hold in a wider class of models.

We have derived a set of mass relations in the NJL model that are a consequence of broken chiral $SU(3) \times SU(3)$ and $U_A(1)$ symmetries. These mass relations identify the eighth scalar meson as a heavy one, *i.e.*, $f_0(1500)$ and the ninth scalar meson f'_0 as a light one, its mass being around 1000 MeV. Since there are two such states ($f_0(980), f_0(\epsilon(1000))$) at essentially the same mass, we must decide which one to identify as the ninth scalar meson. The decay width and branching ratios of Pennington's $f_0(\epsilon(1000))$ [7] are far closer to the predictions of our model than those of $f_0(980)$. These mass relations are based on the observation that in our model the axial flavour-singlet $U_A(1)$ current non-conservation is visible in the scalar meson spectrum, just as it is in the pseudoscalar one. The nature of the breaking is also similar: the flavor-singlet member of the nonet, perhaps mixed with the eighth member of the octet, has its mass split away from the octet, even in the limit of exact $SU(3)$ symmetry. That much follows from $SU(3)$ group theoretical arguments alone [1,2]. In order to determine the size and sign of this splitting, however, we need the dynamical predictions of our model. For that purpose we employ a chiral quark model of the Nambu-Jona-Lasinio [8] kind. This model has several advantages over the potential and bag models: (i) it displays spontaneous symmetry breaking that is dynamical, rather than by a decree; (ii) it satisfies all relevant current algebra theorems; (iii) it is fully relativistic and without center-of-mass problems; (iv) it naturally incorporates 't Hooft's instanton-induced $U_A(1)$ -breaking interaction [6]. The model, of course, has its drawbacks, as well: (i) it does not confine; (ii) it is not renormalizable.

Nambu was apparently the first to point out that the ps meson mass splittings alone imply that " $U_A(1)$ is a very bad symmetry" (pp. 404 in [9]), and Weinberg [10] sharpened and emphasized this " $U_A(1)$ problem" within the context of QCD. It was 't Hooft's great accomplishment [6,11] to have showed how a $U_A(1)$ -breaking effective quark-quark interaction arises from non-perturbative effects in QCD. It is, however, one more step from this 't Hooft interaction to the empirical ps meson masses, which has not yet been taken in QCD proper, due to the complexities of nonabelian gauge theories. [There is one recent study by the Bonn group *et al.* [12] which investigates this question in a confining chiral model of the Adler-Davis variety [13]. Our results are essentially identical to theirs.] What has been done instead, first by Bernard, Jaffe and Meissner [14], is a calculation in a simplified model where four-quark self-interactions of the Fermi type are substituted for the $U_A(1)$ -invariant (multiple) gluon exchange interactions. This sort of model is more manageable than QCD and goes under the name of Nambu-Jona-Lasinio [8,15,16]. This success has been interpreted as a confirmation of 't Hooft's ideas about $U_A(1)$ breaking [11]. What has been neglected thus far is that this model also predicts, in its three-flavor version, a nonet of scalar mesons, which have not been carefully studied as yet.

We adopt the notation, conventions and most, but not all of the methods of Refs. [15,14]. The one important difference is in the algebraic approach to the construction of the "effective $N_f = 3$ NJL Lagrangian": whereas [15,14] use some intricate and labour-intensive methods, we will use certain identities that make the whole evaluation far more straightforward.

The free Lagrangian and the 18 quartic self-interaction terms are $U(3)_L \times U(3)_R$ sym-

metric

$$\mathcal{L}_{\text{NJL}}^{(6)} = \bar{\psi}[i\partial - m^0]\psi + G \sum_{i=0}^8 [(\bar{\psi}\lambda_i\psi)^2 + (\bar{\psi}i\gamma_5\lambda_i\psi)^2] - K [\det(\bar{\psi}(1 + \gamma_5)\psi) + \det(\bar{\psi}(1 - \gamma_5)\psi)] , \quad (1)$$

but the $U(1)_A$ -breaking determinant interaction term is of sixth order in the fermi fields, rather than of fourth order as in the $N_f = 2$ case. It turns out that substantial algebraic simplification comes about due to certain algebraic identities ("Burgoyne identities") first found in Lévy's work [17] on the three-flavor linear sigma model. Thus we find

$$\begin{aligned} \mathcal{L}_{\text{tH}}^{(6)} &= -K [\det(\bar{\psi}(1 + \gamma_5)\psi) + \det(\bar{\psi}(1 - \gamma_5)\psi)] \\ &= -\frac{K}{6} \left\{ D_{ijk}(\bar{\psi}\lambda_k\psi) [(\bar{\psi}\lambda_i\psi)(\bar{\psi}\lambda_j\psi) - 3(\bar{\psi}i\gamma_5\lambda_i\psi)(\bar{\psi}i\gamma_5\lambda_j\psi)] \right. \\ &\quad \left. + \frac{3}{2}\sqrt{6}(\bar{\psi}\lambda_0\psi) \sum_{i=1}^8 [(\bar{\psi}i\gamma_5\lambda_i\psi)^2 - (\bar{\psi}\lambda_i\psi)^2] + 3\sqrt{6}(\bar{\psi}i\gamma_5\lambda_0\psi) \sum_{i=1}^8 (\bar{\psi}i\gamma_5\lambda_i\psi)(\bar{\psi}\lambda_i\psi) \right\}, \quad (2) \end{aligned}$$

where the summation from 0 to 8 for repeated indices is implied and D_{ijk} are the symmetric Gell-Mann SU(3) structure constants defined by

$$\{\lambda_i, \lambda_j\} = 2D_{ijk}\lambda_k , \quad (3)$$

and extended * to U(3) i.e. the ninth generator $\lambda_0 = \sqrt{\frac{2}{3}}1$ is included,

$$D_{ijk} = \begin{cases} d_{ijk}, & i, j, k \in (1, 2, 3, \dots, 8) \\ \sqrt{\frac{2}{3}}\delta_{jk}, & i = 0, j, k \in (0, 1, 2, \dots, 8) \end{cases} . \quad (4)$$

This Lagrangian does not lead to a perturbatively renormalizable field theory, so one must introduce a momentum cut-off Λ . According to Diakonov and Petrov [18], however, this cutoff has a natural explanation in terms of instanton size within 't Hooft's QCD derivation [6] and ought to be around 1 GeV, where indeed it has traditionally been in the NJL model.

One of the most important features of the NJL model is the chiral symmetry and its spontaneous breakdown induced by its own dynamics. It is therefore essential to have an approximate solution that preserves this symmetry. The original nonperturbative approximation scheme introduced by Nambu and Jona-Lasinio does exactly that; it is called the self-consistent Hartree + Random Phase Approximation (RPA).

One cannot work directly with the sixth-order operator Eq. (2) in NJL. So, we proceed to construct an "effective mean-field quartic 't Hooft self-interaction Lagrangian" using Eq.(2) and following instructions in Refs. [15,14]. This leads to consistent chiral dynamics. We find in the SU(3)-symmetric limit ($\langle\bar{\psi}\lambda_0\psi\rangle = \sqrt{\frac{2}{3}}\langle\bar{\psi}\psi\rangle \neq 0$; $\langle\bar{\psi}\lambda_3\psi\rangle = \langle\bar{\psi}\lambda_8\psi\rangle = 0$) the following effective Lagrangian

*Our definition of D_{ijk} Eq. (4) agrees with that of d_{ijk} in Eq. (12.a.4) of B.W. Lee [19].

$$\begin{aligned}
\mathcal{L}_{\text{tH}}^{(4)} = & -\frac{K}{2} \langle \bar{\psi} \lambda_0 \psi \rangle \left\{ \sqrt{\frac{2}{3}} \left[(\bar{\psi} \lambda_0 \psi)^2 - (\bar{\psi} i \gamma_5 \lambda_0 \psi)^2 \right] \right. \\
& + \sum_{i,j=1}^8 D_{ij0} \left[(\bar{\psi} \lambda_i \psi)(\bar{\psi} \lambda_j \psi) - (\bar{\psi} i \gamma_5 \lambda_i \psi)(\bar{\psi} i \gamma_5 \lambda_j \psi) \right] \\
& \left. + \frac{1}{2} \sqrt{6} \sum_{i=1}^8 \left[(\bar{\psi} i \gamma_5 \lambda_i \psi)^2 - (\bar{\psi} \lambda_i \psi)^2 \right] \right\}. \quad (5)
\end{aligned}$$

Simplify this further using Eq.(4)

$$\begin{aligned}
\mathcal{L}_{\text{tH}}^{(4)} = & -\frac{K}{2\sqrt{6}} \langle \bar{\psi} \lambda_0 \psi \rangle \left\{ 2 \left[(\bar{\psi} \lambda_0 \psi)^2 - (\bar{\psi} i \gamma_5 \lambda_0 \psi)^2 \right] \right. \\
& \left. + \sum_{i=1}^8 \left[(\bar{\psi} i \gamma_5 \lambda_i \psi)^2 - (\bar{\psi} \lambda_i \psi)^2 \right] \right\}. \quad (6)
\end{aligned}$$

and then insert the result Eq. (6) into Eq. (1) to find

$$\begin{aligned}
\mathcal{L}_{\text{eff}}^{(4)} = & \bar{\psi} [i \not{\partial} - m^0] \psi + \left[K_0^{(-)} (\bar{\psi} \lambda_0 \psi)^2 + \sum_{i=1}^8 K_i^{(+)} (\bar{\psi} i \gamma_5 \lambda_i \psi)^2 \right] \\
& + \left[K_0^{(+)} (\bar{\psi} i \gamma_5 \lambda_0 \psi)^2 + \sum_{i=1}^8 K_i^{(-)} (\bar{\psi} \lambda_i \psi)^2 \right], \quad (7)
\end{aligned}$$

where

$$K_0^{(\pm)} = G \pm K \langle \bar{q} q \rangle = \frac{1}{2} (G_1 \mp 2G_2) \quad (8a)$$

$$K_i^{(\pm)} = G \mp \frac{1}{2} K \langle \bar{q} q \rangle = \frac{1}{2} (G_1 \pm G_2), \quad i = 1, \dots, 8, \quad (8b)$$

i.e.,

$$G_1 = 2G \quad (9a)$$

$$G_2 = -\frac{1}{3} K \langle \bar{\psi} \psi \rangle = -K \langle \bar{q} q \rangle, \quad (9b)$$

where we defined the quark condensate(s) as follows

$$\langle \bar{q} q \rangle = -i N_C \text{tr} S_F(x, x)^q = -4i N_C \int \frac{d^4 p}{(2\pi)^4} \frac{m_q}{p^2 - m_q^2 + i\epsilon}, \quad q = u, d, s; \quad (10a)$$

$$\langle \bar{\psi} \psi \rangle = \langle \bar{u} u \rangle + \langle \bar{d} d \rangle + \langle \bar{s} s \rangle = -i N_C \text{tr} S_F(x, x). \quad (10b)$$

Eq. (7) is nothing but Klevansky's "effective Lagrangian" Eq. (4.39) in the exact SU(3), or the chiral limit [15]. There is one important *caveat*, though, which has not been properly emphasized in the literature: when used in the SU(3) gap equations

$$m_u = m_u^0 - 4G \langle \bar{u} u \rangle + 2K \langle \bar{d} d \rangle \langle \bar{s} s \rangle \quad (11a)$$

$$m_d = m_d^0 - 4G \langle \bar{d} d \rangle + 2K \langle \bar{u} u \rangle \langle \bar{s} s \rangle \quad (11b)$$

$$m_s = m_s^0 - 4G \langle \bar{s} s \rangle + 2K \langle \bar{d} d \rangle \langle \bar{u} u \rangle \quad (11c)$$

depicted in Fig. 2, the diagram Fig. 2b associated with the Lagrangian Eq. (7) carries a symmetry number (factor) 1/2 whenever the quarks in the the two closed loops are of the *same flavor*, i.e., when they are identical [20]. The reader will easily convince himself that only in that way does the effective Lagrangian Eq. (7) preserve the Goldstone theorem. Now we can use Eq.(7) to derive meson masses.

The meson masses are read off from the poles of their propagators, which in turn are constrained by the gap Eq. (11a-c). The following relations between the meson masses arise

$$m_{a_0}^2 = m_\pi^2 + 4m^2 + \frac{2}{3}m_{\text{tH}}^2(N_f = 3) \quad (12a)$$

$$m_{K_0^*}^2 = m_K^2 + 4m^2 + \frac{2}{3}m_{\text{tH}}^2(N_f = 3) \quad (12b)$$

$$m_{f_0}^2 + m_{f_0'}^2 = m_\eta^2 + m_{\eta'}^2 + 8m^2 - \frac{2}{3}m_{\text{tH}}^2(N_f = 3) \quad (12c)$$

$$m_{f_0}^2 + m_{f_0'}^2 = m_{K_0^{*+}}^2 + m_{K_0^{*0}}^2 - m_{\text{tH}}^2(N_f = 3) \quad (12d)$$

$$m_\eta^2 + m_{\eta'}^2 = m_{K^+}^2 + m_{K^0}^2 + m_{\text{tH}}^2(N_f = 3), \quad (12e)$$

where, to leading order in N_C

$$m_{\text{tH}}^2(N_f = 3) = \left(\frac{3g_{\pi qq}^2 G_2}{G_1^2} \right) + \mathcal{O}(1/N_C^2). \quad (13)$$

Eqs. (12d,e) lead immediately to the *new sum rule*

$$m_\eta^2 + m_{\eta'}^2 - m_{K^+}^2 - m_{K^0}^2 = m_{K_0^{*+}}^2 + m_{K_0^{*0}}^2 - m_{f_0}^2 - m_{f_0'}^2. \quad (14)$$

This sum rule is the main result of this work. It shows that the primary effect of $U_A(1)$ breaking in the three-flavor NJL model is to produce an equal in size ($m_{\text{tH}}^2(N_f = 3)$) but opposite in sign mass-squared splitting between the octet and the singlet for the scalar and the pseudoscalar mesons.

Eq. (14) is: (a) a new consequence of $U_A(1)$ breaking in this NJL model; (b) invariant under the mixing of scalar and/or pseudoscalar isoscalar mesons; (c) correctly including *linear* $SU(3)$ symmetry breaking terms; (d) broken by $\mathcal{O}(\alpha)$ EM interaction effects; (e) an exact, albeit trivial identity ("0=0") in the large- N_C limit; the left-hand side of the sum rule, i.e., the ps meson mass relations, agrees with Veneziano's large- N_C limit result in QCD [21]. This does *not* imply that the sum rule necessarily also holds in QCD. That question is still open at the moment.

That point (b) is true can be seen from the fact that only the mixing-invariant combinations $m_{f_0}^2 + m_{f_0'}^2$ and $m_{f_0}^2 + m_{f_0'}^2$ enter the sum rule. The cancelation of the linear non-chiral corrections (point (c)) to the chiral version of the sum rule follows from the validity of the Gell-Mann-Oakes-Renner (GMOR) relations [3] for the pseudoscalar mesons in the NJL model [15] and the $SU(3)$ breaking relations for the scalar mesons discussed in Sec. II. Point (d) is a consequence of the fact that the EM interactions were ignored in the derivation of Eqs. (12a-e). In particular, we expect the EM splitting between the charged and neutral kaons to be different for the scalar and the ps mesons. Finally, to see that point (e) is correct, recall [16] that $K \sim \mathcal{O}(1/N_C^3)$ in the large N_C limit. Hence $G_2 \sim \mathcal{O}(1/N_C^2)$. Now use this together with $G_1 = 2G \sim \mathcal{O}(1/N_C)$ and $g_{\pi qq}^2 \sim \mathcal{O}(1/N_C)$ in Eq. (13) to find $m_{\text{tH}}^2(N_f = 3) \sim \mathcal{O}(1/N_C)$. This means that both sides

of the sum rule vanish in the large N_C limit. In that limit we recover the $U_A(1)$ symmetry and our sum rule is an $SU(3)$ -breaking formula (identity), *i.e.* a consequence of points (b) and (c); Veneziano's result is a corollary of the above argument (e). Note that the above meson masses coincide with those derived by Lévy [17] in the three-flavor linear sigma model with the second quartic coupling ρ set to zero $\rho = 0$. Thus we have found $\rho = 0$ to $\mathcal{O}(1/N_C^2)$, which is consistent with the large- N_C QCD result $\rho/\lambda \sim \mathcal{O}(1/N_C)$ [22]. We emphasize that our result is consistent with, but not necessarily required by QCD.

In view of the changes in the spectrum of scalar meson masses discussed in the introduction, and the uncertainties related therewith, we are not able to provide definitive answers to a number of important questions. Nevertheless we shall write down formulas for various observables that can be used when the experimental situation settles down. Two sets of observables will be used in this paper: (i) meson masses, and (ii) their decay widths and branching ratios.

The primary effect of the $U_A(1)$ breaking interaction in the three-flavor model is to produce a mass-squared splitting of $m_{\text{tH}}^2(N_f = 3)$ between the members of the octet and the singlet according to the sum rule Eq.(14). We already know the masses of all the pseudoscalar mesons fixing the left-hand side (lhs) of the sum rule as $m_{\text{tH}}^2(N_f = 3) = 0.72 \text{ GeV}^2 = (855 \text{ MeV})^2$, as well as the mass of the scalar "kaon" $K_0^*(1430)$.

To check the above relation we need the masses of the two isoscalar scalar states f_0, f_0' . The masses of these two mesons are bounded from below and from above, by the octet and the singlet mass, according to the Gell-Mann–Okubo relations for the octet and the singlet masses. The scalar mixing angle θ_s is then determined from one of the following two equations

$$m_{88}^2(s) = m_{f_0}^2 \cos^2 \theta_s + m_{f_0'}^2 \sin^2 \theta_s \quad (15a)$$

$$m_{00}^2(s) = m_{f_0}^2 \sin^2 \theta_s + m_{f_0'}^2 \cos^2 \theta_s. \quad (15b)$$

If the mass of the octet member f_0 is taken, following the introduction, as 1500 MeV, we see that it is consistent with the constraint imposed by Eq. (15a): $m_{88} = 1.47 \text{ GeV} \leq m_{f_0} = 1.50 \text{ GeV}$. The remaining question is: what is the mass of the singlet? The answer is given by our sum rule Eq. (14) as $m_{f_0'} = 1030 \text{ MeV}$. This is also in agreement with the constraint imposed by Eq. (15b): $m_{00} = 1.1 \text{ GeV} \geq m_{f_0'} = 1.03 \text{ GeV}$. The resulting scalar meson mass splittings are shown in Fig. 3.

There are two serious candidates for this state in the PDG 96 tables: $f_0(980)$ and $f_0(1300) = f_0(\epsilon(1000))$, where the earlier *caveats* (see Ref. [7]) with regard to the mass of the latter have to be repeated now. Therefore the masses of these two resonances may be considered as roughly equal. Note that the first of these is the early candidate $f_0(980)$. The question which one of these two resonances is the true singlet state ought to be decided on the basis of their decay properties.

The dominant decay mode of both of these states ($f_0(980), f_0(\epsilon(1000))$) is the two-pion one. Now we use our theory to calculate the decay rate of the isoscalar scalar meson (f_0) into two pions. We do so in the first Born approximation, *i.e.*, without final-state rescattering corrections, and find the familiar result

$$\Gamma_{f_0 \rightarrow \pi\pi} = \frac{3g_{f_0\pi\pi}^2}{8\pi m_{f_0}} \sqrt{1 - \frac{4m_\pi^2}{m_{f_0}^2}}, \quad (16)$$

where $g_{f_0\pi\pi}$ is the strength of the $f_0\pi\pi$ meson coupling constant and f_0 stands generically for one of the scalar isoscalar states f_0, f'_0 . The mixing angle is subject to the uncertainty in the a_0 mass, which according to the latest PDG96 is now 1450 MeV, i.e., it exceeds the scalar "kaon" mass and thus violates the notion of octet breaking of SU(3), and on the precise value of the f'_0 mass, which is not available as yet. Consequently, we must postpone detailed comparison until such time arrives when these quantities are better known. We are not prevented from making order of magnitude estimates, however.

With Eqs. (16) and (15a,b) one readily calculates the branching ratios for the f_0 decays into ps meson pairs $\Gamma_{\sigma \rightarrow \pi\pi} \simeq 1.3 - 2$ GeV. This is still an order of magnitude larger than the quoted width $\Gamma_{\sigma \rightarrow \pi\pi} \simeq 150 - 400$ MeV, according to PDG94 [4] and PDG96 [5], but at least in qualitative agreement with Morgan and Pennington's estimate of $\Gamma_{\sigma \rightarrow \pi\pi} \simeq 700$ MeV [23] and Törnqvist and Roos' [24] value of $\Gamma_{\sigma \rightarrow \pi\pi} \simeq 880$ MeV.

At this point one may raise the objection that we are taking a simple model calculation too seriously: confinement effects that are neglected in this model might modify the sum rule. This need not be so, the evidence being the recent calculation by the Bonn group *et al.* [12]. They constructed and solved a relativistic chiral model including confinement and the 't Hooft interaction. They find that the scalar meson masses in their complete SU(3) model agree with our sum rule quite well.

Although it is well known that meson-meson interactions can be very important in analyses of scalar mesons [23], we have omitted all such effects here and have concentrated on the Hartree + RPA meson masses and couplings instead. The reasons for that are of two kinds: (i) the Hartree + RPA results are the starting point on which all higher-order corrections are to be built, and (ii) it is not completely clear which method to employ in such a calculation. Meson cloud effects constitute $1/N_C$ corrections in the NJL model, the exploration of which has only recently begun [25]. These $1/N_C$ corrections have to obey the same chiral symmetry as the Hartree + RPA results [25], however, so that the symmetry-induced predictions of the model ought to be robust. Conversely, the Hartree + RPA approximation predictions of this model that are *not* direct consequences of the underlying symmetries ought to be taken *cum grano salis*.

Last, not least, we have found an answer to the old question: why does the strange quark sometimes behave as if it were light and sometimes as if it were heavy?. The answer, of course, lies in identifying the relevant mass scale with which the comparison is to be made. We will see that that mass scale is the 't Hooft mass (855 MeV) which is manifestly heavier than the light (u,d) quarks, lighter than the heavy (c,b) quarks and comparable with the (constituent) strange quark mass. One indication of the severity of flavor symmetry breaking is the proximity of the mixing angle to the ideal 35.3° : the harder the breaking, the closer the mixing angle to the ideal one. In the vector meson channel, where there are no $U_A(1)$ -breaking effects to speak of, the mixing angle is *de facto* the ideal one, even though the mass difference between the ω and ϕ mesons is smaller than that between the η and η' ps mesons which are *not* ideally mixed. A similar situation holds for scalar mesons. Why is that? The mixing angle formula Eq. (15a), which can be written as

$$\tan 2\theta_s = \frac{(4\sqrt{2}/3) \Delta_s^2}{m_{88}^2(s) - m_{00}^2(s) + (2/3) \Delta_s^2}, \quad (17)$$

where

$$\Delta_s^2 = m_{K_0^*}^2 - m_{a_0}^2 \quad (18a)$$

$$m_{88}^2(s) - m_{00}^2(s) = m_{tH}^2 \quad (18b)$$

provides the answer: to achieve ideal mixing the right-hand side of Eq. (17) has to approach $2\sqrt{2}$. In the vector meson channel $m_{00}(v) = m_{88}(v)$ and this condition is immediately met; whereas in the ps and s channels $m_{00}(ps) \neq m_{88}(ps)$, $m_{00}(s) \neq m_{88}(s)$ respectively. In order to achieve ideal mixing the absolute value of the $s - u$, or $s - d$ quark mass difference would have to exceed the absolute value of the $m_{00} - m_{88}$ mass difference, which in our model equals the 't Hooft mass (855 MeV) in both the scalar and the pseudoscalar channel. That, however, is not the case in Nature, with $m_s - m_{u,d} \simeq 150\text{MeV}$ substantially lighter than 855 MeV. This argument also tells us why the charmed quark belongs to the class of heavy quarks, as advertised above: because $m_c - m_{u,d} \simeq 1.5\text{ GeV}$ is substantially heavier than 855 MeV.

In summary, we have investigated the scalar meson mass spectrum in the two- and the three flavor versions of the NJL model. We found a number of relations between scalar and pseudoscalar masses leading to a new sum rule relating the mass splitting between the scalar singlet and octet on the one hand and the pseudoscalar singlet and octet on the other. This sum rule is a consequence of explicit $U_A(1)$ breaking in our model. We compare our predictions with the experiment and find that states $f_0(1500)$ and $f_0(\epsilon(1000))$ fit the sum rule. If correct, this would be a strong indication of $U_A(1)$ breaking at work among scalar mesons, for it more than doubles the originally expected mass splitting between these two states. We have also shown that $a_0(980)$ *cannot* be a member of the scalar $q\bar{q}$ meson octet irrespective of its decay properties, the "true" isovector scalar mesons being more likely to lie around 1300 MeV. The $f_0(980)$ is highly unlikely a member of the scalar $q\bar{q}$ meson octet due to its decay properties which are incompatible with a simple $q\bar{q}$ state.

In conclusion, we have shown that the $U_A(1)$ symmetry breaking plays an important role in the scalar meson spectrum of the NJL model and that this may be in accord with experimental evidence. This issue is by no means closed, rather it seems to deserve further study, both theoretical and experimental.

- [1] J.J.J. Kokkedee, *The Quark Model*, (W.A. Benjamin, New York, 1969).
- [2] F. E. Close, *An Introduction to Quarks and Partons*, (Academic Press, London, 1979).
- [3] M. Gell-Mann, R. Oakes, and B. Renner, *Phys. Rev.* **175**, 2195 (1968).
- [4] Particle Data Group, L. Montanet *et al.*, *Phys. Rev. D* **50**, 1173 (1994).
- [5] Particle Data Group, R. M. Barnett *et al.*, *Phys. Rev. D* **54**, 1 (1996).
- [6] G. 't Hooft, *Phys. Rev. D* **14**, 3432 (1976), (E) *ibid.* **18**, 2199 (1978).
- [7] M. R. Pennington, p. 36 in *Two-photon physics: From DAΦNE to LEP200 and beyond*, eds. F. Kapusta and J. Parisi, World Scientific, Singapore (1995).
- [8] Y. Nambu, *Phys. Rev. Lett.* **4**, 380 (1960), and Y. Nambu and G. Jona-Lasinio, *Phys. Rev.* **122**, 345 (1961); *Phys. Rev.* **124**, 246 (1961).
- [9] Y. Nambu, p. 391 - 456 in *Symmetry Principles and Fundamental Particles*, (W.H. Freeman and Co., San Francisco, 1967).
- [10] S. Weinberg, *Phys. Rev. D* **11**, 3583 (1975).

- [11] G. 't Hooft, Phys. Rep. **142**, 357 (1986).
- [12] E. Klempt, B. C. Metsch, C. R. Münz and H. R. Petry, Phys. Lett. **B 361**, 160 (1995).
- [13] S. L. Adler and A. C. Davis, Nucl. Phys. **B224**, 469 (1984).
- [14] V. Bernard, R.L. Jaffe and U.-G. Meissner, Nucl. Phys. **B308**, 753 (1988).
- [15] S. P. Klevansky, Rev. Mod. Phys. **64**, 649 (1992).
- [16] T. Hatsuda and T. Kunihiro, Phys. Rep. **247**, 221-367 (1995).
- [17] M. Lévy, Nuov. Cim. **52 A**, 23 (1967).
- [18] D. Diakonov and V. Petrov, in *Quark Cluster Dynamics: Proceedings, Bad Honnef*, eds. K. Goeke, P. Kroll, and H.-R. Petry, Springer, New York (1992).
- [19] B. W. Lee, *Chiral Dynamics*, (Gordon and Breach, New York, 1972).
- [20] C. Itzykson and J.B. Zuber, *Quantum Field Theory*, (McGraw-Hill, New York, 1980).
- [21] G. Veneziano, Nucl. Phys. **B159**, 213 (1979).
- [22] S. Coleman, E. Witten, Phys. Rev. Lett. **45**, 100 (1980).
- [23] D. Morgan and M. R. Pennington, Phys. Rev. D **48**, 1185 (1993).
- [24] N. A. Törnqvist and M. Roos, Phys. Rev. Lett. **76**, 1575 (1996).
- [25] V. Dmitrašinović, R. H. Lemmer, H. J. Schulze and R. Tegen, Ann. Phys. (N.Y.) **238**, 332 (1995).

FIGURES

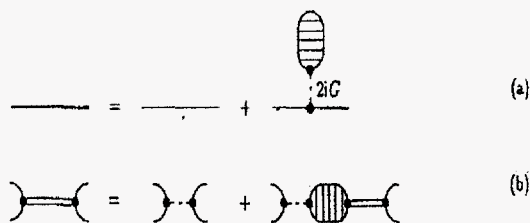


FIG. 1. The Schwinger-Dyson equations defining our approximation: the gap equation (a), and the two-body Bethe-Salpeter equation (b). The dashed line in (a) and (b) denotes a four-fermion vertex $2iG$ of the NJL type; the double line in (b) represents a pion or a sigma meson, and the dashed bubbles represent the quark self-energy (a) or the meson polarization function (b).

Higgs mechanism in a non-perturbative approximation to the scalar ϕ^4 theory coupled to a gauge field, V. Dmitrašinović

In this work we extend the Gaussian functional, or the Hartree + RPA method to the case of an Abelian gauge theory with spontaneous symmetry breaking. In particular, we present the proof of gauge invariance of the Higgs mechanism [1-3] for an Abelian gauge field coupled to an $O(2)$ symmetric bosonic sector of the linear sigma model (the "Higgs model" [1]) within the Gaussian approximation [4].

We will be closest to following the Englert-Brout proof [2] which, in turn, relies heavily on Schwinger's ideas [5]. The Higgs theorem is verified, within the Englert-Brout approach [2], by displaying a zero-mass pole, due to the propagation of the Goldstone boson, in the vacuum polarization tensor. This singularity, in turn, induces a gauge-invariant nonzero-mass pole in the gauge boson two-point Green function.

An essential assumption of the Englert-Brout proof is the validity of the Goldstone theorem, *i.e.*, the existence of massless Goldstone bosons, in the un-gauged theory. We have shown in Ref. [6] that the Hartree + RPA approximation satisfies the Goldstone theorem for $N = 2$ (extension to any finite N is straightforward), albeit in an unexpected way: the Goldstone bosons are composite states of the "elementary" scalar fields. This idiosyncrasy of the present approximation makes the proof of the Higgs mechanism a non-trivial affair. We construct a gauge invariant vacuum polarization tensor within the Hartree + RPA approximation and display a zero-mass pole in it.

We confine ourselves to an $O(2)$ symmetric, *i.e.*, an Abelian theory for the sake of simplicity. The Lagrangian density of the un-gauged theory is given by

$$\mathcal{L} = \frac{1}{2} (\partial_\mu \vec{\phi})^2 - V(\vec{\phi}^2). \quad (1)$$

where

$$\vec{\phi} = (\phi_1, \phi_2),$$

is a column vector and

$$V(\vec{\phi}^2) = -\frac{1}{2} m_0^2 \vec{\phi}^2 + \frac{\lambda_0}{4} (\vec{\phi}^2)^2.$$

We assume here λ_0 and m_0^2 are positive which ensures spontaneous symmetry breaking at the tree level. Then we introduce the gauge field A_μ via minimal substitution into the above Lagrangian Eq. (1)

$$\mathcal{L} = (D_\mu \phi)^* (D^\mu \phi) - V(\phi^* \phi) - \frac{1}{4} F_{\mu\nu}^2. \quad (2)$$

where we have introduced a new charged scalar field ϕ and the covariant derivative D_μ in this way

$$\phi = \frac{1}{\sqrt{2}} (\phi_1 + i\phi_2); \quad D_\mu = \partial_\mu - ieA_\mu,$$

and

$$V(\phi^* \phi) = -m_0^2 (\phi^* \phi) + \lambda_0 (\phi^* \phi)^2.$$

We will work in a class of covariant gauges parameterized by a "gauge parameter" ξ . That amounts to adding the gauge-fixing term

$$\mathcal{L}_{\text{gauge fixing}} = -\frac{1}{2}\xi (\partial_\mu A^\mu)^2, \quad (3)$$

to the lagrangian Eq. (2) and consequently having

$$D^{\mu\nu}(q) = -\frac{1}{q^2} \left[g^{\mu\nu} - \left(1 - \frac{1}{\xi}\right) \frac{q^\mu q^\nu}{q^2} \right], \quad (4)$$

as the bare "photon" propagator. This propagator is dressed by vacuum polarization correction parameterized by the gauge invariant tensor

$$\pi^{\mu\nu}(q) = [q^2 g^{\mu\nu} - q^\mu q^\nu] \pi(q), \quad (5)$$

according to the Schwinger-Dyson equation

$$D^{\mu\nu}(q) = D^{\mu\nu}(q) + D^{\mu\lambda}(q) \pi_{\lambda\sigma}(q) D^{\sigma\nu}(q). \quad (6)$$

The solution to this SDE reads as follows,

$$D^{\mu\nu}(q) = -\frac{1}{q^2} \left[\left(g^{\mu\nu} - \frac{q^\mu q^\nu}{q^2} \right) \frac{1}{1 + \pi(q)} + \frac{1}{\xi} \frac{q^\mu q^\nu}{q^2} \right]. \quad (7)$$

Schwinger [5] observed that when the vacuum polarization $\pi(q^2)$ has a simple pole at $q^2 = 0$, it dresses the photon propagator in such a way that the gauge boson attains a *finite gauge-invariant dressed mass* determined by the residue at the pole. That is indeed the case in the first Born approximation to the present theory, since

$$q^2 (1 + \pi(q)) = q^2 \left(1 - \frac{e^2 v_0^2}{q^2} \right) = q^2 - e^2 v_0^2 = q^2 - M_V^2, \quad (8)$$

where $v_0^2 = m_0^2/\lambda_0$, as Englert and Brout first showed in Ref. [2]. That proof has been extended to arbitrary order of perturbation theory by 't Hooft, Veltman, Lee and Zinn-Justin (see the review by Abers and Lee [7]). We will now extend this argument to a new approximation that sums infinite classes of Feynman diagrams, *i.e.*, that goes beyond perturbation theory.

It was shown in Ref. [6] that the Hartree + RPA/Gaussian approximation to theories with spontaneous symmetry breaking can be formulated as a specific truncation of the exact Schwinger-Dyson equations [8] for the *connected, but one-particle reducible* (OPR) two- and four-point Green functions. These SD Eqs allow a simple diagrammatic representations and that is the route that we follow. The first set of such ("vacuum") SD equations read

$$m_0^2 = \lambda_0 [\langle \phi_1^2 \rangle + 3\hbar I_0(m_1) + \hbar I_0(m_2)] \quad (9a)$$

$$\langle \phi_2 \rangle = 0. \quad (9b)$$

where

$$I_0(m_i) = \frac{1}{2} \int \frac{d\mathbf{k}}{(2\pi)^3} \frac{1}{\sqrt{\mathbf{k}^2 + m_i^2}} = i \int \frac{d^4 k}{(2\pi)^4} \frac{1}{k^2 - m_i^2 + i\epsilon} = G_{ii}(\mathbf{x}, \mathbf{x}). \quad (10)$$

The divergent integral $I_0(m_i)$ is understood to be regularized via an UV momentum cut-off. Eqs. (9b) are identified as a truncated SD equation [8] for the one-point Green function (the scalar field v.e.v.) depicted in Fig. 1. of Ref. [6] with correct symmetry numbers of contributing Feynman diagrams automatically included. As in the ordinary perturbative treatment of the linear sigma model, we associate the nonvanishing v.e.v. with the "sigma meson" field, and the second field will be called the "pion". One also has the following two "gap" equations

$$m_1^2 = 2\lambda_0 \langle \phi_1^2 \rangle = 2 \left[m_0^2 - \lambda_0 \hbar (3I_0(m_1) + I_0(m_2)) \right] \quad (11a)$$

$$m_2^2 = 2\lambda_0 \hbar (I_0(m_2) - I_0(m_1)) \quad (11b)$$

The system of Eqs. (11a,b) admits only massive solutions $m_1 > m_2 > 0$ for real, positive values of m_0^2, λ_0 and a finite ultraviolet cut-off of the momentum integrals $I_{0,1}(m_i)$. We see that at the tree level, $\mathcal{O}(\hbar^0)$, the "pion" is massless, but the non-perturbative one-loop corrections, $\mathcal{O}(\hbar)$, give it a finite mass.

We have shown in Ref. [6] that this does not prove the breakdown of the $O(2)$ symmetry of this approximation. Indeed, we have shown that the Goldstone particle appears as a pole in the *two-particle propagator*, i.e., it is a composite (bound) state of the two distinct massive elementary excitations in the theory. That was proven in terms of the four-point SD or, equivalently, the Bethe-Salpeter equation for the four-point Green function $M(s)$

$$\begin{aligned} -2iM(s) &= -2i\lambda_0 \left[1 + (-2i\lambda_0 v^2) \left(\frac{i}{s - m_2^2} \right) \right] - 2iM(s)\Pi(s) \\ &= -2i\lambda_0 \left[1 + \frac{m_1^2}{s - m_2^2} \right] - 2iM(s)\Pi(s) \end{aligned} \quad (12)$$

with the geometric series solution

$$M(s) = \left[1 + \frac{m_1^2}{s - m_2^2} \right] \frac{\lambda_0}{1 - \Pi(s)} \quad (13)$$

where $s = (p_1 + p_2)^2 \equiv P^2$ is the total center-of-mass (CM) energy. A massless composite (bound) state in the s -channel manifests itself by a pole at $s = 0$. The kernel ("polarization function") $\Pi(s)$ reads

$$\Pi(s) = 2\lambda_0 \left[1 + \frac{m_1^2}{s - m_2^2} \right] \hbar I_{12}(s) \quad , \quad (14)$$

where

$$I_{12}(s) = i \int \frac{d^4 k}{(2\pi)^4} \frac{1}{[k^2 - m_1^2 + i\varepsilon] [(k - P)^2 - m_2^2 + i\varepsilon]} .$$

It was demonstrated in Ref. [6] that $\Pi(0) = 1$, or equivalently that a zero mass pole is present in the two-particle scattering amplitude (13). This composite state plays the role of the "ordinary" Goldstone boson in the conservation of the (axial) Noether current, depicted in Fig. (1),

$$J_{\mu 5}(p', p) = i(p' + p)_\mu + iq_\mu \left(\frac{m_1^2}{q^2 - m_2^2} \right) - 2i\Gamma_{\mu 5}(q)M(q^2) \quad , \quad (15)$$

where $q_\mu = (p' - p)_\mu$. It was shown in Ref. [6] that this current satisfies the Ward identity [9]

$$q^\mu J_{\mu 5}(p', p) = i \left[D_{\phi_2}^{-1}(p') - D_{\phi_1}^{-1}(p) \right], \quad (16)$$

where

$$D_{\phi_i}^{-1}(p) = p^2 - m_i^2; \quad q^\mu = (p' - p)^\mu.$$

The axial current (15) plays an important role in the vacuum polarization tensor $\pi_{\mu\nu}$, so we evaluate it next. Insert the vertex $\Gamma_{\mu 5}(q)$ defined in Ref. [6], together with the two-body propagator $-2iM(q^2)$ (13) into Eq. (15) to find

$$-iJ_{\mu 5}(p', p) = (p' + p)_\mu + q_\mu \left(\frac{m_1^2 - m_2^2}{q^2} \right). \quad (17)$$

Next we explicitly show how the Higgs mechanism works in the Gaussian approximation to the scalar problem. The gauge-invariant polarization tensor $\pi^{\mu\nu}(q)$, depicted in Fig. (2),

$$\begin{aligned} \pi_{\mu\nu}(q) = & -e^2 v^2 \left[g_{\mu\nu} - \frac{q_\mu q_\nu}{q^2 - m_2^2} \right] \\ & - e^2 i \hbar g_{\mu\nu} \hbar \int \frac{d^4 k}{(2\pi)^4} \left[\frac{1}{[k^2 - m_1^2 + i\varepsilon]} + \frac{1}{[(k+q)^2 - m_2^2 + i\varepsilon]} \right] \\ & + e^2 i \hbar \int \frac{d^4 k}{(2\pi)^4} \frac{1}{[k^2 - m_1^2 + i\varepsilon][(k+q)^2 - m_2^2 + i\varepsilon]} \\ & \times \left[(2k+q)_\mu + q_\mu \frac{m_1^2}{q^2 - m_2^2} \right] \left[(2k+q)_\nu + q_\nu \frac{m_1^2}{q^2 - m_2^2} \right] \\ & + e^2 \Gamma_{\mu 5}(q) (2M(q^2)) \Gamma_{\nu 5}(q). \end{aligned} \quad (18)$$

It is manifest that this is indeed a symmetric tensor. It can be rewritten in a less symmetric but perhaps more useful form for the proof of gauge invariance and subsequent evaluation. That is accomplished by employing Eq. (17) to find

$$\begin{aligned} \pi_{\mu\nu}(q) = & -e^2 v^2 \left[g_{\mu\nu} - \frac{q_\mu q_\nu}{q^2 - m_2^2} \right] \\ & - e^2 i \hbar g_{\mu\nu} \hbar \int \frac{d^4 k}{(2\pi)^4} \left[\frac{1}{[k^2 - m_1^2 + i\varepsilon]} + \frac{1}{[(k+q)^2 - m_2^2 + i\varepsilon]} \right] \\ & + e^2 \hbar \int \frac{d^4 k}{(2\pi)^4} \frac{J_{\mu 5}(k+q, k)}{[k^2 - m_1^2 + i\varepsilon][(k+q)^2 - m_2^2 + i\varepsilon]} \left[(2k+q)_\nu - q_\nu \frac{m_1^2}{q^2 - m_2^2} \right]. \end{aligned} \quad (19)$$

Manifestly, one could have written an analogous formula with the index ν singled out in this way instead of μ . In this form the check of gauge invariance is somewhat simpler: contract Eq. (19) with q^μ and use the Ward identity (16) to find

$$\begin{aligned} q^\mu \pi_{\mu\nu}(q) = & -q_\nu e^2 \left\{ v^2 \left[1 - \frac{q^2}{q^2 - m_2^2} \right] + \hbar [I_0(m_1) + I_0(m_2)] \right\} \\ & + e^2 \hbar i \int \frac{d^4 k}{(2\pi)^4} \frac{[(k+q)^2 - m_2^2 - k^2 + m_1^2]}{[k^2 - m_1^2 + i\varepsilon][(k+q)^2 - m_2^2 + i\varepsilon]} \left[(2k+q)_\nu - q_\nu \frac{m_1^2}{q^2 - m_2^2} \right] \\ = & -q_\nu e^2 \left[\frac{m_1^2}{2\lambda_0} \left(\frac{-m_2^2}{q^2 - m_2^2} \right) + \left(\frac{m_1^2}{q^2 - m_2^2} \right) \frac{m_2^2}{2\lambda_0} \right] = 0, \end{aligned} \quad (20)$$

which proves the gauge invariance of the vacuum polarization tensor. Next we evaluate the conserved vacuum polarization function $\Pi(q^2)$ in this approximation. Use the identity

$$i \int \frac{d^4 k}{(2\pi)^4} \frac{(2k+q)_\mu}{[k^2 - m_1^2 + i\epsilon][(k+q)^2 - m_2^2 + i\epsilon]} = \frac{q_\mu}{q^2} (m_2^2 - m_1^2) [I_{12}(q^2) - I_{12}(0)] \\ = \frac{q_\mu}{q^2} \left[(m_2^2 - m_1^2) I_{12}(q^2) - \frac{m_2^2}{2\lambda_0} \right], \quad (21)$$

to find

$$\pi_{\mu\nu}(q) = -e^2 \left(g_{\mu\nu} - \frac{q_\mu q_\nu}{q^2} \right) \left[v^2 - (m_1^2 - m_2^2)^2 \hbar \left(\frac{I_{12}(q^2) - I_{12}(0)}{q^2} \right) \right] \\ + (q_\mu q_\nu - g_{\mu\nu} q^2) \pi_{\text{reg}}^{(b)}(q^2). \quad (22)$$

We will not evaluate $\pi_{\text{reg}}^{(b)}(q^2)$ here since it does not affect the gauge boson mass. All we need to know is that it is regular, i.e., finite at $q^2 = 0$. According to Eq. (22) the "photon" acquires the following mass:

$$M_V^2 = e^2 \left[v^2 - (m_1^2 - m_2^2)^2 \hbar \left(\frac{dI_{12}(q)}{dq^2} \right)_{q^2=0} \right], \quad (23a)$$

$$= e^2 \left\{ v^2 - \frac{1}{(4\pi)^2} \left[\frac{(m_1^2 + m_2^2)}{2} - \left(\frac{m_1^2 m_2^2}{m_1^2 - m_2^2} \right) \log \left(\frac{m_1^2}{m_2^2} \right) \right] \right\}, \quad (23b)$$

where $v^2 = \langle \phi_1^2 \rangle$ is the solution to Eq. (11a). Both v^2 and $m_{1,2}^2$ contain infinities (a cut-off dependence) which presumably can be removed by a process of renormalization. Equally well one may keep the cut-off dependence in the integrals $I_{0,12}$ and view the result as an "effective theory" where the cut-off represents the energy scale at which the theory breaks down. Since the Higgs model does not have immediate physical applications, we will not pursue these questions here. We do note, however, that most of our results are *identities* that do not depend on the subsequent renormalization procedure.

Equation (23b) is a sensible non-perturbative result, as can be seen from the fact that it correctly reproduces three important limiting cases: (a) the Born approximation limit $\hbar \rightarrow 0$, wherein $M_V^2 \rightarrow e^2 v_0^2 = e^2 \left(\frac{m_0^2}{\lambda_0} \right)$; (b) the (regularized, but not renormalized) perturbative one-loop approximation limit $m_2 \rightarrow 0$, where $m_1^2 \rightarrow m^2$, and $M_V^2 \rightarrow e^2 \left[v^2 - \frac{1}{(4\pi)^2} \frac{m^2}{2} \right]$; and (c) the symmetric phase limit $m_1^2 \rightarrow m_2^2$, where $v^2 \rightarrow 0$, $M_V^2 \rightarrow 0$. This comparison with well-understood limits indicates how this result differs from the corresponding perturbative results – through the presence of a non-zero mass m_2 of the "Goldstone field" ϕ_2 .

In conclusion, we have shown that the Gaussian functional approximation is a self-consistent non-perturbative approximation to the Abelian gauged linear sigma model that preserves the Higgs mechanism. These results provide a promise of a self-consistent non-perturbative Higgs mechanism in the Standard Model.

[1] P. W. Higgs, Phys. Lett. **12**, 132 (1964) and Phys. Rev. Lett. **13**, 508 (1964).

- [2] F. Englert and R. Brout, Phys. Rev. Lett. **13**, 321 (1964).
- [3] G. S. Guralnik, C. R. Hagen and T. W. B. Kibble, Phys. Rev. Lett. **13**, 585 (1964).
- [4] T. Barnes and G.I. Ghandour, Phys. Rev. D **22**, 924 (1980), see also references in *Variational Calculations in Quantum Field Theory* ed. L. Polley and D.E.L. Pottinger, World Scientific, Singapore (1987).
- [5] J. Schwinger, Phys. Rev. **125**, 397 (1962), *ibid.* **128**, 2425 (1962).
- [6] V. Dmitrašinović, J. A. McNeil and J. Shepard, Z. Phys. C **69**, 359 (1996).
- [7] E. S. Abers and B. W. Lee, *Gauge Theories*, Phys. Reports. **9 C**, 1 - 141 (1973).
- [8] R.J. Rivers, *Path Integral Methods in Quantum Field Theory*, Cambridge University Press, Cambridge (1987).
- [9] B. W. Lee, *Chiral Dynamics*, Gordon and Breach, New York (1972).

FIGURES

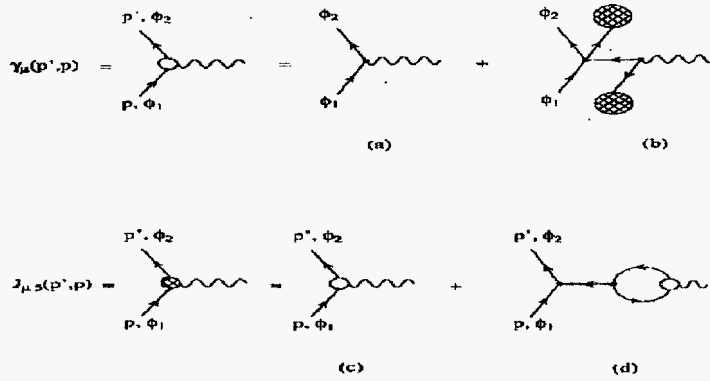


FIG. 1. Feynman diagrams describing the axial current matrix element: the elementary ("convective") current (a), and the m_2 pole term (b). Together these two diagrams define the new axial current vertex γ_μ (empty blob). This new current matrix element enters the definition of the conserved axial current $J_{\mu 5}$ (c and d) (cross-hatched blob). The shaded blob together with the solid line leading to it (the "tadpole") denotes the vacuum expectation value of the ϕ_1 field (*i.e.*, the one-point Green function) and the wiggly lines denote the bare "photons". The dot at the intersection of four solid lines denotes the bare four-point coupling. The double solid line denotes the four-point Green function $-2iM(q^2)$ Eq. (13).

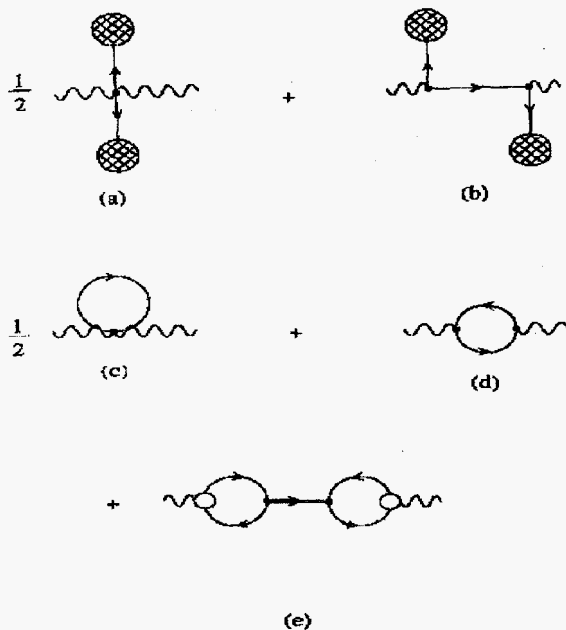


FIG. 2. Feynman diagrams describing the Gaussian approximation to the vacuum polarization tensor: two Born approximation graphs, the sea-gull (a), and the pion-pole diagram (b), the one-loop corrections to the sea-gull graph (c+d), and to the pion-pole diagram (e). Graph (c) stands for two graphs: one for field ϕ_1 in the closed loop, and one for field ϕ_2 . All other symbols are as in Fig. 1. Diagrams are explicitly multiplied by their symmetry numbers.

In this work we discuss to what extent the vector and axial vector spectral densities (ρ^V, ρ^A) generated by the Nambu-Jona-Lasinio [NJL] effective Lagrangian in both its minimal [1] and extended version, containing ρ and A_1 degrees of freedom [2-4], satisfy the celebrated Weinberg sum rules [5]

$$\int_0^\infty \frac{ds}{s} (\rho^V(s) - \rho^A(s)) = f_\pi^2 \quad (1a)$$

$$\int_0^\infty ds (\rho^V(s) - \rho^A(s)) = 0 \quad (1b)$$

In particular we will show that even the spectral densities of the *original* NJL model satisfy the first sum rule exactly, and a modified version of the second sum rule with a non-zero right-hand side equal to $-m\langle\bar{\psi}\psi\rangle$, in exactly the same way as do the spectral densities of the extended model: the presence of explicit vector and axial vector degrees of freedom are not essential for the rules to hold. Here m and $\langle\bar{\psi}\psi\rangle$ are the constituent quark mass and condensate density in the NJL ground state. However, these conclusions only hold under an important proviso: the NJL model as an effective field theory is not fully specified by its Lagrangian density alone – rather the regularization method used must be declared as well. Only certain regularization schemes obey the relevant chiral Ward identities. The above statements thus have to be qualified by the condition that the relevant chiral Ward identities must survive the regularization. This can be accomplished in the present instance by employing the Pauli-Villars [PV] regularization procedure [6].

We emphasize that the spectral weight functions in the original (minimal) NJL model are “slowly varying” with energy and without manifest resonance structures of any kind; yet even they obey the sum rules. The main effect of including interactions between the $\bar{q}q$ pairs in vector channels is to concentrate the vector and axial vector strengths into well-defined peaks, while renormalizing f_π^2 at the same time, such that the Goldberger-Treiman relation continues to hold. We interpret this, perhaps surprising, result as a reflection of the underlying chiral symmetry and its faithful representation by the PV regularization method, even in the high energy regime where one would not, at first sight, expect the NJL model to necessarily lead to sensible results.

The spectral weights can be obtained from the current-current correlators

$$\int d^4x e^{iq \cdot x} \langle 0 | T \{ J_\mu^a(x) J_\nu^b(0) \} | 0 \rangle = -\frac{i}{4} \tilde{\Pi}(q^2) T_{\mu\nu} \delta^{ab} \quad (2)$$

where the dynamics of the quark vector and axial vector currents $J_\mu^a(x) = V_\mu^a(x)$, $A_\mu^a(x)$ of isospin index a are determined by the two-flavor chirally invariant NJL Lagrangian [1,2]

$$\begin{aligned} \mathcal{L}_{\text{NJL}} = & \bar{\psi}[i\not{\partial}]\psi + G_1 [(\bar{\psi}\psi)^2 + (\bar{\psi}i\gamma_5\tau\psi)^2] \\ & - G_2 [(\bar{\psi}\gamma_\mu\tau\psi)^2 + (\bar{\psi}\gamma_\mu\gamma_5\tau\psi)^2]; \end{aligned} \quad (3)$$

G_1 and G_2 are positive coupling constants of dimension $(\text{mass})^{-2}$ which, together with a regulating cutoff Λ that fixes the mass scale, are the model parameters. Both currents are conserved

in the chiral limit as indicated by the transverse tensor $T_{\mu\nu} = (g_{\mu\nu} - q_\mu q_\nu / q^2)$. The effective field theory described by \mathcal{L}_{NJL} in both its minimal ($G_2 = 0$) and extended versions ($G_2 \neq 0$) exhibits spontaneous symmetry breakdown into a nontrivial ground state with constituent quark mass generation and a finite scalar quark condensate. Once the $\tilde{\Pi}(q^2)$ are known, the spectral weights are given by

$$\rho^{V,A}(q^2) = -\frac{1}{4\pi} \text{Im} \tilde{\Pi}^{V,A}(q^2) \quad (4)$$

The $\tilde{\Pi}^{V,A}(q^2)$ are determined by the conserved constituent quark currents of the model to a specified order of approximation. In the ladder approximation [1] these currents are

$$\begin{aligned} V_\mu^a(q^2) &= T_{\mu\nu} \gamma^\nu \frac{\tau^a}{2} F_V(q^2) + \frac{q_\mu q_\nu}{q^2} \gamma^\nu \frac{\tau^a}{2} \\ A_\mu^a(q^2) &= T_{\mu\nu} \gamma^\nu \gamma_5 \frac{\tau^a}{2} G_A(q^2), \end{aligned} \quad (5)$$

where

$$F_V(q^2), G_A(q^2) = \left(1 + 2G_2 \Pi^{V,A}(q^2)\right)^{-1} \quad (6)$$

are vector and axial vector quark form factors. The $\Pi^{V,A}(q^2)$ are the lowest order irreducible vacuum polarization diagrams that appear in Eq. (2). Replacing the bare currents with those given by Eq.(5) at one of the vertices of these diagrams, one includes the effect of interactions to all orders in $\tilde{\Pi}^{V,A}(q^2)$ in the ladder approximation. Then

$$\tilde{\Pi}^{V,A}(q^2) = \Pi^{V,A}(q^2) \left(1 + 2G_2 \Pi^{V,A}(q^2)\right)^{-1} \quad (7)$$

and the resulting spectral weights follow from Eq. (4).

In order to calculate these weights we thus require the Π 's. These polarization diagrams can be expressed in terms of the common loop integral

$$I(q^2) = \int \frac{d^4 p}{(2\pi)^4} \frac{1}{[(p+q)^2 - m^2][p^2 - m^2]} \quad (8)$$

as

$$\begin{aligned} \frac{1}{4} \Pi^V(q^2) &= \frac{2}{3} N_c i \left(2\{m^2[I(q^2) - I(0)]\} + q^2\{I(q^2)\} \right) \\ \frac{1}{4} \Pi^A(q^2) &= \Pi^V(q^2) + f_p^2 F_P(q^2) \end{aligned} \quad (9)$$

where $f_p^2 = -4i N_c m^2 \{I(0)\}$ and $F_P(q^2) = \{I(q^2)\} / \{I(0)\}$ give the pion weak decay constant and electromagnetic form factor of the minimal NJL model to leading order in the number of colors N_c . As stated, PV regularization has been used for all divergent expressions. This is indicated by enclosing the combination to be regulated in curly brackets. The PV-regulated expression for $F_P(q^2)$ then reads

$$F_P(q^2) = 1 - \frac{m^2 N_c}{4\pi^2 f_p^2} \{2\sqrt{f} \coth^{-1} \sqrt{f} - 2\}_{PV} \rightarrow m \langle \bar{\psi} \psi \rangle f_p^{-2} q^{-2} \quad (10)$$

where the asymptotic form for $q^2 \rightarrow \infty$ follows after using the mean field relation [3] $\langle \bar{\psi}\psi \rangle = -(mN_c/2\pi^2)\Sigma_s C_s M_s^2 \log(M_s^2/m^2)$ to introduce the quark condensate density $\langle \bar{\psi}\psi \rangle$. Here $f = 1 - 4m^2/q^2$ and the C_s and M_s^2 are the standard regulating parameters of the PV scheme [6]. From Eqs. (9), $\Pi^V(0) = 0$ and $\Pi^A(0) = f_p^2$ so $F_V(0) = 1$ and $G_A(0) = g_A = (1 + 8G_2 f_p^2)^{-1}$. Thus only the axial current coupling is renormalized by the vector mesons. Write $G_A(q^2) = g_A F_A(q^2)$ so that $F_A(0) = 1$ and identify the renormalized pion weak decay constant as $f_\pi^2 = g_A f_p^2 = f_p^2(1 + 8G_2 f_p^2)^{-1}$. Then, combining Eqs. (4), (6), (7) and (9), one finds

$$\rho^V(q^2) - \rho^A(q^2) = \frac{1}{\pi} \text{Im} \left[f_\pi^2 F_P(q^2) F_V(q^2) F_A(q^2) \right] \quad (11)$$

Both sum rule integrals can be evaluated starting from Eq. (11) by using the analytic properties of the product $f(s) = f_\pi^2 F_P(s) F_V(s) F_A(s)$ with $s = q^2$. To establish the latter note that, apart from the logarithmic branch point at $s = 4m^2$, and further logarithmic branch points at $4M_s^2$ due to their PV regularization, the functions $F_P(s)$, $\Pi_V(s)$ and $\Pi_A(s)$ are all regular on the physical sheet that is cut along the real s-axis from $4m^2$ to ∞ . For $s > 4m^2$, these functions are continued onto the upper lip of the cut in accord with the the Feynman prescription [6]. The form factors $F_V(s)$ and $F_A(s)$ are thus also regular on the physical sheet, apart from possible real poles * below $4m^2$. Thus the product $f(s)$ is also regular on the cut plane. Hence the contour integral of $f(s)$ is zero around the closed contour $C = C_c + C_\infty$, where C_c encircles the cut (together with any real poles if necessary), and is closed by the circle C_∞ at infinity. The contour integral of $f(s)/s$ likewise vanishes if the pole at $s = 0$ is also excluded from C . From Eq. (9) one can show that $\Pi^V(s) \sim \Pi^A(s) \sim (-1/s) \log(-s) \rightarrow 0$ as $s \rightarrow \infty$, so $F_V(s) \rightarrow 1$, and $F_A(s) \rightarrow 1/g_A$. Thus $f(s)$ behaves asymptotically like $f_p^2 F_P(s) \sim m \langle \bar{\psi}\psi \rangle (1/s)$, according to Eq. (10). Hence $f(s)$ has a pole at infinity with residue $m \langle \bar{\psi}\psi \rangle$. The vanishing of the contour integrals of $f(s)/s$ and $f(s)$ thus means that

$$\begin{aligned} \int_0^\infty \frac{ds}{s} (\rho^V(s) - \rho^A(s)) &= \frac{1}{\pi} \int_0^\infty \frac{ds}{s} \text{Im} f(s + i\epsilon) \\ &= f(0) - \frac{1}{2\pi i} \int_{C_\infty} \frac{ds}{s} f(s) = f_\pi^2 \end{aligned} \quad (12)$$

and

$$\begin{aligned} \int_0^\infty ds (\rho^V(s) - \rho^A(s)) &= \frac{1}{\pi} \int_0^\infty ds \text{Im} f(s + i\epsilon) \\ &= -\frac{1}{2\pi i} \int_{C_\infty} ds f(s) = -m \langle \bar{\psi}\psi \rangle, \end{aligned} \quad (13)$$

The first result follows from $f(0) = f_\pi^2$ and the fact that there is no contribution from the circle at infinity, since $f(s)/s \sim (1/s^2)$ on C_∞ . Hence Weinberg's first sum rule is satisfied by the

*Such poles only occur if the coupling G_2 is strong enough. This is not the case for the parameter choice given in Fig.1, which is typical of the literature [2,4]. However, the analytic continuations $\tilde{F}_V(s)$ and $\tilde{F}_A(s)$ of the vector and axial vector form factors across the cut do have poles on the second Riemann sheet [7]. In the case of the vector form factor, this pole lies below $4m^2$ on the real axis of the second sheet, corresponding to a virtual, or anti-bound state of the ρ meson [8]. For a caveat to this interpretation see, however, footnote #3 in Ref. [8].

PV-regulated $\rho^{V,A}(s)$ of the ENJL model. On the other hand, the second sum rule has been altered because $f(s)$ has a pole at infinity on C_∞ . Here this alteration[†] is related to the finite quark condensate that is common to the non-perturbative, chirally broken groundstates of both versions of the NJL model[‡]. If the coupling G_1 is too weak to energetically favour spontaneous symmetry breaking [1], the condensate density vanishes, and the second sum rule will revert back to its original form[§]. It is clear from their method of derivation that Eqs. (12) and (13) will likewise hold for the spectral weights $\rho_0^{V,A}(s) = -(1/4\pi)Im\Pi^{V,A}(s)$ of the minimal NJL model with $f_\pi^2 \rightarrow f_p^2$, as can also be proved by direct integration of $\rho_0^V - \rho_0^A = (1/\pi)Im[f_p^2 F_P]$. The fact that the second Weinberg sum rule is modified dynamically in exactly the *same* way in both versions of the NJL model is all the more surprising in view of the very different behavior of the original and the extended NJL spectral weights as a function of q^2 . This difference is shown in Fig. 1 for the representative parameter choice given there. One observes a radical redistribution of individual vector and axial vector strengths and therefore their difference, to much lower energies in the ENJL case, that nevertheless continues to satisfy Eqs. (12) and (13), with $f_p^2 \rightarrow f_\pi^2$ in the first equation, while the second equation remains unmodified. In the context of the NJL model, this means that the two sum rules are actually insensitive to the introduction of the vector and axial-vector degrees of freedom.

We conclude by re-evaluating the current algebra result of Das et al. [12] for the $\pi^\pm - \pi^0$ mass squared difference,

$$\Delta m^2 = m_{\pi^\pm}^2 - m_{\pi^0}^2 = \frac{3ie^2}{f_\pi^2} \int \frac{d^4 q}{(2\pi)^4} \frac{1}{q^2} \int_0^\infty \frac{ds}{s - q^2} (\rho^V(s) - \rho^A(s)) \quad (14)$$

using PV-regulated spectral weights of the NJL model. It is evident from Eq. (14) that this result depends only on the validity of the *first* Weinberg sum rule and is indifferent to the second one. The residue of $f(s)$ at $s = q^2$ instead of $s = 0$ enters in this case, and

$$\Delta m^2 = 3ie^2 \int \frac{d^4 q}{(2\pi)^4 q^2} F_P(q^2) F_V(q^2) F_A(q^2) \quad (15)$$

[†]It is widely believed [2,4,9] that the ENJL model leads to approximate meson masses and coupling constants that *automatically* obey the original Weinberg relations [5] $g_\rho^2 = g_{A_1}^2$ and $g_\rho^2 m_\rho^{-2} - g_{A_1}^2 m_{A_1}^{-2} = f_\pi^2$ (as distinct from the sum rules) if $\Pi_V(s)$ and $\Pi_A(s)$ are approximated for all s by their low q^2 behavior. Such an approximation is, however, unsuited for investigating the sum rules themselves as now the product $f(s)$ is artificially caused to vanish faster than $1/s$, leading to a vanishing contribution from C_∞ .

[‡]Possible modifications of the second sum rule for specific forms of the Hamiltonian are explored in Ref. [10].

[§]We also remark that the same sum rules, Eqs. (12) and (13), are recovered if the form factors are cut off in $O(4)$ momentum space. The problem then is, however, that Eq. (9) (the "Ward identity"), which lies at the root of both sum rules, is not necessarily valid without introducing additional assumptions to circumvent the non-uniqueness of the $O(4)$ regularization of quadratic divergences, see especially Ref. [11].

This generalization of the Das-Low formula embraces both aspects of the pion as a composite object with internal structure through $F_P(q^2)$ plus its dressing by composite ρ and A_1 mesons through $F_V(q^2)$ and $F_A(q^2)$. If no vector mesons are included, one returns to the minimal NJL model result [14]. On the other hand making the *ad hoc* assumption that all mesons are elementary without internal structure, $F_P \approx 1$, and $F_{V,A} \approx (1 - q^2/m_{\rho,A_1}^2)^{-1}$, leads one back to the Das *et al.* result, $\Delta m^2 \approx (3\alpha/2\pi)m_\rho^2 \log 2$ for $m_{A_1} = \sqrt{2}m_\rho$.

The photon momentum integral in Eq. (15) is still logarithmically divergent since, as noted before, the PV-regulated form factor product behaves like $1/q^2$ asymptotically. Finite energy sum rules [13], smooth matching to short distance QCD [4], or calculating an equivalent $O(4)$ cutoff in the PV scheme [14] all place the photon cutoff at $\sim 2.0 - 2.5 \text{ GeV}$. Then Eq. (15) gives $1113 \text{ MeV}^2 < \Delta m^2 < 1341 \text{ MeV}^2$, that satisfactorily brackets the experimental value [15] of $1261.16 \pm 0.14 \text{ MeV}^2$.

-
- [1] Y. Nambu and G. Jona-Lasinio, Phys. Rev. **122** (1961) 345; Phys. Rev. **124** (1961) 246.
 - [2] S. Klimt et al., Nucl. Phys. A **516** (1990) 429.
 - [3] S. P. Klevansky, Rev. Mod. Phys. **64** (1992) 649.
 - [4] J. Bijnens, E. de Rafael, and H. Zheng, Z. Phys. C **62** (1994) 437.
 - [5] S. Weinberg, Phys. Rev. Lett. **18** (1967) 507; C. Bernard *et al.*, Phys. Rev. D **12** (1975) 792.
 - [6] C. Itzykson and J.B. Zuber, *Quantum Field Theory*, (McGraw-Hill, New York, 1980).
 - [7] See for example, V. Galitskii and A. Migdal, Soviet Physics JETP, **7** (1958) 96.
 - [8] M. Takizawa, K. Kubodera and F. Myhrer, Phys. Lett. B **261** (1991) 221.
 - [9] M. Wakamatsu, Ann. Phys.(N.Y.), **193** (1989) 287.
 - [10] H. T. Nieh, Phys. Rev. **163** (1967) 1769; R. Jackiw, Phys. Lett. B **27** (1968) 96.
 - [11] R. Willey, Phys. Rev. D **48** (1993) 2877.
 - [12] T. Das *et al.*, Phys. Rev. Lett. **18** (1967) 759.
 - [13] S. Narison, *QCD Spectral Sum Rules*, *World Scientific Lecture Notes* (World Scientific, Singapore, 1989) Vol. 26.
 - [14] V. Dmitrašinović *et al.*, Phys. Rev. D **52** (1995) 2855.
 - [15] Review of Particle Properties, Phys. Rev. D **50** Part I (1994) 1173.

FIGURES

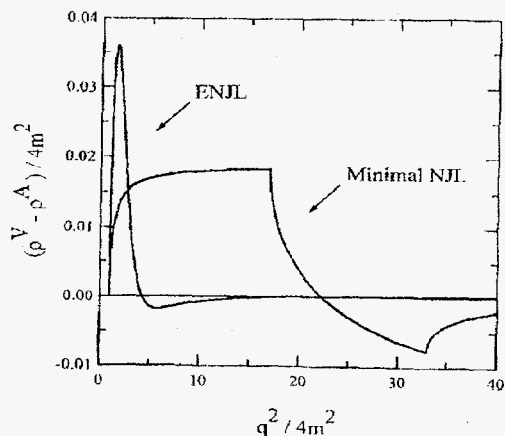


FIG. 1. The vector minus axial vector spectral weights of the NJL and ENJL models as a function of the four-momentum squared for $G_1\Lambda^2 = 2.75$, $G_2\Lambda^2 = 4.03$ and a PV-cutoff of $\Lambda = 1.06\text{GeV}$. These parameters have been obtained using the values $f_\pi = 93\text{MeV}$, $g_A = 3/4$ and $\langle\bar{q}q\rangle = -(300\text{MeV})^3$. The constituent quark mass is then fixed at $m = 0.264\text{GeV}$. The separate vector and axial vector strength distributions (not shown) peak at $q^2 \approx (0.713\text{GeV})^2$ and $(1.027\text{GeV})^2$ resp., that identify the effective ρ and A_1 meson masses of the ENJL model [2,4].

In this instance their ratio of $m_{A_1}/m_\rho = \sqrt{2.07}$ lies close to the original Weinberg estimate [5] of $\sqrt{2}$. One observes that the discontinuities introduced into the minimal NJL model strength functions by PV regularization are strongly suppressed in the ENJL version.

Positivity restrictions in polarized deep-inelastic electron scattering from the deuteron, V. Dmitrašinović

New (DESY) and upgraded electron scattering facilities (SLAC) have revived interest in polarized deep-inelastic electron scattering with polarized beams and targets. The early measurements were made with polarized proton and vector-polarized deuteron [1] in order to measure the neutron's g_1 structure function. The next step, about to be taken in the near future at SLAC and perhaps also at DESY [2], is the measurement of the tensor-polarized deuteron structure functions. There are four new structure functions, in the Hoodbhoy-Jaffe-Manohar notation called b_{1-4} [3], or $W_L(P_{zz})$, $W_T(P_{zz})$, $W_{LT}(P_{xz})$, $W_{TT}(P_{xx} - P_{yy})$ in the notation of Ref. [4], which are observable with tensor-polarized target and unpolarized electron beam. Two of them ($b_{1,2}$) are twist-two while the other two ($b_{3,4}$) are of higher twist [3].

Little is known about these new observables: (i) The two leading twist ones $b_{1,2}$ are expected to satisfy a "Callan-Gross type" relation [3] in the scaling (Bjorken) limit

$$b_2(x) = 2xb_1(x) ;$$

(ii) Hoodbhoy, Jaffe and Manohar have calculated $b_1(x)$ in a toy model (completely unrelated to deuteron) and found a substantial $b_1(x)$, i.e., $b_1(x) \sim \mathcal{O}(F_1(x))$; (iii) Close and Kumano [5] have suggested a parton-model, i.e., non-rigorous, sum rule for $b_1(x)$:

$$\int dx b_1(x) = 0 ,$$

(iv) Hoodbhoy and Khan [6] calculated $b_1(x)$ in a realistic model of the deuteron and found a very small result, $b_1(x) \sim \mathcal{O}(10^{-4})$.

In this work we present a model-independent set of constraints on the deep-inelastic structure functions for spin one targets in the form of inequalities based exclusively on positive definiteness of scattering cross sections, i.e., of probabilities. Such inequalities have already been derived for spin 1/2 targets in Ref. [7]. Here we simply extend that analysis, with some simplifications of the method due to Ref. [8], to the spin 1 case.

We derive the positivity inequalities by demanding that *every* inclusive electron scattering cross section with a spin one target, with polarized or unpolarized beam and/or target, be positive. The cross section is proportional to the contraction of the response tensor $W^{\mu\nu}$ and the lepton tensor $l_{\mu\nu} = \langle j_\mu j_\nu^* \rangle$ (see Ref. [3]), where

$$\begin{aligned} W^{\mu\nu} = & -F_1 \tilde{g}^{\mu\nu} + F_2 \frac{\tilde{p}^\mu \tilde{p}^\nu}{\nu} - b_1 r^{\mu\nu} + \frac{1}{6} b_2 (s^{\mu\nu} + t^{\mu\nu} + u^{\mu\nu}) + \frac{1}{2} b_3 (s^{\mu\nu} - u^{\mu\nu}) \\ & + \frac{1}{2} b_4 (s^{\mu\nu} - t^{\mu\nu}) + i \frac{g_1}{\nu} \epsilon^{\mu\nu\lambda\sigma} q_\lambda s_\sigma + i \frac{g_2}{\nu^2} \epsilon^{\mu\nu\lambda\sigma} q_\lambda (p \cdot q s_\sigma - q \cdot s p_\sigma) , \end{aligned} \quad (1)$$

p^μ is the target four-momentum, q^μ is the four-momentum transfer, $\nu = p \cdot q$ and $F_{1,2}, g_{1,2}$ are respectively the familiar unpolarized and vector-polarized target structure functions, b_i ($i = 1 - 4$) are the four new tensor-polarized structure functions and

$$\tilde{g}^{\mu\nu} = g^{\mu\nu} - \frac{q^\mu q^\nu}{q^2}; \quad \tilde{p}^\mu = p^\mu - \frac{p \cdot q}{q^2} q^\mu .$$

The tensors $l^{\mu\nu}, r^{\mu\nu}, s^{\mu\nu}, t^{\mu\nu}, u^{\mu\nu}$ are defined in Ref. [3] and will not be repeated here.

The electron scattering cross section for tensor-polarized spin one target and unpolarized electrons, in the deep-inelastic limit and *with leading-twist contributions only*, has been worked out and displayed in Sect. 6 of Ref. [3]. The complete inclusive cross section at finite Q^2, ν with and without electron polarization is given in Eqs. (88) and (89), Sect. II.G of Ref. [4] *. The relation between the "L, T form" and the $W_{1,2}$ structure functions is given in Eqs. (90,91) of Ref. [4]. In the scaling limit $W_1 \rightarrow F_1(x); \left(\frac{\nu}{M^2}\right) W_2 \rightarrow F_2(x)$. Analogous relations hold for the two leading-twist tensor polarized structure functions

$$W_1(P_{zz}) = -\frac{1}{3}b_1 \quad (2a)$$

$$W_2(P_{zz}) = -\frac{1}{3} \left(\frac{M^2}{\nu} \right) b_2 \quad (2b)$$

Relations between the two higher-twist tensor polarized structure functions $b_{3,4}$ and $W_{LT}(P_{xz}), W_{TT}(P_{xx} - P_{yy})$ are given by

$$\left(\frac{W}{M} \right) W_{LT}(P_{xz}) = \frac{2\sqrt{2}}{3} \left(\frac{M}{Q} \right) \left[\frac{1}{3}(b_2 - b_4) - b_3 \right] \quad (3a)$$

$$W_{TT}(P_{xx} - P_{yy}) = \frac{1}{3} \left(\frac{M^2}{\nu} \right) \left[\frac{1}{3}b_2 - b_3 \right] \quad (3b)$$

where M is the target (deuteron) mass and $W^2 = (p + q)^2$ is the center of momentum energy squared. At this moment there is no publication, at least that the present author is aware of, dealing with the higher-twist structure functions or associated terms in the inclusive cross section in the notation of Ref. [3]. Therefore, we refer the reader to Ref. [4] and its notation for all additional details.

One can now proceed directly from the positivity of the cross section $j_\mu^* W^{\mu\nu} j_\nu \geq 0$ to the positivity conditions. Note, however, that $W_{\mu\nu}$ has at most nine independent elements for an arbitrary set of deuteron polarization indices, despite being a 4×4 matrix. This is, of course, a consequence of gauge invariance, which relates the longitudinal (third) and the scalar (zeroth) components of this tensor. So, in general, 16 matrix elements can be nonzero and one has a more complicated problem than if one had nine matrix elements to deal with. The key to simplification is to explicitly reduce this four-dimensional matrix to a three-dimensional one either by a clever choice of reference frame, as was done in Ref. [7], or by using covariant photon polarization four-vectors, as was done and advocated in Ref. [8] - the two methods are equivalent [8].

Working in the virtual photon helicity basis with covariant photon polarization four-vectors, we can use the results of Ref. [3] to construct the covariant positive-definite density matrix

$$A_{\lambda H_1; \lambda' H_2} = \varepsilon_\mu^*(\lambda') W^{\mu\nu}(H_1 H_2) \varepsilon_\nu(\lambda)$$

*see in particular the second reference for the justification of vanishing of two inclusive structure functions appearing in Eq. (89) of the first reference.

$$= \begin{pmatrix} W_{++}(H_1 H_2) & W_{+0}(H_1 H_2) & W_{+-}(H_1 H_2) \\ W_{0+}(H_1 H_2) & W_{00}(H_1 H_2) & W_{0-}(H_1 H_2) \\ W_{-+}(H_1 H_2) & W_{-0}(H_1 H_2) & W_{--}(H_1 H_2) \end{pmatrix}, \quad (4)$$

where $W_{\lambda\lambda'}(H_1 H_2)$ are 3×3 submatrices in the deuteron spin space, with indices $(H_1 H_2)$ denoting the third components of deuteron spin. The eight independent matrix elements of this density matrix have already been expressed in terms of the structure functions in Eq. (7) of Ref. [3]:

$$A_{++,+} = F_1 - \frac{1}{3}\kappa b_1 + \frac{M^2}{6\nu} \left(\frac{1}{3}b_2 - b_3 \right) - g_1 + (\kappa - 1)g_2 \quad (5a)$$

$$A_{+0,+} = F_1 + \frac{2}{3}\kappa b_1 - \frac{M^2}{3\nu} \left(\frac{1}{3}b_2 - b_3 \right) \quad (5b)$$

$$A_{+0,0} = \sqrt{\kappa - 1}(g_1 + g_2) + \frac{M}{2\sqrt{Q^2}} \left(\frac{1}{3}b_2 - b_3 \right) + \frac{\kappa M}{4\sqrt{Q^2}} \left(\frac{1}{3}b_2 - b_4 \right) \quad (5c)$$

$$A_{+-,+} = F_1 - \frac{1}{3}\kappa b_1 + \frac{M^2}{6\nu} \left(\frac{1}{3}b_2 - b_3 \right) + g_1 - (\kappa - 1)g_2 \quad (5d)$$

$$A_{+-,0} = \sqrt{\kappa - 1}(g_1 + g_2) - \frac{M}{2\sqrt{Q^2}} \left(\frac{1}{3}b_2 - b_3 \right) - \frac{\kappa M}{4\sqrt{Q^2}} \left(\frac{1}{3}b_2 - b_4 \right)$$

$$A_{+-,-} = \frac{M^2}{\nu} \left(\frac{1}{3}b_2 - b_3 \right) \quad (5e)$$

$$A_{0+,0} = -F_1 + \frac{\kappa F_2}{2x} + \frac{1}{3}\kappa b_1 - \frac{1}{18x} (\kappa^2 + \kappa + 1) b_2 + \frac{1}{6x} (1 - \kappa^2) b_3 + \frac{\kappa}{6x} (1 - \kappa) b_4 \quad (5f)$$

$$A_{00,0} = -F_1 + \frac{\kappa F_2}{2x} - \frac{2}{3}\kappa b_1 + \frac{1}{9x} (\kappa^2 + \kappa + 1) b_2 - \frac{1}{3x} (1 - \kappa^2) b_3 - \frac{\kappa}{3x} (1 - \kappa) b_4, \quad (5g)$$

where $\kappa = 1 + \frac{4x^2 M^2}{Q^2} = 1 + \frac{M^2 Q^2}{\nu^2}$. Further nonzero, but linearly dependent matrix elements are obtained from the above eight by using the parity

$$A_{\lambda H_1; \lambda' H_2} = A_{-\lambda -H_1; -\lambda' -H_2}, \quad (6)$$

and time reversal symmetry properties

$$A_{\lambda H_1; \lambda' H_2} = A_{\lambda' H_2; \lambda H_1}. \quad (7)$$

Inserting the non-zero matrix elements into their places in the submatrices $W_{\lambda\lambda'}$, we find

$$W_{++} = \begin{pmatrix} A_{++,+} & 0 & 0 \\ 0 & A_{+0,+} & 0 \\ 0 & 0 & A_{+-,+} \end{pmatrix} \quad (8a)$$

$$W_{00} = \begin{pmatrix} A_{0+,0} & 0 & 0 \\ 0 & A_{00,0} & 0 \\ 0 & 0 & A_{0+,0} \end{pmatrix} \quad (8b)$$

$$W_{+-} = \begin{pmatrix} 0 & 0 & 0 \\ 0 & 0 & 0 \\ A_{+-,-} & 0 & 0 \end{pmatrix} \quad (8c)$$

$$W_{-+} = \begin{pmatrix} 0 & 0 & A_{+-,-+} \\ 0 & 0 & 0 \\ 0 & 0 & 0 \end{pmatrix} \quad (8d)$$

$$W_{+0} = \begin{pmatrix} 0 & 0 & 0 \\ A_{+0,0+} & 0 & 0 \\ 0 & A_{+-,00} & 0 \end{pmatrix} \quad (8e)$$

$$W_{0+} = \begin{pmatrix} 0 & A_{+0,0+} & 0 \\ 0 & 0 & A_{+-,00} \\ 0 & 0 & 0 \end{pmatrix}, \quad (8f)$$

where submatrices W_{-0}, W_{0-} are related to W_{+0}, W_{0+} by the symmetry properties Eqs. 6, 7. It turns out that those submatrices are not necessary since they do not lead to new inequalities. We have thus reduced the response tensor to an irreducible density matrix with elements expressed in terms of observables. To this we can now apply the mathematical machinery of positivity constraints for quadratic forms [8].

The mathematical statement that a quadratic form (matrix) is positive semi-definite is equivalent to the statement that all of its principal minors are positive semi-definite, *i.e.*, positive or zero. We start with the "smallest" principal minors: those of rank one through three. Since the submatrix W_{++} is diagonal even in the non-scaling case, three "lowest-order" inequalities associated with them are reduced to the condition that the diagonal matrix elements be positive semidefinite

$$A_{+0,+0} \geq 0 \quad (9a)$$

$$A_{++;++} \geq 0 \quad (9b)$$

$$A_{+-,+ -} \geq 0. \quad (9c)$$

By extending the positivity conditions to the fourth- and sixth order minor we find the following two inequalities

$$A_{+0,+0} A_{0+,0+} \geq A_{+0,0+}^2 \quad (10a)$$

$$A_{+-,+ -} A_{00,00} \geq A_{+-,00}^2, \quad (10b)$$

or explicitly

$$\begin{aligned} & \left[F_1 + \frac{2}{3} \kappa b_1 - \frac{M^2}{3\nu} \left(\frac{1}{3} b_2 - b_3 \right) \right] \\ & \times \left[-F_1 + \frac{\kappa F_2}{2x} + \frac{1}{3} \kappa b_1 - \frac{1}{18x} (\kappa^2 + \kappa + 1) b_2 + \frac{1}{6x} (1 - \kappa^2) b_3 + \frac{1}{6x} (1 - \kappa) b_4 \right] \\ & \geq \left[\sqrt{\kappa - 1} (g_1 + g_2) + \frac{M}{2\sqrt{Q^2}} \left(\frac{1}{3} b_2 - b_3 \right) + \frac{\kappa M}{4\sqrt{Q^2}} \left(\frac{1}{3} b_2 - b_4 \right) \right]^2 \end{aligned} \quad (11a)$$

$$\begin{aligned} & \left[F_1 - \frac{1}{3} \kappa b_1 + \frac{M^2}{6\nu} \left(\frac{1}{3} b_2 - b_3 \right) + g_1 - (\kappa - 1) g_2 \right] \\ & \times \left[-F_1 + \frac{\kappa F_2}{2x} + \frac{1}{3} \kappa b_1 - \frac{1}{18x} (\kappa^2 + \kappa + 1) b_2 + \frac{1}{6x} (1 - \kappa^2) b_3 + \frac{1}{6x} (1 - \kappa) b_4 \right] \\ & \geq \left[\sqrt{\kappa - 1} (g_1 + g_2) - \frac{M}{2\sqrt{Q^2}} \left(\frac{1}{3} b_2 - b_3 \right) - \frac{\kappa M}{4\sqrt{Q^2}} \left(\frac{1}{3} b_2 - b_4 \right) \right]^2. \end{aligned} \quad (11b)$$

Inequalities (11a,b) are nontrivial results for finite Q^2 . Hence they might be useful in the study of the *approach to scaling*. In the scaling limit, however, the right-hand sides of ineqs. (10a,b) vanish due to $\kappa \rightarrow 1$ and $\frac{M}{\sqrt{Q^2}} \rightarrow 0$, so that the remnant together with ineqs. (9b,c) lead us to conclude

$$A_{0+,0+} \geq 0 \quad (12a)$$

$$A_{00,00} \geq 0, \quad (12b)$$

or explicitly

$$\left(-F_1 + \frac{1}{2x}F_2\right) \geq -\frac{1}{3}b_1 + \frac{1}{6x}b_2 \quad (13a)$$

$$\left(-F_1 + \frac{1}{2x}F_2\right) \geq \frac{2}{3}b_1 - \frac{1}{3x}b_2. \quad (13b)$$

These two inequalities (13a,b) can be written as

$$-\left(F_1 - \frac{1}{2x}F_2\right) \geq \frac{1}{6}\left(b_1 - \frac{1}{2x}b_2\right) + \frac{1}{2}\left|b_1 - \frac{1}{2x}b_2\right|, \quad (14)$$

which, strictly speaking, is a trivial identity ($0=0$), due to the Callan-Gross relations. Finally, there is one new inequality stemming from “+−” subspace

$$A_{+,-,+} \geq |A_{+,-,-}|, \quad (15)$$

which reduces to ineq. (9c) in the scaling limit, since $A_{+,-,-} \rightarrow 0$.

We see that the scaling limit dramatically reduces the number of non-zero matrix elements of this density matrix: all off-diagonal and two diagonal matrix elements vanish as some power of $1/\sqrt{Q^2}$. Hence the number of non-trivial inequalities is reduced to three. In terms of the structure functions ineqs. (9a,b,c) now read

$$F_1 \geq -\frac{2}{3}b_1 \quad (16a)$$

$$F_1 \geq \frac{1}{3}b_1 + |g_1|. \quad (16b)$$

We can write the first of these as an absolute lower bound

$$b_1 \geq -\frac{3}{2}F_1, \quad (17)$$

which is negative since $F_1 \geq 0$, while the second provides an absolute upper bound

$$b_1 \leq 3(F_1 - |g_1|). \quad (18)$$

Furthermore, multiplying ineq. (16b) by two and adding it to ineq. (16a) we find an upper bound on the modulus of the vector polarized structure function g_1

$$F_1 \geq \frac{2}{3}|g_1|. \quad (19)$$

These three inequalities are the main result of this Brief Report. They are expected to hold for all spin one targets, irrespective of their structure, and not just the deuteron.

The main results are simple and could have been derived without the "heavy machinery" used in this note. Unfortunately, they do not impose very tight bounds on the deuteron b_1 structure function: b_1 is expected to be at least two orders of magnitude smaller than the limits imposed by ineqs. (17,18) [6]. This is due to the loosely bound nature of the deuteron [6] and need not apply to rho mesons, for example. (The question of measurement of such a mesonic structure function remains open.) There are also "higher order" inequalities (11a,b) and (15) involving products of several structure functions that would have been impossible to guess. Unfortunately, all three higher-order inequalities turned out to be either trivial or equivalent to one of the first-order inequalities in the scaling limit. We hope that at least some of these "higher order" inequalities will turn out to be useful in the study of the approach to scaling in polarized electron deuteron scattering.

-
- [1] The E143 collaboration report SLAC-PUB-95-6982 (1995).
 - [2] The Hermes collaboration technical design report (1993).
 - [3] P. Hoodbhoy, R.L. Jaffe and A. Manohar, Nucl. Phys. **B 312**, 571 (1989).
 - [4] V. Dmitrašinović and Franz Gross, Phys. Rev. C **40**, 2479 (1989); Phys. Rev. C **43**, 1495(E) (1991).
 - [5] F. E. Close and S. Kumano, Phys. Rev. D **42**, 2377 (1990).
 - [6] H. Khan and P. Hoodbhoy, Phys. Rev. C **44**, 1219 (1991).
 - [7] M.G. Doncel and E. de Rafael, Nuov. Cim. **4A**, 363 (1971).
 - [8] V. Dmitrašinović, Phys. Rev. C **51**, 1528 (1995).

Hara's theorem in the constituent quark model, V. Dmitrašinović

In a recent review of parity-violating (PV) radiative decays of hyperons [1] attention is focussed on the purported breakdown of Hara's theorem in a nonrelativistic constituent quark model calculation [2]. Hara's theorem [3] is the statement that, in the limit of exact SU(3) symmetry, all parity-violating radiative hyperon decay matrix elements vanish.

We shall show that Hara's theorem is valid in the nonrelativistic constituent quark model. The fault for the breakdown of Hara's theorem in Ref. [2] does not lie with the model, but rather with the gauge-variant calculation: Even though the starting point is a gauge-invariant relativistic quark-quark bremsstrahlung amplitude, its subsequent non-relativistic reduction, as performed in Ref. [2], is incorrect - consequently the calculation ends up violating gauge invariance and the correct threshold (on-shell photon point) behaviour.

There have been similar troubles with maintaining the gauge invariance and the threshold behaviour of the elastic parity-violating EM current nucleon matrix element (the so-called anapole moment of the nucleon [4]). We have solved those problems in Ref. [5], so we shall apply the same methods to the Hara's theorem in the non-relativistic constituent quark model.

There are two independent relativistic parity-violating EM couplings (currents) describing the radiative transition of one baryon, say a hyperon, into another, degenerate, but otherwise distinguishable baryon, e.g. a nucleon:

$$\langle N_2(p') | J_{\mu 5}^{(I)}(0) | N_1(p) \rangle = F_1(q^2) \bar{u}_2(p') \left(\gamma_\mu - \frac{\not{q}}{q^2} \right) \gamma_5 u_1(p) \quad (1)$$

and

$$\langle N_2(p') | J_{\mu 5}^{(II)}(0) | N_1(p) \rangle = F_3(q^2) \bar{u}_2(p') (i \sigma_{\mu\nu} q^\nu) \gamma_5 u_1(p). \quad (2)$$

We use the Bjorken and Drell [6] conventions, in particular the metric has the signature (+ - - -). Each of these currents is separately gauge invariant. Gauge invariance, according to Ref. [5,7], forces the first form factor $F_1(q^2)$ to vanish like $q^2 = q_0^2 - \mathbf{q}^2$ at the threshold, i.e., as $q^2 \rightarrow 0$. It is the failure of the first type of coupling, Eq. (1), to display the expected threshold behaviour that invalidated Hara's theorem in earlier applications of the quark model to this reaction. The second coupling (2) is not constrained in this way, and hence may contribute for on-shell photons. Yet, in the exact SU(3) limit its contribution vanishes due to its symmetry properties (see Sect. 3.1 in [1]). The second coupling corresponds to type II operators, in the language of Ref. [2], which do not endanger Hara's theorem.

We shall henceforth focus exclusively on type I operators. This type of coupling is not new, however: in the elastic scattering limit it corresponds to the parity-violating EM elastic matrix element, a.k.a. the "anapole" moment [5]. We shall work in the nonrelativistic limit, since that is the approximation in which the violation of Hara's theorem was reported. There the matrix element Eq. (1) turns into:

$$\mathbf{J}_5^{(I)} = F_1(q^2) [\boldsymbol{\sigma} - (\boldsymbol{\sigma} \cdot \hat{\mathbf{q}}) \hat{\mathbf{q}}], \quad (3)$$

where $F_1(-\mathbf{q}^2)$ is a function of $-\mathbf{q}^2 = q^2 = -Q^2$ with the expected long-wavelength limit:

$$F_1(-\mathbf{q}^2) = e \frac{G_F}{\sqrt{2}} \mathbf{q}^2 H(\mathbf{q}^2), \quad (4)$$

where $H(\mathbf{q}^2)$ is a new parity-violating EM form factor which is regular (finite) at the threshold, i.e., $H(0) < \infty$, $G_F \simeq 10^{-5} M_N^{-2}$ is the Fermi weak interaction coupling constant, and M_N is the nucleon mass. We need to prove Eq. (4) in the constituent quark model.

There is a general proof of the expected threshold result, due to Serot [7], which is also a substantial simplification over any explicit calculation. Any transverse EM current matrix element, such as the type I current (3), can be decomposed into transverse electric and magnetic current multipoles $\langle \Psi_f | \hat{T}_{J\lambda}^{\text{el}} | \Psi_i \rangle$, $\langle \Psi_f | \hat{T}_{J\lambda}^{\text{mag}} | \Psi_i \rangle$ [8]. In this case, all vanish except the transverse electric dipole

$$\int d\mathbf{R} \mathbf{J}_{fi} \cdot \hat{\epsilon}_\lambda \exp(i\mathbf{q} \cdot \mathbf{R}) = -i \sqrt{6\pi} \langle \Psi_f | \hat{T}_{1\lambda}^{\text{el}} | \Psi_i \rangle, \quad (5)$$

where

$$\langle \Psi_f | \hat{T}_{1\lambda}^{\text{el}} | \Psi_i \rangle = \frac{1}{i|\mathbf{q}|\sqrt{2}} \int d\mathbf{R} \left\{ -\mathbf{q}^2 (\mathbf{J}_{fi} \cdot \mathbf{R}) + (\nabla \cdot \mathbf{J}_{fi}) [1 + (\mathbf{R} \cdot \nabla)] \right\} j_1(|\mathbf{q}|R) Y_{1M}(\hat{\mathbf{R}}), \quad (6)$$

and $\mathbf{J}_{fi} = \langle \Psi_f | \mathbf{J} | \Psi_i \rangle$ is the *exact* conserved, elastic parity-violating electromagnetic (EM) current matrix element, j_1 is a spherical Bessel function, and Y_{1M} is a spherical harmonic. Note that $j_1(|\mathbf{q}|R) \sim \frac{1}{3}|\mathbf{q}|R$ in the long wavelength limit. Hence the first and second terms on the right-hand side of Eq. (6) are in agreement and in conflict, respectively with Eq. (4). In order to show that the offending term vanishes just use the EM current conservation

$$\nabla \cdot \mathbf{J}_{fi} = -i \langle \Psi_f | [H, \rho] | \Psi_i \rangle = i(E_i - E_f) \rho_{fi} \quad (7)$$

where $\rho_{fi} = \langle \Psi_f | \rho | \Psi_i \rangle$ is the associated charge density and $E_{i,f}$ are the *exact* energy eigenvalues. Since we are working in the Breit frame, and despite our initial and final states not being identical (this is hyperon *decay*) they are degenerate $E_i = E_f$, as a consequence of the assumed *exact* SU(3) symmetry. This means that the offending term is exactly zero, as advertised.

Thus we have proven that Hara's theorem holds. The above proof being exact and model-independent, it ought to hold in the constituent quark model, too. The three crucial assumptions are: (i) EM current conservation, and (ii) the use of *exact* nucleon wave functions, (iii) the SU(3) symmetry is *exact*. If the theorem fails in some explicit calculation, it has to be because one or more of these three assumptions is violated. In the rest of this note we explore one scenario in which that possibility actually occurred: the perturbative treatment of the weak interaction in Ref. [2].

In Ref. [2] the gauge-invariant set of four Feynman diagrams Fig. 1 describing the quark-quark bremsstrahlung in the Fermi interaction limit of the Salam-Weinberg model were used as the underlying theoretical model. These diagrams were then reduced to a two-quark non-relativistic PV EM interaction Hamiltonian, which apparently violates Hara's theorem. There are terms that are due to the ordinary one-body EM current and the PV admixtures in the hyperon and nucleon wave function induced by the action of the PV quark-quark potential. They were completely neglected in Ref. [2]. We show that in a consistent analysis the one-body current contributions exactly cancel the offending two-body current terms, due to gauge invariance

$$\nabla_{\mathbf{R}} \cdot \mathbf{J}(\mathbf{R}) \equiv \nabla \cdot \mathbf{J} = -\frac{\partial \rho(\mathbf{R})}{\partial t} . \quad (8)$$

In quantum mechanics, this can be written as a relation between the divergence of the three-current and the commutator of the Hamiltonian and the charge density:

$$\nabla \cdot \mathbf{J} = -i [H, \rho(\mathbf{R})] \quad (9)$$

where the total Hamiltonian

$$H = H_0^{\text{PC}} + V^{\text{PV}}$$

is the sum of the parity-conserving (PC) Hamiltonian H^{PC} (which equals the kinetic $T = \sum_{i=1}^3 \mathbf{p}_i^2 / 2m_i$ plus the PC potential $V_{2-b}^{\text{PC}} = \sum_{i<j}^3 V_{2-b}^{\text{PC}}(ij)$ energy) and the parity-violating potential $V_{2-b}^{\text{PV}} = \sum_{i<j}^3 V_{2-b}^{\text{PV}}(ij)$ of the interacting system, and $\rho(\mathbf{R})$ is the charge density. In the following we shall drop the "label" \mathbf{R} in all EM currents and densities, except when necessary to avoid confusion. The one-body electromagnetic current is the usual sum of non-relativistic convection and magnetization currents, which in configuration space reads

$$\begin{aligned} \mathbf{J}_{1-b}(i) &= \mathbf{J}_{1-b}^c(i) + \mathbf{J}_{1-b}^m(i) \\ &= \frac{e(i)}{2m_q} [\{\mathbf{p}_i, \delta(\mathbf{R} - \mathbf{r}(i))\} - \nabla_{\mathbf{R}} \times \boldsymbol{\sigma}(i) \delta(\mathbf{R} - \mathbf{r}(i))] . \end{aligned} \quad (10)$$

The charge density $\rho(\mathbf{R})$ is just the one-body charge density

$$\rho_{1-b}(\mathbf{R}) = \sum_{i=1}^3 e(i) \delta(\mathbf{R} - \mathbf{r}(i)) ,$$

where $e(i) = \frac{1}{2}[\frac{1}{3} + \tau_3(i)]$. Then, the divergence of the one-body electromagnetic current equals $-i$ times the commutator of the kinetic energy and the one-body charge density (we set $\hbar = 1$)

$$\nabla \cdot \mathbf{J}_{1-b} = -i [T, \rho_{1-b}(\mathbf{R})] . \quad (11)$$

Thus, the simplest test of electromagnetic current density conservation is whether or not the two-body potential commutes with the one-body charge density. If not, then one needs a two-body electromagnetic current density \mathbf{J}_{2-b} to compensate for the induced temporal change of charge density:

$$\nabla \cdot \mathbf{J}_{2-b} = -i [V_{2-b}, \rho(\mathbf{R})] . \quad (12)$$

The complete potential is the sum of the parity-conserving and the parity-violating ones. Similarly, the two-body electromagnetic current density is a sum of a polar vector (parity-conserving) and an axial (parity-violating) vector terms $\mathbf{J}_{2-b} = \mathbf{J}_{2-b}^{\text{PC}} + \mathbf{J}_{2-b}^{\text{PV}} = \sum_{i<j}^3 \mathbf{J}_{2-b}(ij)$. Each one of these must satisfy its own EM current conservation equation; one does not normally assume PC forces that exchange the electric charge between two quarks, so we may set all PC two-body currents equal to zero. The PV strangeness-changing weak potential V_{2-b}^{PV} between two quarks is also (electric) charge-changing, so we know that there will *have* to be some PV two-body currents $\mathbf{J}_{2-b}^{\text{PV}}$ to account for that

$$\nabla \cdot \mathbf{J}_{2-b}^{\text{PV}} = -i [V_{2-b}^{\text{PV}}, \rho(\mathbf{R})] . \quad (13)$$

It is manifest that one can only recover Eq. (9) by adding Eqs. (11) and (13), i.e., if the latter two are valid. It is an immediate corollary that no calculation which employs only the one-body, or only the two-body current for that matter, can be gauge invariant, i.e., neither satisfies Eq. (9). Since Ref. [2] did not include the one-body EM current contribution, the above argument explains their breaking of EM current conservation and consequently of Hara's theorem. A number of authors did include the one-body EM current contributions, within the quark model version of the (modern) "pole model" [12-14], but some of them omitted the PV two-body EM current. [Gavela *et al.* [12] explicitly included the contributions of the low-lying negative parity baryon multiplet (70, 1⁻). That is sufficient for maintaining Hara's theorem due to the simplicity of harmonic oscillator wave functions used by them.] Yet, even calculations with the complete EM current *operator* may still have trouble maintaining the conservation of the EM current *matrix element*, which is the necessary condition of Hara's theorem.

The resolution of this puzzle lies in the fact that the baryon wave functions have entered our considerations by way of the second line in Eq. (7). Even if the EM current *operator* satisfies Eq. (9), it need not be enough to ensure the conservation of the EM current *matrix element*, and with it the validity of Hara's theorem, since the second line in Eq. (7) is only satisfied when the initial and final wave functions are the *exact* eigenstates of the total Hamiltonian H . The PV interactions are weak and hence tractable in first order perturbation theory: that is the approach adopted in Ref. [12]. We shall show that a necessary condition for the conservation of an EM current matrix element in perturbation theory is the retention of *all* excited ("intermediate") states in the admixtures to the initial and final wave functions.

The PV weak interaction between quarks implies the existence of a small, $\mathcal{O}(G_F)$, abnormal-parity, strangeness-violating admixture in the baryon (hyperon/nucleon) wave function. To determine this admixture, we shall use the first-order time-independent (Rayleigh-Schrödinger) perturbation approximation to the quark dynamics described by the Hamiltonian $H = H_0^{\text{PC}} + V^{\text{PV}}$. The ground state of the nucleon/hyperon $|\Psi_0\rangle$ is given by

$$|\Psi_0\rangle = |\Phi_0\rangle + \sum_{n \neq 0} |\Phi_n\rangle \frac{\langle \Phi_n | V^{\text{PV}} | \Phi_0 \rangle}{E_0 - E_n} + \mathcal{O}(G_F^2) \quad (14a)$$

$$= |\Phi_0\rangle + \sum_{n \neq 0} \varepsilon_{n0} |\Phi_n\rangle + \mathcal{O}(G_F^2), \quad (14b)$$

where $|\Phi_n\rangle$ are the *exact* eigenstates of the PC Hamiltonian H_0^{PC} : $H_0^{\text{PC}} |\Phi_n\rangle = E_n |\Phi_n\rangle$, and

$$\varepsilon_{na} = \frac{\langle \Phi_n | V^{\text{PV}} | \Phi_a \rangle}{E_a - E_n} \sim \mathcal{O}(G_F) \quad (15)$$

are the admixture coefficients to the baryon a . The abnormal parity admixtures in the initial and final wave functions generate a parity-violating electromagnetic current hyperon-nucleon matrix element Eq. (1). Since the PV potential is of $\mathcal{O}(G_F)$, Eq.(13) demands that the PV two-body electromagnetic current also be of $\mathcal{O}(G_F)$. Hence, to $\mathcal{O}(G_F)$, the EM current matrix element reads

$$\mathbf{J}_{fi} = \langle \Phi_f | \mathbf{J}_{2-b}^{\text{PV}} | \Phi_i \rangle + \sum_{n \neq i, f} \left\{ \langle \Phi_f | \mathbf{J}^{\text{PC}} | \Phi_n \rangle \varepsilon_{ni} + \varepsilon_{nf}^* \langle \Phi_n | \mathbf{J}^{\text{PC}} | \Phi_i \rangle \right\}. \quad (16)$$

Eq. (7) ought to hold order by order in perturbation theory, or equivalently, in the expansion in the weak coupling constant G_F . We shall now explicitly demonstrate the significance of

keeping all intermediate states in the calculation. To evaluate the divergence start from Eq. (16)

$$\begin{aligned}\nabla \cdot \mathbf{J}_{fi} &= \nabla \cdot \langle \Phi_f | \mathbf{J}_{2-b}^{\text{PV}} | \Phi_i \rangle + \sum_{n \neq i, f} \left\{ \nabla \cdot \langle \Phi_f | \mathbf{J}^{\text{PC}} | \Phi_n \rangle \varepsilon_{ni} + \varepsilon_{nf}^* \nabla \cdot \langle \Phi_n | \mathbf{J}^{\text{PC}} | \Phi_i \rangle \right\} \\ &= -i \langle \Phi_f | [V^{\text{PV}}, \rho] | \Phi_f \rangle + \sum_{n \neq i, f} \left\{ \langle \Phi_f | [H_0^{\text{PC}}, \rho] | \Phi_n \rangle \varepsilon_{ni} + \varepsilon_{nf}^* \langle \Phi_n | [H_0^{\text{PC}}, \rho] | \Phi_i \rangle \right\}.\end{aligned}$$

Now use the definition of the admixture coefficients ε_n Eq. (15) with $a = i, f$: the fact that the unperturbed states are eigenfunctions of H_0^{PC} , implies that

$$\langle \Phi_f | [H_0^{\text{PC}}, \rho] | \Phi_n \rangle = (E_f - E_n) \langle \Phi_f | \rho | \Phi_n \rangle$$

which in turn leads to:

$$\begin{aligned}\nabla \cdot \mathbf{J}_{fi} &= \nabla \cdot \langle \Phi_f | \mathbf{J}_{2-b}^{\text{PV}} | \Phi_i \rangle - i \sum_{n \neq f} (E_i - E_n) \langle \Phi_f | \rho | \Phi_n \rangle \frac{\langle \Phi_n | V^{\text{PV}} | \Phi_i \rangle}{E_f - E_n} \\ &\quad - i \sum_{n \neq i} \frac{\langle \Phi_f | V^{\text{PV}} | \Phi_n \rangle}{E_i - E_n} (E_n - E_f) \langle \Phi_n | \rho | \Phi_i \rangle \\ &= -i \langle \Phi_f | [V^{\text{PV}}, \rho] | \Phi_i \rangle - i \sum_{n \neq f} \langle \Phi_f | \rho | \Phi_n \rangle \langle \Phi_n | V^{\text{PV}} | \Phi_i \rangle + i \sum_{n \neq i} \langle \Phi_f | V^{\text{PV}} | \Phi_n \rangle \langle \Phi_n | \rho | \Phi_i \rangle \\ &\quad + i(E_i - E_f) \langle \Phi_f | \rho | \Phi_i \rangle + i(E_i - E_f) \sum_{n \neq fi} \left\{ \langle \Phi_f | \rho | \Phi_n \rangle \varepsilon_{ni} + \varepsilon_{nf}^* \langle \Phi_n | \rho | \Phi_i \rangle \right\}.\end{aligned}\quad (17)$$

The terms explicitly excluded from the sums in the first line of Eq. (17) are identically zero, due to the good parity of *unperturbed* states $|\Phi_n\rangle$. Hence the sums can be extended over *all* intermediate states, which form a complete set $\sum_n |\Phi_n\rangle \langle \Phi_n| = 1$. The second line of Eq. (17) can be further simplified using Eq. (14b) for the initial and final states, leading to

$$\begin{aligned}\nabla \cdot \mathbf{J}_{fi} &= -i \langle \Phi_f | [V^{\text{PV}}, \rho] | \Phi_i \rangle - i \langle \Phi_f | \rho V^{\text{PV}} - V^{\text{PV}} \rho | \Phi_i \rangle \\ &\quad + i(E_i - E_f) \langle \Psi_f | \rho | \Psi_i \rangle + \mathcal{O}(G_F^2) \\ &= i(E_i - E_f) \langle \Psi_f | \rho | \Psi_i \rangle + \mathcal{O}(G_F^2)\end{aligned}\quad (18)$$

which, together with the degeneracy of nucleons and hyperons, $E_i = E_f$, in the SU(3) limit leads to the final result

$$\nabla \cdot \mathbf{J}_{fi} = 0. \quad (19)$$

Note that Eq. (7) differs from Eq. (18) only in that it involves the *exact* eigen-energies $E_{i,f}$, which are also degenerate in the exact SU(3) limit, rather than the perturbative ones $E_{i,f}$, i.e., to $\mathcal{O}(G_F)$ the two equations coincide, as they should. This completes the proof that type I operators do *not* violate Hara's theorem.

To summarize, we have shown how the correct threshold behaviour, in the exact SU(3) limit of the constituent quark model, of the radiative PV hyperon decay amplitude is in agreement with Hara's theorem as long as the EM current matrix element is exactly conserved. This means not only that the EM current operator satisfies the continuity equation, but also that the consistent wave functions are used.

- [1] J. Lach and P. Żenczykowski, *Int. Jour. Mod. Phys. A* **10**, 3817 (1995).
- [2] A. N. Kamal and Riazuddin, *Phys. Rev. D* **28**, 2317 (1983).
- [3] Y. Hara, *Phys. Rev. Lett.* **12**, 378 (1964).
- [4] Ia. B. Zel'dovich, *Sov. Phys. JETP* **6**, 1184 (1958), and Ya. B. Zel'dovich and A. M. Perelomov, *Sov. Phys. JETP* **12**, 777 (1961).
- [5] V. Dmitrašinović, *Nucl. Phys. A* **537**, 551 (1992).
- [6] J.D.Bjorken and S.D.Drell *Relativistic Quantum Mechanics* (McGraw-Hill, 1964).
- [7] B.D. Serot, *Nucl. Phys. A* **322**, 408 (1979).
- [8] J.D. Walecka, *Theoretical Nuclear and Subnuclear Physics*, Oxford University Press, New York (1995).
- [9] R.K. Bhaduri, *Models of the Nucleon*, Addison-Wesley, Redwood City CA (1988).
- [10] A. LeYaounac, LL. Oliver, O. Pene and J.-C. Raynal, *Hadron Transitions in the Quark Model*, Gordon and Breach, New York (1988).
- [11] ed. M. Rho and D. Wilkinson, *Mesons in Nuclei*, North Holland, Amsterdam (1979).
- [12] M.B. Gavela, A. LeYaounac, LL. Oliver, O. Pène, J.-C. Raynal and T.N. Pham, *Phys. Lett. B* **101**, 417 (1981).
- [13] F. Close and H. Rubinstein, *Nucl. Phys. B* **173**, 477 (1980).
- [14] K. G. Rauh, *Z. Phys. C* **10**, 81 (1981).

FIGURES

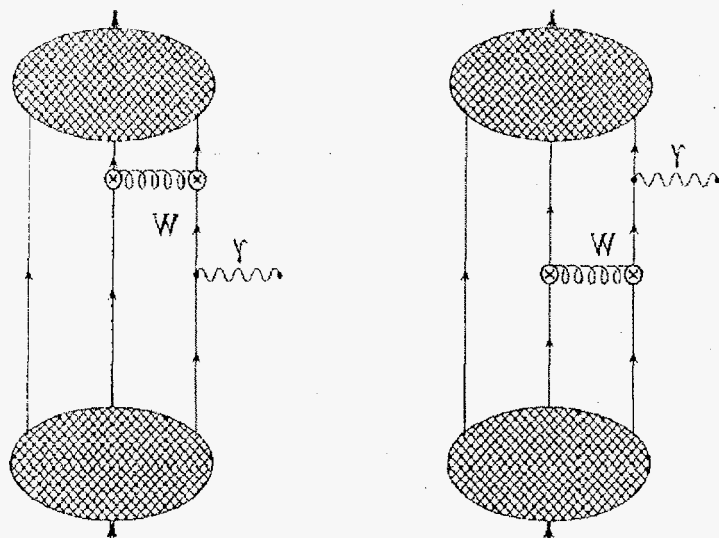


FIG. 1. Two of four Feynman diagrams describing the parity-breaking contribution to the EM axial-vector currents. The solid line denotes the quarks, the wavy line is the photon and wiggly line is the charged intermediate vector boson W^\pm . The shaded blob together with the three solid lines and one double solid line leading to it denotes the nucleon wave function. The remaining two graphs have their photon lines attached to the "other" quark line.

Renormalization Group Effective Potentials for Bosons and Yukawa Coupled Fermions at Finite Temperature. J.D. Shafer and J.R. Shepard (University of Colorado)

Following on our RG treatments of scalar field theories at zero-temperature [1] and finite temperature [2], we wish to extend previous zero temperature developments of RG flow equations for theories with scalar fields plus Yukawa-coupled fermions [3] to finite temperature. We begin by considering the finite temperature euclidean action [4,5] for such a system with potentials $U^{(\Lambda)}(\phi)$ and $V^{(\Lambda)}(\phi)$ at momentum scale Λ :

$$S^{(\Lambda)} = \int_0^\beta d\tau \int d^{d-1}x \left\{ \frac{1}{2}(\partial_\mu \phi)^2 + U^{(\Lambda)}(\phi) + \bar{\psi} \left[\gamma^0 \frac{\partial}{\partial \tau} - i\vec{\gamma} \cdot \nabla + V^{(\Lambda)}(\phi) \right] \psi \right\} \quad (1)$$

where $\phi(x)$ is a single component scalar field and $\psi(x)$ is a Dirac spinor with N_f flavors. We may compute the momentum space action by expanding the fields $\phi(x)$ and $\psi(x)$ as Fourier sums,

$$\phi(\vec{x}, \tau) = \phi_0 + \left(\frac{\beta}{V} \right) \sum_{\vec{q}_i, n \neq 0}^{(\Lambda)} e^{i(\vec{q}_i \cdot \vec{x} + \omega_n^B \tau)} \phi_n(\vec{q}_i), \quad (2)$$

$$\psi(\vec{x}, \tau) = \Psi_0 e^{i\frac{\pi}{\beta}\tau} + \frac{1}{\sqrt{V}} \sum_{\vec{q}_i, n \neq 0}^{(\Lambda)} e^{i(\vec{q}_i \cdot \vec{x} + \omega_n^F \tau)} \psi_n(\vec{q}_i). \quad (3)$$

Here, $V = \int d^{d-1}x$, and the bosonic and fermionic Matsubara frequencies are given by $\omega_n^B = \frac{2n\pi}{\beta}$ and $\omega_n^F = \frac{2(n+1)\pi}{\beta}$, respectively. The superscript Λ on the sums of eqs. 2 and 3 denotes that only modes such that $0 < (q_i^2 + \omega_n^2)^{1/2} \leq \Lambda$ are included in the sum. We have assumed periodic boundary conditions in the spatial directions, and normalizations have been chosen so that the Fourier amplitudes are dimensionless.

We now expand our potentials, $U^{(\Lambda)}(\phi)$ and $V^{(\Lambda)}(\phi)$, in terms of the expression of eq. 2 to obtain

$$U^{(\Lambda)}(\phi) = U^{(\Lambda)}(\phi_0) + \left. \frac{dU^{(\Lambda)}}{d\phi} \right|_{\phi=\phi_0} (\phi - \phi_0) + \frac{1}{2!} \left. \frac{d^2 U^{(\Lambda)}}{d\phi^2} \right|_{\phi=\phi_0} (\phi - \phi_0)^2 + \dots, \quad (4)$$

and a similar expression for $V^{(\Lambda)}(\phi)$. We substitute these expansions into the action of eq. 1 and use

$$\frac{1}{V} \int d^{d-1}x e^{i\vec{q}_i \cdot \vec{x}} = \delta_{\vec{q}_i, 0}, \quad (5)$$

and

$$\frac{1}{\beta} \int_0^\beta d\tau e^{i\frac{2n\pi}{\beta}\tau} = \delta_{n, 0}. \quad (6)$$

Retaining only those contributions containing at most two powers of field components with $n \neq 0$, we find

$$\begin{aligned}
S^{(\Lambda)} \simeq & \beta V[U^{(\Lambda)}(\phi_0) + \bar{\Psi}_0 V^{(\Lambda)}(\phi_0) \Psi_0] \\
& + \frac{\beta^2}{2} \sum_{\vec{q}_i, n \neq 0}^{(\Lambda)} [q_i^2 + \omega_n^{B^2} + U''^{(\Lambda)}(\phi_0) + \bar{\Psi}_0 V''^{(\Lambda)}(\phi_0) \Psi_0] \phi_n^*(\vec{q}_i) \phi_n(\vec{q}_i) \\
& + \beta \sum_{\vec{q}_i, n \neq 0}^{(\Lambda)} \bar{\psi}_n(\vec{q}_i) [-\not{q}_i + V^{(\Lambda)}(\phi_0)] \psi_n(\vec{q}_i) \\
& + \beta^{3/2} \sum_{\vec{q}_i, n \neq 0}^{(\Lambda)} [\bar{\psi}_n(\vec{q}_i) \phi_n(\vec{q}_i) \Psi_0 + \bar{\Psi}_0 \phi_n^*(\vec{q}_i) \psi_n(\vec{q}_i)] V'^{(\Lambda)}(\phi_0). \quad (7)
\end{aligned}$$

We may calculate the action at a new, smaller momentum scale, $\Lambda - \Delta\Lambda$, via the relation

$$e^{-S(\Lambda - \Delta\Lambda)} = \prod_{\vec{q}_i, n}^{(\Lambda)} \int_{shell} d\phi_{\vec{q}_i, n} d\phi_{\vec{q}_i, n}^* d\bar{\psi}_{\vec{q}_i, n} d\psi_{\vec{q}_i, n} e^{-S^{(\Lambda)}}, \quad (8)$$

where the shell denotes the set of modes $\{\vec{q}_i, \omega_n\}$ such that $\Lambda - \Delta\Lambda < (q_i^2 + \omega_n^2)^{1/2} \leq \Lambda$, and the prime and superscript Λ on the product indicate that it ranges only over modes in the shell. This result is exact in the limit of vanishing shell thickness. To proceed, we employ the local potential approximation by setting all remaining non-uniform (*i.e.*, $n \neq 0$) field components to zero [6]. Integration over the Grassmann variables corresponding to fermion field components in the shell is accomplished by making use of

$$\int d\bar{\eta} d\eta e^{[-\bar{\eta} M \eta + J \eta + \bar{\eta} J]} = \det M e^{[J M^{-1} J]}, \quad (9)$$

where η and $\bar{\eta}$ are Grassmann variables, and M is a Hermitian matrix. The integration over the remaining scalar field components in the shell is a matter of evaluating a multi-dimensional Gaussian integral; after doing so, we obtain

$$\begin{aligned}
U^{(\Lambda - \Delta\Lambda)}(\phi_0) + \bar{\Psi}_0 V^{(\Lambda - \Delta\Lambda)}(\phi_0) \Psi_0 = & U^{(\Lambda)}(\phi_0) + \bar{\Psi}_0 V^{(\Lambda)}(\phi_0) \Psi_0 \\
& - \frac{1}{\beta V} \sum_{\vec{q}_i, n \neq 0}^{(\Lambda)} \left[\frac{N_f C_d}{2} \ln \left(q_i^2 + \omega_n^{F^2} + V^{(\Lambda)}(\phi_0)^2 \right) \right] \\
& + \frac{1}{2\beta V} \sum_{\vec{q}_i, n \neq 0}^{(\Lambda)} \ln \left[q_i^2 + \omega_n^{B^2} + U''^{(\Lambda)}(\phi_0) \right. \\
& \left. + \bar{\Psi}_0 \left(V''^{(\Lambda)} - 2 \frac{(\not{q}_i + V^{(\Lambda)}(\phi_0))}{q_i^2 + \omega_n^{F^2} + V^{(\Lambda)}(\phi_0)^2} V'^{(\Lambda)}(\phi_0)^2 \right) \Psi_0 \right], \quad (10)
\end{aligned}$$

where we have made use of the fact that

$$\det[\beta(V^{(\Lambda)}(\phi_0) - \not{q}_i)] = \beta^{N_f C_d} \left(q_i^2 + \omega_n^{F^2} + V^{(\Lambda)}(\phi_0)^2 \right)^{N_f C_d/2} \quad (11)$$

and

$$(-\not{q}_i + V^{(\Lambda)}(\phi_0))^{-1} = \frac{\not{q}_i + V^{(\Lambda)}(\phi_0)}{q_i^2 + \omega_n^{F^2} + V^{(\Lambda)}(\phi_0)^2}. \quad (12)$$

We note that the prime and superscript Λ on the sums indicate that they run only over in-shell field components, and C_d is the dimensionality of the Clifford algebra, given by $2^{d/2}(2^{(d-1)/2})$ for d even (odd).

In order to obtain a continuum RG equation, we must evaluate the limit of eq. 10 as the volume of our spatial "box" becomes infinite. In this limit,

$$\frac{1}{V} \sum_{\vec{q}_i, n \neq 0} '(\Lambda) \rightarrow \sum_{n=-N_{B,F}}^{N_{B,F}} \int \frac{d^{d-1}q}{(2\pi)^{d-1}} \theta(\Lambda^2 - q^2 - \omega_n^2) \theta(q^2 + \omega_n^2 - (\Lambda - \Delta\Lambda)). \quad (13)$$

Here, $N_{B,F}$ is a limit of summation determined by the theta function constraint. Since

$$\Lambda^2 = q^2 + \omega_n^2, \quad (14)$$

for a particular Λ , there are only a finite number of integers, n , for which eq. 14 may be satisfied. For boson modes, the limit of summation is $N_B = [\frac{\beta\Lambda}{2\pi}]$, while for fermions, it is $N_F = [\frac{1}{2}(\frac{\beta\Lambda}{\pi} - 1)]$. The brackets denote the largest integer less than the value of the expressions they enclose. Thus, although the spatial modes of the fields become continuous in the large volume limit, the temporal modes remain discrete.

By integrating the spatial modes over the theta functions of eq. 13 and equating coefficients of like powers of $\bar{\Psi}_0\Psi_0$, we finally obtain the following coupled equations for the potentials, $U^{(\Lambda-\Delta\Lambda)}(\phi_0)$ and $V^{(\Lambda-\Delta\Lambda)}(\phi_0)$:

$$\begin{aligned} \frac{dU^{(\Lambda)}(\phi_0)}{d\Lambda} = & \frac{-A_{d-1}}{2\beta} \left\{ \sum_{n=-N_B}^{N_B} \left(\Lambda^2 - \left(\frac{2n\pi}{\beta} \right)^2 \right)^{\frac{d-2}{2}} \ln \left(\Lambda^2 + U^{(\Lambda)}(\phi_0) \right) \right. \\ & \left. - \sum_{n=-N_F}^{N_F} \left(\Lambda^2 - \left(\frac{(2n+1)\pi}{\beta} \right)^2 \right)^{\frac{d-2}{2}} N_f C_d \ln \left(\Lambda^2 + V^{(\Lambda)}(\phi_0)^2 \right) \right\}, \end{aligned} \quad (15)$$

$$\begin{aligned} \frac{dV^{(\Lambda)}(\phi_0)}{d\Lambda} = & \frac{-A_{d-1}}{2\beta} \left\{ \sum_{n=-N_B}^{N_B} \left(\Lambda^2 - \left(\frac{2n\pi}{\beta} \right)^2 \right)^{\frac{d-2}{2}} \left(\Lambda^2 + U^{(\Lambda)}(\phi_0) \right)^{-1} \right. \\ & \left. \times \left(V^{(\Lambda)}(\phi_0) - \frac{2V^{(\Lambda)}(\phi_0)^2 V^{(\Lambda)}(\phi_0)}{\Lambda^2 + (4n+1)\frac{\pi^2}{\beta^2} + V^{(\Lambda)}(\phi_0)^2} \right) \right\}. \end{aligned} \quad (16)$$

These are our coupled RG flow equations for a theory with a scalar field plus Yukawa-coupled fermions at finite temperature $\frac{1}{\beta}$.

We may now examine the high and low temperature limits of these expressions. In the low temperature ($\beta \rightarrow \infty$) limit

$$\frac{1}{\beta} \sum_{n=-N_{F,B}}^{N_{F,B}} \rightarrow \int \frac{d\omega}{(2\pi)}, \quad (17)$$

and we find

$$\frac{dU^{(\Lambda)}(\phi_0)}{d\Lambda} = \frac{-A_d}{2} \Lambda^{d-1} \left\{ \ln \left(\Lambda^2 + U^{(\Lambda)}(\phi_0) \right) - N_f C_d \ln \left(\Lambda^2 + V^{(\Lambda)}(\phi_0)^2 \right) \right\}, \quad (18)$$

$$\frac{dV^{(\Lambda)}(\phi_0)}{d\Lambda} = \frac{-A_d}{2} \Lambda^{d-1} \left\{ \left(\Lambda^2 + U^{(\Lambda)}(\phi_0) \right)^{-1} \left(V^{(\Lambda)}(\phi_0) - \frac{2V^{(\Lambda)}(\phi_0)^2 V^{(\Lambda)}(\phi_0)}{\Lambda^2 + V^{(\Lambda)}(\phi_0)^2} \right) \right\}. \quad (19)$$

These are the appropriate expressions for zero temperature [3].

In the high temperature limit, $\beta \rightarrow 0$, and $N_{F,B} \rightarrow 0$. For fermions, the shell of integration, Λ , is defined as

$$\Lambda^2 = q_i^2 + \left(\frac{(2n+1)\pi}{\beta} \right)^2. \quad (20)$$

Obviously, as $\beta \rightarrow 0$, $\frac{(2n+1)\pi}{\beta}$ becomes large without bound, even if $n = 0$. Hence, there is a lower bound on β for modes satisfying eq. 20. This bound is $\beta_{min} = \frac{\pi}{\Lambda}$. For β smaller than β_{min} , there are no fermion modes over which we may integrate. We may therefore proceed as in eq. 7, but now integrate only over the scalar modes. Setting all nonuniform modes outside the shell to zero, and neglecting irrelevant constants, we find,

$$\frac{dU^{(\Lambda)}(\phi_0)}{d\Lambda} = -\frac{A_{d-1}}{2\beta} \Lambda^{d-2} \ln \left(\Lambda^2 + U''^{(\Lambda)}(\phi_0) \right), \quad (21)$$

$$\frac{dV^{(\Lambda)}(\phi_0)}{d\Lambda} = -\frac{A_{d-1}}{2\beta} \Lambda^{d-2} \frac{V''^{(\Lambda)}(\phi_0)}{(\Lambda^2 + U''^{(\Lambda)}(\phi_0))}. \quad (22)$$

If we now perform a scaling transformation, and define $\tilde{U}^{(\Lambda)}(\tilde{\phi}_0) \equiv \beta U^{(\Lambda)}(\phi_0)$, $\tilde{V}^{(\Lambda)}(\tilde{\phi}_0) \equiv \beta V^{(\Lambda)}(\phi_0)$, and $\tilde{\phi} \equiv \sqrt{\beta} \phi$, eqns. 21 and 22 become

$$\frac{d\tilde{U}^{(\Lambda)}(\tilde{\phi}_0)}{d\Lambda} = -\frac{A_{d-1}}{2} \Lambda^{d-2} \ln \left(\Lambda^2 + \tilde{U}''^{(\Lambda)}(\tilde{\phi}_0) \right), \quad (23)$$

$$\frac{d\tilde{V}^{(\Lambda)}(\tilde{\phi}_0)}{d\Lambda} = -\frac{A_{d-1}}{2} \Lambda^{d-2} \frac{\tilde{V}''^{(\Lambda)}(\tilde{\phi}_0)}{(\Lambda^2 + \tilde{U}''^{(\Lambda)}(\tilde{\phi}_0))}, \quad (24)$$

where primes now denote derivatives with respect to $\tilde{\phi}$. We observe the dimensional reduction of the expression for the boson potential, $U^{(\Lambda)}(\phi)$, since eq. 23 is simply the high temperature limit of the effective potential in a theory with only bosons [1,2]. Furthermore, in a theory with Yukawa coupling, $V''^{(\Lambda)}(\phi)$ is zero, and so the fermion effective potential does not evolve in this limit. Thus the fermions make no contribution to the scalar flow nor does the Yukawa coupling flow in the high temperature limit.

Further work in this area is ongoing, including numerical integration of eqns. 15 and 16.

¹ J. R. Shepard, V. Dmitrašinović and J. A. McNeil, Phys. Rev. **D51**, 7017 (1995).

² J. D. Shafer and J. R. Shepard, submitted to Phys. Rev. D, (July 1996).

³ M. Maggiore, Z. Phys. **C41**, 687 (1989).

⁴ T. Matsubara, Prog. Theor. Phys. **14**, 351 (1955).

⁵ J.I. Kapusta, Finite-Temperature Field Theory, Cambridge University Press, Cambridge (1989).

⁶ A. Hasenfratz and P. Hasenfratz, Nucl. Phys. **B270**, 687, (1986).

Renormalization Group Flow Equations for Sigma Models. J.R. Shepard (University of Colorado) and A.S. Johnson and J.A. McNeil (Colorado School of Mines)

To study chiral symmetry in the context of Renormalization Group (RG) flow equations we consider an extension of our leading order (LO) flow equations for field theories with self interacting bosons and generalized Yukawa coupled fermions [1-3] to sigma models [4] with linear and quadratic chiral symmetry breaking terms. Consider the action,

$$S = \int d^d x \left[\frac{1}{2} (\partial_\mu \phi^a)^2 + V^{(\Lambda)}(\rho, \sigma) + \bar{\psi}^\alpha [\not{\partial} + U^{(\Lambda)}(\rho, \sigma, \Gamma)] \psi^\alpha \right] \quad (1)$$

with $\phi^a = \begin{pmatrix} \sigma \\ \pi^i \end{pmatrix}$, $\Gamma^a = \begin{pmatrix} 1 \\ i\gamma^5 \tau^i \end{pmatrix}$, $\rho^2 = \phi^a \phi^a = \sigma^2 + \pi^i \pi^i$, $\Gamma^a \phi^a = \Gamma = \sigma + i\gamma^5 \vec{\tau} \cdot \vec{\pi}$, (τ^i are the Pauli matrices) for $i = 1, 2, 3$ and $\alpha = 1, \dots, n_f$, the fermion flavor index. The potentials can be expanded in the form:

$$V(\rho, \sigma) = V_0(\rho) + \sigma V_1(\rho) + \frac{\sigma^2}{2} V_2(\rho) + \dots$$

$$U(\rho, \sigma, \Gamma) = m(\rho, \sigma) + \Gamma g(\rho, \sigma) \quad (2)$$

where $m(\rho, \sigma)$ and $g(\rho, \sigma)$ are expanded similarly to $V(\rho, \sigma)$. In the present we truncate these expansions retaining only those terms shown explicitly. Then the action (1) with $m(\rho, \sigma)$, $g_1(\rho)$, $g_2(\rho)$, $V_1(\rho)$, and $V_2(\rho) = 0$ (i.e. only $V_0(\rho)$ and $g_0(\rho)$ nonzero) is symmetric with respect to chiral $SU(2) \times SU(2)$ transformations. Deviations from chiral symmetry are included through $m(\rho, \sigma)$, $g_1(\rho)$, $g_2(\rho)$, $V_1(\rho)$, and $V_2(\rho)$. Flow equations for the nine functions $V_i(\rho)$, $m_i(\rho)$, and $g_i(\rho)$ for $i = 0, 1, 2$ can be derived by decomposing the fields $\phi^a(x)$, $\bar{\psi}(x)$, and $\psi(x)$ into uniform and nonuniform pieces,

$$\phi^a(x) = \phi_0^a + \varphi^a(x), \quad \varphi^a(x) = \sum_{q \neq 0} \phi_q^a e^{-iq \cdot x},$$

$$\psi^\alpha(x) = \psi_0^\alpha + \sum_{q \neq 0} \psi_q^\alpha e^{-iq \cdot x}, \quad (3)$$

$$\bar{\psi}^\alpha(x) = \bar{\psi}_0^\alpha + \sum_{q \neq 0} \bar{\psi}_q^\alpha e^{-iq \cdot x},$$

Taylor expanding the potentials,

$$V^{(\Lambda)}(\phi^a) = V^{(\Lambda)}(\phi_0^a) + V'^{(\Lambda)a}(\phi_0^a) \varphi^a + \frac{1}{2} V''^{(\Lambda)ab}(\phi_0^a) \varphi^a \varphi^b + \dots \quad (4)$$

(similarly for U) and substituting into Eq.(1) using,

$$\int d^d x e^{iq \cdot x} = (\text{Vol}) \delta_{q,0}, \quad (5)$$

to get,

$$\frac{S^{(\Lambda)}}{\text{Vol}} = V^{(\Lambda)}(\phi_0^a) + \bar{\psi}_0 U^{(\Lambda)}(\phi_0^a) \psi_0$$

$$+ \sum_{q \neq 0} \left[\frac{1}{2} \phi_{-q}^a [\delta^{ab} q^2 + V''^{(\Lambda)ab}(\phi_0^a) + \bar{\psi}_0 \psi_0 U''^{(\Lambda)ab}(\phi_0^a)] \phi_q^b + \bar{\psi}_{-q}^\alpha [i \not{q} + U^{(\Lambda)}(\phi_0^a)] \psi_q^\alpha \right.$$

$$\left. + U'^{(\Lambda)a}(\phi_0^a) (\bar{\psi}_0 \phi_{-q}^a \psi_q + \bar{\psi}_{-q} \phi_q^a \psi_0) \right] + \dots \quad (6)$$

The effective action is generated by integrating out all degrees of freedom with momentum in the shell $\Lambda - \Delta\Lambda < q < \Lambda$,

$$e^{-S^{(\Lambda-\Delta\Lambda)}} = \int \prod_{\Lambda-\Delta\Lambda < q < \Lambda} d\phi_q^a d\bar{\psi}_q d\psi_q e^{-S^{(\Lambda)}}. \quad (7)$$

Performing these Gaussian integrations and projecting onto uniform field components one arrives at,

$$\begin{aligned} \frac{S^{(\Lambda-\Delta\Lambda)}}{\text{Vol}} &= V^{(\Lambda-\Delta\Lambda)}(\phi_0^a) + \bar{\psi}_0 U^{(\Lambda-\Delta\Lambda)}(\phi_0^a) \psi_0 \\ &= V^{(\Lambda)}(\phi_0^a) + \bar{\psi}_0 U^{(\Lambda)}(\phi_0^a) \psi_0 \\ &\quad - \frac{1}{2\text{Vol}} \text{tr} \ln \left[\delta^{ab} q^2 + V''^{(\Lambda)ab}(\phi_0^a) + \bar{\psi}_0 \left(U''^{(\Lambda)ab}(\phi_0^a) - \frac{2U'^{(\Lambda)a}(\phi_0^a)U'^{(\Lambda)b}(\phi_0^a)}{i\hbar + U^{(\Lambda)}(\phi_0^a)} \right) \psi_0 \right] \\ &\quad + \frac{1}{\text{Vol}} \text{tr} \ln(i\hbar + U^{(\Lambda)}(\phi_0^a)) + \dots \end{aligned} \quad (8)$$

Now after substituting each of the following (dropping Λ superscripts and notation of functional dependences),

- $\text{tr} \ln(i\hbar + U) = \frac{1}{2} n_f c_d \sum_q \ln(q^2 + U^2)$, $c_d = 2^{d/2}(2^{(d-1)/2})$ for d even (odd).
- $(i\hbar + U)^{-1} \simeq \frac{U^\dagger}{D_F}$ where $D_F = q^2 + m^2 + g^2 \rho^2 + 2mg\sigma$ and we've used $\langle \hbar \rangle_{\text{angle}} = 0$.
- $\Sigma^{ab} \equiv \delta^{ab} q^2 + V''^{ab}$
- $\Omega^{ab} \equiv U''^{ab} - \frac{2U'^a U'^b}{i\hbar + U}$
- $\text{tr} \ln \left[\delta^{ab} q^2 + V''^{ab} + \bar{\psi}_0 \left(U''^{ab} - \frac{2U'^a U'^b}{i\hbar + U} \right) \psi_0 \right] = \ln \det \Sigma^{ab} + \text{tr} [(\Sigma^{ac})^{-1} \bar{\psi}_0 \Omega^{cb} \psi_0]$

into Eq.(8) we have,

$$\begin{aligned} V^{(\Lambda-\Delta\Lambda)} &= V^{(\Lambda)} - \frac{1}{2\text{Vol}} \sum_q (\ln \det \Sigma - n_f c_d \ln D_F) \\ U^{(\Lambda-\Delta\Lambda)} &= U^{(\Lambda)} - \frac{1}{2\text{Vol}} \sum_q \text{tr} \Sigma^{-1} \cdot \Omega. \end{aligned} \quad (9)$$

Finally letting,

$$\begin{aligned} \sum_q f(q) &= (\text{Vol}) A_d \Lambda^{d-1} \Delta\Lambda f(\Lambda) \\ \lim_{\Delta\Lambda \rightarrow 0} \Lambda \frac{X^{(\Lambda-\Delta\Lambda)} - X^{(\Lambda)}}{\Delta\Lambda} &= -\Lambda \frac{\partial X^{(\Lambda)}}{\partial \Lambda} \end{aligned} \quad (10)$$

(where $A_d = \int \frac{d\Omega_d}{(2\pi)^d}$ and $X = V$ or U) we arrive at,

$$\Lambda \frac{\partial V^{(\Lambda)}}{\partial \Lambda} = -\frac{A_d}{2} \Lambda^d (\ln \det \Sigma - n_f c_d \ln D_F) \quad (11)$$

$$\Lambda \frac{\partial U^{(\Lambda)}}{\partial \Lambda} = -\frac{A_d}{2} \Lambda^d \text{tr} (\Sigma^{-1} \cdot \Omega). \quad (12)$$

Eq.(11) represents three equations for the V 's and Eq.(12) represents six equations for the m 's and the g 's. Note that even though we've considered the $O(4)$ case, Eqs. (11) and (12) are valid, in principle, for $O(N)$ although the explicit derivation of the flow equations for $O(N)$ field theories with broken chiral symmetry is impeded by the calculation of $\det \Sigma$ and $\text{tr}(\Sigma^{-1} \cdot \Omega)$.

To obtain the explicit flow equations for $V_i(\rho)$, $m_i(\rho)$, and $g_i(\rho)$, $i = 0, 1, 2$, one computes the elements of the matrices Σ and Ω and evaluates the determinant and the trace, equating the coefficients of σ^0 , Γ , σ , $\sigma\Gamma$, σ^2 , $\sigma^2\Gamma$ on each side of Eqs. (11) and (12). This will result in nine nonlinear coupled partial differential equations. The evaluation of the determinant and trace are greatly simplified by performing a similarity transformation on Σ and Ω . We choose a transformation that picks out the zeroth or σ -component of the scalar field, $\vec{\phi}$,

$$\mathbf{S} \cdot \vec{\phi} = \rho \begin{pmatrix} 1 \\ 0 \\ 0 \\ 0 \end{pmatrix} = \rho \hat{\sigma}. \quad (13)$$

Such a matrix is constructed by rotating an arbitrary 4-vector (in isospin space) through three successive angles bringing it coincident with the σ -axis. For a particular choice of rotations we have

$$\mathbf{S} = \begin{pmatrix} \sigma & \pi_1 & \pi_2 & \pi_3 \\ -\pi'_1 & \frac{\sigma\pi_1}{\pi'_1} & \frac{\sigma\pi_2}{\pi'_1} & \frac{\sigma\pi_3}{\pi'_1} \\ 0 & -\frac{\rho\pi'_2}{\pi'_1} & \rho \frac{\pi_2\pi_1}{\pi'_2\pi'_1} & \rho \frac{\pi_3\pi_1}{\pi'_2\pi'_1} \\ 0 & 0 & -\rho \frac{\pi_3}{\pi'_2} & \rho \frac{\pi_2}{\pi'_2} \end{pmatrix}. \quad (14)$$

One can easily verify that $\mathbf{S} \cdot \vec{\phi} = \rho \hat{\sigma}$ and $\mathbf{S} \cdot \mathbf{S}^T = 1$. A similarity transformation with Eq.(14),

$$\begin{aligned} \Sigma' &= \mathbf{S} \cdot \Sigma \cdot \mathbf{S}^T \\ \Omega' &= \mathbf{S} \cdot \Omega \cdot \mathbf{S}^T, \end{aligned} \quad (15)$$

now returns Σ' with only 6 elements nonzero,

$$\Sigma' = \begin{pmatrix} \Sigma_{00} & \Sigma_{01} & 0 & 0 \\ \Sigma_{10} & \Sigma_{11} & 0 & 0 \\ 0 & 0 & \Sigma_{22} & 0 \\ 0 & 0 & 0 & \Sigma_{33} \end{pmatrix}. \quad (16)$$

As can be seen, this simplifies the calculation of the determinant and the trace in Eqs. (11) and (12).

The derivation of the flow equations to $\mathcal{O}(\sigma^2)$ as outlined above is underway. Results for a special case in which the flows of m and g in Eq.(1) are ignored are well understood at present. Previously obtained results from the flow equations for generalized Yukawa coupled fermions [1] show (for moderate bare Yukawa couplings) the running of $g(\Lambda)$ to be nearly constant. Thus we expect the results for this special case to be little changed by the inclusion of the m and g flows. For this case one only has Eq.(11) with $D_F = \Lambda^2 + m_0^2 + g_0^2 \rho^2$ and the flow equations have the form,

$$\begin{aligned}
\Lambda \frac{\partial V_0}{\partial \Lambda} &= -\frac{A_d}{2} \Lambda^d (\ln F_0(\rho) - n_f c_d \ln D_F) \\
\Lambda \frac{\partial V_1}{\partial \Lambda} &= -\frac{A_d}{2} \Lambda^d \frac{F_1(\rho)}{F_0(\rho)} \\
\Lambda \frac{\partial V_2}{\partial \Lambda} &= -\frac{A_d}{2} \Lambda^d \frac{F_2(\rho)}{F_0(\rho)}
\end{aligned} \tag{17}$$

with $F_0(\rho)$, $F_1(\rho)$, $F_2(\rho)$ defined through,

$$\det \Sigma' = F_0(\rho) + \sigma F_1(\rho) + \frac{\sigma^2}{2} F_2(\rho). \tag{18}$$

As a check, we see that the result for $O(4)$ chirally symmetric scalar field theory is obtained for $F_1 = F_2 = n_f = 0$ and,

$$F_0(\rho) = (\Lambda^2 + \frac{1}{\rho} V_0'(\rho))^3 (\Lambda^2 + V_0''(\rho)) \tag{19}$$

so that,

$$\Lambda \frac{\partial V_0(\rho)}{\partial \Lambda} = -\frac{A_d}{2} \Lambda^d [\ln (\Lambda^2 + V_0''(\rho)) + 3 \ln (\Lambda^2 + \frac{1}{\rho} V_0'(\rho))]. \tag{20}$$

(cf Eq.(8) in Ref. [5].)

The equations (17) can be numerically integrated using finite difference formulae with a polynomial fit to the potentials at each momentum step [1,5]. Inputs to the calculation are Λ_{UV} , Λ_{IR} , the ultraviolet and infrared momentum scales respectively, m_0 , the current quark mass, and λ_0 , the bare boson 4-point coupling, all at zero density; m_0^B , the bare boson mass, is tuned so that $f_\pi = \langle \phi \rangle_{vac} = 93 \text{ MeV}$, then $g_0 = M/3f_\pi$ where M is the nucleon mass. The model then predicts m_π and m_σ at zero density. A crude extension to finite density is made by simply turning off the fermion loops when the momentum scale reaches k_F , the fermi momentum. More sophisticated finite density calculations are under investigation. Fig. 1 shows the results of a calculation for $\Lambda_{UV} = 935 \text{ MeV}$, $\Lambda_{IR} = 139 \text{ MeV}$, $m_0 = 7.2 \text{ MeV}$, and $\lambda_0 = 10$. Λ_{UV} and Λ_{IR} were chosen to coincide roughly with nucleon and pion masses, the momenta, respectively. The value of m_0 was taken from the particle data book [6]. For $k_F = 0$, $m_\sigma = 581 \text{ MeV}$ and $m_\pi = 130 \text{ MeV}$. For $k_F \approx \text{nuclear density} = 270 \text{ MeV}$, $m_\sigma = 487 \text{ MeV}$, $m_\pi = 137 \text{ MeV}$, and $f_\pi = 84 \text{ MeV}$. These numbers are consistent with the restoration of chiral symmetry at finite density. Note that the primary contribution to V comes from V_0 as expected since the current quark mass only weakly breaks chiral symmetry. Scattering lengths $a_{\pi\pi}$ and $a_{\pi N}$ are computed. We see that $a_{\pi\pi} \rightarrow 0$ when $m_0 \rightarrow 0$.

Extensions to include the Yukawa and current quark mass flow are underway as well as a systematic comparison of our results with other sigma model calculations and experimental results.

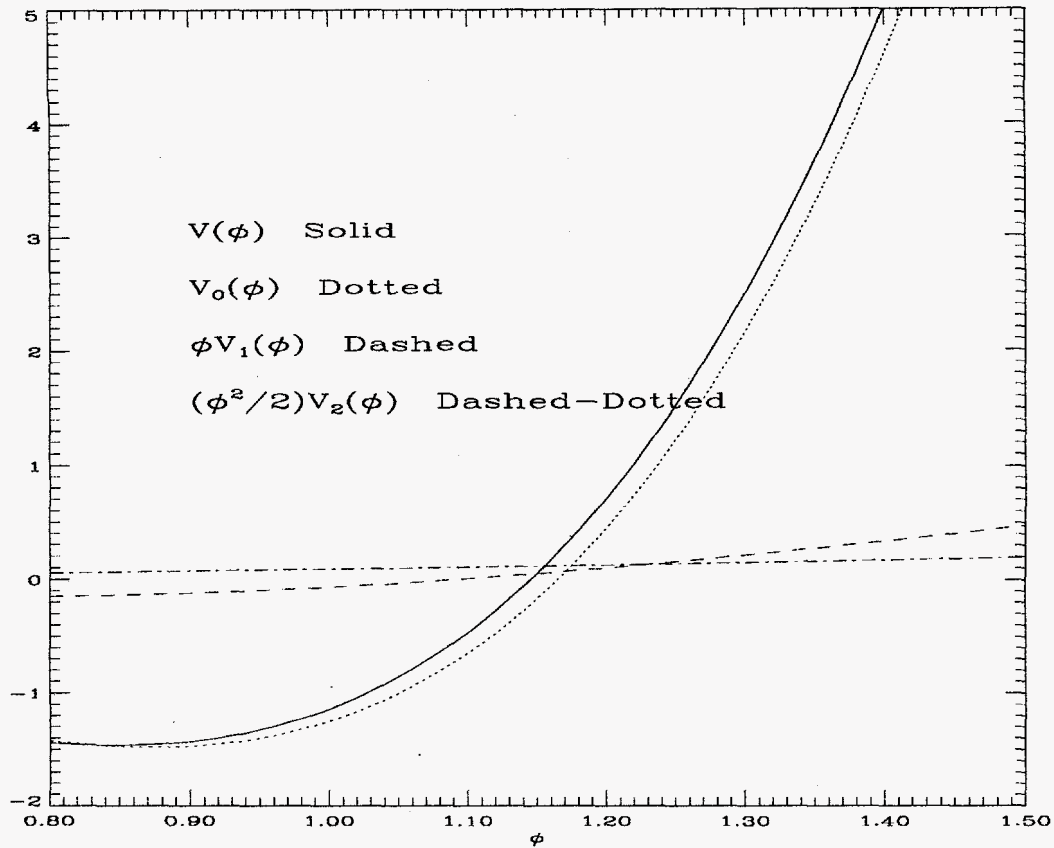


Figure 1. Renormalization Group Effective potentials for the sigma model for $\Lambda_{UV} = 935\text{MeV}$, $\Lambda_{IR} = 135\text{MeV}$, $m^{(0)} = 7.2\text{MeV}$, and $\lambda_0 = 10$.

-
- ¹ J.R. Shepard, A.S. Johnson, and J.A. McNeil, *University of Colorado at Boulder Nuclear Physics Laboratory Technical Progress Report*, September, 1995
- ² M. Maggiore, *Z. Phys.* **C41**, 687 (1989).
- ³ T.E. Clark, B. Haeri and S.T. Love, *Nucl. Phys.* **B402**, 628 (1993).
- ⁴ M. Gell-Mann and M. Lévy, *Nuovo Cimento*, **16**, 705, (1960)
- ⁵ J.R. Shepard, V. Dmitrašinović and J.A. McNeil, *Phys. Rev.* **D51**, 7017 (1995).
- ⁶ Particle Data Group, *Phys. Rev.* **D54**, 1 (1996)

Renormalization Group Effective Potentials in ϕ^4 Scalar Field Theories at Finite Temperature. J.R. Shepard and J.D. Shafer (University of Colorado)

The application of renormalization group techniques to the calculation of zero temperature effective potentials [1] has motivated us to extend these techniques to systems at finite temperature. We begin by considering the bare action for a single component scalar field theory in d euclidean dimensions at inverse temperature β :

$$S_0 = \int_0^\beta d\tau \int d^{d-1}x \left(\frac{1}{2} (\partial_\mu \phi)^2 + U^{(\Lambda_0)}(\phi) \right). \quad (1)$$

Here, $U^{(\Lambda)}(\phi)$ is the bare potential at the UV cutoff scale, Λ_0 . We now proceed to develop an RG differential equation which will enable us to determine the finite temperature effective potential, $U^{(\Lambda)}(\phi_0)$, for the uniform field component, ϕ_0 , at a new, lower momentum scale, Λ . To accomplish this, we use the euclidean approach of Matsubara [2], [3] by defining a new temporal variable, $\tau = it$. Our scalar fields are then periodic in the temporal direction with period β , and may be decomposed as

$$\phi(\vec{x}, \tau) = \phi_0 + \varphi(\vec{x}, \tau) \quad (2)$$

with uniform field component, ϕ_0 , given by

$$\phi_0 = \left(\frac{1}{\beta V} \right) \int_0^\beta d\tau \int d^{d-1}x \phi(\vec{x}, \tau), \quad (3)$$

and

$$\varphi(\vec{x}, \tau) = \left(\frac{\beta}{V} \right)^{1/2} \sum_{\vec{q}, n \neq 0}^{(\Lambda)} e^{i(\vec{q} \cdot \vec{x} + \omega_n \tau)} \phi_{\vec{q}, n}, \quad (4)$$

a sum over Fourier modes, with the superscript Λ denoting that only modes such that $0 \leq (q^2 + \omega_n^2)^{1/2} \leq \Lambda$ are summed. Periodic boundary conditions are assumed in the spatial direction, with $V = \int d^{d-1}x$ denoting the volume of the spatial "box". Since scalar field statistics are bosonic, the temporal frequencies, $\omega_n = \frac{2n\pi}{\beta}$, ensure that the field is appropriately periodic in the temporal direction.

We now proceed by expanding $U^{(\Lambda)}(\phi)$ in a Taylor series about the uniform field component, ϕ_0 . Inserting this, and eqs. 3 and 4 into our expression for the action given by eq. 1, we obtain, to second order in the field amplitudes,

$$S^{(\Lambda)} \simeq \beta V U^{(\Lambda)}(\phi_0) + \frac{\beta^2}{2} \sum_{\vec{q}, n \neq 0}^{(\Lambda)} [q^2 + \omega_n^2 + U''^{(\Lambda)}(\phi_0)] \phi_{\vec{q}, n} \phi_{\vec{q}, n}^*. \quad (5)$$

This expression now allows us to calculate the action at a smaller momentum scale, $\Lambda - \Delta\Lambda$, by means of the RG flow relation,

$$e^{-S(\Lambda - \Delta\Lambda)} = \prod_{\vec{q}, n}^{(\Lambda)} \int d\phi_{\vec{q}, n} d\phi_{\vec{q}, n}^* e^{-S^{(\Lambda)}}, \quad (6)$$

where the primed product indicates that only modes corresponding to momenta in a shell satisfying $\Lambda - \Delta\Lambda \leq (q^2 + \omega_n^2)^{1/2} \leq \Lambda$ are integrated. It is for this reason that we have neglected terms higher than second order in eq. 5 above. For each field amplitude, the number of in-shell modes is proportional to the shell thickness, $\Delta\Lambda$. Thus, when we take the limit of an infinitesimally thin shell, terms in the action containing m powers of the field amplitudes vanish as $(\Delta\Lambda)^m$ as $\Delta\Lambda \rightarrow 0$.

After integrating over the in-shell modes, we project out the effective potential by setting all remaining non-uniform field amplitudes to zero. After a bit of algebra, we obtain,

$$U^{(\Lambda-\Delta\Lambda)}(\phi_0) = U^{(\Lambda)}(\phi_0) + \frac{1}{2\beta V} \sum_{\vec{q},n} {}^{(\Lambda)} \ln \left[q^2 + \omega_n^2 + U''^{(\Lambda)}(\phi_0) \right] - \frac{1}{2\beta V} \sum_{\vec{q},n} {}^{(\Lambda)} \ln \left(\frac{2\pi}{\beta^2} \right). \quad (7)$$

Since we are concerned only with the ϕ_0 dependence of the effective potential for a specific β , we may neglect the last term of this expression. We pass to the continuum by noting that as $V \rightarrow \infty$,

$$\frac{1}{V} \sum_{\vec{q}} {}^{(\Lambda)} \rightarrow \int \frac{d^{d-1}q}{(2\pi)^{d-1}} \theta(\Lambda - |q^2 + \omega_n^2|) \theta(|q^2 + \omega_n^2| - \Lambda + \Delta\Lambda). \quad (8)$$

Integrating over the shell defined by the theta functions, and taking the limit as $\Delta\Lambda \rightarrow 0$, we obtain our RG equation for the finite temperature effective potential,

$$\frac{dU^{(\Lambda-\Delta\Lambda)}(\phi_0)}{d\Lambda} = -\frac{A_{d-1}}{2\beta} \sum_{n=-[\frac{\beta\Lambda}{2\pi}]}^{[\frac{\beta\Lambda}{2\pi}]} \left[\Lambda^2 - \left(\frac{2n\pi}{\beta} \right)^2 \right]^{\frac{d-2}{2}} \ln \left[\Lambda^2 + U''^{(\Lambda)}(\phi_0) \right], \quad (9)$$

where we have defined $A_d \simeq \int \frac{d\Omega_d}{(2\pi)^d} = [2^{d-2} \pi^{d/2} \Gamma(d/2)]$, and $[\frac{\beta\Lambda}{2\pi}]$ denotes the largest integer less than $\frac{\beta\Lambda}{2\pi}$. The constrained sum arises as a consequence of the fact that even in the continuum limit the temporal spectrum of our Fourier decomposed field is quite discrete. We may therefore take the continuum limit of the $d-1$ dimensional spatial coordinates, but must sum, not integrate, over the discrete temporal spectrum. The constraint appears because $\Lambda^2 = q^2 + \frac{2n\pi}{\beta}$, and since Λ^2 is finite, there are only a finite number of values of n which can satisfy this equality. Effectively, we integrate over a series of $d-1$ dimensional shells in momentum space, with the radius of the n^{th} shell, q_n , equal to $(\Lambda^2 - \omega_n^2)^{1/2}$.

We note that as $T \rightarrow 0$ ($\beta \rightarrow \infty$),

$$\lim_{\beta \rightarrow \infty} \frac{1}{\beta} \sum_{n=-\infty}^{\infty} \rightarrow \int \frac{d\omega}{(2\pi)}, \quad (10)$$

with ω_n now a continuous variable, ω . Consequently, we recover the familiar zero temperature limit of [1]:

$$\frac{dU^{(\Lambda)}(\phi)}{d\Lambda} = -\frac{A_d}{2} \Lambda^{d-1} \ln \left[\Lambda^2 + U''^{(\Lambda)}(\phi) \right]. \quad (11)$$

In the limit of very high temperature, as $\beta \rightarrow 0$, the sum over Matsubara modes of eq. 9 collapses to a single term. In this case,

$$\frac{dU^{(\Lambda)}(\phi)}{d\Lambda} = -\frac{A_{d-1}}{2\beta}\Lambda^{d-2}\ln\left[\Lambda^2 + U''^{(\Lambda)}(\phi)\right]. \quad (12)$$

Defining $\tilde{U}^{(\Lambda)}(\tilde{\phi}) \equiv \beta U^{(\Lambda)}(\phi)$, and $\tilde{\phi} \equiv \sqrt{\beta}\phi$, we observe that

$$\frac{d\tilde{U}^{(\Lambda)}(\tilde{\phi})}{d\Lambda} = -\frac{A_{d-1}}{2}\Lambda^{d-2}\ln\left[\Lambda^2 + \tilde{U}''^{(\Lambda)}(\tilde{\phi})\right], \quad (13)$$

with primes now denoting differentiation with respect to $\tilde{\phi}$. Clearly, in this limit the temperature parameter β decouples from the theory and we are left with the familiar zero-temperature result of Ref. [1] in $d-1$ dimensions. This is consistent with the phenomenon of dimensional reduction at high temperature.

We may proceed to integrate eq. 9 numerically by expanding $U^{(\Lambda)}(\phi)$ as a finite power series in ϕ ,

$$U^{(\Lambda)}(\phi) = \sum_{j=1}^M \mathcal{U}_{2j}(\Lambda)\phi^{2j}, \quad (14)$$

with the boundary condition that the bare and effective potentials coincide at the UV cutoff, Λ_0 , i.e.,

$$\mathcal{U}_2(\Lambda_0) = m_0^2, \quad \mathcal{U}_4(\Lambda_0) = \lambda_0, \quad \text{and} \quad \mathcal{U}_{2j}(\Lambda_0) = 0 \quad \text{for} \quad j \geq 3. \quad (15)$$

The range of the Λ integration is divided into N equal length intervals, $\Delta\Lambda$, given by

$$\Lambda_n = \Lambda_0 - n\Delta\Lambda, \quad (16)$$

where $\Lambda_{IR} = \frac{2\pi}{N_{lat}}$ is the infrared scale appropriate for N_{lat} sites in each of the spatial directions. Λ is now discretized so that $\Lambda_n = \Lambda_0 - n\Delta\Lambda$. The field variable, ϕ is similarly discretized, and integration is accomplished by fitting the potential $U^{(\Lambda_n)}(\phi)$ with the expansion of eq. 14, and computing $U''^{(\Lambda_n)}(\phi)$ from the expansion coefficients. The potential $U^{(\Lambda_{n+1})}(\phi_i)$ is then determined by

$$U^{(\Lambda_{n+1})}(\phi_i) = U^{(\Lambda_n)}(\phi_i) + \frac{A_{d-1}\Delta\Lambda}{2\beta} \sum_{n=-\lceil\frac{\beta\Lambda_n}{2\pi}\rceil}^{\lceil\frac{\beta\Lambda_n}{2\pi}\rceil} \left(\Lambda_n^2 - \left(\frac{2n\pi}{\beta}\right)^2 \right)^{\frac{d-2}{2}} \ln\left[\Lambda_n^2 + U''^{(\Lambda_n)}(\phi_i)\right] \quad (17)$$

for each ϕ_i . This process is iterated until Λ_{IR} is reached. The resulting quantities $\mathcal{U}_m(\Lambda_{IR})$ are renormalized m -point couplings at momentum scale Λ_{IR} .

A latticized version of eq. 9 may be formulated by making use of the fact that, for a uniform system on an $N_x^{d-1} \times N_\tau$ lattice with periodic boundary conditions, the lattice normal modes are momentum eigenstates with wavenumbers $\kappa_{n_x} = \frac{2n_x\pi}{N_x}$ in the spatial directions, and $\kappa_{n_\tau} = \frac{2n_\tau\pi}{N_\tau}$ in the temporal direction. Here, $n_x = 1, 2, \dots, N_x$, and $n_\tau = 1, 2, \dots, N_\tau$. Taking the lattice constant to be unity, we observe the equivalence of the following expressions:

$$\frac{1}{\beta} \sum_{n=-\infty}^{\infty} \int \frac{d^{d-1}q}{(2\pi)^{d-1}} f(q^2) \Theta\left[\Lambda^2 - (q^2 + \omega_n^2)\right] \rightarrow \frac{1}{V} \sum_{n_1=1}^{N_x} \dots \sum_{n_{d-1}=1}^{N_x} \sum_{n_\tau=1}^{N_\tau} f(k_{n_1}^2 + \dots + k_{n_{d-1}}^2 + k_{n_\tau}^2). \quad (18)$$

The appearance of $k_{n_i}^2 \equiv 4 \sin^2(\frac{\kappa_{n_i}}{2})$ is due to the finite difference approximation of lattice derivatives, and $\mathcal{V} = N_\tau \times N_x^{d-1}$. We may now define

$$k_N^2 \rightarrow k_{n_1, n_2, \dots, n_{d-1}, n_\tau}^2 \equiv k_{n_1}^2 + k_{n_2}^2 + \dots + k_{n_{d-1}}^2 + k_{n_\tau}^2. \quad (19)$$

These quantities may be sorted by magnitude and relabeled, with the result that

$$k_1^2 \geq \dots \geq k_N^2 \geq k_{N+1}^2 \geq \dots \geq k_{N_x^{d-1} N_\tau}^2, \quad (20)$$

where $k_1^2 = 4d$ and $k_{N_x^{d-1} N_\tau}^2 = 0$. With these definitions, the evolution of the RG effective potential on the lattice at finite temperature is described by

$$U^{(k_{N+1}^2)}(\phi_i) = U^{(k_N^2)}(\phi_i) + \frac{1}{2\mathcal{V}} \ln \left[k_N^2 + U''^{(k_N^2)}(\phi_i) \right], \quad (21)$$

subject to the boundary condition

$$U^{(k_1^2)}(\phi_i) = U^{(\Lambda_0)}(\phi_i). \quad (22)$$

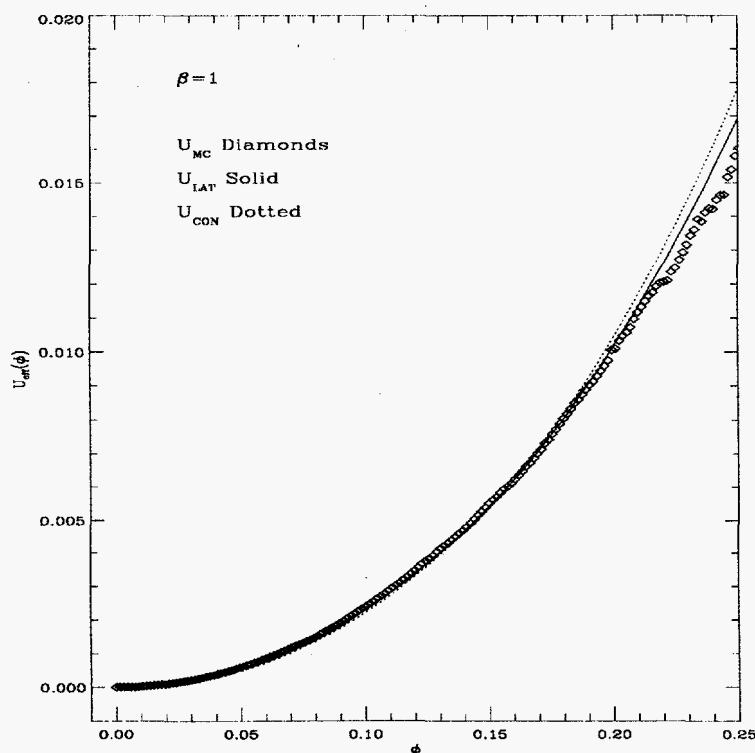


Fig. 1. Effective potentials for the $d=4$, $O(1)$ case at $\beta = 1$. Circles represent MC results while the solid lines correspond to LRG calculations. Statistical uncertainties for the MC effective potentials are not shown, but are typically smaller than the circles.

Finally, we perform a straight Monte Carlo calculation using the action of eq. 1. Here, as above, we employ a lattice with N_x sites in each of the $d - 1$ spatial directions, and N_τ sites in the temporal direction. N_τ corresponds to the inverse temperature, β , so it can vary from 1 (corresponding to infinite temperature) to N_x (corresponding to zero temperature). Periodic boundary conditions are assumed in each direction.

By performing a Monte Carlo calculation, we construct a histogram of the number of field configurations generated vs. the average value of the field on the lattice for these configurations. If $d\mathcal{N}$ is the number of field configurations with average field values in an interval $d\bar{\phi}$ about $\bar{\phi}$, the average field on the lattice for a given configuration, then

$$d\mathcal{N}(\bar{\phi}) \propto \exp[-\mathcal{V}U_{eff}(\bar{\phi})]d\bar{\phi}. \quad (23)$$

So, to within an irrelevant constant,

$$U_{eff}(\bar{\phi}) = \frac{-1}{\mathcal{V}} \ln \left[\frac{d\mathcal{N}(\bar{\phi})}{d\bar{\phi}} \right]. \quad (24)$$

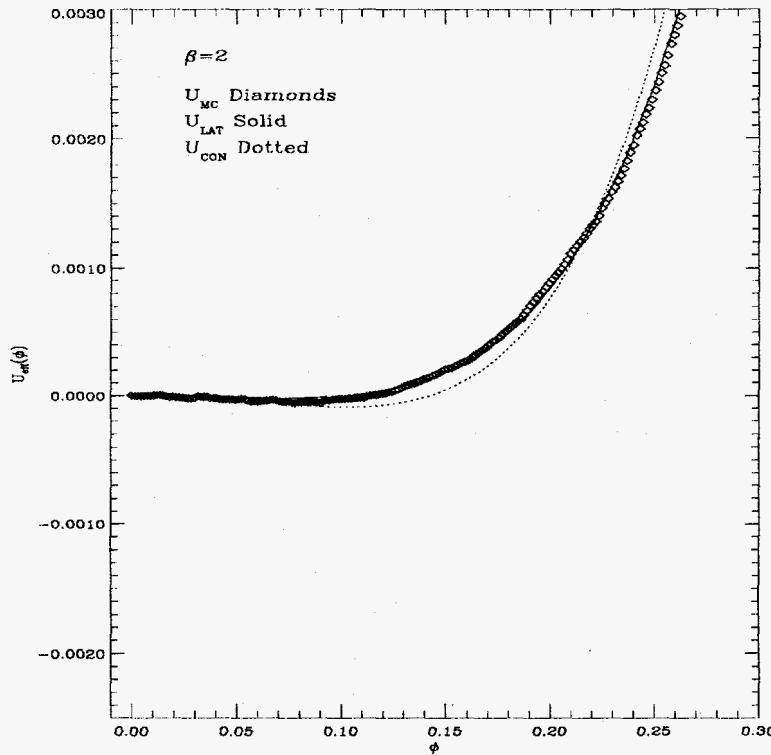


Fig. 2. Same as Fig.1, but for $\beta = 2$.

We have numerically calculated the Monte Carlo and lattice and continuum RG effective potentials for an 8^4 lattice, corresponding to zero temperature, as well as those for $8^3 \times 4$, $8^3 \times 2$, and $8^3 \times 1$ lattices, which correspond to successively higher temperatures. To compute the continuum RG potential, the infrared cutoff, Λ_{IR} , is set to $\frac{2\pi}{N_{lat}}$. However, the UV cutoff, Λ_0 , is ambiguous, and may be determined by requiring that the phase space volumes integrated over in the continuum and lattice cases be identical. This is ensured by choosing Λ_0 so that

$$\frac{1}{\beta} \sum_{n_r = -\left[\frac{\beta\Lambda_0}{2\pi}\right]}^{\left[\frac{\beta\Lambda_0}{2\pi}\right]} A_{d-1} \int_0^{\sqrt{\Lambda_0^2 - \left(\frac{2n_r\pi}{\beta}\right)^2}} k^{d-2} dk = 1. \quad (25)$$

For the Monte Carlo calculations shown below, the bare mass, m_0 , and bare coupling, λ_0 , were fixed at 1.965i and 10, respectively. This value of m_0 was chosen or "tuned" to yield a

small renormalized mass, m , and a correspondingly large correlation length. The four-point coupling, λ , and renormalized mass were determined by fitting the MC effective potentials with a polynomial of the form

$$U_{eff}(\phi) = \frac{1}{2}m^2\phi^2 + \frac{1}{4}\lambda\phi^4. \quad (26)$$

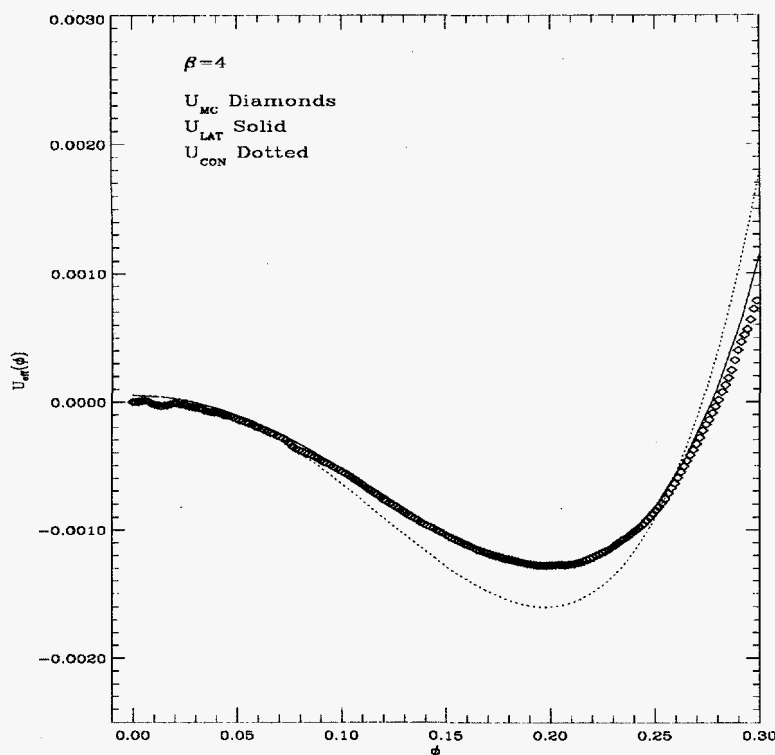


Fig. 3. Same as Fig.1, but for $\beta = 4$.

For each lattice and continuum RG calculation, the bare coupling was also fixed at $\lambda_0 = 10$, and the bare mass, m_0 , was tuned to yield a value of $\langle \phi^2 \rangle$ equal to that of the corresponding MC calculation. For the MC case, $\langle \phi^2 \rangle$ is simply the average of the square of the field values over the lattice. In the case of the lattice and continuum RG calculations, it is defined as

$$\langle \phi^2 \rangle = \frac{\int d\phi \phi^2 \exp - [U_{eff}(\phi)V]}{\int d\phi \exp - [U_{eff}(\phi)V]}, \quad (27)$$

with V the volume of the appropriate space. Examination of figures 1-4 shows excellent agreement of Monte Carlo and lattice RG potentials. The continuum RG potentials do not exhibit the same close agreement with the Monte Carlo results; however, some disagreement with lattice results is to be expected since the continuum RG does not include lattice artifacts. We note that the figures show that the symmetry of the system is effectively broken as the value of the inverse temperature, β , is raised from $N_\tau = 1$ to $N_\tau = 8$. Effectively, we see the system "freeze" as the temperature is lowered. Clearly, our continuum RG potential exhibits the correct qualitative behavior as the temperature parameter, β , is raised, and the system undergoes

a phase change, as expected. The close quantitative agreement between Monte Carlo results, which we may consider to be exact, and our lattice RG effective potentials inspires confidence in the RG method and suggests we may reliably calculate physical effective potentials using the continuum RG formulation. Our plans for future research in this area include extension of these techniques to systems involving interacting multi-component boson and fermion fields.

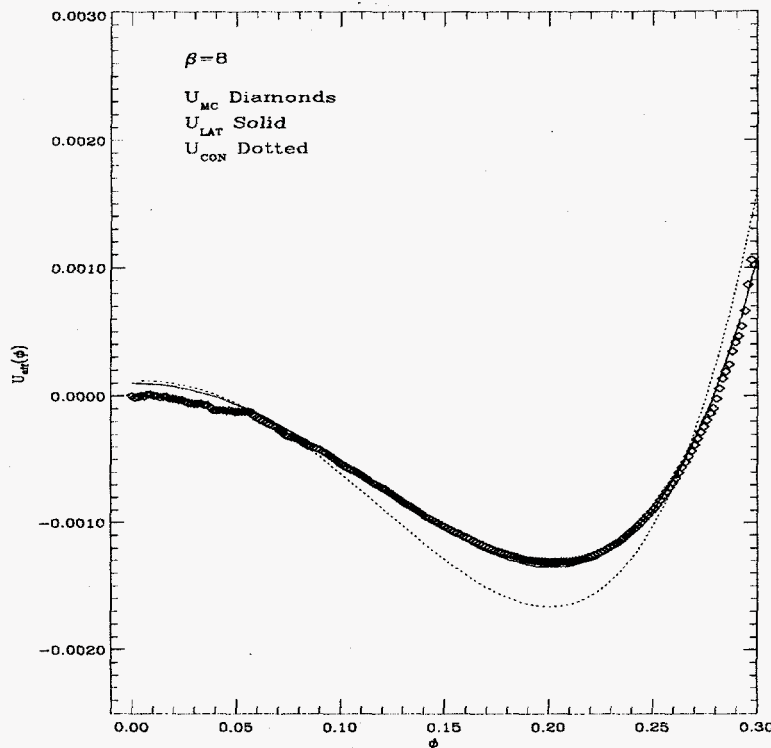


Fig. 4. Same as Fig.1, but for $\beta = 8$.

¹ J. R. Shepard, V. Dmitrašinović and J. A. McNeil, Phys. Rev. **D51**, 7017 (1995).

² T. Matsubara, Prog. Theor. Phys. **14**, 351 (1955).

³ J.I. Kapusta, Finite-temperature field theory, Cambridge University Press, Cambridge (1989).

1. Published Articles

1. "Isospin-breaking corrections to nucleon electroweak form factors in the constituent quark model", V. Dmitrašinović and S.J. Pollock, *Physical Review C* **52** 1061 (1995)
2. "Electron-nucleon cross section in (e,e'p) reactions ", S.J. Pollock, H.W.L. Naus, J.H. Koch, *Physical Review C* **53**, 2304 (1996).
3. "Goldstone Theorem in the Gaussian Functional Approximation to the Scalar ϕ^4 Theory", V. Dmitrašinović, J.R. Shepard and J.A. McNeil, *Z. Phys. C* **69**, 359-363 (1996).
4. " $U_A(1)$ Breaking and Scalar Mesons in the Nambu and Jona-Lasinio model", V. Dmitrašinović, *Phys. Rev. C* **53**, 1383-1396 (1996).
5. "Positivity restrictions in polarized deep-inelastic electron scattering from the deuteron", V. Dmitrašinović, *Phys. Rev. D* **54**, 1237-1240 (1996).
6. "A Comment on General Formulae for Polarization Observables Deuteron Electrodisintegration and Linear Relations", V. Dmitrašinović and F. Gross, *Few-Body Systems* vol. **20**, 41-46 (1996).
7. "The Pion and Quark Electromagnetic Self-Masses in the Nambu-Jona-Lasinio Model", V. Dmitrašinović, R.H. Lemmer, H.J. Schulze and R. Tegen, *Phys. Rev. D* **52**, 2855-2877 (1995).

2. Articles Accepted or Submitted for Publication

1. "Higgs mechanism in the Gaussian functional approximation", V. Dmitrašinović, to appear in *Nuovo Cimento A*, (1996).
2. "Weinberg sum rules in an effective chiral field theory", V. Dmitrašinović, S. P. Klevansky and R.H. Lemmer, to appear in *Phys. Lett. B* (1996).
3. "Axial current conservation in the Bethe-Salpeter approach to nuclear two-body problem", V. Dmitrašinović, to appear in *Phys. Rev. C* (1996).
4. "Hara's theorem in the constituent quark model" V. Dmitrašinović, to appear in *Phys. Rev. D*, (1996).
5. "Monte Carlo and Renormalization Group Effective Potentials in Scalar Field Theories at Finite Temperature", J. D. Shafer and J.R. Shepard, submitted to *Phys. Rev. D*

3. Invited and Contributed Papers and Abstracts

1. "Isospin-breaking corrections to nucleon weak form factors" V. Dmitrašinović and S.J. Pollock. Abstract submitted to "Gordon Conference on Photonuclear Reactions" Tilton, NH, July 1996

2. "Renormalization Group Studies of Field Theories of Interacting Bosons and Fermions", A. Johnson, J.A. McNeil, J.R. Shepard. Abstract and contributed talk, submitted to BAPS Vol 41 no. 2, E711, APS Indianapolis, Indiana meeting, Apr 1996
3. "Renormalization Group Flow Equations for Linear Sigma Models", A. Johnson, J.A. McNeil, J.R. Shepard. Abstract and contributed talk, submitted to BAPS DNP 96, FD-11, Cambridge MA meeting, Fall '96

C PERSONNEL

1. Academic and Scientific

P.D. Kunz	Emeritus Professor
J.R. Shepard	Professor
S.J. Pollock	Assistant Professor
J.A. McNeil	Colo. School of Mines (separate funding)
V. Dmitrašinović	Postdoctoral Researcher

2. Research Assistants

J. Shafer
M. Welliver
A. Johnson (PRA)